Turning halite fluid inclusions into accurate paleothermometers with Brillouin spectroscopy : development of a new method and application to the Last Interglacial in the Dead Sea

Emmanuel Guillerm

UNIVERSITÉ DE LYON

Université Claude Bernard Lyon 1

N° d'ordre NNT :

THÈSE de DOCTORAT DE L'UNIVERSITÉ DE LYON
Opérée au sein de :
l'Université Claude Bernard Lyon 1

Ecole Doctorale 52
Physique et Astrophysique

Spécialité de doctorat : Géosciences de l'environnement

Soutenue publiquement le 06/12/2019, par :
Emmanuel Guillerm

Turning halite fluid inclusions into accurate paleothermometers with Brillouin spectroscopy

Development of a new method and application to the Last Interglacial in the Dead Sea

---

Devant le jury composé de :

David A. Hodell	**Rapporteur**
Woodwardian Professor of Geology, University of Cambridge	
Tim K. Lowenstein	**Rapporteur**
Distinguished Professor, Binghamton University	
Mouna El Mekki-Azouzi	**Examinatrice**
Maître de Conférences, Université de Bizerte	
Ina Neugebauer	**Examinatrice**
Researcher, GFZ, Helmholtz Zentrum, Potsdam	
Christophe Lécuyer	**Examinateur**
Professeur, LGL-TPE, Université Claude Bernard Lyon 1	
Véronique Gardien	**Directrice de thèse**
Maître de Conférences, LGL-TPE, Université Claude Bernard Lyon 1	
Frédéric Caupin	**Co-Directeur de thèse**
Professeur, ILM, Université Claude Bernard Lyon 1	

Acknowledgments/Remerciements

To the members of the jury
I would like to express my deepest gratitude to David Hodell and Tim Lowenstein who accepted to review this work. Your relevant remarks and corrections helped greatly enrich it. I am extremely grateful to Ina Neugebauer, Mouna El Mekki-Azouzi and Christophe Lécuyer who accepted to be part of the defense committee.

Pour la reproduction de ce manuscrit
Merci Sam, tu fais un travail de grande qualité. Tu es le premier être humain que l'on rencontre à la fin d'une rédaction de thèse, et il est heureux de passer cette première journée de semi-liberté avec une personne si fascinante, d'une grande richesse intérieure, et consciencieuse avec ça !

A mes encadrants (et quasi-encadrant)
Véro, passer ces 4 années avec une encadrante aussi humaine que toi a été une grande chance. Tout au long de cette aventure, tu t'es souciée non seulement du bon déroulé scientifique de ma thèse mais aussi de tout ce qui va à côté. Tu m'as encouragé à faire, et tu as financé, nombre de conférences, workshops, summer schools qui ont été déterminants dans le mûrissement de mon travail ainsi que dans le tissage de mon réseau. Je t'en suis profondément reconnaissant. Je n'oublierai pas non plus ce fabuleux terrain en Ardèche, où tu m'as tant appris. Y passer du bon temps autour de quelques bouteilles de Saint Jo et de tranches de rire au beau milieu des vertes montagnes a constitué une belle ponctuation dans cette intense dernière ligne droite. Ta bonne humeur et ton calme dans les tempêtes ont été pour moi un trésor à la valeur inestimable pendant tout ce temps.
Fred, je te suis infiniment reconnaissant pour tout ce temps et toute cette énergie que tu as impliqués pour me transmettre les connaissances théoriques et expérimentales nécessaires à l'accomplissement de ma thèse. J'ai le sentiment d'être devenu un scientifique, et tu y es pour beaucoup. Camarade de galères en tout genre et de bricolages du dimanche, je te remercie pour avoir eu la patience de bidouiller le spectro avec un co-équipier aussi maladroit que moi ! Ta constance et ta persévérance dans les épreuves m'ont été chères.
Daniel, je t'inclus aussi dans ce paragraphe car si tu n'étais pas officiellement encadrant, ton implication dans mon travail et tes nombreux conseils ont été cruciaux dans l'accomplissement de ma thèse. Grâce à toi j'ai découvert la Mer Morte, j'ai accédé à plein d'échantillons, je suis entré en contact avec de nombreux scientifiques. Ta

simplicité, ta bienveillance et ton aura ont grandement facilité mes contacts avec des pairs. Gracias Don Ariztegui !

A ceux qui ont aidé au financement de ma fin de thèse
Je dois un grand merci à tous ceux qui ont supporté financièrement ma fin de thèse, je dois beaucoup à votre acte de solidarité. Merci Cécile et toute l'équipe Liquides, merci Dominique, merci Emanuela, merci aux différents thèmes du LGL et à leurs représentants. Merci aussi, à nouveau, Frédéric et Véronique, pour vous être démenés pour produire ce contrat de fin de thèse.

To my collaborators and those who assisted me in my scientific progression
Thank you Vincent Holten for your very useful help on the use of Mathematica, and for your codes which proved vital for my PhD! Thank you Bruno Issenmann for your help on the use of liquid nitrogen. Thank you Ingrid Antheaume for taking care of me when I got hurt with the liquid nitrogen! Thank you Michel Dubois and Ronald Bakker for your decisive help in the understanding of the petrography and physics of fluid inclusions. Thank you Döme Tanguy for your advice, and for the books you gave me, so that I could understand the mechanical processes at stake in my halite crystals. Thank you Olivier Pierre Louis for our discussions on the possible mechanisms for the entrapment of fluid inclusions in NaCl. Thank you Pascal for the many tips about the use of Cast&m. Thank you Damien Bouffard for the time you took to explain to me the thermal processes at stake in lakes. Thank you Arnault Lassin for inviting me to your RST session and introducing me to the work of your team. Thank you Adeline Lach for all this time you took to explain to me the nuts and bolts of PhreeSCALE. Thanks a million to Nicolas Waldmann for this fantastic field trip in the Dead Sea region and in Israel, which had a decisive impact on my work. Thank you Markus Schwab for your warm welcome at Potsdam and your valuable help in sampling core 5017-1. The latter was also made possible thanks to the very welcome assistance of Leo. Thank you Ina Neugebauer for sharing your knowledge on the Dead Sea. Thanks a million to Kristian Olson and Tim Lowenstein; collaborating on your work on Searles Lake shed a complete new light on my understanding of evaporites deposits.

A ceux qui m'ont aidé dans ma tâche d'enseignant
Merci Nico pour tes bons conseils quant aux méthodes d'enseignement, ainsi que pour tes fantastiques modèles pédagogiques. Merci Renaud et Jean-Philippe pour m'avoir ouvert la voie au chapitre des enseignements de L1. Merci Lutin de m'avoir filé un bon coup de pouce pour les cours d'évolution des espèces. Merci Manu et Fanny de m'avoir pris sous votre aile pour les cours de pétro, et à vous deux et Véro de m'avoir confié vos

bons filons. Merci Marianne pour ton aide précieuse pour les cours de géophysique. Merci Oriane pour ton travail précieux à la gestion des enseignements.

A l'école doctorale

Merci à Dany Davesne et à Sylvie Flores d'avoir su m'accompagner et trouver des solutions au moment le plus difficile. Votre gestion humaine des problèmes est précieuse pour tout doctorant.

Aux copain.e.s de géologie

Les rencontres que j'ai faites au labo de géologie (ou en lien avec le labo) ont pronfondément marqué ma vie, et j'espère que beaucoup d'entre vous resteront des amis pour encore longtemps.

Cori, mon copain de manif, j'ai trouvé en toi le gôchiste dont j'avais besoin pour poursuivre ma route sur le tapis rouge de la pensée marxisante; si j'avais su que ce serait un bourgeois des Monts d'or qui achèverait ma conversion ! J'espère qu'on se conseillera des bouquins autour d'une bière encore longtemps. Romain, à défaut d'avoir eu un intérêt scientifique, cette EGU 2016 aura eu la bonne idée de tisser nos liens à grand renfort de pintes, de saucisses au fromage, de poiriers et de soirée rooftop improbable; depuis lors, l'une de mes motivations pour poursuivre dans la science, c'est de refaire une telle conf avec toi ! Guillaume, c'est aussi à cette EGU que j'ai eu le grand bonheur de vraiment faire connaissance avec toi; tu constitues l'une des preuves, pour moi, qu'on peut devenir titulaire en restant simple, hilarant et bienveillant; je trouverai bien un prétexte scientifique bidon pour collaborer avec toi un jour ! Lutin, petite boule d'énergie pure; j'ai toujours été admiratif de tes qualités naturalistes, toujours sur les sentiers pour photographier les merveilles de la Nature sous leur meilleur jour; tu m'emmèneras en rando un jour ? Alex: en voilà un qui ne finira pas vieux con ! j'ai toujours eu un plaisir immense à discuter pendant des heures de questions philosophiques avec toi; ta sagesse n'a d'égal que ta connerie en soirée ! Claire (Duch), merci pour ton humour cynique inimitable ; et merci d'avoir eu la patience d'organiser mes trajets de conférences malgré ma catastrophique tendance à toujours oublier comment procéder pour les démarches ! Axelle, tu es une fille drôle, pleine d'énergie, engagée et inspirante. J'ai été touché que toi et Cori fassiez le déplacement pour ma soutenance de si loin. Jean-mi, Kévin, longtemps je n'ai entendu ces noms que comme une légende, jusqu'à cette funeste semaine caennaise. Heureusement que votre humour indestructible était là pour percer la grisaille normande. Camille, on s'est croisés de nombreuses fois au labo, mais il a fallu attendre le field trip en Mer Morte pour que je puisse vraiment te découvrir. Merci pour tous les conseils que tu as pu me donner, et merci pour les good vibes que tu propages.

Et maintenant, les potos du R6 ! Max, mon co-bureau intemporel, mais bien plus encore : la touche de bonté et d'humour qui adoucissait même mes journées les plus sombres.

Tu as été mon véritable remède au blues. A quand le prochain MarioKart-pinard ? Claire, ton énergie et ta bonne humeur ont été l'un des fers de lance de l'âge d'or du R6 ! David, tu es un mec d'une rare intelligence avec qui la discussion est toujours riche. J'adorerais que l'on revive nos soirées hilarantes downtown, à l'époque où nous étions jeunes et insouciants ! Arnauld, en parlant de ces soirées, je pense forcément à toi aussi. Tu es pour moi un véritable modèle de courage et de droiture, je t'admire. L'ami en qui l'on peut avoir confiance; et qui n'oublie pas d'être bien con ! Ivan le terrible, l'homme aux mille talents, je suis heureux de te compter parmi mes amis. A ce propos, pour Noël je veux: une guitare en bois de santal, un porte-flasque de whisky en cuir, et deux extensions mécaniques pour index afin de pouvoir écrire mes candidatures de postdoc en restant vautré au fond de ma chaise; merci d'avance. Fanny, merci pour les cours de karaté, mais la prochaine fois je te dose ! Je suis content d'avoir une fille rayonnante comme toi parmi mes amis. Niels, kleiner Bruder, le pouvoir du Brillouin est en toi. Tu es le premier être humain avec qui j'ai pu partager les affres du Brillouin, ça a changé ma vie ! Merci à Clément, Mélissa, Sylvain, Chloé, Maëlis, Rémy, Victor, Mélanie et tous les autres pour les soirées déjantées, les parties de rigolade en salle café, les marches et manifs.

Aux copain.e.s de physique

J'ai toujours considéré ce labo comme un havre de paix, et n'oublierai jamais les personnes rencontrées. Je remercie tout d'abord l'équipe Liquides; la bienveillance au sein de cette équipe, l'attention portée les uns envers les autres, m'ont beaucoup marqué et aidé. Un merci tout particulier à Agnès, tu es toujours là pour donner des conseils ou un coup de main, toujours avec sourire et jovialité.

Quentin, quel spécimen ! Un esprit qui tourne à mille à l'heure, l'homme avec qui on ne s'ennuie jamais. Nos bières sur les péniches, avec Ronan, me manquent ! Ronan, la force tranquille, l'homme apaisant, avec qui boire un café ou une bière est le meilleur des remèdes pour oublier les tracas de la thèse. On se capte sur Crozon ? Marie-Emeline, tout d'abord, merci de m'avoir appris les rudiments de Cast&m; j'en ferai quelque chose un jour, c'est certain ! Merci aussi pour ces moments de rigolade quand nous étions co-bureaux, ta pêche et ton humour fin, intelligent et un brin sarcastique me font délirer. Laurent, ton passage sur Lyon a été trop bref, mais je n'oublie pas nos bières et tes conseils musicaux. Alex, Flo, Félix, Seb, les anciens quoi, merci d'avoir fait une place parmi vous au géologue que je suis ! Leo, tes capacités sociales me fascinent, tu es quelqu'un avec qui le contact est si simple. Merci pour ces discussions politiques dans toutes les langues ; mais je t'assure que tu fais fausse route : je suis nul en espagnol ! Dolachai, je suis désolé de t'avoir donné le spectacle d'une chaise vide en lieu et place d'un co-bureau en chair et en os ; sache que j'ai beaucoup apprécié le peu de co-bureautage que l'on a passé ensemble. Tu es une personne bonne, sincère, et d'une tranquillité infaillible et apaisante. Ong, je t'écris en français car je souhaite que tu puisses réviser le français avant de revenir pour ta soutenance ! C'est un honneur de te

connaître et de t'avoir comme amie, j'ai beaucoup d'admiration pour ta gentillesse et ton ouverture d'esprit. Anto, merci d'avoir enrichi ma culture geek & memes. Romain, merci d'avoir été là lorsque j'étais seul géologue parmi des milliers de physiciens à Ljubljana !

Aux copain.e.s de la Mer Morte
Je n'oublierai jamais ce terrain en Israël, où j'ai rencontré des gens inoubliables. Antoine, Marta, J-C, Ines, Nicolo, à quand le prochain week-end ? Chaque fois que l'on se revoit est un moment mémorable. Voilà une autre motivation pour continuer dans la recherche : revivre des moments comme l'Israël ou l'IMS de Toulouse avec vous.

Sur Lyon
Merci Laura d'avoir déployé toute l'envergure de ta bienveillance pour m'intégrer sur Lyon. Ça a été une chance inouïe que l'on puisse habiter si près l'un de l'autre et raffermir nos liens d'amitié. Je ne crois pas avoir rencontré de personnes plus positives que toi, et te suis reconnaissant de m'avoir prodigué ces nombreux shots de bonne humeur durant ma thèse.
Merci Martin de m'avoir compté parmi tes amis. Nos sorties bière à la Croix Rousse ont beaucoup compté pour moi, et m'ont offert un véritable sas de décompression. J'espère pouvoir te visiter prochainement en Irlande !
Anne & Max, merci à vous deux pour ces nombreux moments passés ensemble. La vie est simple et croustillante avec vous ! Les soirées impro musicales restent gravées dans ma mémoire.
Morgane, j'aurais tant à dire ! Ces remerciements sont censés s'adresser à tous ceux qui m'ont apporté durant ma thèse, donc je me restreindrai au « moment lyonnais » de notre amitié. Je ne saurais quantifier l'inestimable chance de t'avoir eue à la maison chaque soir que je suis rentré (souvent bredouille) de mes journées de recherche. Merci pour ton soutien et notre indéfectible amitié, qui m'ont été si chers pendant ces premières années de thèse.

Ici et là/here and there
Merci Chloé pour ces formidables moments vécus à Urbino, dans les Alpes, à Rome, et où sais-je encore. Tu es une fille débordante de vie, engagée, dont la rencontre a été un moment important de ma vie ces dernières années. Merci aussi de m'avoir fait rencontrer toute ta bande d'amis aixois.
Thank you Rishie, too, for these fabulous moments in Italy. I thank you also for showing me that all americans are not like the cliché we have about them: they can surprisingly be dangerous quasi-communists like you! You're a fascinating man, and our discussions had a true influence on the way I envision the world.

Thank you Maxime, Maxence, Chiara, Shaun, Julia, Shlomit, Ruth and all the others for this fantastic moment in Urbino.
Nicau, aka Jean-Philippe Jarsson, je suis très heureux que les rencontres de la vie nous aient amenés à renouveler les liens amicaux et radiophoniques qui nous unissaient. Merci pour ces grands moments de rigolade à Aix et à Lyon.
Merci Quentin et Belen d'être revenus en France, vous m'aviez beaucoup manqué. Maintenant que la thèse est terminée, je promets que l'on trouvera moult occasions pour emmener ensemble le petit Gaspard au sommet des montagnes !
Merci Tinmar de nous avoir invités dans ton oasis omanaise. Cette escapade tropicale m'a rechargé à fond pour retourner au combat contre mon spectroscope. Et comme l'a dit le sage, « que l'étendue de notre amitié n'ait d'égal que l'infini des dunes d'Oman ».
Zineb, j'ai eu à chaque fois le même immense plaisir de te recevoir à la maison sur Lyon. Merci de m'avoir apporté ta lumineuse présence à plusieurs reprises pendant ma thèse.
Mélo, merci beaucoup d'avoir fait le déplacement de Toulouse pour ma soutenance, ça m'a beaucoup touché.

Ma famille
Merci à Claudine et Philippe de m'avoir ouvert les portes de leur petit paradis périgourdin. Ces séjours reposants et délicieux m'ont beaucoup apporté. Merci à Teimur, Nourana, Revan, Nihat et Fatima pour leur bonne humeur. Merci à Cracou, Darky, Artémis, Noiraud, Rikik, Pateline, Patchouli et Titus pour les docus animaliers en live, c'est très instructif.
Merci à mes frères David et Christophe et soeur Qing d'avoir senti que la vie loin de leur petit frère était dénuée de sens, et d'avoir ainsi déménagé sur Lyon. Les repas du dimanche avec vous ont sans doute été les moments parmi les plus salvateurs dans ces années de thèse, durant lesquels j'ai pu recharger mes batteries. J'ai de la chance d'avoir des frères et sœur aussi formidables que vous ! Merci Ewen d'être venu m'apporter du soutien pour s'occuper de tes parents, au moment où je n'avais plus le temps de supporter cette charge. Merci Jack pour tes conseils avisés et ton entrain à toute épreuve, reste comme tu es.
Merci Maman et Papa pour avoir fait de moi ce que je suis, avec mes défauts et mes qualités. J'ai lu une partie des travaux du sociologue Pierre Bourdieu, d'où je sais qu'il n'y pas de réussite sans transmission : je vous dois beaucoup pour être parvenu si loin dans les études, et pouvoir ainsi (croisons les doigts) pratiquer le métier dont j'ai toujours rêvé. Merci Maman pour ces sacrifices que tu as consentis pour notre éducation. Merci Papa de m'avoir transmis ta curiosité pour les sciences et l'histoire. Merci à tous deux de nous avoir transmis votre gentillesse et votre tendresse naturelles.

A mon amour, à qui je dédicace ce travail

Il est une personne à qui je dois bien plus qu'à toute autre, et sans qui ce travail n'aurait sans doute pu être achevé ; cette personne c'est toi, bien sûr, Céline. Je n'oserais compter les fois où je suis rentré le soir, le vague à l'âme, et où tu m'as redonné le courage de poursuivre. Tu es la condition matérielle et morale de la possibilité du travail présenté dans cet ouvrage. Ta gentillesse, ton ouverture et ta finesse d'esprit, ton humour, tes convictions et ton engagement, me rendent fier et m'offrent chaque jour l'enrichissement nécessaire pour aller plus loin.

Résumé

La détermination des températures continentales passées est un aspect essentiel des reconstructions paléoclimatiques, car les continents sont plus sensibles que les océans aux variations du climat. Des changements globaux modestes peuvent provoquer un réarrangement de la circulation atmosphérique et donc induire d'importantes réorganisations de la répartition régionale des flux de chaleur et d'humidité. Par conséquent, dans la perspective d'une meilleure compréhension du climat continental, il est nécessaire d'étudier un grand nombre d'archives climatiques présentant une distribution spatiale dense. Malheureusement, contrairement aux domaines océanique et polaire, la plupart des masses continentales manquent de telles archives. Les dépôts continus sont rares et les outils utilisés par les paléoclimatologues pour les déchiffrer ont tous leurs propres biais, qui sont généralement contournés au moyen d'une approche multi-proxy. Une telle approche nécessite la disponibilité de plusieurs proxies. Cependant, un simple coup d'oeil sur la carte de localisation des registres de températures utilisés pour la célèbre synthèse des températures de l'Holocène par Marcott et al. (2013) nous rappelle que les proxies applicables au domaine continental font cruellement défaut. Les environnements arides en particulier, où la rareté de l'eau empêche les potentielles archives organiques de se développer et de se déposer, ne présentent pour ainsi dire aucune pierre de Rosette permettant de déchiffrer les fluctuations passées des températures. En gardant cela à l'esprit, les inclusions fluides (IFs) de halite se sont révélées très prometteuses lorsque Roberts and Spencer (1995) ont montré pour la première fois leur potentiel d'enregistrement de la température passée des lacs salés en appliquant la méthode microthermométrique. En effet, ces micro-gouttelettes de solution-mère emprisonnées dans des cavités au sein des cristaux de sel conservent leur densité initiale, et donc la température de piégeage, tout comme la densité du mercure indique la température ambiante dans un thermomètre classique. Cependant, Lowenstein et al. (1998) ont montré que les IFs étaient endommagées au cours de l'étape requise de nucléation de phase vapeur dans le congélateur. Depuis lors, les études paléoclimatiques utilisant des IFs de halite ont été peu nombreuses. Au cours de cette thèse, nous avons développé une nouvelle méthodologie, basée sur la spectroscopie Brillouin (BS), permettant de contourner les limites de la microthermométrie. Cette technique, basée sur la mesure de l'interaction inélastique entre la lumière et les fluctuations thermodynamiques dans le fluide pour en déduire la vitesse du son, permet de déterminer la densité des IFs, et donc leur température de piégeage. Cette approche non destructive ne nécessite pas la nucléation préalable d'une bulle, et évite donc de soumettre des échantillons à des écarts de température importants. Dans la mesure où notre méthode garde les IFs intactes, nous avons restauré leur potentiel en tant que paléothermomètre. Nous montrons que la BS sur les IFs de halite révèle la température de piégeage au degré Celsius près.

En réalisant des tests de résistance mécanique par spectroscopie Brillouin, nous avons pu mesurer la température empirique au-delà de laquelle les IFs se détériorent, ce qui nous a permis de proposer une équation empirique de l'endommagement des IFs en fonction de leur taille et de la température, laquelle sert de cordon de sécurité dans la perspective de mesurer des paléotempératures non biaisées. Pour permettre le calcul de la limite de sécurité pour une large gamme de compositions d'IFs, nous avons développé un modèle qui s'applique au système Na-K-Mg-Ca-H_2O. Le modèle, basé sur le formalisme de Pitzer et le principe d'additivité des mélanges de Young, calcule la densité des solutions multi-électrolytes en fonction de la température, de la pression et de la salinité. En prédisant la réponse mécanique élastique du cristal hôte aux changements de densité de l'IF, le modèle calcule ensuite la pression interne de l'inclusion. Connaissant la pression à l'intérieur de l'IF, on peut alors prédire la température à laquelle elle risque l'endommagement. À l'avenir, l'extension du modèle à SO_4 et à $(H)CO_3$ permettra de déterminer la pression pour tous les principaux types de compositions d'IF de halite.

Pour illustrer l'efficience de la thermométrie Brillouin, nous avons échantillonné plusieurs dizaines d'intervalles de halite dans la longue carotte 5017-1 (450 m de long) forée en 2010-2011 dans la partie la plus profonde de la Mer Morte, en Palestine, dans le cadre du projet Dead Sea Deep Drilling Project (DSDDP, un projet du International Continental Scientific Drilling Program). L'application de la thermométrie Brillouin à cet enregistrement fournit une quantification unique des changements de température dans cette région au cours du dernier interglaciaire (LIG, il y a ~135 000 à 115 000 ans). De plus, nous montrons que la spectroscopie Brillouin permet dans le même temps de quantifier le niveau de la mer Morte et son évolution. En utilisant la courbe reconstituée de niveau du lac pour quantifier les paléo-précipitations, nous proposons donc une reconstruction complète températures-précipitations qui nous permet de définir un récit radicalement nouveau du climat de la région au

cours de cette période. Nous montrons que les températures hivernales au cours du LIG étaient généralement inférieures à celles d'aujourd'hui et que les précipitations étaient beaucoup plus élevées, quoique sur une tendance baissière. En opposition aux estimations précédentes, la région n'a jamais connu de sécheresse extrême et n'a atteint des conditions aussi sèches qu'aujourd'hui qu'en fin de période. Les liens clairs qui se dégagent d'avec la Méditerranée et l'Atlantique, ainsi que les tendances climatiques clairement observées, nous amènent à suggérer un forçage orbital majeur de la circulation atmosphérique dans cette partie du globe. L'exemple de la mer Morte montre que la spectroscopie Brillouin sur les IFs de halite est en mesure de fournir des données précieuses pour tester l'efficacité des modèles climatiques.

Mots clés: Inclusions fluides, halite, paléothermomètre, spectroscopie Brillouin, Mer Morte, dernier interglaciaire.

Abstract

Determining past continental temperatures is a key aspect of paleoclimate reconstructions, as continents are more sensitive than oceans to climate variations. Modest global changes may cause a rearrangement of the atmospheric circulation and may thus induce large changes in the distribution of heat and moisture over lands. Therefore, in the perspective of understanding continental climate, it is necessary to investigate a large number of climate archives displaying a dense spatial distribution. Unfortunately, contrary to the oceanic and polar realms, most landmasses are lacking such archives. Continuous deposits are rare, and the tools used by paleoclimatologists to decipher them all have their own biases, which are usually circumvented by means of a multi-proxy approach. Such an approach requires the availability of several proxies. However, a mere glance at the location map of temperature datasets used for the famous Holocene global temperature stack of Marcott et al. (2013) reminds us that proxies applicable to the continental realm are sorely lacking. Arid environments in particular, where the scarcity of water prevents potential organic archives from thriving and depositing, present, as it were, no Rosetta stone to decipher their past temperature fluctuations. With this in mind, halite fluid inclusions (FIs) revealed very promising when Roberts and Spencer (1995), using the microthermometry technique, first showed their potential to hold past saline lakes temperature. Indeed, these micro-droplets of parent brine trapped inside cavities of the salt crystals happen to keep their initial density, and therefore the entrapment temperature, like the density of mercury indicating the temperature in the thermometer. However, Lowenstein et al. (1998) soon showed that FIs undergo damages during the requisite step of vapor phase nucleation in the freezer. Since then, paleoclimate studies using halite FIs have been few. During this thesis, we have developed a new methodology, based on Brillouin spectroscopy (BS), to bypass the limitations of microthermometry. This technique utilizes the inelastic interaction between light and spontaneous (thermal) density fluctuations in the fluid to measure its speed of sound, hence allowing for the determination of its density, ergo entrapment temperature. This non-destructive approach avoids submitting samples to large temperature gaps, as it does not require the presence of a bubble in the FI as a prerequisite. As our method keeps FIs intact, we have restored their potential as an accurate paleothermometer. We show that BS on halite FIs reveals the entrapment temperature with an accuracy better than $\pm 1\,^{\circ}\mathrm{C}$.

Using Brillouin spectroscopy as a mechanical sensor, we were able to measure the empirical temperature beyond which FIs deteriorate, allowing us to propose a quantified size-dependent safety limit to avoid measuring wrong temperatures. To make the calculation of the safety limit possible for a wide range of FI compositions, we have developed a model that applies to the Na-K-Mg-Ca-H_2O system. The model, based on the Pitzer formalism and the Young mixing rule, calculates the density of multi-electrolyte brines as a function of temperature, pressure and salinity. Through predicting the elastic mechanical response of the host crystal to the FI density changes, the model then backcalculates the FI internal pressure. Knowing the pressure inside FIs then enables us to predict the temperature at which they get damaged. In the future, extending the model to SO_4 and (H)CO_3 will allow the determination of pressure for all major types of FI compositions.

To illustrate the power of Brillouin thermometry, we sampled several tens of halite intervals from the 450-meters-long core 5017-1 drilled in 2010-2011 in the deepest part of the Dead Sea in Palestine within the framework of the Dead Sea Deep Drilling Project (DSDDP, a project of the International Continental Scientific Drilling Program). The application of Brillouin thermometry to this record provides a unique quantification of temperature changes in this region during the Last Interglacial (LIG, ~135,000 to 115,000 years ago). Furthermore, we show that Brillouin spectroscopy allows, at the same time, the quantification of the Dead Sea level and its evolution. Using the reconstructed lake level curve to quantify paleorainfall, we thus propose a complete temperature-precipitation reconstruction that enable us to outline a radically new narrative for the climate of the region during this period. We show that the LIG winter temperatures were mostly lower than today, and precipitation were much higher, albeit on a drying trend. Contrary to previous estimations, the region never experienced extreme drought during the LIG, and only reached conditions as dry as today towards the end of the period. The clear connections with the Mediterranean and the Atlantic exhibited by the record, along with the clear climatic trends observed, lead us to suggest a strong orbital forcing of the atmospheric circulation over this part of the globe. The example of the Dead Sea shows that Brillouin spectroscopy on halite FIs is in position to provide valuable data to test the efficiency of climate models.

Keywords: Halite, fluid inclusions, paleothermometer, Brillouin spectroscopy, Dead Sea, Last Interglacial.

Contents

List of Figures

List of Tables

CHAPTER 1

General Introduction

1.1 Main features of the current climate

1.1.1 The average state climate

The surface of the Earth is covered with fluid envelopes: oceans -the hydrosphere- and gases -the atmosphere. These fluids move as a function of space and time, typically at day-scale: this is *weather*. These fluid envelopes have an average state the variation of which, in the pure sense, is only a function of space: this is *climate*. The driving force that sets Earth fluids in motion is the Sun. As the Earth is a sphere, the energy provided by the Sun is unevenly distributed over the surface of the planet. The intertropical area receives a maximum of energy on ground, while the poles receive the least. This disequilibrium is enhanced by the albedo, which increases poleward and implies a maximum heat loss -compared to insolation- at the poles. This equatorial surplus and polar deficit of energy (Figure 1.1) forms the basis of the average state fluxes on Earth: the oceans and the atmosphere tend to transfer the equatorial heat energy surplus towards the poles. This meridional transport (in the sense of a North-South axis of movement, irrespective of the direction of this movement) constitutes the framework of the atmospheric and oceanic circulations.

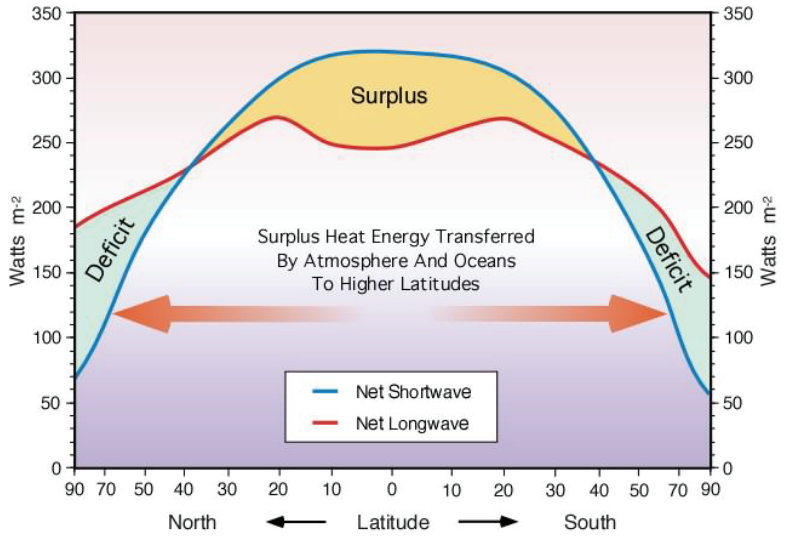

Figure 1.1: ***Balance between annual mean absorbed and outgoing heat fluxes.*** *The latitudinal variation of insolation heat absorbed on ground (blue line) is not comparable to the latitudinal variation of infrared heat radiated outward (red line). The unbalance implies an equator to pole heat transfer. From Pidwirny (2006).*

The atmospheric circulation This poleward transfer of energy, first suggested by George Hadley in the first half of the 18th century, is made possible by the convective upward motion of warm air masses in the tropical belt. The convective flux in this area is all the stronger as it is bolstered by the release of latent heat due to massive condensation during the migration of the vapor-saturated air masses towards the colder upper layers of the troposphere. At the top of the troposphere, the atmosphere is stable and the uplift stops. Air masses are then pushed poleward. On a still planet, this poleward advection would run its course up to the poles, cool, subside and migrate back equatorward to fill the low sea level pressure (SLP) in the tropical belt. However, each hemisphere does not comprise one but three convection cells (Table 4.2). This more complex structure is justified by the rotation of the Earth. Due to the conservation of angular momentum and the Coriolis effect, winds are deflected to the right in the Northern Hemisphere (NH) and to the left in the Southern Hemisphere (SH). They spin up and get all the more eastward trended till they reach the subtropical jet stream latitude at $30°$. At this latitude, air flow in the upper troposphere is almost purely zonal (i.e. remains at same latitude) and eastward. The fast moving air then breaks down into large eddies. This is also accompanied by a large sinking motion. Once they reach the ground, part of the air masses trend equatorward with an eastward deflection: these are the easterlies, the famous winds that pushed navigators to America five hundred years ago. NH and SH easterlies join at the Intertropical Convergence Zone (ITCZ), bringing moisture collected on the route and thus wrapping up the Hadley cell. The rest trends poleward with a westward deflection: these are the westerlies, the winds that bring mild and wet air to large parts of Eurasia in the NH. The latter reach a second uplift zone at $60°$, as they are forced upward by the cold air masses shifting from the poles. This second cell, delimited by the $30°$ high SLP belt and the $60°$ low SLP belt, is the Ferrel cell. This overall circulation framework accounts for a large part of the spatial climatic variability across the planet.

On top of this come an additional seasonal variability and a continent-sea discrepancy. As the Earth axis is tilted by $23.44°$, the annual revolution of the Earth around the Sun entails opposite 6-month periods of increased insolation from one hemisphere to the other. In addition to a fluctuation in direct insolation-driven heat supply to land and sea, seasonality induces reversals of regional circulation. Indeed, continents and oceans have low and high heat capacities, respectively. Therefore, while the former warm and cool rapidly, the latter are subject to smaller temperature amplitudes. These seasonal continent-sea gradients of temperature convert into pressure gradients. This is particularly noticeable in the tropics. In summer, warmer air masses over continents lift. Cool and wet oceanic air masses are thus drawn towards the land, warmed up, and thereby end up lifting in their turn. Massive vapor condensation reinforces the overall mechanism through the release of latent heat and generates very large rainfalls: this is monsoon. Conversely, during winter, cold continental air masses are drawn towards warmer oceans. The dry continental winds, along with subsidence over lands, generate a dry climate. Overall and irrespective of the global atmospheric circulation, insolation driven seasonality and the switching continent-sea gradient lead to wet summers and dry winters, especially in the tropics.

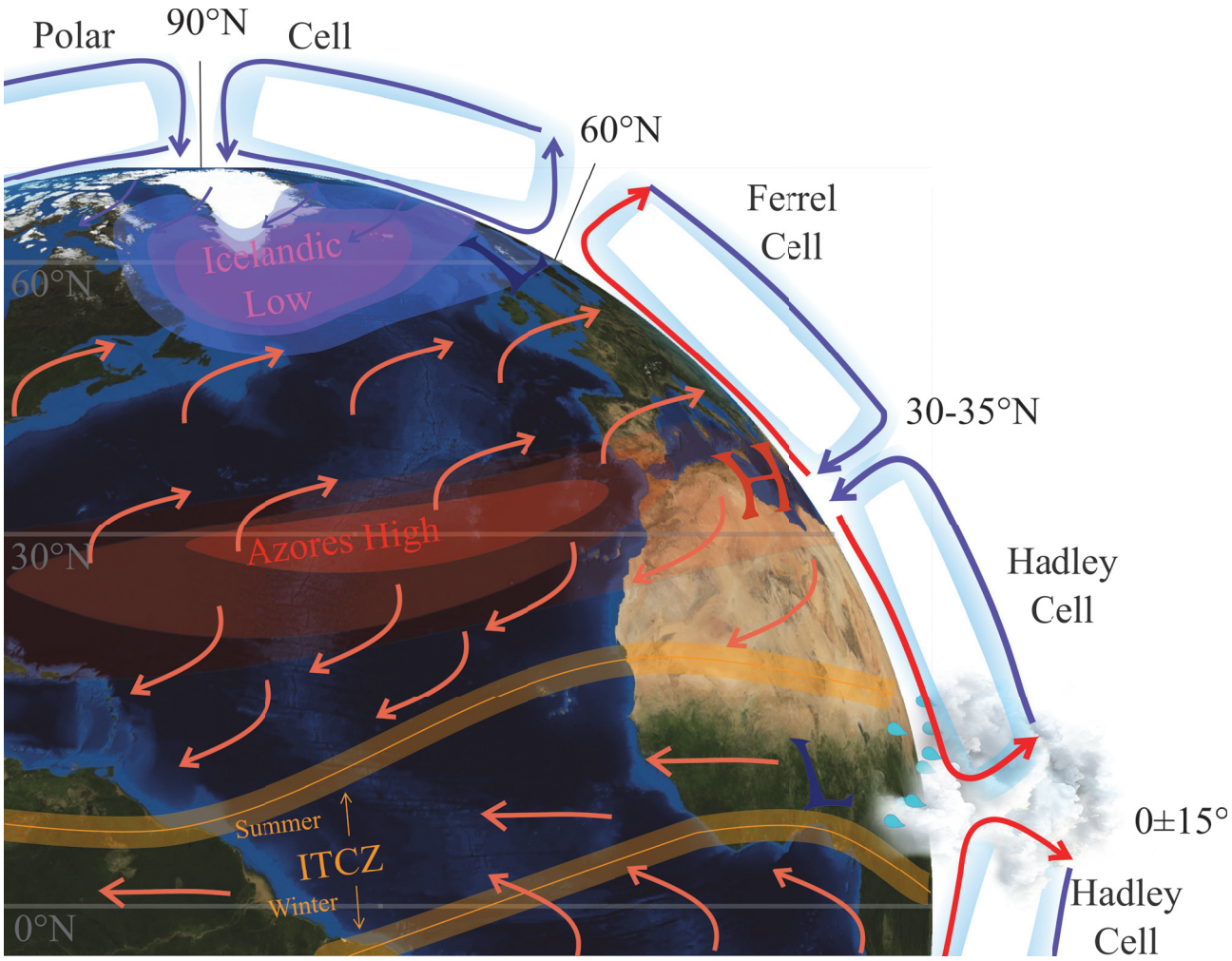

Figure 1.2: ***The atmospheric circulation.*** *L: low SLP; H: High SLP. The Intertropical Convergence Zone (ITCZ) shifts continuously throughout the seasons, July and January approximate positions are indicated. Average location of border between boreal and austral Hadley cells was chosen, note however that it corresponds to the location of the ITCZ at any time t. Geographic projection: orthographic.*

Atmosphere-ocean interactions Such as the atmosphere, oceans have a specific circulation that is is controlled by density gradients -which in turn depend on temperature and salinity gradients-, continents borders, and last but not least, the atmospheric circulation itself, which play a preeminent role in the motion of surface waters. Overall, at large basin scales, the causal relation of atmospheric circulation driving the oceanic dynamic, but also thermal, responses has long been established (Ekman, 1905; Bjerknes, 1964; Bunker, 1976). The prevailing thermal interaction between oceans and atmosphere over the globe is, by far, evaporative latent heat transfer from ocean to atmosphere (Bjerknes, 1964). The stronger the winds, the larger the evaporation and the energy used for it. This justifies the atmosphere to ocean causality suggested by the negative correlation between near-surface wind speed and sea surface temperature (SST; Liu et al. 1994; Mantua et al. 1997; Okumura et al. 2001). Over the last two decades however, this narrative has been subject to a deep questioning. The advent of new spaceborne technologies has led to a better coverage of wind stresses over the ocean (Liu et al., 2000), made possible the detection of SST through clouds (Wentz et al., 2000) and allowed the refining of spatial resolution down to eddy-scale (White and Annis, 2003; Small et al., 2005). These new observations

pointed out a mesoscale (i.e. 10s to 100s km) positive correlation between SST and wind speeds at oceanic fronts (i.e. oceanic currents boundaries; e.g. Liu et al. 2000; Chelton et al. 2001; Hashizume et al. 2001; O'Neill et al. 2003; Tokinaga et al. 2005; Minobe et al. 2008), suggesting an ocean to atmosphere forcing in these areas. This has raised concern on a likely significant underestimation of heat fluxes at oceanic fronts by coupled atmosphere-ocean general circulation models (AOGCMs) with spatial resolution larger than 1° (Rouault et al., 2003; Maloney and Chelton, 2006; Chelton and Xie, 2010). Even more challenging, several studies have highlighted the unability of models to fully assess the influence of SST on wind speed even when the spatial grid is refined to mesoscale (< 1°; Bryan et al. 2010; Small et al. 2014). This has raised the need to better understand the mechanisms at stake in the SST-to-wind forcing. Recent studies have highlighted the importance of finely resolving moist diabatic processes in order to better assess the genesis of cyclones (Willison et al., 2013). Particular focus on high-resolution modelling of the Kuroshio current front, off the japanese coast, has shown the intricate feedbacks between moist diabatic processes, mesoscale SSTs and the generation of large-scale cyclones and storms (Ma et al., 2015a, b, 2016a, b). These new findings on mesoscale air-sea interactions point out the need for highly resolved climate models that take into account the mechanisms so far overlooked. This is of critical importance in the perspective of accurately predicting regional climatic variability (Haarsma et al., 2016; Collins et al., 2018).

1.1.2 Climate variability at interannual and decadal scale: the example of the North Atlantic Oscillation

The variability affecting the mean climate state presented above is usually referred to as "anomalies", that is, the difference between the instantaneous state and the average climatology. Such anomalies are evident at interannual and decadal scale. Here, we propose a brief overview of the main variability affecting the NH: the North Atlantic Oscillation (NAO). As depicted in Table 4.2, the atmospheric circulation in the NH is characterized by a zonal high pressure belt in the subtropics (~30°N) and a zonal low pressure belt at the polar front (~60°N). These zones of high and low pressures are particularly well expressed around the Azores (the "Azores High") and around Iceland (the "Icelandic Low"), respectively. Records since 1864 show that these two centers of SLP extrema have been subject to interannual and decadal variabilities, with periods of increased high pressure at the Azores and lower pressure around Iceland, associated with sped up and northward shifted winds in the midlatitudes (Hurrell, 1995). This is defined as the positive phase of the NAO. Conversely, other periods have shown a reduced pressure contrast between Icelandic Low and Azores High, with slower westerlies shifted southward. This is defined as the negative phase of the NAO (see difference between the two modes in Figure 1.3). This oscillation is quantified with the NAO index, which is usually calculated as the difference of normalized pressures between two stations that are close to the centers of action (e.g. Lisbon for the Azores High and Reykjavik for the Icelandic Low). As the Azores-Iceland pressure gradient, best expressed in wintertime, is responsible for the westerlies that bring mild and moist air to large parts of the midlatitudes landmasses, its modulation with the NAO leads to a significant interannual variability of winter climate over

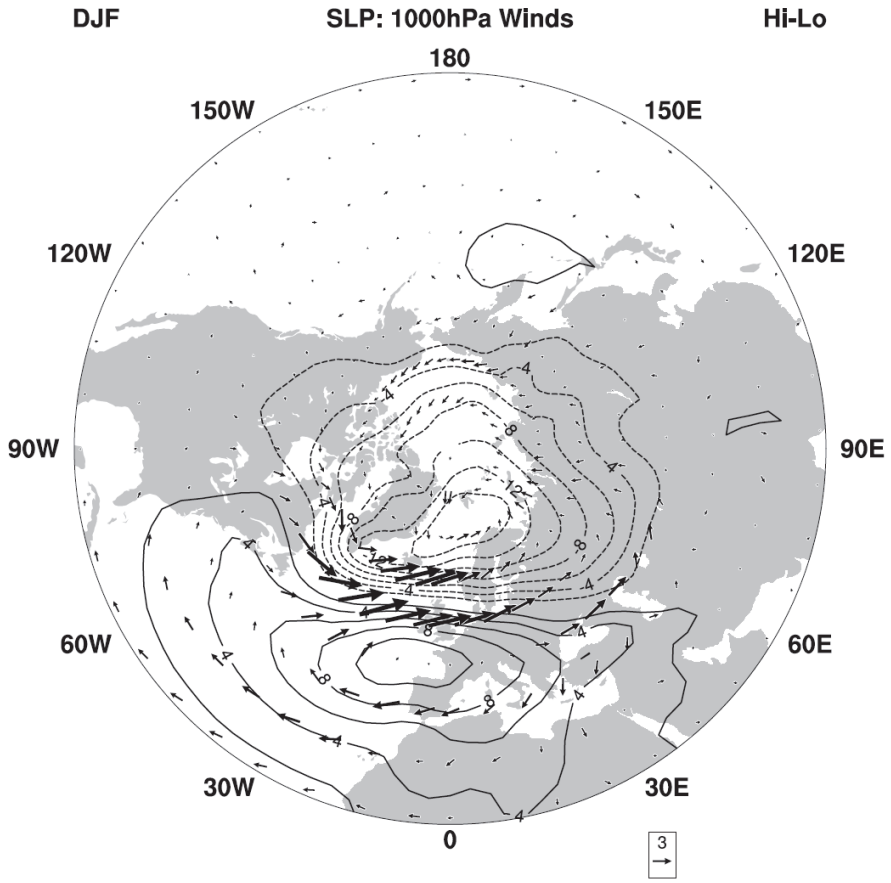

Figure 1.3: ***The difference in boreal winter (December-February) mean sea level pressure and 1000 hPa vector winds between positive (hi) and negative (lo) index phases of the NAO.*** *Construction based on the difference between the 9 most positive and 9 most negative winters during 1958-2001. SLP contour increment: 2 hPa, with dashed contour showing negative values; scaling vector: 3 m s^{-1}. Note the northward shifted centers of action compared with the average state showed in Table 4.2, characteristic of the NAO+ mode. From Hurrell et al. (2003).*

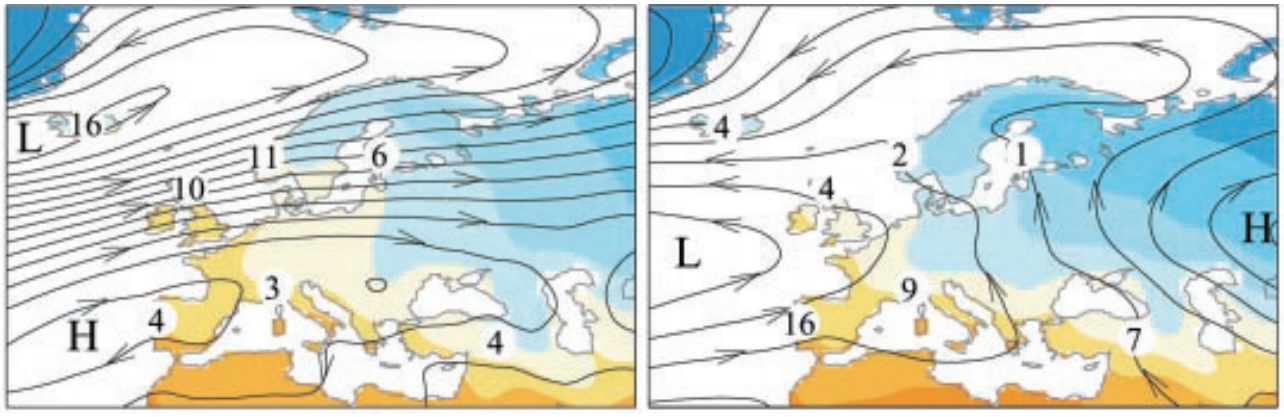

Figure 1.4: ***Composite maps of surface air temperature, sea-level pressure and precipitation for positive (left panel) and negative (right panel) winter NAO.*** *Based on January to March data (1958-1997). Contour increments: 5 °C for temperature (blue shade indicate lower than 0 °C), and 3 millibars for SLP (with highest contour 1025 mb). Precipitation in cm month^{-1}. Note that these two composite maps were constructed based on the NAM index (see text). From Thompson and Wallace 2001.*

these lands (Hurrell and Van Loon, 1997). The positive NAO mode will lead to increased winter precipitation and warmth over northern Europe along with winter drought and cold over the Mediterranean and the Middle-East, while the negative mode will have the opposite consequences (Figure 1.4). The NAO is highly correlated with the Arctic Oscillation (AO), an even larger climatic signature that encompasses the whole NH and has its low pressure center of action in the North pole (Thompson and Wallace, 1998; Ambaum et al., 2001); together, they constitute a boreal hemisphere-wide climatic signature referred to as the Northern Annular Mode (NAM; Thompson and Wallace 2001). In the following, we will only refer to the NAO, keeping in mind that these oscillations are deeply linked.

The strong variability of winter climate in the North Atlantic has been noticed long ago. In its description of the end of the world, the scandinavian myth of "Ragnarok" predicts it will begin with the occurrence of harsh winters, when "snow shall drive from all quarters; frosts shall be great then, and winds sharp; there shall be no virtue in the sun. Those winters shall proceed three in succession, and no summer between; but first shall come three other winters, such that over all the world there shall be mighty battles" (Sturluson and Brodeur, 2006). This "succession of three winters" can be imagined as a succession of three years in strongly negative NAO mode. The scandinavians, who used to sail across the seas of the North Atlantic, were well aware of the spatial and temporal climatic variability in these northerly regions where the NAO leaves particularly strong marks (Figure 1.4). Hans Egede Saabye, a Danish missionary who documented the history, climate, fauna and flora of Greenland (Egede, 1745), made the following remarks in one of his diaries (van Loon and Rogers, 1978): "In Greenland, all winters are severe, yet they are not alike. The Danes have noticed that when the winter in Denmark was severe, as we perceive it, the winter in Greenland in its manner was mild, and conversely." This commentary leads one to believe that the atmospheric teleconnections between landmasses had been noticed for a long time already. In a passage of the "King's mirror", a Norwegian book appeared around 1230 AD and presented in the form of a dialogue between a son and his father (Larson, 1917), one finds, in a description of winter climate in Greenland, a remarkable hint to a NAO feature where it is clearly stated that clear sky and cold is usually associated with storminess over other lands. In the 19th century, temperature stations made possible the first scientific investigations of this matter. Building temperature time series, several scholars quantitatively assessed the winter temperature seesaw between northern Europe on the one hand and North America, Siberia and Greenland on the other hand (Dove, 1839, 1840; Hann, 1890). One major step ahead was achieved by Teisserenc de Bort (1883), who first correlated the spatial distribution of anomalies in winter climate with the position of several pressure centers, including the Azores High, Russian High and Icelandic Low. This opened the way to the designing of the NAO index and the production of correlation maps and tables between the index and winter climatic variables. The reader can find a review of the history of the research on the NAO in Stephenson et al. (2003).

Following a long period of doldrums, interest in the research on the NAO has been rekindled as of the mid-1990s, following a persistent positive NAO mode that settled in the 1970s and strengthened in the years around 1990 (Figure 1.5), possibly constituting the strongest increase in NAO index since medieval times (Trouet

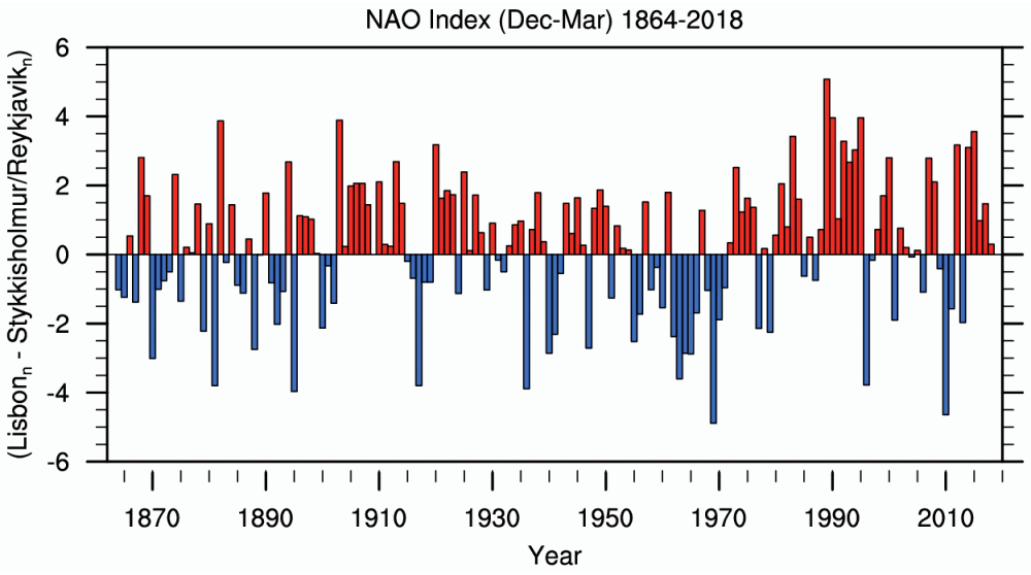

Figure 1.5: ***The winter NAO index from 1864 to 2018.*** *Calculated for period December through March, based on SLP at Lisbon and Reykjavik. Normalization achieved by removing the long-term mean and by dividing by the long-term standard deviation. From Hurrell and (Eds) (2018).*

et al., 2009). From this period, concern has raised about possible impacts of anthropogenic greenhouse gases (GHGs) forcing (Gillett et al., 2003; Osborn, 2004), or any other external forcing, as numerical models have excluded the responsibility of the sole internal NAO variability (Osborn et al., 1999; Osborn, 2004). The debate has been all the more vivid as some parts of the world, especially the Mediterranean realm, have experienced unprecedented series of dry years since 1990 that bore the mark of the positive NAO (Hoerling et al., 2012). So far, the NAO had been considered unpredictable and as arising from the internal chaotic variability of the atmospheric system, since purely atmospheric general circulation models (GCMs) that do not include SST, sea ice or land surface variability successfully simulate the spatial pattern, amplitude and lack of strong interannual coherence of the NAO (Hurrell et al., 2003; Thompson et al., 2003; Czaja et al., 2003). Since then, external forcings have been investigated, and some have shown good correlation with NAO and satisfactory numerical simulation and have stood the test of time to be regarded as potential drivers until now, among them: SST (Rodwell et al., 1999; Rodwell and Folland, 2002; Scaife et al., 2011), El Ninño (e.g.Moron and Gouirand 2003; Ineson and Scaife 2009), solar activity (possibly by means of lagged ocean-atmosphere interactions; Ineson et al. 2011; Scaife et al. 2013; Dunstone et al. 2016) and volcanic eruptions (although weakly supported by models; Driscoll et al. 2012; Smith et al. 2016). Smith et al. (2016) reviewed these various external forcings. In particular, and echoing back to the conundrum previously exposed in Section 1.1.1, they emphasized the mounting evidence that models reproduce too weakly the impact of SSTs on the NAO (Rodwell and Folland, 2002; Minobe et al., 2008; Scaife et al., 2013; Gastineau et al., 2013).

1.2 Climate long-term variability

1.2.1 Glacial/Interglacial cycles

100 ka cycles Climate during the Holocene, i.e. over the past ~10 thousand years (ka,) is considered quite stable (e.g. Ditlevsen et al. 1996; Johnsen et al. 2001; Stuiver et al. 1995), and the climate average state and its short-term variability described above can be applied, to some extent, to the whole period. Beyond however, it was subject to large global-scale shifts from cold periods (glacials) to warm periods (interglacials) and vice versa, each alternation occurring within a ~100 ka cycle (Wolff et al., 2010). Interglacials can be defined as relatively warm period comparable to the Holocene -the latter being also called Present Interglacial (PIG). During such warm periods, ice sheets in the NH are confined to Greenland (Past Interglacials Working Group of PAGES, 2016) and sea level is comparable to today. Conversely, during glacials, ice sheets of the NH and SH build up due to a larger annual amount of snowfall compared to the annual volume loss by melting and ablation. The level of the seas decreases with an amplitude larger than 100 meters below current level (e.g. Waelbroeck et al. 2002). These variations are very well identified in the ice core records of Greenland (Andersen et al., 2004) and Antarctica (Jouzel et al., 2007), as well as in the oxygen isotope records of benthic foraminifera at global scale (Lisiecki and Raymo, 2005). As deep oceans chemistry responds slowly to climatic shifts, at the millenial pace of the global oceanic circulation, the latter records constitute excellent sensors of global-scale variability. The fact that the glacial/interglacial alternations constitute the main feature in the benthic records -to the extent the Marine Isoptopic Stages (MIS) they highlight are used as the stratigraphic frame in the Quaternary paleoclimatology (Emiliani, 1955; Shackleton, 1967; Shackleton and West, 1969; Shackleton et al., 2003)-, along with their coeval expression in the ice cores of both poles (Figure 1.6), is the demonstration of the global signature of the glacial/interglacial alternations.

One striking feature in the global records is the asymmetry in the cycles (Figure 1.6). The overall pattern is (i) a slow demise of interglacial conditions transitioning towards glacial, explained by the gradual build-up of ice sheets over tens of thousands of years, and (ii) an abrupt end of glacial conditions, also called "Termination", explained by the collapse of ice sheets occurring within some millennia (Broecker and van Donk, 1970). The former (i) is coeval with a slow decrease in CO_2 atmospheric concentration (Lüthi et al., 2008) and a gradual slowdown of the Atlantic Meridional Overturning Circulation (AMOC; Guihou et al. 2010). The latter (ii) is associated with an abrupt increase in atmospheric CO_2 and disruptions of the oceanic circulation caused by the sudden input of large volumes of meltwater (e.g. Weaver et al. 2003). Both the collapse and following resumption of the oceanic circulation are thought to have occurred very rapidly (McManus et al., 2004). In addition to the aformentioned marine and polar rearrangements, terminations also have impacts on the atmospheric circulation, as evidenced by the observed shift of the ITCZ (e.g. Cheng et al. 2009). The modification of climate forcings associated with a termination, especially the decrease in the Earth's albedo and the increase in atmospheric CO_2 due to massive release by the oceans (Denton et al., 2010; Deaney et al., 2017), is responsible for the ~5 °C difference in global average temperature between glacial and interglacial

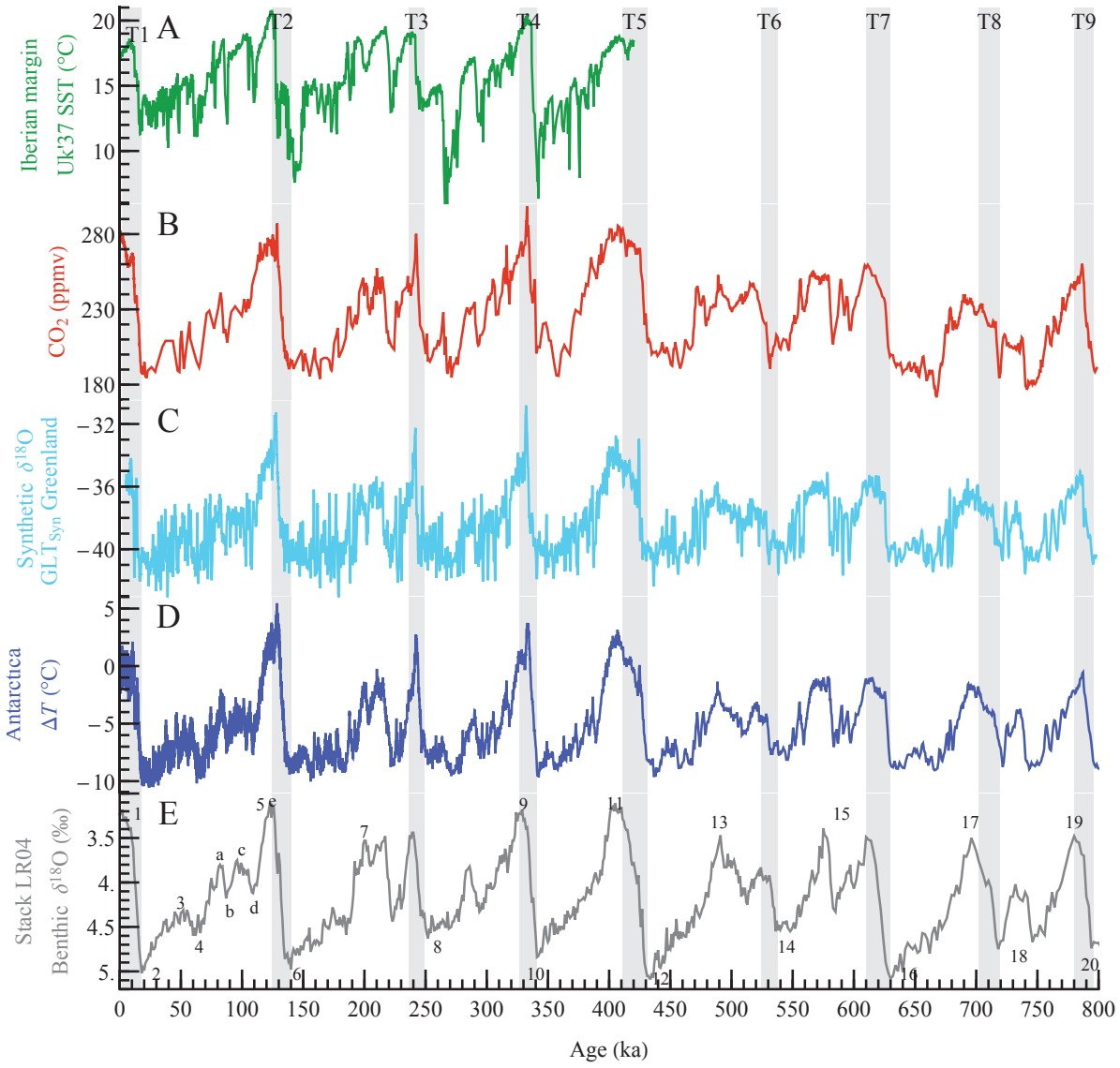

Figure 1.6: ***Climate variability at global scale over the past 800,000 years.*** *A: Alkenones SSTs off the Iberian coast (Martrat et al., 2007). B: Atmospheric CO_2 concentration as measured in the Antarctic Vostok and EPICA Dome C ice cores (Lüthi et al., 2008). C: Synthetic record of Greenland climate variability based on the thermal bipolar seesaw model (Barker et al., 2011); mainly driven by Greenland temperature variability. D: Temperature variability reconstructed from the δD_{ice} measured in the Antarctic ice core EPICA Dome C (Jouzel et al., 2007). E: Oceans benthic $\delta^{18}O$ variability, obtained from stacking of deep ocean records from all over the world (Lisiecki and Raymo, 2005); variability driven by ice volume and deep ocean temperature; numbers represent Marine Isotopic Stages (MIS). Gray bands are Glacial Terminations as in (Past Interglacials Working Group of PAGES, 2016).*

(e.g. Shakun and Carlson 2010).

Variability at millennial scale Within the 100 ka variability, a millennial-scale oscillation is observed in the oxygene istopes records of the late Quaternary. It consists in events with rapid onset and demise (10 to 200 years; Steffensen et al. 2008) and a large amplitude (8 to 15 °C in Greenland; Huber et al. 2006). Two types of such events were identified: Dansgaard-Oeschger cycles (D-O, Dansgaard et al. 1982, 1984) and Heinrich stadials (HS, Heinrich 1988).

- D-O consist in ~2 ka cycles of warming/cooling. 25 such cycles are identified in the sole Last Glacial (Wolff et al., 2010).

- HS correspond to cooling events in the NH, associated with massive ice break-up and ice rafting in the North Atlantic. They were first identified and are defined by detrital layers occurring in marine cores (Ice-rafted debris, IRD, Heinrich 1988; Bond et al. 1992). They usually occurr after 2 to 5 D-O cycles (Bond et al., 1993).

D-O and HS were first described in the Last Galcial records of Greenland and North Atlantic regions, but these climate changes have further been identified in all glacials (McManus et al., 1999; Jouzel et al., 2007; Wang et al., 2008) and among diverse and globally-distributed records, such as NH continental midlatitudes (e.g. Allen et al. 1999; Genty et al. 2003), SH continental midlatitudes (e.g. Kanner et al. 2012) and Antarctica (e.g. EPICA Community Members 2006; Wolff et al. 2010). The latter shows a peculiar pattern: when records in Greenland point out a phase of warming, Antarctica records highlight a phase of cooling, and vice versa (Broecker, 1998; Stocker, 1998). This phenomenon, called the "bipolar seesaw", is best explained by modifications in the intensity of the AMOC, as the latter is responsible for a large transfer of heat from the SH to the NH. When the AMOC weakens or collapses, the SH warms up and the NH cools down, and vice versa (e.g. Stocker and Johnsen 2003).

Still debated is the amplitude and global outreach of these events, as some cycles well expressed in Greenland ice cores and North Atlantic records are not recorded elsewhere, and signals in other regions may vary in terms of amplitude (e.g. Johnsen et al. 1992; Sánchez Goñi et al. 2008; Sanchez Goñi and Harrison 2010; Wolff et al. 2010). Furthermore, while D-O and HS cyclicities are well expressed in the glacial records, the occurrence and amplitude of such millennial-scale cyclicities during interglacials are still debated. The disappearance of the cyclicity in Greenland ice cores once full interglacial is reached is patent, and corroborated by North Atlantic sediment cores throughout the Pleistocene (McManus et al., 1999; Hodell et al., 2013, 2015; Barker et al., 2015). Although an intra-interglacial centennial to millennial variability is documented, especially during the Holocene (see Wanner et al. 2008 for a review), an identification at global scale and a determination of its forcings are still lacking (Past Interglacials Working Group of PAGES, 2016).

1.2.2 Causes of the long-term variability: the Milanković cycles

An astronomical trigger The long-term variability of climate during the Quaternary (2.6 Millions years (Ma) to today) has been documented at least for more than one century and a half, with a first clear observation and description of past glacials in the Alps (Penck and Brückner, 1909) and the identification of a previous interglacial in northern Europe (Harting, 1874; Jensen and Milthers, 1928; Florschütz, 1930; Louman, 1934). However, the explanation for such a long-term variability has long remained elusive. The Serbian engineer and mathematician Milutin Milanković believed the solution to this issue was astronomical. Therefore he worked for several decades on the development of equations characterizing the variations of the orbital parameters of

the Earth and the resulting variations in insolation, and finally released in 1941 the paper (Milankovitch, 1941) that still serves as the basis of our understanding of Quaternary climate. The central idea of this theory is that three orbital variables (Figure 1.7) govern the intensity and distribution of solar radiation on the planet:

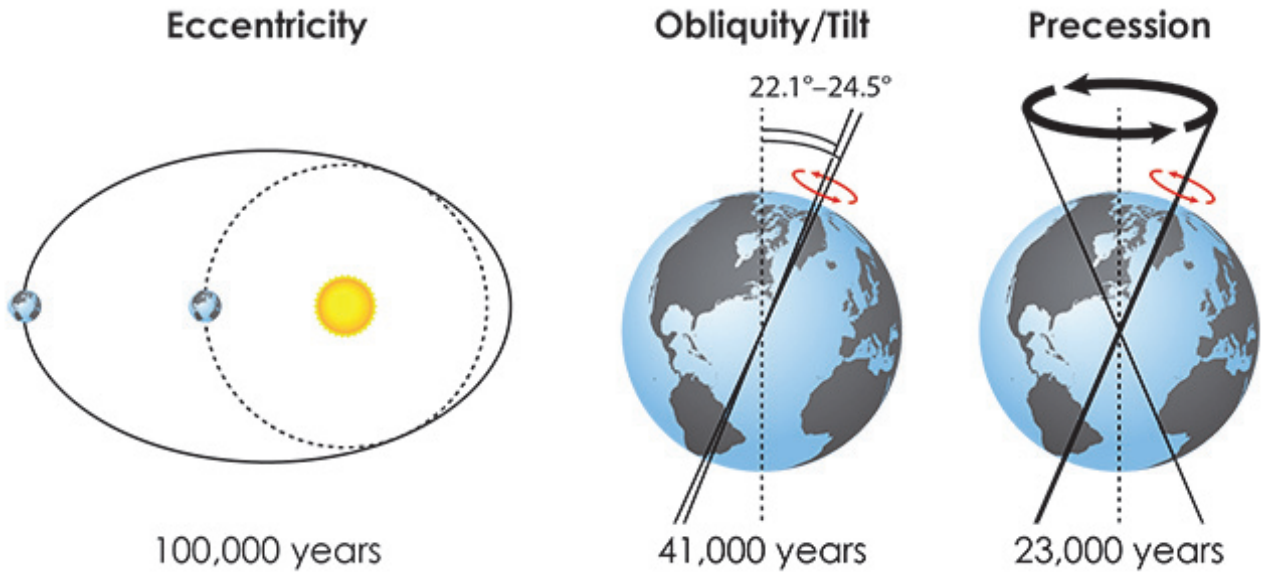

Figure 1.7: ***The three main parameters of the Milanković cycles.*** *Eccentricity variation is exaggerated. Image credit: K. Cantner, AGI.*

- Eccentricity (periods 100,000 and 413,000 years) describes the shape of the Earth's orbit. An eccentricity index e equal to 0 is a perfect circle; $0 < e < 1$ characterizes an ellipse. Over the last million years (Laskar et al., 2011), it has varied between ~0 and ~0.06 (mildly elliptical). An eccentricity superior to 0 entails an orbital position of minimum distance to the Sun (perihelion) and an opposite position of maximum distance (aphelion). There are two main consequences of eccentricity variations on the Earth's heat budget: (i) an increased (decreased) insolation at perihelion (aphelion), with a difference in solar energy reaching the planet between the two positions that can amount up to 23% when e is maximum; and (ii) the modification of the length of seasons. Indeed, Kepler's second law states that a body in orbit traces equal areas over equal times, hence an increased orbital speed and shortened season at perihelion and lower speed and lengthened season at aphelion.

- Obliquity (period 41,000 years) refers to the angle of the Earth's axis with respect to a normal line to the orbital plane. With a current value of 23.44°, it is roughly halfway between its extreme values 22.1 and 24.5°. Increased obliquity increases the amplitude of seasonal insolation. It also results in increased annual insolation over high latitudes and the reverse over close-to-equator latitudes.

- Precession (periods 23,000 and 19,000 years) is the variation of the direction of the Earth's axis. The precession index is defined as $e.\sin(\omega_s)$ (Berger, 1978), with ω_s the longitude of the perihelion and e the eccentricity. When $\sin(\omega_s) = 1$, the NH winter insolation is at its highest, and when it equals -1 the NH

summer insolation is at its highest. The amplitude of the oscillations of the precession index is controlled by eccentricity.

The variations in global heat supply due to the latter three parameters is negligible. However, the idea of Milanković was that the modification of seasonal insolation over the asymmetrical hemispheres of the Earth would have global effects. In particular, his idea was that summer insolation over the high latitudes of the NH has been a critical parameter controlling the volume and spatial extent of sea ice and ice sheets. Conversely, the position of landmasses in the SH would make it less sensitive to variations in summer insolation. For this reason he believed that obliquity cyclicity would be the leading driver of climate changes insofar a it has a prominent impact on the quantity of solar heat received by the poles.

Among the first attempts to support Milanković's theory, we can cite Emiliani (1955) and Emiliani and Geiss (1959), who found good correlations between the δ^{18}O measured in pelagic foraminifera from Atlantic, Caribbean and Pacific deep-sea cores and the summer insolation curve. However, studies dating back to this period were facing major hurdles. First, the lack of understanding about the meaning of the variations in marine δ^{18}O, considered as a temperature proxy, while it was later shown that the main driver of these variations is the ice sheets volume (Shackleton, 1967). A second and even greater obstacle at the time was the limitations of dating methods (Broecker, 1966; Hays et al., 1976), periods beyond ^{14}C applicability being extrapolated from the constraints on the sedimentation rates of the last 55,000 years. Later progress in dating methods (e.g. Hays et al. 1969; Shackleton and Opdyke 1973) made possible the establishment of reliable core chronologies beyond the critical 150,000 years limit. This led to the decisive work of Hays et al. (1976). Using δ^{18}O of planktonic foraminifera and radiolarian assemblages-based SST estimations from two well-dated marine cores spanning the last 450,000 years, they constructed geological time-series and tested their phasing with the calculated orbital data. They showed that the climatic variance was concentrated in three distinct spectral peaks 23,000, 42,000 and ~100,000 years corresponding to the precession, obliquity and eccentricity periods, respectively. Thus, they demonstrated that changes in the Earth's orbital geometry are the fundamental cause of Quaternary glacial/interglacial variability. They further highlighted the linear response of climate to precession and obliquity, and suggested the response to eccentricity was dominant and non-linear. Their work confirmed the strong influence of orbital parameters on Quaternary climate theorized by Milanković; however, it questioned his idea of a climate mainly controlled by obliquity.

Since then, continuous and highly-resolved records from deep-sea cores have extended further back in time. In particular, the 5.3-Ma LR04 stack of benthic δ^{18}O records from 57 globally distributed sites (Lisiecki and Raymo, 2005), along with the development of astronomical solutions reliable over the last 10 Ma or more (Berger and Loutre, 1991; Laskar et al., 2004, 2011), have made possible the comparison of climate and orbital cycles over the whole Quaternary and Pliocene periods (2.6-0 Ma and 5.3-2.6 Ma, respectively). As illustrated in Figure 1.8, such comparisons have allowed for the identification of several million year-scale phases. Asymmetrical ~100-ka glacial/intergalcial cycles have only occurred for the last ~1 Ma. A transition took place during the Mid-Pleistocene (MPT, between 1.25 and 0.7 Ma ago; Opdyke 1976; Pisias and Moore Jr 1981;

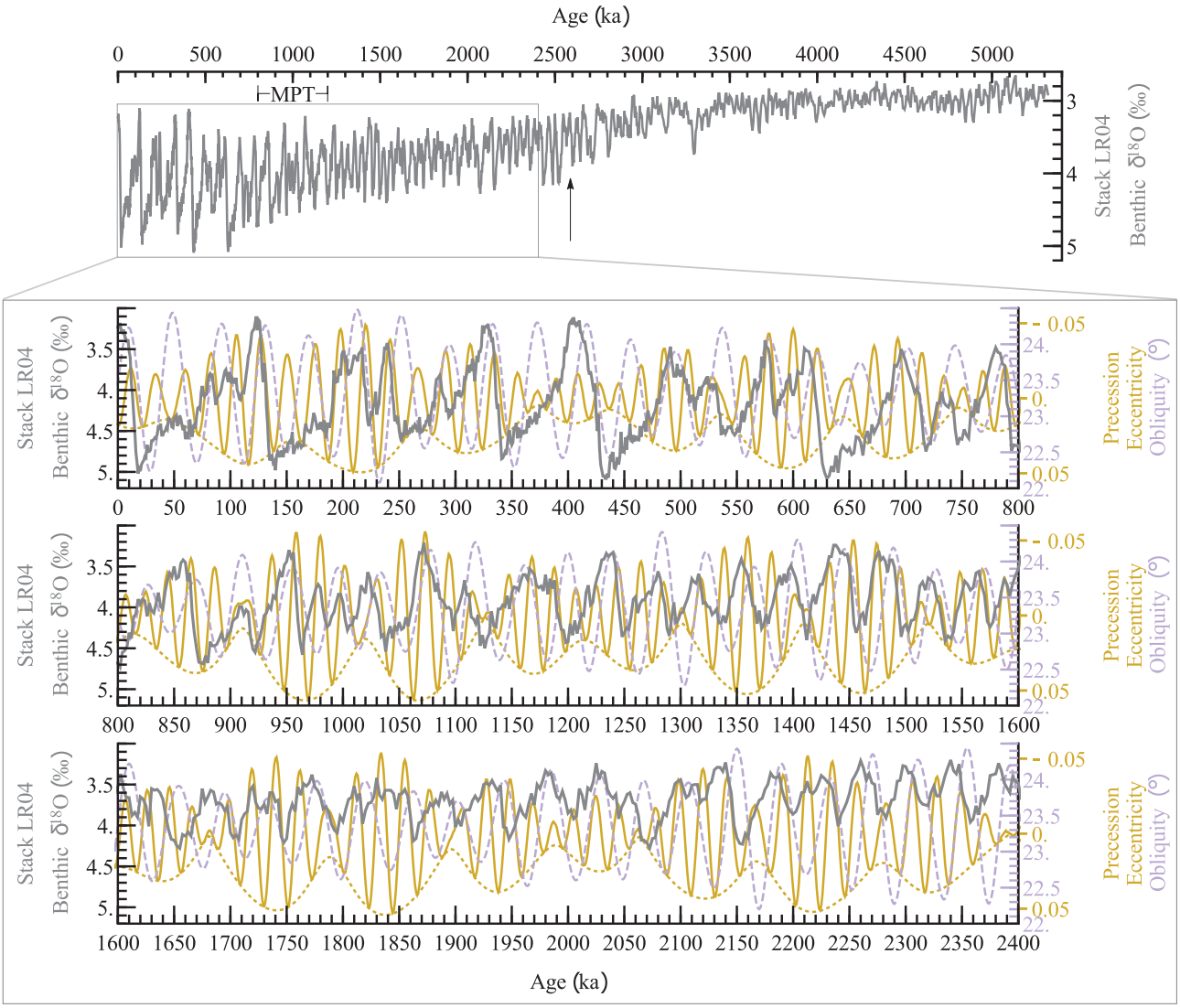

Figure 1.8: ***Deep oceans δ^{18}O during the Plio-Pleistocene, and connections with orbital cycles during the Pleistocene.*** *Benthic oxygen isotope stack from Lisiecki and Raymo (2005). Obliquity (dashed), eccentricity index (dotted) and precession index (solid) from Berger and Loutre (1991). Arrow shows official onset of the Quaternary/Pleistocene. MPT: Mid-Pleistocene transition (see text).*

Clark et al. 2006), before which climate primarily responded linearly to the obliquity cycles. Another transition can be observed in Figure 1.8 between the Pliocene and Pleistocene periods, at ~2.6 Ma, before which the stable and low value of benthic δ^{18}O highlights reduced ice volumes and decorrelation of climate with the astronomical forcing.

Mechanisms and forcings The observation of the cyclicity of climate, as well as the occurrence of the rather sharp transitions from no astronomical forcing (before 2.6 Ma) to obliquity forcing (2.6-1 Ma) and then to eccentricity forcing (1 Ma to today), paved the way to the next question: *how* do orbital changes influence climate ? This question is a vast one and is still under debate. Here we just propose a brief outline of the main mechanisms at stake.

The fact that orbital modulations only modify the distribution of solar radiation on Earth without changing

the global insolation budget implies that feedbacks play a prominent role in changing the global heat budget and accounting for the ~5 °C difference in global average temperature between glacial and interglacial (e.g. Shakun and Carlson 2010). Milanković predicted that an increase in solar radiation over the poles, resulting in the reduction of ice and snow surface areas, would lead to a decrease in global albedo and an increase in global heat absorption. Schnitker (1979), Boyle and Keigwin (1987) and Duplessy et al. (1988) showed that the oceanic thermohaline circulation was weakened during glacials, reducing the transport of heat from low latitudes to high latitudes. Ice cores recovered in the Antarctic revealed a close coupling between atmospheric greenhouse gases (GHGs; CO_2 and CH_4) and glacial/interglacial cycles (Petit et al. 1999; Monnin et al. 2001; Lüthi et al. 2008; see also Figure 1.6). In a series of two papers, Imbrie et al. (1992, 1993) proposed a model integrating the aforementioned feedbacks into a coherent astronomical framework:

- In their model, glaciation cycles with periods near 23,000 and 41,000 years are continuous, linear responses to precession and obliquity changes. These responses are involved in a causal chain which is led by the Arctic Ocean. When summer insolation decreases in the northern high latitudes, surface waters in the Arctic and the Nordic Seas freshen because of a decrease in evaporation and a larger extent of sea-ice. This stops the subsidence of Arctic and Nordic waters and thus slows and eventually nearly shuts off both the transport of warmer deep waters towards the Southern Ocean and the pumping of low latitudes warm surface waters towards the North Atlantic. This weakening of the Atlantic overturning leads to the cooling of the Antarctic Ocean and the increase in austral sea-ice extent. In turn, this affects the distribution of nutrients in the Southern Ocean, driving down atmospheric CO_2. This early active role of the Southern Ocean as a carbon trap is essential. It further drives the global cooling that allows for the growth of land-based ice sheets. Each element in the chain of action presents a specific inertia that brings lags in the succession of feedbacks. All the chain of feedbacks described here in glaciation mode works the other way round in deglacial state, still with the same order in the responses.

- The 100,000-years glacial cycle is associated with a non-linear response to the 100-ka orbital cycle. Indeed, while this cycle is the dominant pattern observed in climate variations of the last million years, the amplitude of insolation changes at June 65°N due to eccentricity are 1 order of magnitude smaller than that of precession and obliquity. Thus it is clear that eccentricity alone cannot be the dominant forcing. They show that the onset of the 100-ka regime coincides with the growth of large northern hemisphere ice sheets, the latter being an essential condition for the development of feedbacks to drive the 100-ka ice volume cycle. They show that the inertia of northern hemisphere ice sheets has a time constant 15,000 years. Such a sluggish system can only be modestly affected by the precession and obliquity rather fast half-periods (11,500 and 20,500 years, respectively). Conversely, during the 50-ka growth period of a 100-ka cycle, 96% of the ice sheet equilibrium response would be achieved. This inertia leads northern ice sheets to tune up with the longest of the three astronomical cycles. By changing the albedo and affecting air masses, they greatly amplify the modest response of the system to the eccentricity forcing,

changing oceanic circulations, heat transfer to the Southern Ocean and CO_2 atmospheric concentration. Thus, it appears that northern ice sheets equilibrium paces the 100-ka cycle. After a long period of growth, when the size of ice sheets departs too far from equiibrium, a Milanković cycle-forced sea level rise may trigger a critical unstability of the portion of ice sheets that lies on the continental shelves, leading to their collapse and to a cascade of feedbacks that results in deglaciation. This sets the phase of one new wave in the train of 100-ka cyclicity.

This picture gives an insight into potential mechanisms and triggers. However, several revisions have emerged since then. Long Antarctic ice cores have offered an insight into the evolution of GHGs atmospheric concentration over several glacial cycles (Petit et al., 1999), and led Shackleton (2000) to show that ice volume changes lagged CO_2, temperature and eccentricity; this suggests that ice sheets are enslaved to rather than driver of the 100-ka climatic cycle. Furthermore, the bipolar seesaw mechanism was discovered in the late 1990s (Broecker, 1998; Stocker, 1998; Stocker and Johnsen, 2003), and has led authors to revise the causal chain. Like in the model of Imbrie et al. (1993), and following the observations of Raymo (1997), Denton et al. (2010) emphasize the presence of very large volumes of ice sheets in the NH, grounding on isostatically depressed continental shelves with marine-based components, as a prerequisite for the initiation of deglaciation. Rising NH summer insolation due to decreasing precessional index leads to partial melting of excess ice sheet volume, delivering fresh water to the North Atlantic. The resulting reduction of AMOC brings NH warming to a complete halt, and in turn the SH rapidly warms, which is a major difference compared to the model of Imbrie et al. (1993). Warming of the Southern Ocean is associated with strengthened upwelling and a large release of CO_2, above threshold necessary to sustain interglacial conditions. This timing, implying a summer insolation-triggered blockage of the AMOC, followed by an atmopsheric CO_2 increase which fuels a subsequent global warming, is supported by global records stacks (Shakun et al., 2012). Recently, a nonlinear sensitivity of climate to CO_2 atmospheric concentration, with a threshold of 220 ppmv above which the Pacific ocean would warm three times as fast, has been proposed as an additional contribution to global nonlinear response during deglaciations (Lo et al., 2017).

The outline of the three main cycles presented above shows that the mechanisms involved, the roles of forcings and "slaves", are still under debate. In particular, the nonlinear response of the 100-ka cycle still remains an intriguing issue. Answers might be found in the investigation of the reasons of the appearance of this cycle about 1 Ma ago, during the MPT. It is thought that CO_2 levels were too high for NH ice sheets to be sustained before ~2.7 Ma (Lunt et al., 2008; Willeit et al., 2015). Reasons for the shift from obliquity-driven to eccentricity-driven climate 1 Ma ago are less understood; while some invoke a gradual decline in CO_2 atmospheric concentration (Lunt et al., 2008; Tan et al., 2018), others suggest a removal of regolith - the thick dusting that covers rocks when exposed to weathering for several 10^7 years- by successive glaciers erosion in northern Europe and North America (Clark and Pollard, 1998; Ganopolski and Calov, 2011; Tabor and Poulsen, 2016). A new model reconciles both theories and shows that combined CO_2 decline and regolith removal are necessary to account for the transition from the 41,000 to the 100,000-year world (Willeit et al.,

2019). A high CO_2 concentration had prevented large ice sheets to develop in the NH. Large areas covered with regolith had enhanced sliding velocity of ice as well as covered the southern margin of NH ice sheets, thereby decreasing their albedo. Both sliding velocity and albedo decrease due to thick regolith, combined with high atmospheric CO_2, had been obstacles to the full extent of NH ice sheets. In turn, their gradual removal and decrease, respectively, would have constituted a basis for the onset of 100-ka cycles. Contrasting with these gradual forcings however, Elderfield et al. (2012) found that the transition was initiated by an abrupt increase in Antarctic ice volume 900,000 years ago.

1.3 Climate variability on continents

We have seen in the above sections that polar ice and marine cores have revealed valuable clues towards the understanding of global climate. Changes in oceans and ice sheets have a global outreach, and the changes they record have a global signature. Furthermore, the latter records have a wide geographical distribution and are generally continuous. Conversely, on continents, records are sparse and often discontinuous, while climatic variability is stronger. Also, in addition to direct solar radiation, climate on continents is mainly influenced by atmospheric circulation. Therefore, it is generally studied through the quantification, or qualitative estimation, of the main expression of atmopsheric circulation, that is, temperature and precipitation. In this section, we give a brief overview of the tools that are used to better understand continental climate, namely proxies and models. We evoke how they compare and point out some significant discrepancies. We mainly use examples of the last climatic cycle (the Last Glacial and, above all, the Holocene), as the latter is by far the most explored and documented period. Also, we mainly focus our attention on the temperature parameter.

1.3.1 Tools

Proxies In the polar regions, temperature is derived from the isotopic composition of water molecules (δ^{18}O and δD) in ice cores. The strong physical basis of this proxy was demonstrated by Jouzel et al. (1997). In the marine realm, sea surface temperatures (SSTs) are the main temperature parameter used to characterize past climates. Generally their estimation is based on the identification and quantification of paleontological data, as organisms, their metabolism and their composition are sensitive to temperature. The work of Imbrie and Kipp (1971) on assemblages of marine foraminifera, and the development of mathematical methods (transfer functions), allowed the first quantification of SSTs in the past. This faunal method rapidly thrived in the following decades (e.g. Prell and Hutson 1979; Prell 1981, 1985). Since then, several geochemical methods have appeared. Among them, the Mg/Ca ratio measured in the shells of planktonic foraminifera (Nürnberg et al., 1996; Elderfield and Ganssen, 2000; Anand et al., 2003), the calibration-based paleothermometer $U^{k'}_{37}$ relying on the relative abundance of saturations in the long-chain alkenones produced by Haptophytes algae (Prahl and Wakeham, 1987), and the calibration-based paleothermometer TEX_{86} relying on the relative abundance of cycles in the isoprenoid glycerol dialkyl glycerol tetraethers (iGDGTs; Schouten et al. 2002). These three marine

paleothermometers are now widely used (see, for instance, Fig. S1 in Marcott et al. 2013). On the continental realm, the diversity of proxies that can be used is large, but each step further back in time reduces sharply this diversity. For the centuries or few millennia predating instrumental record, temperatures are mainly derived from ice cores, tree rings and indices based on historical documents (Luterbacher et al., 2004; Mann et al., 2008), along with some other proxies such as speleothems and corals. These records allow for reconstruction with a high temporal resolution. Further back in time however, documents and trees are not available. In the following, we mention some of the main tools that are used for temperature reconstructions on millennial and longer time scales.

The determination of late Quaternary temperature and precipitation changes are to a large extent based on observed changes in vegetation patterns, which are mainly inferred from pollen records from lake and peat sediments. Geographic distributions of plant species can be approximated by climatic"envelopes". These envelopes are determined by several parameters like annual temperature, temperature seasonality and water availability. This situation arises because of the existence of bioclimatic limits. These limits determine the ecological niche of plant taxa. However, these limits are not sharp and each climatic parameter does not influence species distribution independently of the other parameters. Taxa may have overlapping fundamental niches, and vary in abundance, with an optimum near physiological optima which can be displaced by competition. Palynologists have developed statistical and process-based methods that have allowed for quantitative seasonal temperature and precipitation assessments based on these plants distributions; a review of these methods can be found in Bartlein et al. (2011). One of the strength of pollen-based quantitative climatic assessements is that they shed light on the seasonality of reconstructed climatic variables, making possible the assessment of winter and/or summer precipitation and temperature (e.g. Bartlein et al. 1998; Rousseau et al. 2006; Cheddadi and Bar-Hen 2009; Peyron et al. 2011). On the other hand, the complexity of vegetation signals has given rise to the development of numerous methods to interpret them, which may sometimes yield conflicting results (e.g. Peyron et al. 2011).

Organism-based inference models can also be used to infer past temperatures from fossil assemblages (Birks, 1995; Lotter et al., 1997). In particular, larvae of chironomids -a midge of the *Diptera* order- from lake sediments have been used as indicators of past summer temperatures, especially July temperatures (e.g. Heiri et al. 2003). Heiri et al. (2003) noticed that, at least for Holocene reconstructions, chironomid-assemblages-inferred temperature reconstructions were rather scant; they associated this situation with the rather large predicted error (~1.5°C), comparable to the temperature fluctuations during this period.

Temperature reconstructions based on statistical assessments of pollens and chironomids assemblages, along with some other paleoecological assemblages, have been the most widely used on continents. All these approaches rely on assumptions and principles (Birks 1995); the most important assumption, uniformitarianism (or actualism), states that all processes at work today should have already existed in the past, implying that any response of an organism to a change in one climatic variable has applied equally in the past and in the present. This assumption is rarely completely verified, as biological assemblages are a complex function of multiple

variables, and the latter are not all well constrained. Most paleolimnological environments, for instance, are subject to the variation of secondary parameters which might significantly affect signals (Juggins, 2013). The best way to avoid biases in reconstructions is to compare several independent proxies (Heiri and Lotter, 2005).

In addition to the paleothermometers based on paleontological assemblages, other techniques based on physico-chemical processes can be mentioned, although their use is not as widespread as the aforementioned methods. The δ^{18}O value of speleothems only depends on the temperature of deposition and on the δ^{18}O of the water from which the speleothems were precipitated; in turn, the δ^{18}O composition of cave water depends on the reservoir composition (the clouds, ergo the sea surface), atmospheric and hydrological evolution of rainfall (distance from marine source, altitude, rainfall amount, air temperature, and rainfall seasonality) and interaction of water with rock and soil (Bar-Matthews et al., 2003). Therefore, provided other variables are constrained, it is possible to use speleothems δ^{18}O as a thermometer. Such reconstructions (e.g. Constantin et al. 2007) are rare, however, as variables to constrain are numerous, rainfall amounts in the first place. Carbonate "clumped isotopes" thermometry, based on the abundance of ^{13}C-^{18}O bonds in the carbonate lattice, can also be used to determine the growth temperature of carbonates irrespective of the isotopic composition of the parent water (Ghosh et al., 2006); however, it suffers from a quite large uncertainty when used on speleothems, and needs a large amount of material (Affek et al., 2008; Meckler et al., 2015). Coupling δ^{18}O measurements of gypsum hydration water with δ^{18}O measurements in coeval gastropods and ostracods shells in a tropical lake, Hodell et al. (2012) were able to differentiate the temperature and lake water composition signal, thus proposing a new paleothermometer for lake temperature. Such developments show that in some cases δ^{18}O may reveal adapted for paleothermometry, provided independent constraints on the water composition exist.

Models Modelling past climates is generally used either to test the reliability of GCMs involved in the assessment of present and future climate (e.g. Fischer et al. 2018), or to understand the dynamics of glacial-interglacial cycles or the start or end of it. Model types used to simulate past climates may range from complex models, namely full Earth System Models (ESMs) and Atmosphere-Ocean coupled General Circulation Models (AO-GCMs) to Earth models of intermediate complexity (EMICs).

By far the most common approach that is used to model past climates is to carry snapshot simulations, that is, study only one or several particular time slices within the period of interest (e.g. Kaspar et al. 2005; Lunt et al. 2013; Otto-Bliesner et al. 2013; Capron et al. 2014; Kutzbach et al. 2014). This is explained by the fact running such simulations is extremely time-consuming, especially when runs span several millennia. Another reason is that model-data comparisons, when investigating periods beyond the ^{14}C limit, display no other option than use records with low temporal resolution and with sparse geographical distribution, which makes necessary the gathering of data within one single or few time slices (e.g. Otto-Bliesner et al. 2013; Lunt et al. 2013). When simulating interglacials, these models usually assume that current parameters such as the extent of ice sheets or vegetation, as well as the aerosols content of the atmosphere, were identical during other interglacials; they adapt better constrained values such as GHGs concentration and insolation (Past Interglacials

Working Group of PAGES, 2016).

Transient simulations, that is, simulations running over a whole period of time and the variables of which evolve through time, are necessary to observe the evolution of climate patterns. Their use is particularly critical for evaluating sharp transitions in climate and their mechanisms, such as glacial terminations. For the late Last Glacial and the Holocene, for which well-resolved paleo-data sets exist, they are particularly relevant to compare trends and test both models and proxies (Liu et al., 2009, 2014). However, due to computer resources limitations, running this kind of simulation over several thousands of years remains very challenging. Bakker et al. (2014), for instance, led a comparison of transient models run over the whole LIG and PIG; however, they had to use either EMICs or low-resolution GCMs. Another option used when running transient models is sometimes to accelerate astronomical forcings (typically by a factor 10^1 to 10^2; Felis et al. 2004; Hall et al. 2005; Lohmann 2017), which does not come without biases, since several planetary patterns show strong inertia.

In a review dedicated to assessing the role comparisons with paleoclimatic data can have in the process of improvement of climate models, Braconnot et al. (2012) concluded, given the model-datacomparisons, that models "reproduce the direction and large-scale patterns of past changes in climate, but tend to underestimate the magnitude of regional changes".

1.3.2 Proxies and models outputs: how do they compare ?

The Holocene is the most adapted period to compare models and proxies, as it is by far the period for which the largest amount of reconstructions is available, and for which values of the input parameters for the models are best-constrained. Here, through the study and comparison of several key records and models of the period, we shed light on some of the main Holocene conundrums. In doing so, we aim at emphasizing the strengths and limitations of the models and temperature reconstructions that are used today.

The Holocene global annual temperature stack of Marcott et al. (2013) and the Holocene Thermal Maximum conundrum Through compiling Holocene records (mainly $U^{k'}_{37}$, Mg/Ca, TEX_{86}, ice cores, chironomids and pollens) from all continents and oceans, Marcott et al. (2013) produced a reconstruction of global temperatures for the past ~11 ka. The latter shows a clear early Holocene warming trend, a plateau spanning 10 to 7 ka, and a global cooling during the following 7 ka. This mid-Holocene maximum is referred to as the "Holocene Thermal Maximum". It is one of the main conundrums of the period, as CO_2 concentrations have increased steadily during the whole Holocene, thus one would expect a monotonic increase of global temperatures. Marcott et al. (2013) argued that the HTM was consistent with the summer insolation trend; however, models show that CO_2 should lead and global mean annual temperatures should increase steadily, by approximately 0.5°C (Liu et al. 2014; see also Figure 1.9). Through splitting the stack into 3 latitudinal bands, it appears that the main discrepancy between models and records lies in the extratropical northern hemisphere. Liu et al. (2014) suggested that the problem lies in the over-representation of North Atlantic $U^{k'}_{37}$ records within the stack, as the latter are suspected to bear a summer signature. Running a simulation including a seasonal

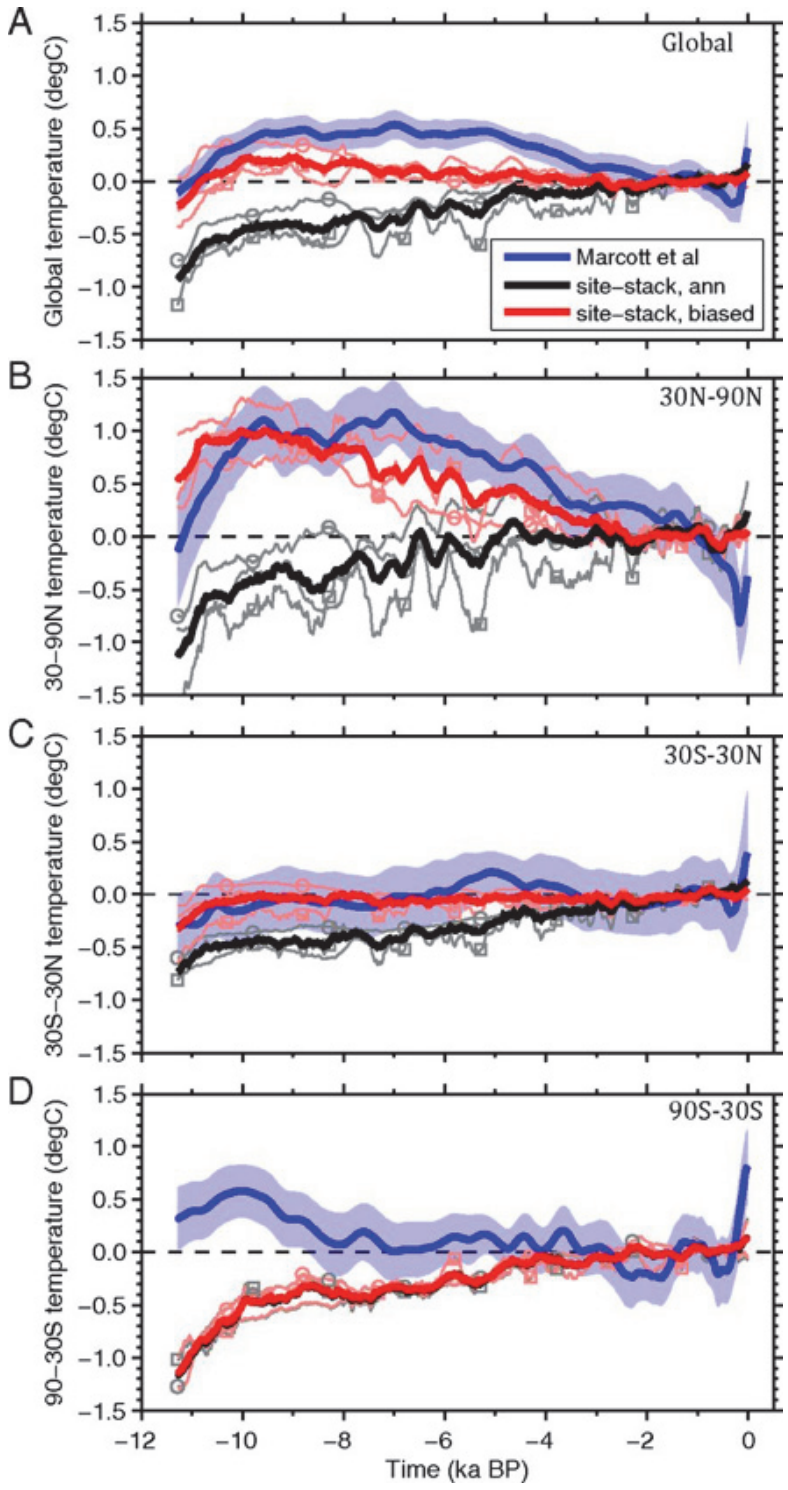

Figure 1.9: ***Comparison of Holocene global temperature as reconstructed with records stacks and as modelled.*** *Comparison of mean annual temperatures reconstructed from records stack (blue curve, Marcott et al., 2013) and simulated by the models with (red curve) or without (black curve) introduction of a seasonal bias (Liu et al., 2014) at global scale (A), for the northern hemisphere (B, 30 - 90° N), the tropical zone (C, 30° S - 30° N) and the southern hemisphere (D, 30 - 90° S). The results of the models are presented as an average of all the models (CCSM3, LOVECLIM and FAMOUS, thick curves) and individually (fine curves) for the LOVECLIM (round) and FAMOUS (square) models. From Liu et al. (2014).*

bias, they managed to reproduce a temperature curve with a HTM (see Figure 1.9); the amplitude of the simulated "biased" curve, however, remained weaker than that of Marcott et al. (2013). Many pollen-based annual

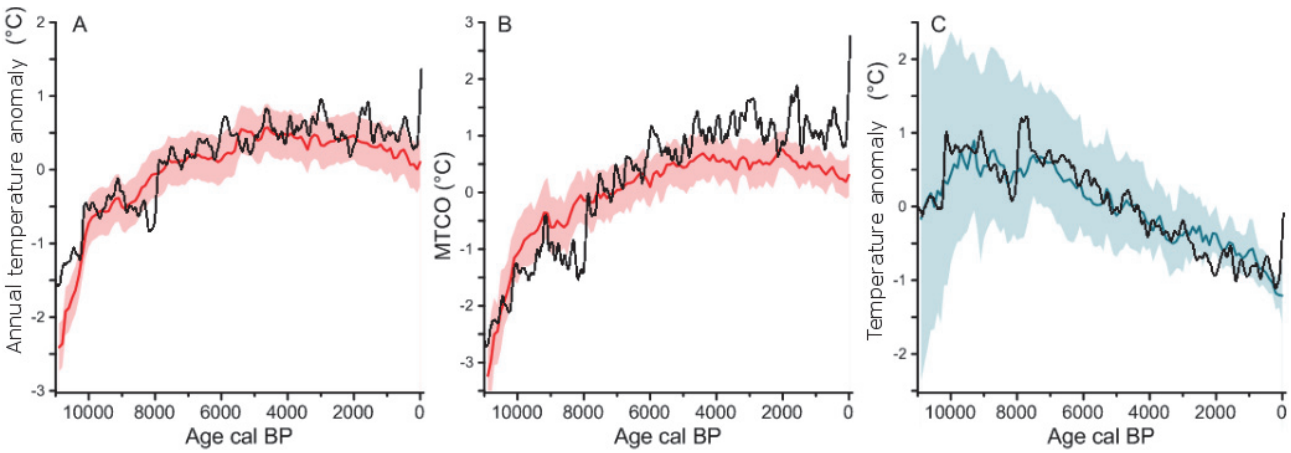

Figure 1.10: ***Simulated and reconstructed annual and seasonal temperatures in North America, Europe and the northern ocean margins.*** *Comparison of reconstructions from pollen assemblages (red curve and uncertainty envelope at 2.5 - 97.5%) and simulations by CCSM3 (100-year averages, black curve) for mean annual temperatures (A) and for the temperatures of the coldest month (MTCO, B). C: Synthesis of ocean temperatures (blue curve) and simulation of average temperatures from June to August by the CCSM3 model (100-year averages, black curve). Data from Marsicek et al. (2018). From Martin (2018).*

temperature reconstructions are consistent with models, as they also discard any significant cooling during the second part of the Holocene, and even show a slight warming trend (e.g. Davis et al. 2003; Viau et al. 2006; Mauri et al. 2015; Marsicek et al. 2018). Thus, evidence point towards a seasonal bias in alkenones-based temperature reconstructions. Liu et al. (2014) concluded, however, that an additional significant bias of models could not be excluded, as the simulated bias introduction was not enough to reproduce the amplitude of the HTM of Marcott et al. (2013).

The pollen/models seasonal mismatch As a test for the HTM conundrum detailed above, Marsicek et al. (2018) produced a Holocene stack of temperature records for North America and Europe, which they compared to models (see Figure 1.10). They found no HTM, and only a slight cooling starting at 2 ka BP. They also showed that pollen-based summer temperature reconstructions perfectly match simulations. However, winter temperatures are significantly overestimated by models as of 5 ka BP. Similarly, Mauri et al. (2015) produced a gridded pollen-based reconstruction of Holocene climate in Europe. According to their reconstruction, warming during the mid-Holocene was greater in winter than in summer, an apparent paradox that is not consistent with direct insolation forcing and model simulations. In a previous paper using the same database (Mauri et al., 2014), they argued that the spatial pattern of the temperature and precipitation reconstructed through their dataset closely resembled that of the North Atlantic Oscillation. Thus, they suggested that models largely underestimate atmospheric circulation, thereby missing the trends and amplitude of regional climatic changes highlighted by pollens.

The pollen/chironomid mismatch Through comparing Holocene chironomid-based and pollen-based southern Europe summer temperatures, along with SST reconstructions, glacier dynamics in Italy and model simu-

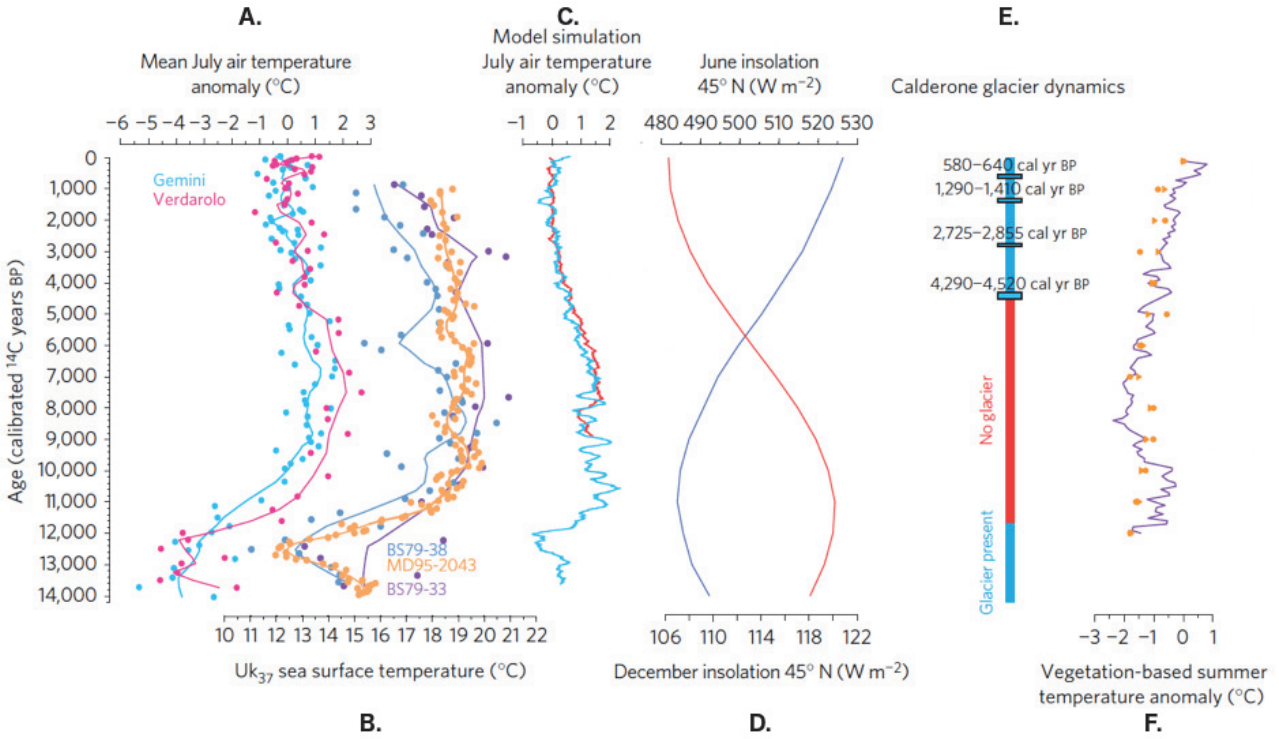

Figure 1.11: ***Comparison of Holocene summer temperatures in southern Europe sites as simulated by models and as reconstructed by several proxies.*** *A: July temperature anomalies for two sites in northern Italy reconstructed from Chironomidae assemblages (Samartin et al., 2017). B: SSTs as measured with $U^{k'}_{37}$ from marine cores of the Western Mediterranean (Cacho et al., 2001). C: July temperature in northern Italy as simulated by climate models ECBilt-CLIO-VECODE (red curve, Renssen et al. 2009) and NCAR CCSM3 (blue curve, Liu et al. 2009, 2014). D: June (red curve) and December (blue curve) insolations at 45°N (Berger and Loutre, 1991). E: Presence (blue vertical bar) and advances (blue horizontal bar) of the Calderone glacier in Italy (Giraudi et al., 2011). F: Anomalies of the armest month temperatures reconstructed from the vegetation in southern Europe (purple curve, Davis et al. 2003) and anomaly of summer temperatures in northern and central Italy (circles) and in Europe below 45°N (triangles; Mauri et al. 2015). From Samartin et al. (2017).*

lations, Samartin et al. (2017) showed that all but pollen-based reconstructions matched very well, displaying a mid-Holocene peak consistent with the maximum in insolation forcing (see Figure 1.11). Pollens, in turn, show an increase in summer temperatures starting at ~9 ka and spanning the whole period up to today. They interpreted this mismatch by a precipitation bias in the pollen reconstruction. Conversely, Mauri et al. (2015) compared their own reconstruction to several proxies and demonstrated that each type of proxy but the chironomids matched well their reconstruction. The apparent paradox may be explained by the fact that most multi-proxy comparisons led by Mauri et al. (2015) were carried in northern Europe in the case of summer temperatures. It is possible that pollens reproduce well all climatic variables apart from summer temperatures in southern Europe, and that chironomid-based reconstructions, in turn, are more reliable in southern than in northern Europe.

Models are now able to reproduce the general trend and amplitude of global cooling and warming for the previous climatic cycles, and the mechanisms that govern variabilities, from interannual to million-year scale, have received some convincing explanations. There still remains major limitations that need urgent answer:

- The understanding of the causal chain of the 100-ka cycle, and above all its nonlinear response to astronomical forcings, still remains elusive. This aspect is one of the keys to understanding abrupt changes in climate.
- Current models do not fully simulate the amplitude of ocean-to-atmosphere interactions. Heat and moisture transfers and the impact of sea surface temperature on wind speed are strongly underestimated at the key location of oceanic currents boundaries. This is partly due to a resolution coarser than required to account for mesoscale fluid dynamics processes. Such an overlooked phenomenon may be one of the reasons of the failure, until recently, to identify the influence sea surface temperatures have on atmospheric circulations patterns such as the North Atlantic Oscillation.
- When compared to paleodata, models generally show limitations in simulating the amplitude and even sometimes the direction of regional trends. This is all the more patent for seasonal trends. To explain this, some authors have emphasized the deficiency of models when it comes to simulate the variability of atmospheric circulation in the past.
- Models deficiencies are all the harder to identify as proxies also suffer from major shortcomings. In some regions and for some seasons, different proxies yield different results. Major discrepancies have been identified between two of the most widely used continental proxies, pollens and chironomids assemblages. The latter discrepancies probably arise because of limitations of the uniformitarianism assumption.

1.4 Goal of the thesis

Fluid inclusions (FIs) are micro-cavities of fluid trapped inside minerals. They can form during the growth of the mineral; in this case, they are called primary fluid inclusions (Roedder, 1962a). Alternatively, they may result from the healing of fractures during subsequent stages of the rock history (Roedder, 1984); in this case, they are called secondary FIs. Both primary and secondary FIs give invaluable information on the genesis and geological path of rocks. In particular, they have been used as geothermometers and geobarometers for more than 150 years (e.g. Sorby 1858). Indeed, once it is trapped inside a mineral, and assuming that the inclusion walls sustain mechanical stress and that there is no leakage nor any chemical exchange, the fluid keeps the density it had at the moment of entrapment. For this reason, the vapor phase that may nucleate in FIs disappears at a precise temperature, T_h, that gives precious information on the pressure and temperature conditions of entrapment (see Figure 1.12).

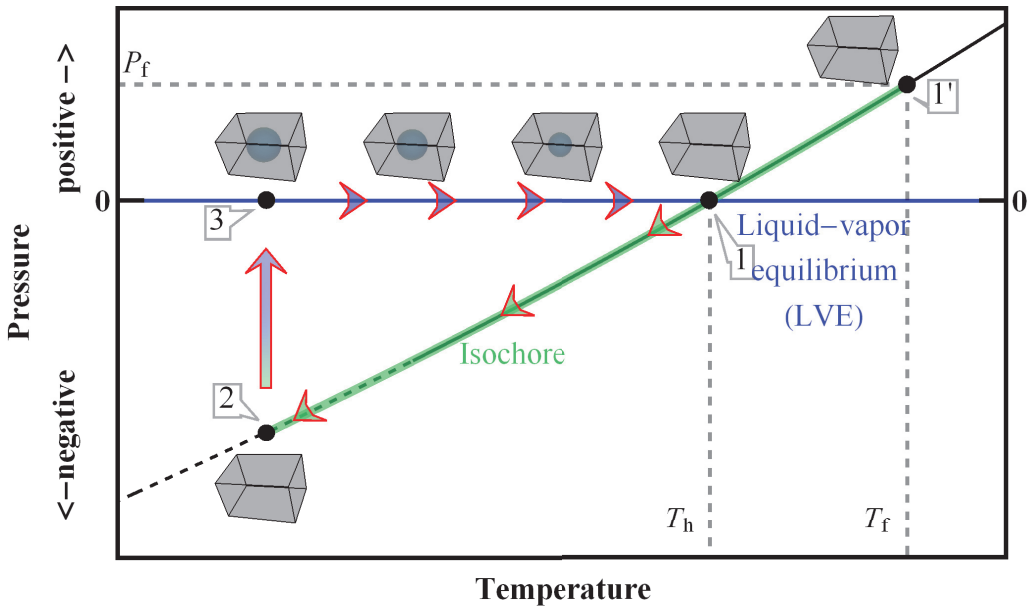

Figure 1.12: ***The pressure-temperature path of a fluid inclusion.*** *A fluid inclusion trapped at conditions {P_f, T_f} (1') keeps entrapment density, thus it follows a line of constant volume, that is, an isochore. The fluid inclusion (FI) only contains liquid (monophasic FI). When temperature decreases, the FI follows the isochore. If sufficiently cooled down, pressure inside the monophasic FI becomes negative, and the liquid enters the vapor pressure-temperature domain: it is metastable. The FI remains metastable and may be cooled until (2) the energy inside the stretched liquid becomes sufficient to nucleate a bubble; then the negative pressure is released and the FI is not metastable anymore; it is at liquid-vapor equilibrium (LVE; 3). Upon heating, the FI remains at LVE (close to 0 MPa), the bubble shrinks and eventually disappears at homogenization temperature T_h (1). Further heating leads to abrupt increase in pressure, along the isochore. Note that if the FI was trapped at subsurface conditions ($P \approx 0$), then $T_h = T_f$ and (1) = (1').*

The use of FIs in deep rocks to reconstruct pressure and temperature conditions is well established in economic geology and metamorphic geology (e.g. Roedder and Bodnar 1980; Van den Kerkhof and Hein 2001; Touret 2001). For (sub)surface rocks, the information provided by FIs is even more straightforward. Since entrapment pressure, namely atmospheric pressure, is near 0, T_h is equivalent to the entrapment temperature T_f. And yet, studies using FIs for paleoclimatic purposes have long remained nonexistent. There are at least

two reasons accounting for this situation: (i) subsurface rocks are generally softer than deep rocks, and are therefore less suitable for the preservation of the FI density, as they may not sustain large pressures or tensions; (ii) the liquid can sustain several 10s of megapascals under metastable conditions, therefore, in the case of low pressure and temperature conditions of entrapment, tension is generally too mild to nucleate a bubble.

To our knowledge, the first convincing attempt to reconstruct paleotemperatures using FIs in subsurface rocks dates back to the paper of Roberts and Spencer (1995). In this study, they had the idea of cooling halite samples down to very low temperatures in the freezer in order to trigger bubble nucleation in FIs. Then, heating up samples in a temperature-controlled stage under the microscope, they measured T_h, which they identified as the water body temperature. However, a later study showed that FIs apparently suffered from irreversible damages in the freezer (Lowenstein et al., 1998); we tackle this issue in detail in Chapter 3. Since then, paleoclimatic studies using halite FIs have been few.

More recently, Krüger et al. (2007, 2011) developed a method to trigger bubble nucleation in FIs by means of femtosecond laser pulses. Once the bubble is nucleated, T_h is measured with the classical way under the stage; it is combined with another method based on the measurement of the bubble radius (Marti et al., 2012). Because of surface tension issues (related to the bubble), the technique cannot apply to cold (< 10 - 15 °C) environments, and requires numerous and large FIs (Marti et al., 2012; Spadin et al., 2015). Also, it requires discarding the highest T_h values, as leakages from some FIs are suspected (Krüger et al., 2011; Spadin et al., 2015). However, temperature reconstructions from minerals precipitated in warm environments with large FIs have proved convincing, both in cave gypsum (Krüger et al., 2013) and cave calcite (Meckler et al., 2015).

The goal of this thesis is to promote fluid inclusions in subsurface minerals to the rank of routine paleothermometers. Fluid inclusions are exceptional temperature archives, since the temperature signal they supply is physically-based. It is based on the same physical principles as the everyday mercury thermometer, whose density indicates ambient temperature at home. Such a thermometer would be of great help in testing model simulations in the past, and also in verifying the reliability of calibration-based thermometers, or assemblages-based thermometers, in regions, seasons or periods of time for which their applicability is questioned. As we have seen above, the main limitation of FIs paleothermometry is the need for a bubble, both because nucleating it may damage FIs and because it is associated with surface tension issues. Therefore, the idea of this thesis is to develop a new method that does not require the presence of a bubble as a prerequisite. The method consists in using the non-destructive signal yielded by the inelastic interaction of light with the thermodynamic fluctuations of the inclusion fluid, by means of a Brillouin spectroscope. A first proof of principle of the validity of the method was given by El Mekki-Azouzi et al. (2015) on FIs trapped at high temperature in deep rock stiff minerals (quartz). In this thesis, we focus on a soft subsurface mineral: halite. We will endeavor to answer questions among which:

- How to use Brillouin spectroscopy as a reliable paleothermometer ?
- Can we get reliable entrapment temperatures out of halite FIs, despite their fragility ?

- Are there physical rules underlying the damaging of halite FIs ? If so, can we predict limits beyond which FIs are not suitable for paleothermometry anymore ?

We will then see how the method applies to natural case studies. Using Brillouin thermometry on halite samples obtained from the long core 5017-1 that was drilled in the deep Dead Sea in 2010/2011 through the Dead Sea Deep Drilling Project (DSDDP), we will try to give answers to the following questions:

- Can we measure reliable temperatures from halite grown in such environments ? Is the complex composition a problem, and how to overcome the issue of thermometry on crystals grown under several megapascals of pressure ?
- How to interpret a deep lake temperature signal as a paleoclimatic indicator ?
- What can the Dead Sea temperature reconstructions teach us about climate in the Eastern Mediterranean and the Near-East during hte Last Interglacial, some 125,000 years ago ? How can we contribute to disentangle the intricate climate conundrums in this region ?
- Can Brillouin spectroscopy on halite fluid inclusions bring other paleoclimatic information in addition to temperature ?

We will first give details on the setup and on the main technical developments achieved during the thesis in Chapter 2. Then in Chapter 3 we will expand on the principles of Brillouin thermometry, and show the results on halite FIs. Still in Chapter 3, we will investigate the mechanisms that underlie the loss of entrapment temperature signal in FIs. In Chapter 4, we will elaborate on a model that we developed to calculate pressures in FIs and predict the limit at which they get damaged. Lastly, we will present our work on the Last Interglacial Dead Sea in Chapter 5. In this last chapter, we will show that Brillouin spectroscopy can reveal information on both temperatures and hydrology. We will see how these information can be used to understand regional climatic trends during the Last Interglacial in the region.

CHAPTER 2

Setup, physical concepts and technical developments

Foreword This chapter briefly describes the setup and the physical concepts and details the main technical advances made in the field of spectroscopy during the course of the thesis. It details the calibrations and corrections that will be used, often implicitly, in the next chapters.

I mention here two other contributions in physics which will not be described further. My experience in Brillouin spectroscopy allowed me to contribute to a published work on the compressibility anomalies in water under negative pressure (Holten et al., 2017). Through measuring the speed of sound inside quartz-hosted pure water fluid inclusions at negative pressure, this study revealed the existence of a line of compressibility maxima in the phase diagram of water, thereby achieving a great stride towards the understanding of the anomalous physical behaviour of water. My work on Raman spectroscopy presented in Section 2.6 also led me to contribute to a study (Goy et al., 2018) that have reached, and measured accurately, the lowest temperature ever observed for supercooled water -below the melting point but still a liquid. The method consisted in the ultrafast cooling of water droplets generated from a laminar liquid jet and evaporated in vacuum, and simultaneously measured with Raman spectroscopy to determine their size and deduce their temperature.

2.1 Brillouin scattering

2.1.1 Physical concept

Named after Léon Brillouin, Brillouin scattering refers to the inelastic interaction between an incoming light and the thermodynamic fluctuations of matter, be it solid or liquid (Landau et al., 1984). A monochromatic light ray undulates with a frequency ν and has an energy E. Condensed matter endlessly undergoes fluctuations of its density (thermodynamic fluctuations) that propagate at the speed of sound. The interaction between the light-wave and the fluctuating matter (Figure 2.1) results in elastic (i.e. without energy change) and inelastic (i.e. implying loss or gain of energy) scattering of light. In the inelastic case, the incoming photon absorbs or emits a phonon and thus gains (anti-Stokes process) or loses (Stokes process) a fraction of its energy, hence an increase or decrease of its frequency, respectively. The resulting shift in frequency is called "Brillouin frequency shift" (Δf_B).

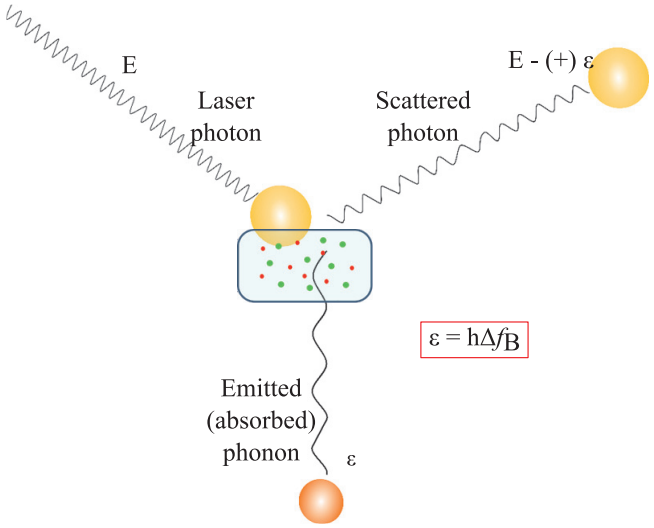

Figure 2.1: ***Brillouin scattering of light in a liquid.*** *Incoming photon has energy E. Interaction with thermal fluctuations of the liquid emits (absorbs) a phonon of energy ϵ. The energy of the scattered photon is thus E minus (plus) ϵ. h is the Planck constant.*

2.1.2 How to measure it

In this thesis, we measured Δf_B in liquids, especially in halite fluid inclusions, for multiple purposes. To this end, we used a setup adapted for the measurement of Δf_B, presented in Figure 2.2 and previously detailed in several studies (Pallares et al., 2014; El Mekki-Azouzi et al., 2015; Pallares et al., 2016; Holten et al., 2017). The monochromatic green light of the laser is focused to a 1μm-large spot onto the sample (Figure 2.3A), and the backscattered light is then directed towards the Brillouin spectroscope. The latter comprises 2 Fabry-Perot interferometers (FPs), each consisting in a pair of two mirrors with a spacing L. Such interferometers are used for high resolution spectroscopy where a resolution of MHz to GHz is required. They act as wavelength

selectors: only light with wavelength (λ) satisfying

$$L = \frac{1}{2} p\lambda \tag{2.1}$$

for integer values of p, will be transmitted. Within subsecond cycles (~0.64 s with the configurations used in this work) and for each FP, the translation stage on which is mounted one of the 2 mirrors modifies the spacing by a maximum amount d, called "scan amplitude". This 200 nm (~37.6 GHz) scanning around a value $D = 3$ mm will let pass the light from the sample only when the spacing L satisfies Equation (2.1). With the laser emission frequency measured during each cycle (see Figure 2.2) and arbitrarily set to 0 GHz, the spacing at which backscattered light is transmitted through the two FPs and reaches the detector therefore gives Δf_{B}. An example of resulting spectrum in the case of the analysis of a (monophasic) halite fluid inclusion (FI) is shown in Figure 2.3B, where one sees that it consists in two inelastic peaks located at $-\Delta f_{\mathrm{B}}$ and $+\Delta f_{\mathrm{B}}$ corresponding to the Stokes and anti-Stokes shifts, respectively.

2.1.3 Fit of Brillouin spectrum and calculation of the speed of sound

As previously mentioned, Δf_{B} is a function of the speed of sound w. In a first approximation Δf_{B} is proportional to the speed of sound w in the liquid:

$$\Delta f_{\mathrm{B}} = 2\frac{n.w}{\lambda_{\mathrm{laser}}}, \tag{2.2}$$

where λ_{laser}=532 nm is the wavelength of the laser light, and n is the refractive index of the liquid.

This neglects sound dispersion, that is, the frequency dependence of the speed of sound. Because the Brillouin shift is large, around 9.3 GHz in our experiments, this effect cannot always be neglected. Indeed, if the liquid exhibits relaxation on a timescale of the order of the inverse frequency (around 100 ps), dispersion is expected. In the work of El Mekki-Azouzi et al. (2015), performed with a smaller Brillouin shift and at high temperature where the relaxation time is very short, dispersion is negligible. In other works of our group dealing with pure water at low temperature, dispersion effects were corrected using the viscoelastic formalism in the memory function approach. We refer the reader to Pallares et al. (2014) for a detailed explanation with the relevant equations. In the present thesis, where analyses are mainly carried out on saturated salt solutions at low temperature which are even more slowly relaxing than pure water, the same correction is needed.

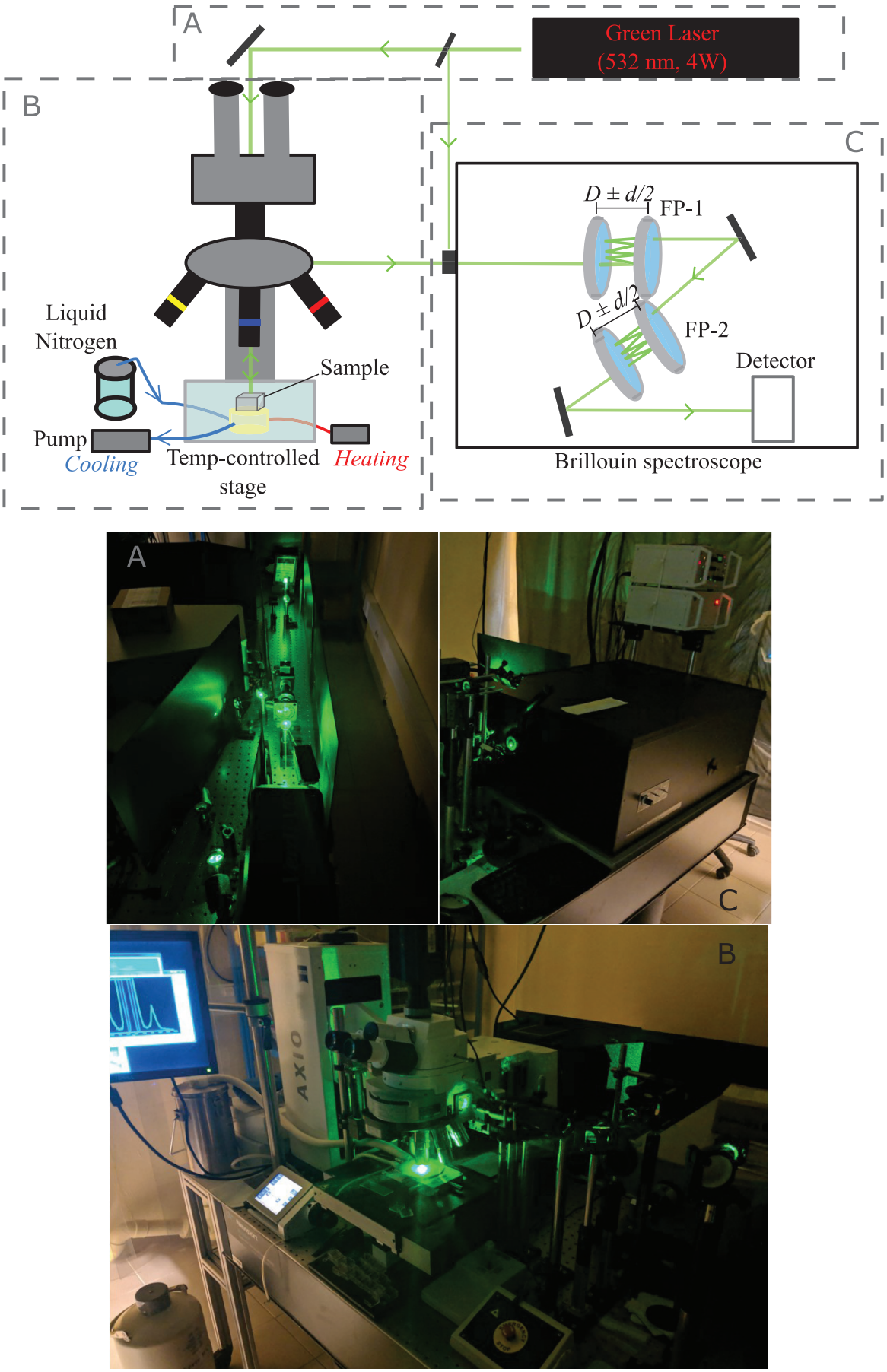

Figure 2.2: ***The Brillouin spectroscopy setup.*** *FP: Fabry-Perot interferometer. D: Distance between the two mirrors of a FP. d: scan amplitude. Note that the Brillouin spectroscope receives light from two sources: the light backscattered from the sample and the light directly originating from the laser; a shutter located at the entrance pinhole switches back and forth once during each cycle to let each light source pass one after the other. Pictures: K. J. Olson.*

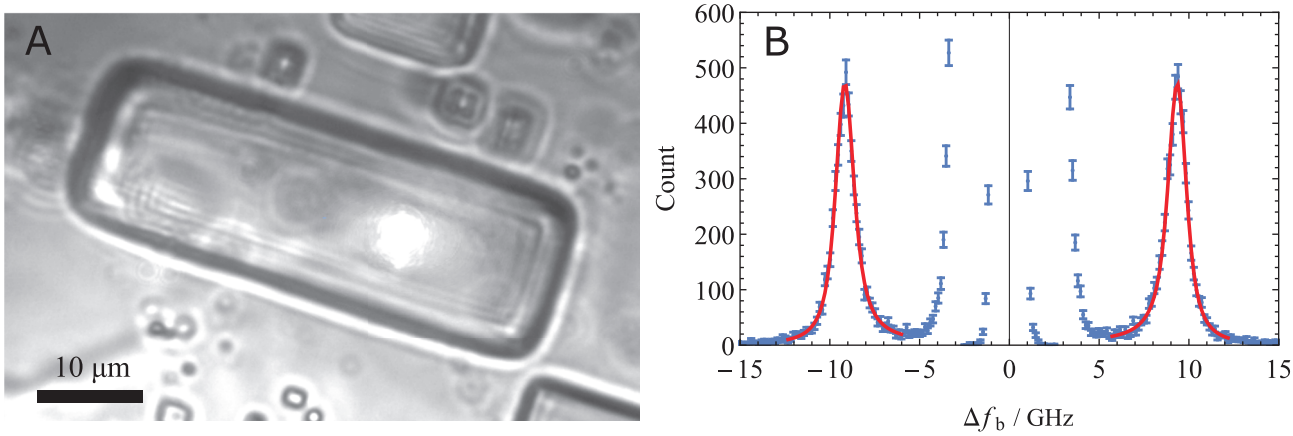

Figure 2.3: ***Example of analysis in a monophasic fluid inclusion.*** *A: the laser spot is focused on the halite FI. B: The resulting Brillouin spectrum shows two inelastic peaks, on the right and on the left of the excitation frequency.*

The Brillouin spectrum can then be fitted (red curve in Figure 2.3B) with a formula having three free parameters (the peak amplitude, the relaxation time, and the speed of sound at zero frequency w) and two input parameters: the speed of sound at infinite frequency c_∞, and the refractive index n. For pure water, c_∞ = 3000 m s^{-1}, as determined from x-ray measurements (Bencivenga et al., 2009). As we are not aware of a corresponding value for saturated salt solutions, we use the same value as for pure water. For the refractive index n, we used the following procedure. We assumed the validity of the Gladstone-Dale relation between the density ρ and the refractive index n at λ = 532 nm of a NaCl solution of molality m at temperature T and pressure P:

$$n(T, P, m) = 1 + K(m)\rho(T, P, m) \tag{2.3}$$

where K is a function of molality only. We measured n at T =25 °C, P = 0.1 MPa and for a series of NaCl molalities using a Schmidt-Haensch ATR-L refractometer. This yields

$$K(m) = 0.3352254.10^{-3} - 3.113319.10^{-6}\mathrm{m} + 7.013441.10^{-8}\mathrm{m}^2 \tag{2.4}$$

with m in mol kgH_2O^{-1}. Then, to determine the density ρ in the liquid, we used the parameterization from Al Ghafri et al. (2012) for ρ(T, P, m), which was established for T from 298 to 472 K, P from 0.1 to 68.5 MPa, and m from 0 to 6.0 molal. We extrapolate it to slightly higher m to cover saturated solutions. For measurement in liquid at equilibrium with vapour and saturated with respect to NaCl (the case of a halite fluid inclusion with a bubble, biphasic FI), we approximate the vapour pressure by a constant 0.1 MPa (this causes a negligible error) and assume that the molality m is the saturation value $m_{\mathrm{sat}}(T, 0.1\ \mathrm{MPa})$ at the temperature of interest; this is justified by considering the short time needed for precipitation/dissolution in comparison with the experimental times. For $m_{\mathrm{sat}}(T, 0.1\ \mathrm{MPa})$, we used the empirical fit by Farelo et al. (1993) based on data from 293 to 360 K at ambient pressure. Comparison with an empirical fit by Sawamura et al. (2007) based on data from 273 to 313 K and from 0.1 to 300 MPa shows that the extrapolation of the fit by Farelo et al. (1993)

is valid down to 273 K (deviation less than 0.2%). The refractive index is thus calculated as:

$$n(T) = 1 + K[m_{\text{sat}}(T, 0.1MPa)].\rho(T, 0.1MPa, m_{\text{sat}}(T, 0.1MPa)). \tag{2.5}$$

For a halite fluid inclusion without bubble (monophasic FI), we use the same expression as for a biphasic FI. This introduces a small error which increases with pressure, because the density and saturated concentration are pressure dependent. In the range of temperature used in this thesis, we estimate this error to a few tenths of percent. Note that this has no effect on the thermometry measurements achieved in the following chapters, as the error made on the monophasic FI vanishes when approaching entrapment temperature (see Chapter 3).

2.2 Control of temperature measurements

2.2.1 Calibration of the temperature-controlled stage

Samples measured in Brillouin spectroscopy are placed in a temperature-controlled stage (Linkam, THMS600). The silver block on which the sample lies has a very high thermal conductivity, and thus quickly cools (by means of cold N_2 flux) and heats down and up to the required temperature with an accuracy better than $0.1\,^{\circ}\text{C}$ in the range -195 to +600 °C. However, the 0.15mm-thick glass cover separating the block from the sample prevents full thermal contact. Furthermore, the light aperture below the sample and the lower thermal conductivity of the sample might induce thermal gradients. Therefore, determining the temperature of the sample with accuracy requires a thermal calibration.

Correction for the temperature gradient inherent to the incomplete thermal contact We measured phase transitions inside two fluid inclusions to calibrate the stage:

- a CO_2-H_2O FI trapped in a quartz host, which yields two clear phase transitions at $-59.59\,^{\circ}\text{C}$ and $10.0\,^{\circ}\text{C}$ (Diamond, 2001)
- a pure H_2O FI trapped in a quartz host, which yields a clear phase transition at $0.01\,^{\circ}\text{C}$ (Diamond, 2001)

The linear fit of the "measured minus actual" temperature as a function of measured temperature (Figure 2.4) brings an uncertainty comparable to the stage accuracy of $0.1\,^{\circ}\text{C}$. This equation was used to correct measurement temperature in this work. Note that the linearity of the calibration curve was confirmed by Mekki-Azouzi and Ramboz (2019) on the range -56.6 to +574 °C

Checking potential horizontal and vertical temperature gradients inside the sample A horizontal thermal gradient may establish between the center of the sample that lies above the 2.0mm⌀light aperture and the edge that lies directly above the silver block. Similarly, a gradient may establish between bottom and top of sample. We checked the horizontal gradient issue by measuring the temperature of phase changes in quartz-hosted FIs at

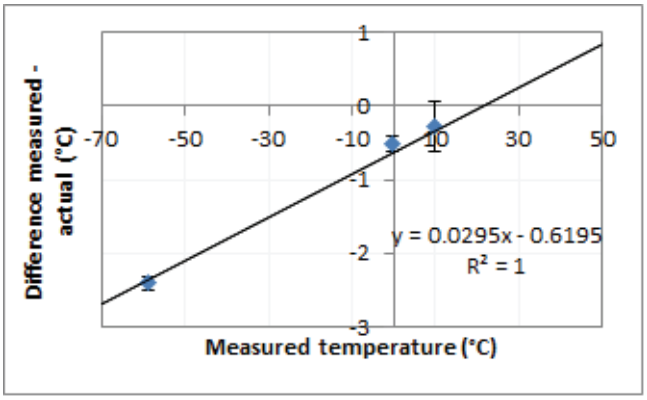

Figure 2.4: ***Calibration fit for the determination of sample temperature.*** *Note that the root of the equation is* 21.0 °C*, that is, the temperature of the room.*

the edge and center of the light aperture. We checked the vertical gradient issue by measuring the temperature of phase changes in quartz-hosted FIs and re-measuring it after having flipped the sample, thereby modifying the FI depth by ~0.5 mm. At 0 °C, using the ice to water phase transition in the quartz-hosted pure water FI, we observed no horizontal nor vertical temperature difference higher than the instrumental uncertainty 0.1 °C. El Mekki-Azouzi (2010) estimated a vertical gradient of 3 to 4 °C per mm of quartz thickness at 570 °C. In our conditions where T excursions away from room temperature rarely exceed ±20 °C, this would convert in maximum gradients in quartz of no more than 0.14 °C-0.18 °C per mm of thickness, which is consistent with the fact we did not observe any gradient. Note that as halite conveys heat about three times as good as quartz (Robertson, 1988), thermal gradients are all the smaller in halite.

2.2.2 Checking potential laser heating

To evaluate the potential heating due to the laser, we measured Δf_B in a halite FI at constant temperature (24.9 °C) using several values of laser power (Figure 2.5). Indeed, if the laser heats the sample, then measuring the Brillouin shift with a different laser power should yield different results. The usual power on sample is 50±5 mW. We measured Brillouin spectra with power down to 5 mW. As a control, we measured Δf_B in the same halite FI at a different temperature, and deduced a dependence of Δf_B on temperature of 7.3 MHz °C^{-1}. Results show that whatever the power of the laser results are comparable within the uncertainty. We conclude that laser heating is comprised within our experimental uncertainty 0.1 °C.

2.3 Correction of the instrumental drift

During this thesis, we discovered the existence of an instrumental drift, evidenced when measuring a FI at several moments during the course of the day. Indeed, as shown in Figure 2.6, the speed of sound measured in one FI may vary up to 1% along the course of the day and from one day to another. As the drift is the same for all measured FIs, it confirms the instrumental origin of the drift, presumably due to thermal expansion of

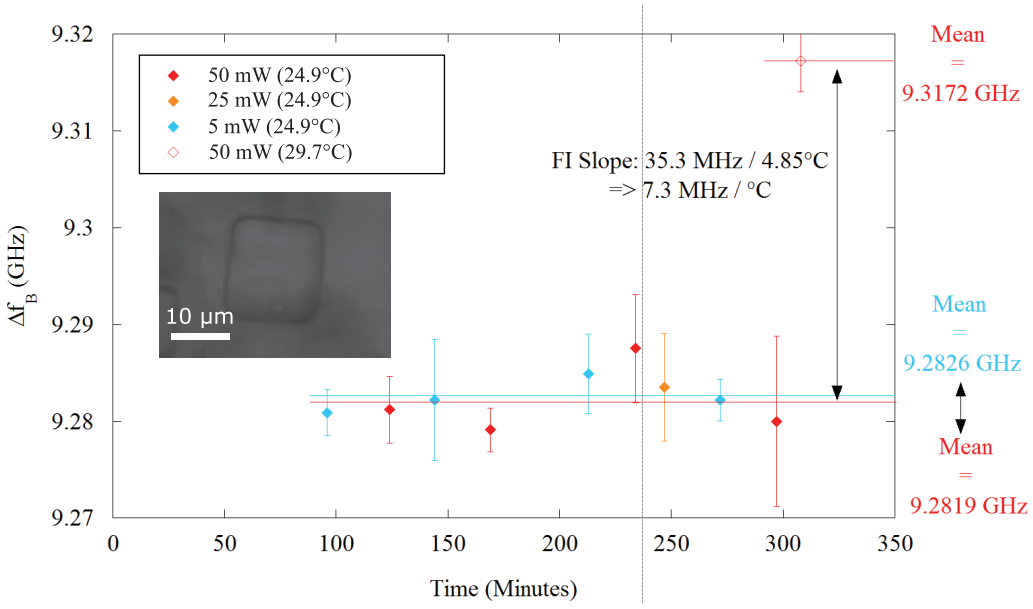

Figure 2.5: ***Testing the impact of the laser on the temperature of the sample.*** *Each data point is the mean value of a 3-5 replicate with error bars standing for the standard error on the mean. Laser power values as measured at sample location, with a 10% uncertainty.*

the spectrometer setup. Thus, measuring the value of a reference FI throughout the day of experiments enables us to estimate the drift and correct all measurements for it. The results in Figure 2.6 show a very good reproducibility of the speed of sound measured in the halite FI once corrected for the drift, to within almost 0.02%. However, as the standard error on each cluster is on average 0.05%, we cannot claim a reproducibility better than 0.05%. Anyway, this is much lower than our estimate of the short-term instrumental error, 0.1% (that is, the standard deviation on measurements repeated one after the other on the same FI during several tens of minutes). Therefore, these reproducibility experiments lead us to regard the uncertainty on the drift correction as negligible and to estimate the overall uncertainty as 0.1%. However, the setup can reveal less stable some days, involving a larger uncertainty on the drift correction. Hence, all in all, the overall uncertainty lies somewhere between 0.1% and 0.15%. This is further discussed in the appendix of the next chapter (Section 3.B). In previous works using the same setup but without correction for the drift (Pallares et al., 2014; El Mekki-Azouzi et al., 2015; Pallares et al., 2016; Holten et al., 2017), the error was estimated as 0.3%.

In this thesis we divided all the speed of sound values $w(T, \text{time})$ by ${w^{\text{LVE}}}_{\text{ref}}(25\,^{\circ}\text{C}, \text{time})$, that is, the value of a reference biphasic FI which is regularly measured all along the day of experiments and fitted with a linear or parabolic equation as a function of time. Two different reference FIs have been used during the course of the thesis: a pure water FI in a synthetic quartz crystal and a NaCl-H_2O FI in a synthetic halite crystal. Note that for the clarity of the manuscript all $w(T, \text{time})$ values divided by ${w^{\text{LVE}}}_{\text{ref}}(25\,^{\circ}\text{C}, \text{time})$ were then multiplied by a constant factor, ${w^{\text{LVE}}}_{\text{ref,mean}}(25\,^{\circ}\text{C})$. This factor was obtained through averaging 1284 and 447 measurements on the reference inclusions. Its value is equal to 1471.7 m s^{-1} and 1779.3 m s^{-1} for the pure water FI and for the halite FI, respectively. Unless specified differently, measurements presented in this thesis were corrected for the drift by means of one of the two reference inclusions.

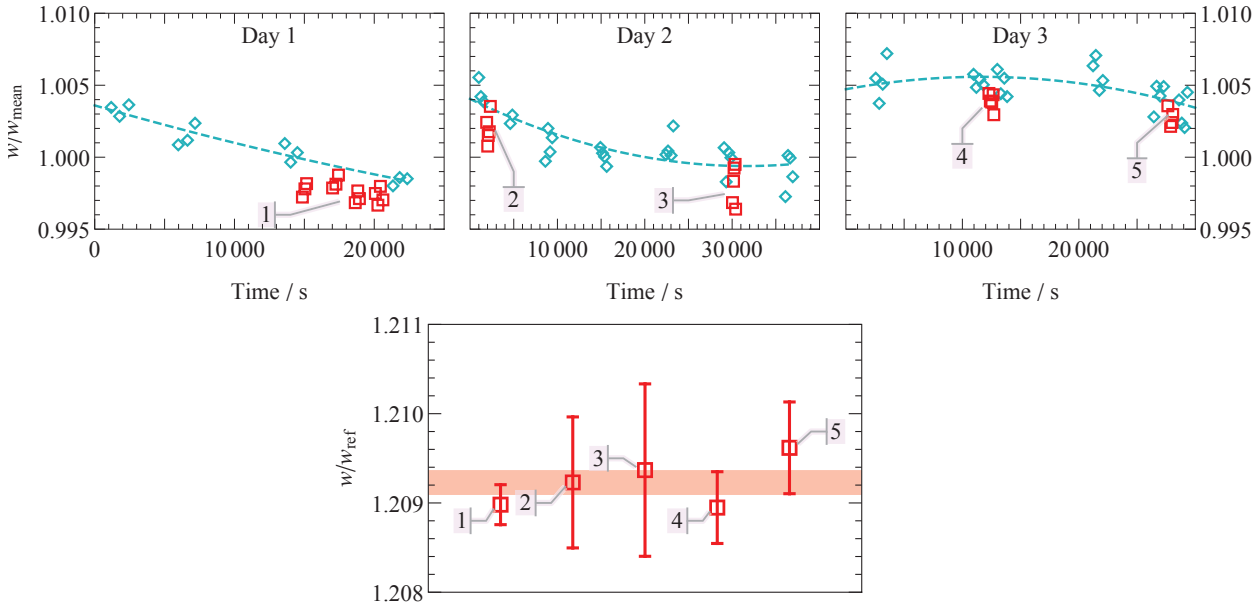

Figure 2.6: ***Daily drift of the spectroscope revealed by reproducibility measurements on one halite FI and the reference pure water FI.*** *The 3 top panels show repeated measurements at 25 °C of the speed of sound as a function of time in the reference pure water FI (w^{LVE}_{ref}(25 °C, time), blue hollow diamonds) and one halite FI (red hollow rectangles). Blue dashed lines are parabolas fitted to w^{LVE}_{ref}(25 °C, time). All values are divided by a constant: w^{LVE}_{ref}(25 °C, time) values are divided by the average value of the pure water FI, $w^{LVE}_{ref,mean}$(25 °C) (see text), while the halite FI speed of sound values are divided by its average speed of sound 1782.2 m s^{-1} (average from dozens of measurements taken over several days). The bottom panel shows the mean speed of sound for each of the 5 clusters plotted above divided by the parabolic fits of w^{LVE}_{ref}(25 °C, time). Error bars are the standard error on the mean for each cluster. The red horizontal strip is the average of the 5 mean values; its thickness accounts for the standard deviation of the 5 mean values.*

2.4 Focus and sample positions

2.4.1 Impact of focus location on measurements

To check the impact of the laser spot location on measurements in a FI, we performed Brillouin measurements at various x,y and z locations in the reference quartz-hosted pure water FI (Figure 2.7). Results show no significant change when moving the laser spot some microns away from the usual location on the horizontal plane. When changing depth (z), there might be a difference of the order of magnitude 0.1%.

2.4.2 Impact of sample angle on measurements

To check the potential occurrence of systematic deviations depending on the angle of the sample, we performed repeated measurements on the two reference inclusions with different angles Figures 2.8 and 2.9. In the case of the quartz-hosted pure water inclusion, a clear dependence on the sample angle is observed. It can amount up to 1% when rotating the sample by 180°. In the case of the halite fluid inclusion, a dependence on the angle may exist, albeit limited to $< \pm 0.1\%$. The difference observed as a function of the host crystal is probably linked to the differences in optical properties: quartz is an anisotropic crystal while halite is optically isotropic.

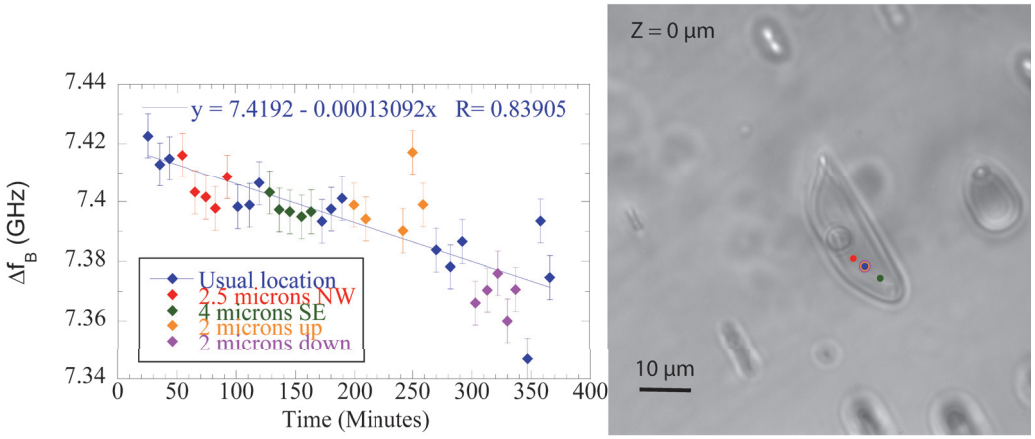

Figure 2.7: ***Testing Δf_B measurements on various locations in a fluid inclusion.*** *Note that values are not corrected for the drift; instead, regular re-measurements on the reference location (blue diamonds) are shown and fitted with a line. Error bars: $\sigma_w = 0.1\%$. NW: "Northwest"; SE: "Southeast". Z=0 μm corresponds to the reference location depth.*

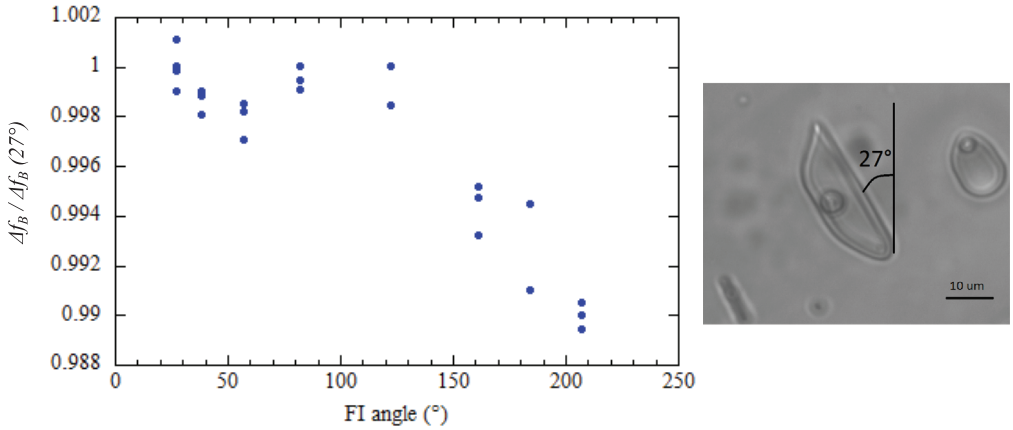

Figure 2.8: ***Δf_B as a function of angle with quartz-hosted fluid inclusion.*** *Usual "reference" angle: 27±1°. Measurements were all carried out the same day*

2.5 How w measured with Brillouin spectroscopy compares with empirical values from the literature

Because c_∞ chosen for the fit of the Brillouin spectrum is not adapted for salt solutions and also because the angle of collection of the backscattered light is not perfectly equal to 0°, Brillouin spectroscopy does not yield exact values of w. The mean value measured in the quartz-hosted pure water FI, 1471.7 m s^{-1}, is lower than the value provided by the equation of state of the International Association for the Properties of Water and Steam (IAPWS-95, Wagner and PruSS 2002), $w^{\mathrm{LVE}}(24.9\,^\circ\mathrm{C})$ =1496.4 m s^{-1}. In halite FIs, the difference is smaller. In Figure 2.10, we observe that the factor between measured and expected values does not depend on temperature. Therefore, Brillouin spectroscopy yields consistent speed of sound measurements to within a constant factor close to 1 (~1.0091 in the case of NaCl-H_2O halite FIs).

Interestingly also, the fact that the parabola fitted to the whole dataset in Figure 2.10 reproduces very well

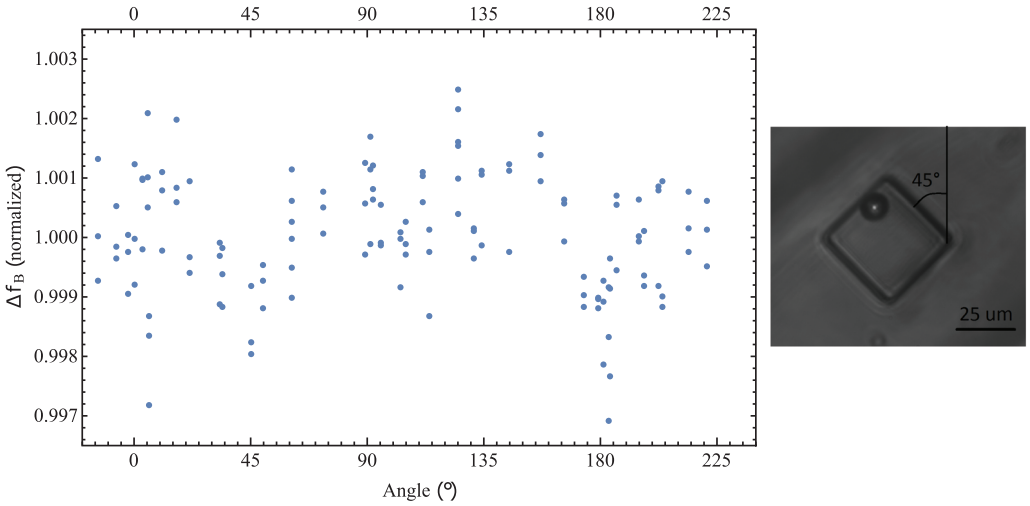

Figure 2.9: Δf_B ***as a function of angle with halite-hosted fluid inclusion.*** *Usual "reference" angle:* $0\pm1°$. *Values are divided by the average of all values. Measurements were carried out on 4 different days.*

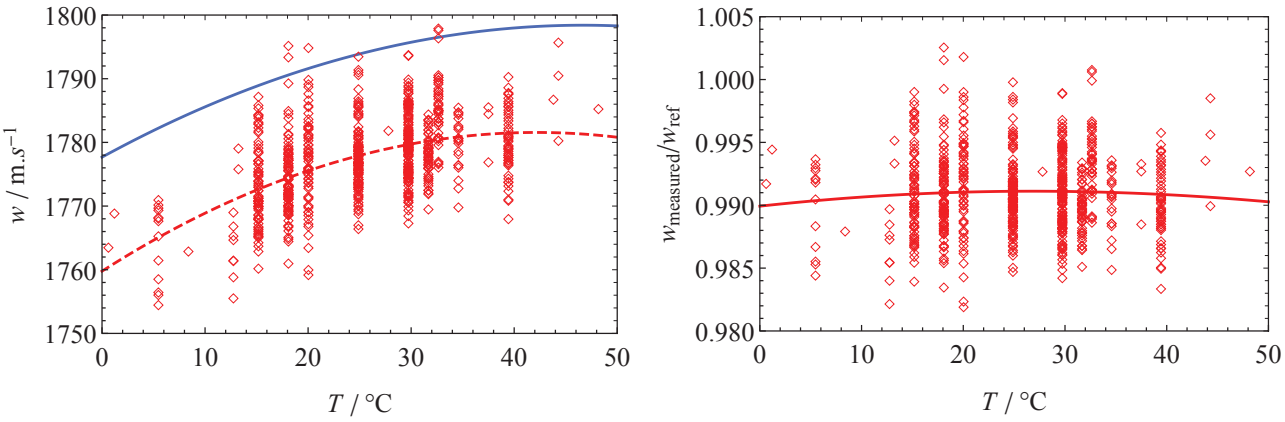

Figure 2.10: ***Speed of sound as a function of temperature in biphasic NaCl-H_2O FIs.*** *A total number of 704 values were obtained in 270 synthetic NaCl-H_2O halite FIs with Brillouin spectroscopy. Left Panel: Dotted red line is a parabola fitted to the whole data set; Blue solid line is the speed of sound expected for a saturated NaCl solution (Millero et al., 1987; Sawamura et al., 2007). Right Panel: red markers are the same data points as in left panel, divided by the expected speed of sound as a function of temperature (the blue line of left panel); red line is the same parabolic fit as in left panel, divided by the expected speed of sound as a function of temperature.*

the trend of the empirical curve of the speed of sound in water saturated with NaCl (calculated and slightly extrapolated from the empirical equation of the speed of sound in NaCl-H_2O as a function of temperature and molality of Millero et al. 1987, with the saturation molality of NaCl in water as a function of temperature from Sawamura et al. 2007) shows that halite FIs composition equilibrates fast upon shifting temperature. Temperature-dependent saturation is obviously reached within experimental timescale, that is, some minutes. If equilibration was much longer and FIs remained under- or supersaturated with respect to NaCl upon changing temperature, we calculate that the slope of $w(T)$ in the 0-40 °C range would be 25% lower. Fast equilibration is expected: the diffusivity of NaCl in a highly concentrated aqueous solution, D_{NaCl}, is of the order of magnitude 1.10^{-9} m^2 s^{-1} (Vitagliano and Lyons, 1956; Mathew et al., 1990). The time constant for the diffusion of NaCl

in a fluid inclusion is expressed:

$$\tau = \frac{R_{\mathrm{FI}}^2}{D_{\mathrm{NaCl}}}, \tag{2.6}$$

with R_{FI} the radius of the fluid inclusion. Upon changing temperature, we calculate that any FI with radius lower than 31, 100, 315, 1000 or 1895 μm will reach saturation within faster than 1, 10, 100, 1000 or 3600 seconds, respectively.

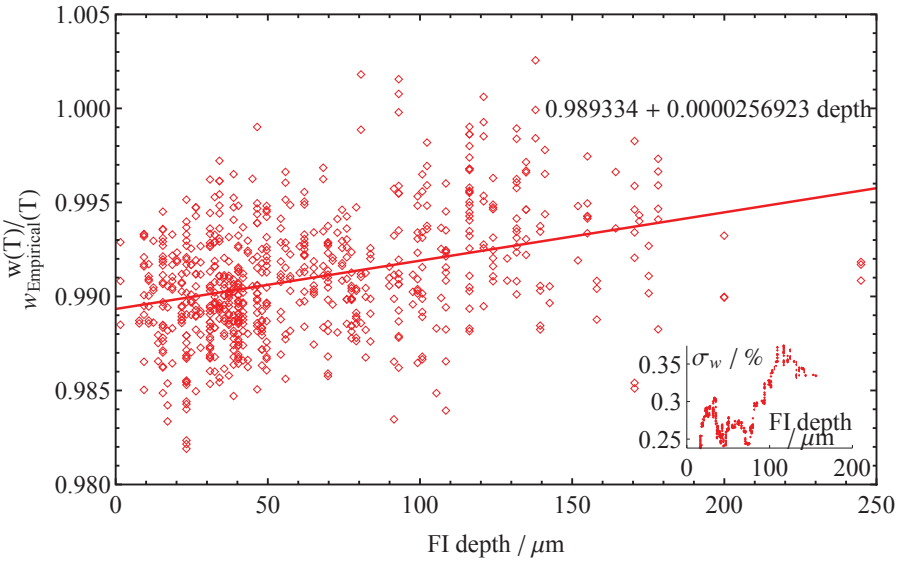

Figure 2.11: ***Dependence of w on the depth of the FI in the crystal.*** *Same biphasic FIs as in Figure 2.10. Each $w(T)$ value is divided by the value calculated at the same temperature with the empirical equation of Millero et al. (1987). Inset shows the standard deviation of the speed of sound as a function of FI depth (%); we applied a moving average computed by averaging runs comprising 10% of all the data points.*

We observe a positive correlation when plotting w values as a function of the depth of the fluid inclusion in the crystal (Figure 2.11). We conclude depth is one of the parameters affecting w and accounting for the discrepancy between FIs of equal temperature and composition. As the standard deviation σ_w as a function of depth is higher than 0.25%, hence greater than the instrumental uncertainty 0.1-0.15%, we also conclude that other parameters so far not uncovered affect w and account for the discrepancy between FIs. Lastly, we notice that σ_w gets higher at depths > 100 μm.

In the range of working temperatures 0-40 °C mostly used in this thesis the calibration equation of the stage allows constraining the temperature of the sample within 0.1 °C irrespective of the vertical and horizontal positions inside the sample, provided the sample is not thicker than some millimeters, conducts heat at least as well as quartz (e.g. halite) and has a good thermal contact with the block (i.e. flat basal surface). The impact of the laser on the fluid inclusion temperature proved to be negligible, at least when the host is halite.

We strongly recommend measuring regularly a reference FI when performing Brillouin spectroscopy and using the linear or parabolic fit of the reference values as a function of time to correct the data from the instrumental drift. This improves measurements precision by 2 to 3 times.

It is very important to take care that FIs hosted in anisotropic materials be always measured with the same angle. We also recommend to pay attention to the angle of halite FIs, although a rotation of a few degrees should not change significantly the results. More tests should be led to check any statistical deviation of the results as a function of the horizontal and vertical locations of the focus, as we were not able to rule out potential deviations within ~$\pm$0.1%; in the meantime, we suggest to stick as far as possible to the same measurement location, especially when it comes to measuring the reference FI.

Brillouin spectroscopy yields consistent values of speed of sound inside biphasic NaCl-H_2O fluid inclusions to within a constant correction factor which differs depending on the host crystal and the depth of the fluid inclusion inside the host. Furthermore, it seems that the precision of measurements deteriorates below a depth of 100 μm, therefore we recommend to stick to rather shallow FIs when possible.

2.6 Developments in Raman spectroscopy

In addition to the Brillouin spectroscope, the configuration of our setup allows the light backscattered from the sample to be simultaneously directed towards a Raman spectroscope (not shown in Figure 2.2). Like Brillouin spectroscopy, Raman spectroscopy measures shifts in frequency of scattered light. However, involved frequency shifts in Raman scattering are orders of magnitude larger as they imply interaction of light with molecular vibrations, such as the high energy O-H bonds of water (e.g. Walrafen 1964). The latter comprise two main modes, bending and stretching, and the intensities of the two vibration modes are affected by temperature and the presence of solutes. Therefore, the structure of the Raman spectra measured with Raman spectroscopy shows a visible dependence on temperature and salinity.

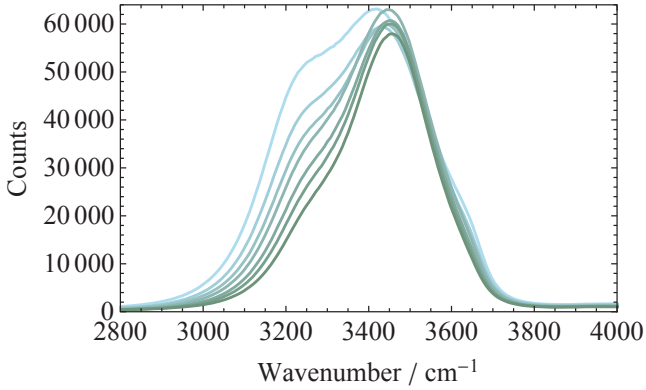

Figure 2.12: ***Example of Raman spectra measured in solutions of increasing salinity at*** $20\,^{\circ}\mathrm{C}$***.*** *Measurements achieved in capillaries with square section 500x500 μm. From light blue to deep blue, 0, 1, 2, 3, 4, 5 and 6.15 molal of NaCl. The wavenumber is the inverse of the wavelength.*

The example of spectra measured at $20\,^{\circ}\mathrm{C}$ in aqueous solutions with variable NaCl concentrations (Figure 2.12) shows that aqueous solutions yield a two-bump broad spectrum, where the intensity of the low frequency bump (centered at ~3260 cm^{-1}) diminishes in comparison to the high frequency one (centered at ~3425 cm^{-1}) when salinity increases. The ratio of intensities can be quantified and fitted as a function of temperature and salinity, which can then serve as a calibration equation to determine temperature or salinity in a $NaCl_{(aq)}$ solution. We thus prepared a series of solutions which we sealed with wax inside square-section capillaries (500x500 μm), and measured it at several temperatures. The best 2-parameters parabolic fit ($\chi^2 = 1.86$) gave (Figure 2.13):

$$m^2(0.00426631 - 0.0000424667T) + m(0.000385862T + 0.161581) + 0.0000158759T^2 + 0.00474223T + 1.09935, \tag{2.7}$$

with T the temperature in $^{\circ}\mathrm{C}$ and m the molality in mol kgH_2O^{-1}.

Lastly, we compared two methods to get the best calibration of the temperature dependence of the Raman spectra of pure water. We were able to measure Raman spectra of pure water in 500 ţm square cross-section capillaries down to -35°C before it froze. We first subtracted a two-point baseline fitted to data points at 2700

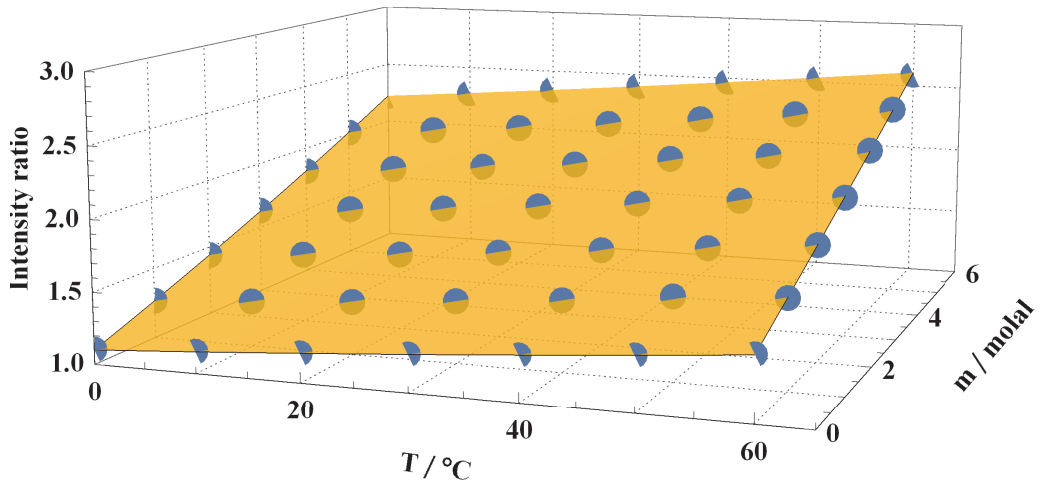

Figure 2.13: ***Two-band intensity ratio as a function of temperature and NaCl molality.*** *Intensity ratio of band 3425 cm^{-1} on band 3260 cm^{-1}.*

and 3950 cm^{-1} following the method of Caumon et al. (2013). Then we calculated the ratio of the two bands as previsouly detailed, and concurrently calculated the ratio between the area under the curve for frequency shifts less than 3400 cm^{-1} and the area under the curve for frequency shifts above 3400 cm^{-1}. Both fits are shown in Figure 2.14. It comes out an excellent linear relation is found when plotted as a function of the inverse of temperature, especially in the case of the areas ratio.

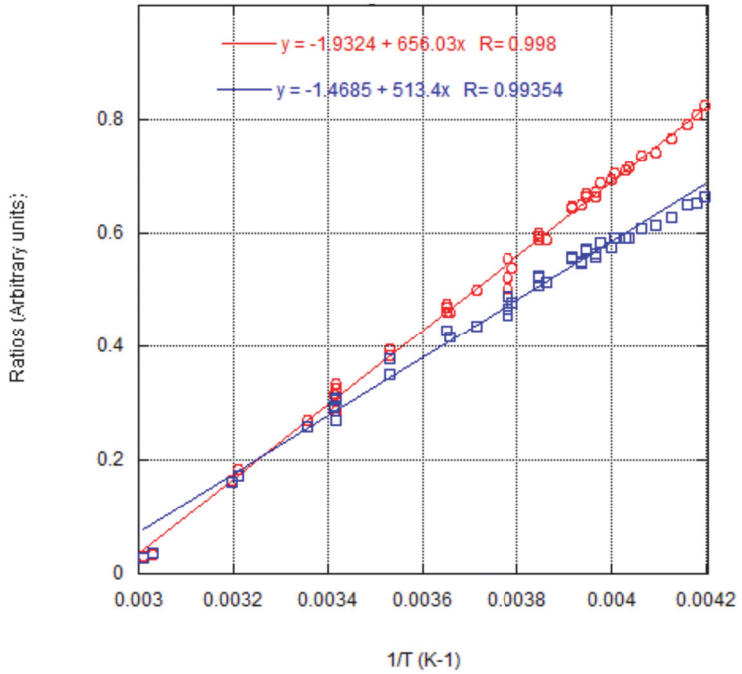

Figure 2.14: ***Intensity ratios in pure water as a function of temperature: methods comparison.*** *Red: ratios of areas* $\frac{I<3400\text{cm}^{-1}}{I>3400\text{cm}^{-1}}$*; Blue: ratios* $\frac{I_{3260}}{I_{3425}}$

CHAPTER 3

Restoring halite fluid inclusions as an accurate paleothermometer: Brillouin thermometry versus microthermometry

---

ABSTRACT Halite traps inclusions of the mother fluid when precipitating. When unaltered, the density of these fluid inclusions (FIs) records the water temperature T_{f} at the time of crystal formation. As halite is ubiquitous on Earth and throughout the ages, its FIs possess a high potential as temperature archives. However, the use of FIs in halite as an accurate paleothermometer has been yet hampered due to limitations of microthermometry, the most commonly used analytical method. Here we show how Brillouin spectroscopy in halite FIs bypasses these limitations, and allows recovering T_{f} to within $1\,^{\circ}\mathrm{C}$ or less. To demonstrate this, we measured samples synthetized at $24.6 \pm 0.5\,^{\circ}\mathrm{C}$ and $33 \pm 1\,^{\circ}\mathrm{C}$, and obtained $24.8 \pm 0.4\,^{\circ}\mathrm{C}$ and $31.9 \pm 0.4\,^{\circ}\mathrm{C}$, respectively. This novel approach thus provides an accurate paleothermometer for lacustrine and marine environments with high temporal resolution. Moreover, Brillouin spectroscopy solves the long-standing debate on halite fluid inclusions damaging through quantifying the elasticity limit $\left(l/(1\mu\mathrm{m})\right)^{-0.64}$ x $(90\,^{\circ}\mathrm{C})$, where l is the FI size. This threshold is lower for FIs close to either the surface of the host crystal or to another FI. We also list "best practices" for applying both microthermometry and Brillouin thermometry.

Foreword A different version of the work presented in this chapter is under review at *Geostandards and Geoanalytical Research*.

List of abbreviations and definitions

FI Fluid inclusion

FIA Fluid inclusion assemblage, that is, the most finely discriminated, petrographically associated group of coeval inclusions

T_f Formation temperature of the FI (°C)

T_{Min} Minimum temperature undergone by a FI since its entrapment (°C). For fluid inclusions measured with microthermometry, it corresponds to the cooling temperature used in the stage to nucleate a bubble (°C)

T_{Max} Maximum temperature undergone by a FI since its entrapment (°C)

ΔT Maximum value between the amplitude of cooling below T_f, $T_f - T_{Min}$, and the amplitude of heating above T_f, $T_{Max} - T_f$

ΔT_{lim} Maximum ΔT a FI can bear without irreversible volume change

$P_{FI,lim}$ Maximum internal negative or positive pressure a FI can bear without irreversible shrinkage or stretching, respectively

T_{Cav} Temperature at which cavitation (i.e. bubble nucleation) occurs in a FI

T_h Temperature of homogenization (bubble disappearance) obtained with microthermometry (°C)

T_x Crossing temperature obtained with Brillouin thermometry (°C)

$T_{h/x}$ T_h or T_x

$T_{h/x,mean}$ Average $T_{h/x}$ in a group of FIs (°C)

$T_{h/x,min}$ Minimum $T_{h/x}$ in a group of FIs (°C)

$T_{h/x,max}$ Maximum $T_{h/x}$ in a group of FIs (°C)

BS Brillouin spectroscopy

w Speed of sound in a FI (m s^{-1})

w^{mono} Speed of sound in a monophasic FI (m s^{-1})

w^{LVE} Speed of sound at liquid-vapour equilibrium in a biphasic FI (m s^{-1})

$\sigma_{\mathbf{w}}$ 1-sigma uncertainty on the speed of sound

$\sigma_{\mathbf{Th}}$ Standard deviation of a T_{h}distribution

$\sigma_{\mathbf{Tx}}$ Standard deviation of a T_{x} distribution

$\Delta f_{\mathbf{B}}$ Brillouin frequency shift in a FI (GHz)

$\Delta f_{\mathbf{B}}^{\mathbf{LVE}}$ Brillouin frequency shift at liquid-vapour equilibrium in a biphasic FI (GHz)

3.1 Introduction

The determination of past temperatures is a key parameter in reconstructing paleoclimates and associated environmental conditions. Continental sedimentary deposits provide an excellent choice when searching for reliable temperature archives. As such, evaporites are of great interest. Evaporites form either from the evaporation of the free water column or from saline pore water within the sediment. Although arid climates and confined environments favor the formation of evaporites, their current distribution on the Earth's surface shows that they deposit in a wealth of different settings (Warren, 2010). They are found at most latitudes, from the tropical sabkhas of the Persian Gulf (Schreiber and El Tabakh, 2000) to the northern salt lakes of Saskatchewan (Last, 1993), and at a wide range of altitudes, from the Dead Sea located 430 meters below sea level (Niemi et al., 1997) to the Andean salt pans at 4000 meters (Alonso et al., 1991). Described in sedimentary series since the Precambrian (Kah et al., 2001) to modern times (Piovano et al., 2002), evaporites hold a true potential in the record of past climates in these arid continental to marine-related environments (Warren, 2016). To cite but a few, halite and other evaporitic minerals have been used to infer depositional conditions such as water budget or lake level (Lowenstein and Hardie, 1985; Li et al., 1996; Rigaudier et al., 2011; Schreiber and El Tabakh, 2000); halite bromine content has served as a genetic criterion for evaporitic basins (Valiashko, 1956; Holser, 1966); and halite fluid inclusions (FIs) chemistry has been used to reconstruct past seawater composition (Brennan et al., 2013; Rigaudier et al., 2012; Timofeeff et al., 2001; Zimmermann, 2001). A summary of some of the major proxies that can be used on halite to reconstruct paleo-environments was recently published (Blamey and Brand, 2019). Twenty five years ago, Roberts and Spencer (1995) proposed using halite primary FIs as a paleo-thermometer for brines, by measuring their homogenization temperature (T_{h}). For a FI containing liquid and vapour (biphasic FI), T_{h} is the temperature at which the vapour bubble disappears upon heating, the FI then becoming monophasic (Figure 3.1A). Measuring T_{h} has long been used to obtain formation temperatures of metamorphic minerals usually containing biphasic FIs at ambient temperature, as they are trapped at elevated conditions of temperature and pressure (Sorby, 1858). Conversely, most FIs in evaporites are monophasic because they form at subsurface conditions. To circumvent the absence of a vapour bubble in halite FIs, Roberts and Spencer (1995) first placed the crystals inside a freezer to cool them down to -20°C. Because the fluid is thus cooled at nearly constant volume, this generates negative pressure, which was enough to nucleate a bubble

in some FIs. Roberts and Spencer (1995) subsequently heated the FIs in a temperature-controlled microscope stage up to T_h. This T_h is assumed to be equal to the FI entrapment temperature (T_f) and, thus, the brine temperature. They further proposed several tests to check if the FIs followed the "Roedder's rules" (Roedder, 1984) preserving the FI initial mass, volume and composition. (Benison and Goldstein, 1999) further validated the applicability of the technique to reconstruct ancient climates, showing consistent homogenization temperatures within individual fluid inclusions assemblages (FIAs, i.e. a group of coeval FIs in a crystal) in chevrons from Permian halites. However, (Lowenstein et al., 1998) applied the same protocol on synthetic and natural modern halites, and found broad T_h distributions showing unexpected results:

- A large number of FIs had a T_h far below the temperature at which halite grew
- Only the maximum T_h in the distribution, $T_{h,max}$, correlated well with the highest temperature measured in the brine during the period of crystal precipitation

Since these early experiments, several practices can be found in the literature about the most relevant value to use in paleoclimate reconstructions: $T_{h,max}$ (Lowenstein et al., 1999; Meng et al., 2011, 2013; Sun et al., 2017); $T_{h,mean}$ (Speranza et al., 2013; Rigaudier et al., 2011); various properties of the T_h distribution (range, mean and extrema), meaning that every single T_h has a paleoclimatic signification (Benison and Goldstein, 1999; Losey and Benison, 2000; Satterfield et al., 2005a, b; Kovalevych et al., 2009; Zambito and Benison, 2013; Zhao et al., 2014; Zhang et al., 2015; Yang, 2016; Zhang et al., 2016, 2017; Xu et al., 2019). Which of them is the best practice is still an unsettled debate. Another issue, often overlooked, is the Laplace pressure difference between the vapour bubble and the liquid, which causes the bubble to collapse before T_f (Fall et al., 2009; Krüger et al., 2011). This bias can lead to underestimating T_f by several degrees Celsius. All these uncertainties have certainly discouraged many scientists from using this technique. Nevertheless, FIs from sub-surface rocks hold a large potential as temperature archives, as their density is a direct physical record of paleo-temperatures. As such, fluid inclusions are more than a temperature proxy that needs to be calibrated, and should be regarded as real paleo-thermometers. Here we propose a new technique based on Brillouin spectroscopy (BS), which relies on the inelastic interaction between light and spontaneous (thermal) density fluctuations in matter, causing a frequency shift (Δf_B) between incident and scattered light. Our results show that BS yields substantially narrow T_x distributions, in agreement with the formation temperature of halite. As it does not require the presence of a bubble, BS is a non-destructive method that does not need cooling the samples to generate large negative pressures (Figure 3.1B) and, thus, it is free from the bias due to Laplace pressure. It consists in measuring the speed of sound as a function of temperature in the monophasic FI, and deducing the FI entrapment temperature T_x from the intersection between the resulting curve $w^{mono}(T)$ and the curve at liquid-vapour equilibrium $w^{LVE}(T)$. BS as a paleothermometer was first introduced in a preliminary study by El Mekki-Azouzi et al. (2015), who validated this principle using one synthetic and three natural FIs in quartz crystals with high T_h. Although the results showed good agreement, the applicability of the method remains to be proven for evaporites with low T_f values. Here we report an in-depth study of FIs from lab-grown

halite crystals. Through the comparison of the statistical distribution of our BS results with microthermometry data on the same samples, we demonstrate that BS is a powerful tool for more accurate, more precise and faster paleothermometric reconstructions. Thus, this novel approach provides an accurate paleothermometer for lacustrine and marine environments that can be applied with high temporal resolution. Moreover, we use the speed of sound measurement in fluid inclusions to estimate the internal negative pressure at which the inclusion walls start to deform in a plastic mode. We obtain an empirical equation predicting the maximum temperature excursion FIs in halite can withstand before irreversibly changing volume. This finding solves the long-standing debate on the ability of halite FIs to record past temperatures. Finally, based on our findings, we propose good practices to follow when using microthermometry or Brillouin thermometry on halite FIs.

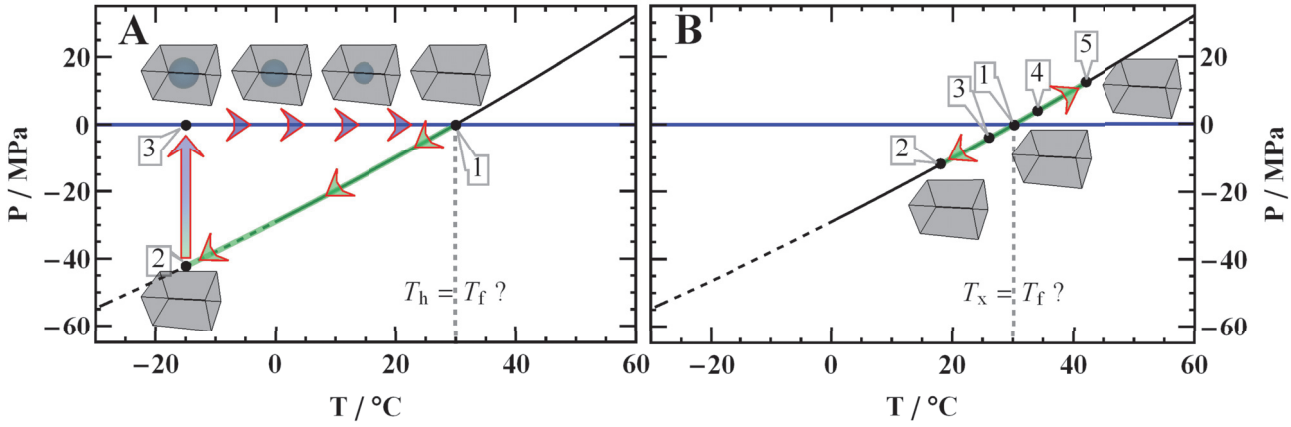

Figure 3.1: ***Thermodynamic path followed by a fluid inclusion (FI) with (A) microthermometry and (B) Brillouin spectroscopy (BS).*** *(A) Upon trapping in shallow water, FI is at liquid-vapor equilibrium (LVE) (point "1"). Upon cooling (1 → 2), follows quasi-isochore curve and becomes metastable: fluid occupies a larger volume than at equilibrium, and may reach negative pressures. Upon cavitating, LVE is restored (2 → 3). Upon heating (3 → 1), FI follows LVE, bubble shrinks and eventually disappears at T_h. Liquid recovers volume it occupied at trapping, and equality between T_h and T_f is assumed. (B) FI trapped under the same conditions (point "1") is measured in monophase state at several different temperatures (2 → 3 → 4 → 5), providing the speed of sound in monophase state $w^{mono}(T)$. After forced cavitation (see text), the speed of sound in the bipasic FI, $w^{LVE}(T)$, is measured. $w^{mono}(T)$ intersects $w^{LVE}(T)$ at T_x, equal to the entrapment temperature T_f. Note that with BS, FIs undergo considerably weaker stresses (~4 times here) than with microthermometry. Below 0 °C, P-T curve is extrapolated (dashed black line).*

3.2 Materials and methods

3.2.1 Setup

The BS setup is described in El Mekki-Azouzi et al. (2015); Pallares et al. (2014, 2016); Holten et al. (2017) and in Chapter 2. Brillouin scattering experiments were performed in backscattering geometry through the microscope objective (Mitutoyo PlanApo, 100x magnification). The sample is illuminated with a 54 mW beam from a single longitudinal mode laser (Coherent, Verdi V6) with wavelength λ= 532 nm. The laser beam, focused to a 1 µm spot, allows measuring FIs a few microns in size without damaging it. The light

backscattered from the sample is analyzed with a 6-pass tandem FabryPerot interferometer (JRS Scientific, TFP-1), with entrance and exit pinholes 300 and 450 µm in diameter, respectively. The sample is placed in a temperature controlled stage (Linkam, THMS600) whose temperature is calibrated with synthetic pure water and pure CO_2-H_2O FIs hosted in quartz. The typical rate for temperature change was $\pm$ 20 °C min^{-1}. As 1 °C change in halite FIs converts to 1 MPa (Figure 3.1), and as the elastic stiffness C11 of NaCl is 47.1 GPa (Szomor, 1968), typical strain rates applied to FIs walls were 7x10-6 s^{-1}.

3.2.2 Materials

We prepared two 60 mL NaCl-H2O solutions saturated with respect to NaCl (at 20 °C, 6.15 mol kg^{-1}) by dissolving NaCl (VWR AnalaR NORMAPUR, purity = 99.5%) in ultrapure water (ELGA PURELAB Flex; resistivity at 25 °C: 18.2 MΩcm; TOC: 1 ppb). Each solution was set to evaporate at a different temperature in polypropylene flat bottom beakers dipped in thermal baths (respectively set to 26 °C and 36 °C). The room temperature was air-conditioned to 20 $\pm$ 0.5 °C. Total evaporation of the solutions required approximately 20 hours. The temperature of the brines was monitored all along the evaporation process by means of a Pt100 Resistance Temperature Detector (dimensions 2x2x1 mm), calibrated with a Dostmann P795 thermometer with a Pt100 probe calibrated in 4 points to reach a 0.1 °C accuracy. Due to space and time-related temperature fluctuations inside the brine, the final uncertainty on crystals growth temperature was higher. The temperature measured inside the two brines was 24.6 $\pm$ 0.5 °C and 33 $\pm$ 1 °C, respectively. Note that the uncertainties shown here are not standard deviations but brackets due to temporal and spatial temperature fluctuations in the brines. Crystals precipitated at the surface of the solution, coalesced progressively to form floating rafts, and then sank to the bottom of the beaker where they kept growing. From the salt crust remaining at the end of evaporation, we selected some of the millimeter-size flat rectangular crystals for microthermometry and BS analyses. Most of them contained numerous rectangular FIs aligned along the crystal growth bands and observable under the microscope (Figure 3.2). In this work, batches of halite crystals are named according to their synthesis temperature, as follows: SyntHal24.6 is the name given to the batch of crystals which grew in the brine of temperature 24.6 $\pm$ 0.5 °C, and SyntHal33 is that of crystals grown in the brine of temperature 33 $\pm$ 1 °C. In several cases, we have added a subscript, such as in SyntHal33$_{16}$, to indicate the minimum temperature (T_{Min}) undergone by the sample (16 °C in the given example). The samples were never exposed to temperatures higher than T_{f} before measurements.

3.2.3 Methods

In this work, the reported observable is the speed of sound w. BS measures the Brillouin frequency shift Δf_{B}. Details on Δf_{B} and its conversion into w are reported in Chapter 2. The speed of sound in a FI depends on the composition, temperature and pressure of the liquid. At liquid-vapour equilibrium (LVE), the speed of sound of the liquid as a function of temperature, $w^{\mathrm{LVE}}(T)$, can be obtained through measurement in a biphasic FI. Conversely, a monophasic FI does not follow the LVE when warmed or cooled, but an isochore at density ρ

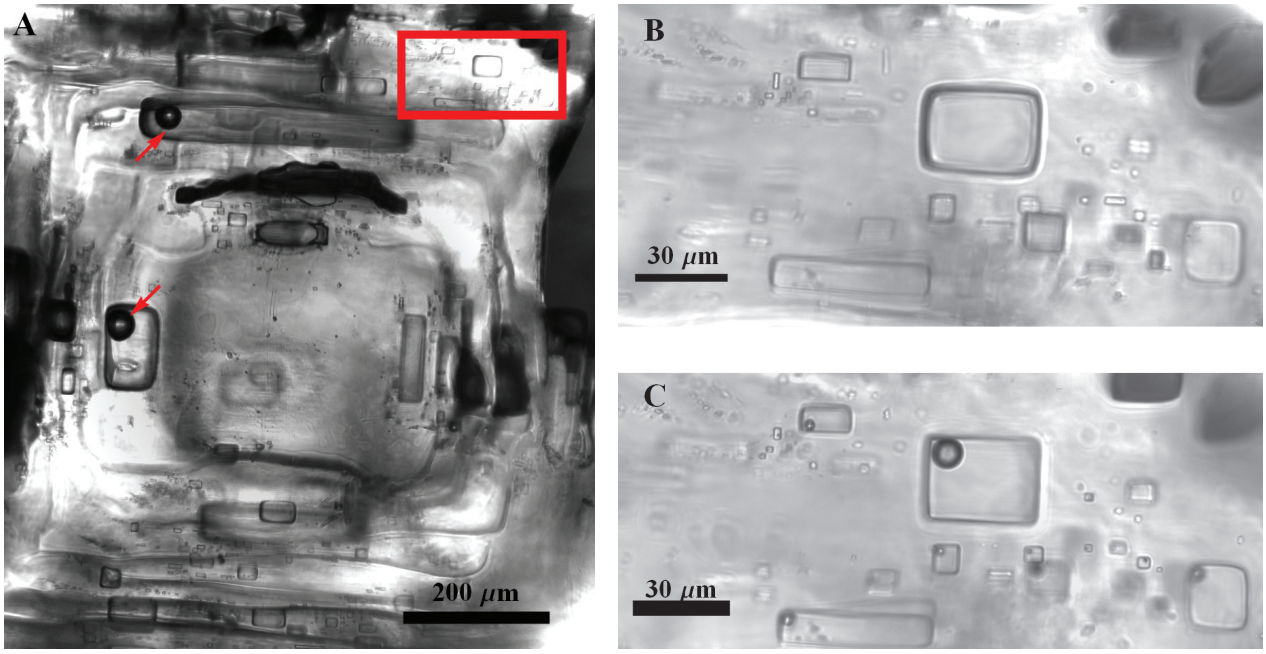

Figure 3.2: ***Lab-grown halite.*** *SyntHal33$_{16}$ crystal. (A) FIs are aligned along growth bands, and concentrically arranged around the crystal center (at photograph center). Some large FIs are elongated parallel to growth fronts. Red arrows show air bubbles pre-existing in some FIs, certainly trapped during halite formation. Region delimited by red rectangle in (A) is magnified in (B), showing several monophasic FIs. (C) Same region after heating-cooling cycle up to* 130 °C *and back to room temperature: almost all FIs cavitated*

(Figure 3.1), along which the speed of sound varies with temperature, defining the curve $w^{\text{mono}}(T)$, uniquely determined by ρ. The curve $w^{\text{mono}}(T)$ for the monophasic FI intersects $w^{\text{LVE}}(T)$ at T_{x} (Figure 3.3). By definition, the density along the LVE equals ρ at T_{x}, which, therefore, we identify with T_{f}, at which the liquid with density ρ was trapped.

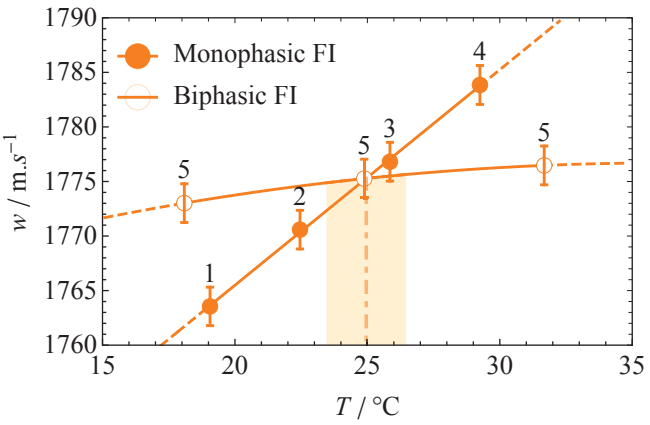

Figure 3.3: ***Method for determination of T_x with BS.*** *The temperature-dependent speed of sound curves in monophasic and biphasic states, $w^{mono}(T)$ and $w^{LVE}(T)$, are fitted to data points measured in the FI at monophase (disks) and two-phase (circles) states, respectively. Error bars: σ_w = 0.1%. Fitted curves intersection gives T_x (dashed-dotted line), with estimated standard deviation σ_{Tx} = 1.5 °C (shaded area).*

Strictly speaking, the thermodynamic path followed by a FI is a quasi-isochore rather than an isochore.

This is due to combined effects of thermal expansion and elasticity of the crystal, and of temperature variation of the saturation concentration as regards NaCl. Nevertheless, as T remains the only independent variable, the $w^{\text{mono}}(T)$ curve for halite FIs crosses $w^{\text{LVE}}(T)$ at T_{x}. Once we have performed all $w^{\text{mono}}(T)$ measurements in monophasic FIs of a given sample, we heat the sample up to 130 °C for several minutes before cooling it back to room temperature; this triggers cavitation of a significant number of FIs. Indeed, most FIs reequilibrate -i.e. acquire a new T_{h}- at such high temperatures, and become biphasic when cooling back to room temperature, allowing us to perform $w^{\text{LVE}}(T)$ measurements. Note that it is important to measure individual $w^{\text{LVE}}(T)$ curves rather than only one average over several FIs, as the standard deviation on repeated measurements on one FI (0.1%) is lower than the standard deviation of the distribution of measurements (0.3%). This variation between FIs of equal composition partly arises because they lie at various depths within the crystal, affecting the optical path followed by the laser and causing small additional deviation in Brillouin measurements between FIs (more details in Chapter 2).

For each FI we measured 4 and 3 data points along $w^{\text{mono}}(T)$ and $w^{\text{LVE}}(T)$, respectively. We performed simulations of our experiments to estimate the impact of different protocols on the resulting T_{x} distribution. These results show that our choice is a good compromise between measurement time and accuracy, and also that other protocols can be suitable (see Appendices, Table 3.B.1).

The microthermometry measurements were carried out in the same temperature-controlled stage as the Brillouin measurements. In order to trigger cavitation, we cooled most samples directly in the stage and kept them at low temperature for about 30 minutes, according to the procedure of Speranza et al. (2013). Homogenization temperatures of biphasic FIs were measured by heating the samples with a 1 °C min^{-1} ramp. T_{h} measurements precision was $\pm$ 0.5 °C. All results reported here were further corrected for Laplace pressure.

In this work, all the FIs selected for measurements were initially monophasic and rectangular-shaped. We used the usual criteria to discard secondary FIs (Roedder, 1962a). We avoided FIs with size below 3 µm (Brillouin) or 7 µm (microthermometry). Indeed, very small FIs require an excessively long Brillouin spectrum acquisition time, while they render difficult the determination of an accurate T_{h} with microthermometry, as already noticed by Krüger et al. (2011). Halite FIs are cuboids, with different length (a), width (b) and height (c). Since it was not possible to measure c in this work, sizes are all expressed as a function of a and b, through the relation $l = (ab)^{0.5}$, with l the side of a square of equivalent surface. In average in this work, $a = 1.67b$; c is thus unlikely to differ much from a and b, so that we expect l to be close to $(abc)^{\frac{1}{3}}$.

3.3 Results

T_{h} and T_{x} values obtained on several crystals from batches SyntHal24.6 and SyntHal33 are presented in Sections 3.3.1 and 3.3.2, respectively, and in Figure 3.4. In Section 3.3.3, the two techniques used successively on the same FIs are compared directly. This comparison was only possible when FIs measured with BS subsequently cavitated through cooling down to −20 °C. The statistical data of all T_{h} and T_{x} measurements are

summarized in Table 3.1.

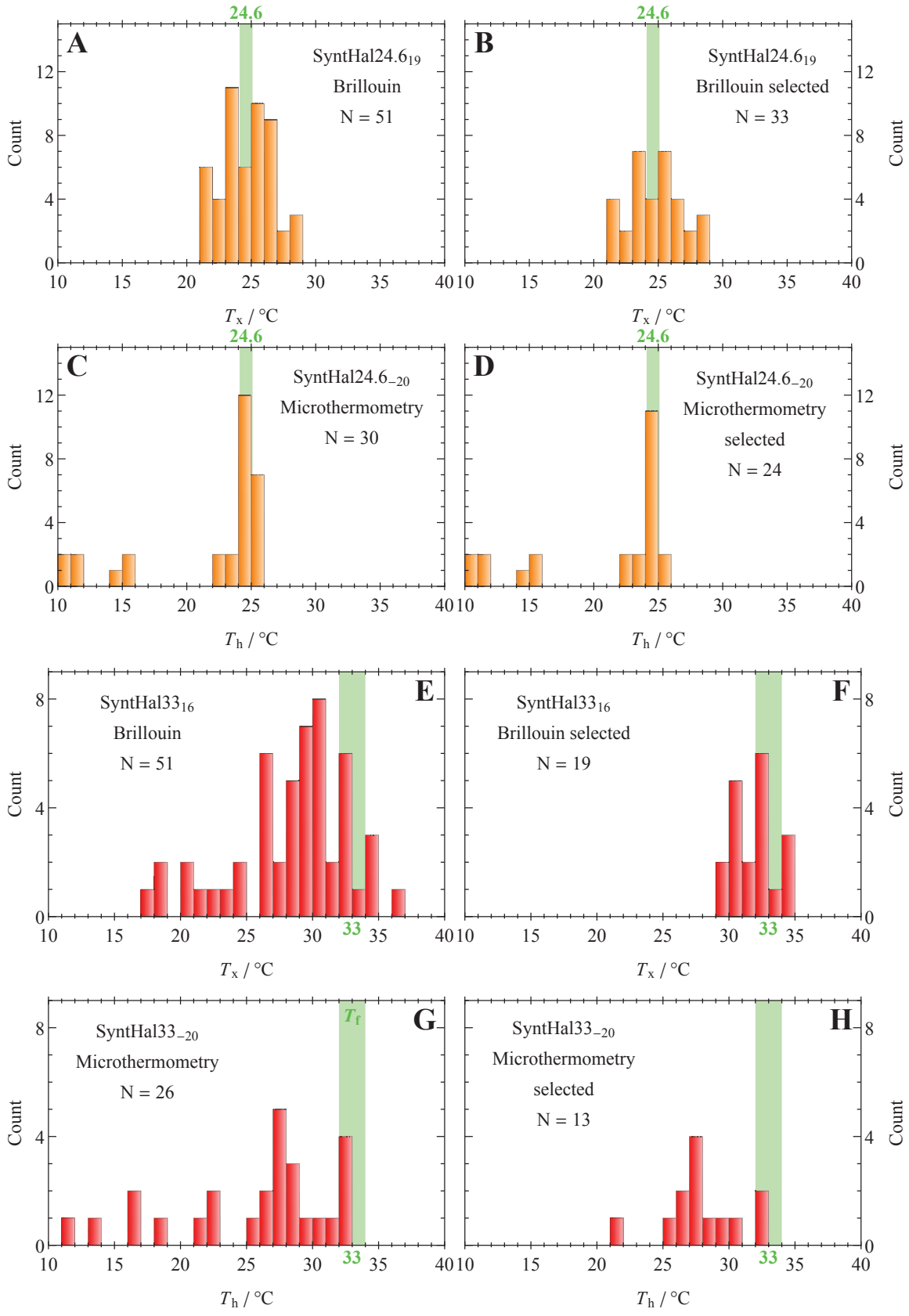

Figure 3.4: ***Histograms of T_x and T_h distributions.*** *Panels A to D: SyntHal24.6; Panels E to H: SyntHal33. T_x distribution for all FIs (A and E), and after selection (B and F). T_h distribution for all FIs (C and G), and after selection (D and H). See text for details on selection criteria.*

3.3.1 Comparison of microthermometry and BS on a low T_f sample

The T_x histogram obtained with BS (Figure 3.4A) on SyntHal24.6 crystals displays values well centered on the synthesis temperature, with $T_{x,mean}$ lying within the T_f range (Table 3.1). The distribution is normal and the difference between mean and median is as low as $0.2\,°C$. The T_h histogram obtained with microthermometry (Figure 3.4C) shows a mode consistent with the synthesis temperature, along with a significant amount of T_xs far below synthesis temperature. Altogether, this results in a $T_{h,mean}$ ~$3\,°C$ below T_f, and a standard deviation almost 3 times larger than the one obtained with BS. $T_{h,max}$ corresponds to T_f within $\pm\,1\,°C$. Using an "isolation" criterion to discard FIs too close to each other or to the crystal surface (see Section 3.4.1), we obtained the histograms for T_xs and T_hs shown in Figure 3.4B and Figure 3.4D, respectively. This selection does not yield any significant difference, as it barely affects statistical values $T_{h/x,mean}$ and σ.

3.3.2 Comparison of microthermometry and BS on a high T_f sample

T_x and T_h histograms (Figure 3.4B and Figure 3.4D respectively) of SyntHal33 present averages lower than T_f, by 4.6 and $7.3\,°C$, respectively. They both show a broad distribution towards low temperatures (Table 3.1). Distributions are non-normal, as shown by rather large $T_{h/x,median}$ - $T_{h/x,mean}$ values (Table 3.1). In addition to the isolation criterion (Section 3.3.1), we apply a size criterion: FIs larger than 13 µm were discarded (see Section 3.4.2). The corresponding T_x and T_h histograms are shown on Figure 3.4F and Figure 3.4H, respectively. After this combined selection process, the average T_x lies within the T_f range to within the standard error, and the standard deviation is reduced to a very low value of $1.5\,°C$. The spread of T_h is also halved through applying the selection criteria, but the average T_h remains some $5\,°C$ below T_f. $T_{h,max}$ corresponds to T_f within $\pm\,1\,°C$.

3.3.3 Direct comparison between T_h from micro-thermometry and T_x from BS

Once all Brillouin measurements were made on the samples, we cooled them down to $-20\,°C$ for 15 to 30 minutes. Cavitation occurred in 8 FIs out of the total 147 FIs previously analyzed through BS, which allowed us to get as many T_hs. The direct comparison of temperatures obtained by microthermometry and BS on the same FIs (Figure 3.5) shows that, for each of the 8 FIs and within the error bars, $T_h \leq T_x$. The discrepancy between T_h and T_x is larger for larger FIs and/or when cooling to lower temperature. While the 2 FIs submitted to ΔT = $33\,°C$ prior to BS ($SyntHal33_0$, see Section 3.4.2 for more explanations on this batch) show $T_h \approx T_x$, the 6 FIs submitted to a milder ΔT prior to BS, $17\,°C$ and $5.6\,°C$ for $SyntHal33_{16}$ and $SyntHal24.6_{19}$ respectively, show $T_h < T_x$. Among the latter, one notices that larger FIs show $T_h \ll T_x \ll T_f$, while smaller FIs show $T_h < T_x \approx T_f$. This experiment shows that FIs may yield $T_{h/x}$ lower than T_f both with BS and microthermometry. However, when this bias is present, it is more pronounced for microthermometry (up to $10\,°C$ lower).

	N	T_f (°C)	$T_{h/x,mean}$ (°C)	$T_{h/x,median}$ (°C)	$T_{h/x,median}$ - $T_{h/x,mean}$ (°C)	$T_{h/x,max}$ (°C)	$T_{h/x,min}$ (°C)	σ (°C)	SE (°C)
SyntHal24.6$_{19}$ (BS)	51	24.6 ± 0.5	24.7	24.9	0.2	29	21.1	1.9	0.27
SyntHal24.6$_{19}$ selected (BS)	33	24.6 ± 0.5	24.8	25	0.2	29	21.1	2	0.36
SyntHal24.6$_{-20}$ ($\mu\theta$)	30	24.6 ± 0.5	21.8	24.5	2.7	25.8	10.2	5.2	0.98
SyntHal24.6$_{-20}$ selected ($\mu\theta$)	24	24.6 ± 0.5	20.9	24.2	3.3	25.8	10.2	5.5	1.18
SyntHal33$_{16}$ (BS)	51	33 ± 1	28.4	29.2	0.8	36.1	17	4.4	0.63
SyntHal33$_{16}$ selected (BS)	19	33 ± 1	31.9	32.2	0.3	34.9	29.3	1.7	0.41
SyntHal33$_{-20}$ ($\mu\theta$)	26	33 ± 1	25.7	27.7	2	32.8	12	6	1.23
SyntHal33$_{-20}$ selected ($\mu\theta$)	13	33 ± 1	28.1	27.9	-0.2	32.7	21.4	3	0.9

Table 3.1: ***Statistics of the $T_{h/x}$ distributions.*** *Each set of measured data is analyzed as a whole, and after selection following the criteria described in the text. SE, the standard error, is the uncertainty on the mean within a 68.27% confidence interval (1-sigma) with respect to a Student's t-distribution. $\mu\theta$: microthermometry.*

3.4 Discussion

The meaning and relevance of homogenization temperatures from FIs in halite have long been questioned. When the rocks are buried several kilometers deep, inclusions may stretch due to the pressure that accumulates upon heating of the trapped solution (Roedder, 1984). Conversely, halite FIs reach significant negative pressures when brought to a typical cooling temperature of $-20\,°C$ (Figure 3.1; for more details about liquids at negative pressure, that is, under tension, see Caupin and Herbert 2006; Caupin et al. 2012). Absolute negative pressures constitute a critical factor to consider in order to understand FIs reequilibration. Surprisingly, it is often overlooked or misinterpreted in the literature. For instance, the collapse of FI walls has been erroneously ascribed to the much smaller differential pressure between internal vapour pressure and external atmospheric pressure (e.g. Lowenstein et al. 1998). As halite is prone to plastic deformation, negative pressures could easily trigger irreversible shrinkage. Both our microthermometry and BS experiments are consistent with the occurrence of a non-reversible collapse of inclusions walls upon cooling, resulting in the lowering of the $T_{h/x}$ yielded by FIs. As a matter of fact, it appears with both techniques that some FIs resist to collapse while others do not. In the following, we address the causes that can potentially account for these observations.

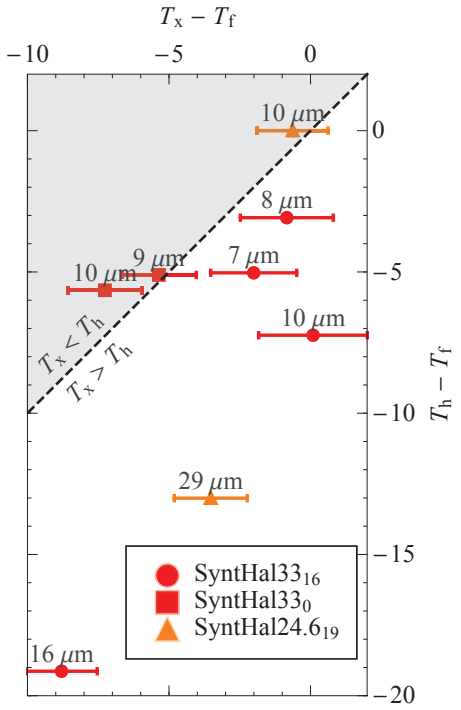

Figure 3.5: ***Comparison of Txs and Ths successively obtained in the same 8 FIs.*** *If both methods were in perfect agreement, data points would fall on dashed line.*

3.4.1 The vicinity of FIs as a mechanical softener

A FI applies a stress on its host as soon as it undergoes a temperature different from T_f. If spherical, the FI is surrounded by a stress field which is maximal at the inclusion rim and diminishes asymptotically towards 0 MPa in the host away from the inclusion. Zhang (1998) addressed the case of the elastic equilibrium and plastic deformation of a host/inclusion system. For a simplified system consisting in a spherical inclusion centered inside a spherical host, he determined the internal pressure at which the host interface with the inclusion begins to yield. At atmospheric external pressure, this can be written as follows:

$$P_{\text{FI,lim}} = \frac{2}{3} Y_S \left(1 - \frac{R_{\text{FI}}^3}{(R_{\text{FI}} + d_{\text{host}})^3}\right). \tag{3.1}$$

$P_{\text{FI,lim}}$ is the FI internal pressure that triggers plastic deformation at the FI rim, R_{FI} the radius of the FI, d_{host} the distance between the host surface and FI rim, and Y_S the yield stress of the host. This relation highlights the importance of the ratio between the FI size and its depth in the host, and shows that a very weak internal pressure is sufficient to trigger plastic deformation when this ratio approaches 1. In other words, big FIs close to the surface are more prone to plastic deformation (Figure 3.6). Nevertheless, $P_{\text{FI,lim}}$ tends to a constant $\frac{2}{3} Y_S$ when $\frac{R_{\text{FI}}}{R_{\text{FI}}+d_{\text{host}}} \to 0$. For $\frac{R_{\text{FI}}}{R_{\text{FI}}+d_{\text{host}}} < 0.5$, the effect has an impact lower than 13%, and for $\frac{R_{\text{FI}}}{R_{\text{FI}}+d_{\text{host}}} < 0.2$, the effect has an impact lower than 1%. This weakening effect due to host surface proximity should be generalizable to any surface proximity, such as a neighboring FI. In a finite element model, Burnley and Schmidt (2006) tested the effect of proximity between two FIs on their volume change and noticed that from a distance smaller than

one FI size, FIs started "feeling each other". Based on these two works, we define a concept of isolation that takes into account both host surface and neighboring FIs following the equation:

$$Iso_{\mathrm{FIa}} = Max\Big(\frac{R_{\mathrm{FIa}}}{(R_{\mathrm{FIa}} + d_{\mathrm{host}})}, \frac{R_{\mathrm{FIa}}}{(R_{\mathrm{FIa}} + d)}, \frac{R_{\mathrm{FIb}}}{(R_{\mathrm{FIb}} + d)}\Big)^{-1} - 1. \tag{3.2}$$

Iso_{FIa} is the isolation of an inclusion $\mathrm{FI_a}$, R_{FIa} and R_{FIb} the respective radii of $\mathrm{FI_a}$ and $\mathrm{FI_b}$, d the distance between $\mathrm{FI_a}$ and $\mathrm{FI_b}$ rims, and d_{host} the distance between host surface and $\mathrm{FI_a}$ rim. By construction, $Iso_{\mathrm{FI}} > 0$. This approach is admittedly an oversimplification, as it does not take into account the influence of FI shape, the host anisotropy or the interaction between stress fields of neighbouring FIs. Consequently, this criterion should be considered only as a semi-quantitative one. In this work, the isolation criterion (see Sections 3.3.1 and 3.3.2) consists in discarding FIs with $Iso_{\mathrm{FI}} \leq 1$. Our experiments reveal the role of isolation in FI reequilibration

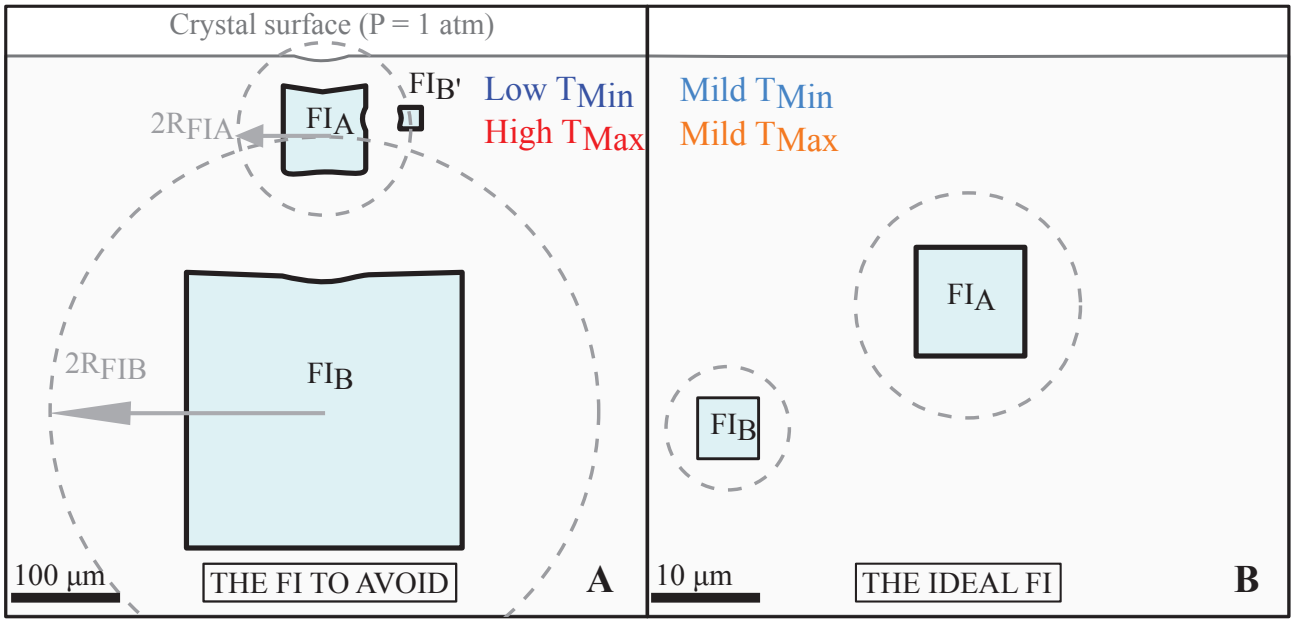

Figure 3.6: ***The "bad" and the "good" FI when performing thermometry on halite FIs.*** *(A) 2-radii circles drawn around FIs illustrate violations of isolation criterion used in this work. Stress field of FI_A, selected for $T_{h/x}$ measurement, encompasses two surfaces: that of host crystal and of FI_B'. It contributes to lowering of FI_A elasticity limit and leads to plastic deformation of its walls. Similarly, FI_A lies in region of FI_B strong stress field, which also contributes to the plastic deformation of its walls. Moreover, its large size and the large thermal range to which it was subjected also expose it to plastic deformation. (B) FI_A is distant enough from any other FI and the surface, it is small, and thermal extrema undergone are mild.*

(Figure 3.7A, C and E). Many FIs with a low Iso_{FI} exhibit a T_{x} lower than that of more isolated FIs of comparable size. This is especially visible for $\mathrm{SyntHal33_{16}}$ (Figure 3.7C), as crystals from this batch exhibit the densest populations of FIs (e.g. crystal shown in Figure 3.2).

3.4.2 T_{Min} and FIs size, decisive drivers of reequilibration

The T_x-size relation for SyntHal24.6$_{19}$ and SyntHal33$_{16}$ is shown in Figure 3.7 (A and C, respectively). In addition, in order to test the effect of a very large ΔT on the T_x-size trend, we performed BS on a third sample, SyntHal33$_0$ (Figure 3.7E). T_x can strongly depend on the FI size, and this dependence is even stronger for samples which underwent $T_{Min} \ll T_f$ before thermometry measurement. While SyntHal24.6$_{19}$ shows no systematic variation of T_x with size, SyntHal33$_{16}$ and SyntHal33$_0$ show a strong and very strong variation, respectively. This can be explained by the growing values of ΔT: 5.6, 17 and 33 °C, respectively. Searching for a potential size threshold, we plot the cumulative $T_{x,mean}$ from smallest to largest isolated FI for each of the cases (Figure 3.7B, D and F). Three situations are observed, depending on ΔT:

- With a small ΔT (SyntHal24.6$_{19}$), the cumulative $T_{x,mean}$ is constant and equal to T_f, whatever the size. No FI underwent discernible reequilibration.

- With a moderate ΔT (SyntHal33$_{16}$), the cumulative $T_{x,mean}$ is constant and equal to T_f up to a size threshold 13 µm, and then decreases. The tension built inside FIs was enough to induce plastic deformation of the wall of FIs bigger than 13 µm.

- With a high ΔT (SyntHal33$_0$), we observe no threshold, $T_{x,mean}$ decreasing steadily with larger FIs. Virtually no FI could withstand the strong tension. Fitting a power law curve to T_xs as a function of size, and pinpointing the crossing with T_f, we find a potential threshold size of 4.1 µm.

When testing the influence of FI size on T_h obtained with microthermometry a lower correlation is found (Figure 3.7G and I). The cumulative $T_{h,mean}$ as a function of size (Figure 3.7H and J) shows a decreasing trend comprising not one but several thresholds. We explain this non-monotonic trend by the random nature of cavitation. Each FI underwent a distinct maximum tension although each one of them was cooled down to an identical $T_{Min} = -20$ °C. Indeed, each FI cavitated at a different temperature, often before reaching -20 °C. Since a biphasic FI is back to "safety", with a vapour pressure close to 0 MPa, the maximum tension undergone by a FI during microthermometry analysis is the tension at T_{Cav}, not at T_{Min}. Therefore, in microthermometry, FI size is not the only parameter controlling reequilibration: the propensity for cavitation is another one. This aspect is crucial, as many authors incorrectly assume that the absence of T_h-size relation is a sufficient criterion to prove FIs are undamaged.

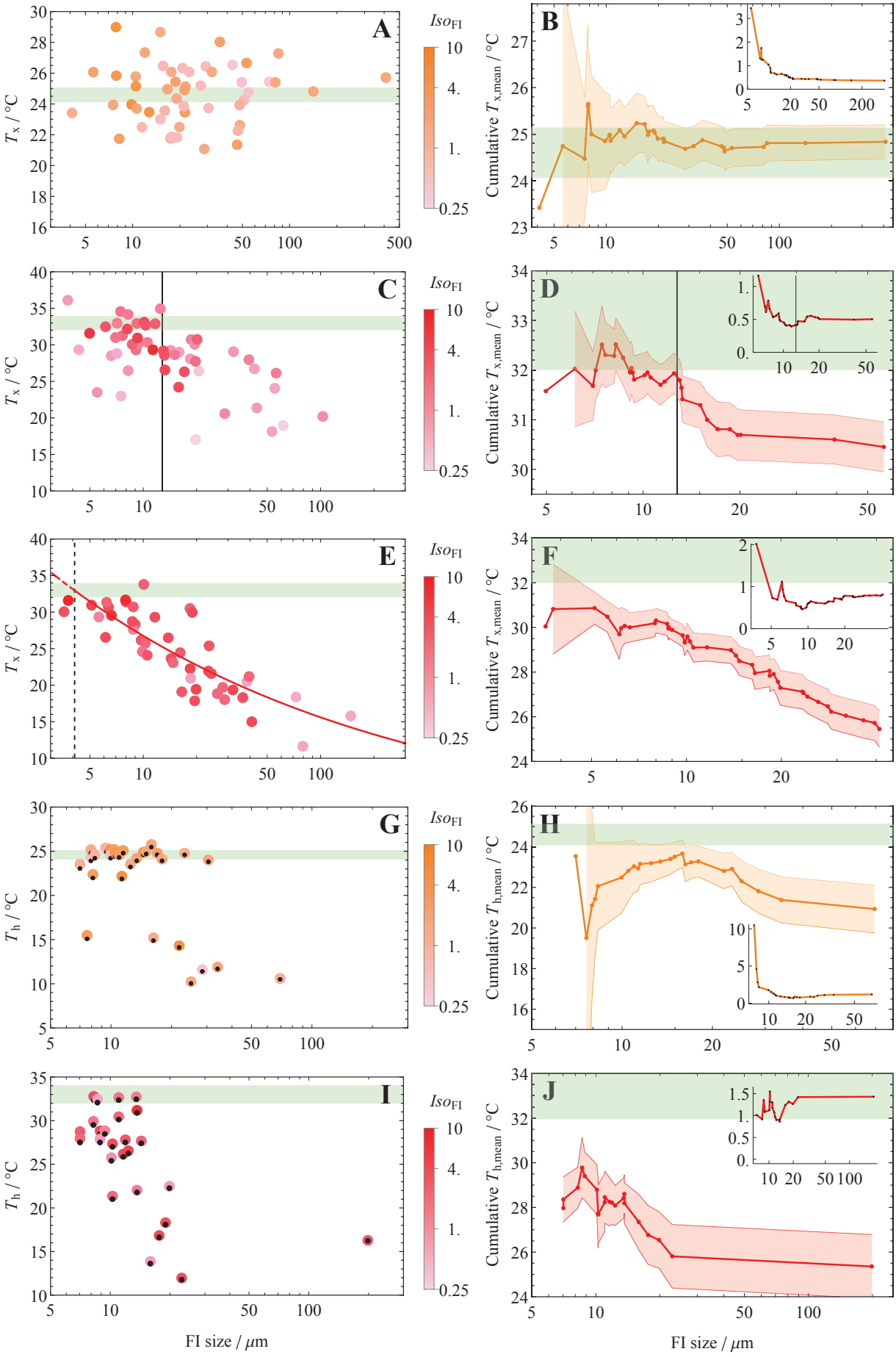
A
B
C
D
E
F
G
H
I
J
T_x / °C
T_h / °C
Cumulative $T_{x,mean}$ / °C
Cumulative $T_{h,mean}$ / °C
Iso_{FI}
10
4.
1.
0.25
FI size / μm

Figure 3.7

Figure 3.7: ***The $T_{h/x}$-size dependence.*** *Left column: $T_{h/x}$ as a function of FI size in crystals from SyntHal24.6$_{19}$ (A), SyntHal33$_{16}$ (C), SyntHal33$_{0}$ (E), SyntHal24.6$_{-20}$ (G) and SyntHal33$_{-20}$ (I). Points are colored according to their Iso_{FI} value (see Section 3.4.1). Right column: cumulative $T_{h/x,mean}$ for SyntHal24.6$_{19}$ (B), SyntHal33$_{16}$ (D), SyntHal33$_{0}$ (F), SyntHal24.6$_{-20}$ (H) and SyntHal33$_{-20}$ (J); the average was calculated over successive data subsets, adding one by one FIs ordered by ascending size. Insets show the standard error on the cumulative $T_{h/x,mean}$ (°C) as a function of size (μm). Only isolated FIs ($Iso_{FI} > 1$) were used for these cumulative $T_{h/x,mean}$ plots. Break of slope around 13 μm in panel D is used to determine threshold size under which FIs are undamaged (black solid vertical line). The size at which the power-law curve fitted to the reequilibrated FIs (red line in panel E; weakly isolated FIs are given a weaker weight in the fit) reaches T_f, 4.1 μm, determines threshold size under which FIs are undamaged (black dashed vertical line). Small dots in Panels G and I are T_h values before Laplace pressure correction.*

The blurred relation between halite FIs size and T_h was already noticed by Lowenstein et al. (1998). Clearer correlations were observed in gypsum FIs by Krüger et al. (2013), as they triggered all cavitations at the same temperature using their femtosecond laser technique (Krüger et al., 2007, 2011). On the positive side of pressure in the *P-T* diagram, some authors observed a strong T_h-size correlation when overheating samples prior to T_h measurement, in minerals like quartz (Bodnar et al., 1989), fluorite and sphalerite (Bodnar and Bethke, 1984), and empirical equations adjusted to the data revealed best fitted with power or logarithmic laws. The size dependence of materials yield stress has been observed, described and explained by the community of physicists in solid mechanics these last fifteen years. Through applying uniaxial compression tests on gold micro-pillars, Greer and Nix (2006) showed that the process accounting for such a mechanical behavior is dislocation starvation: the smaller the volume of material, the higher the probability that preexisting mobile dislocations annihilate at a nearby free surface. Thus, in the case of a very small dislocation-starved material, plasticity is accommodated by the nucleation and motion of new dislocations rather than by the motion of former dislocations.

To better constrain the process of halite FI reequilibration, we measured w at several T in 6 FIs from SyntHal24.6 through complete thermal cycles, from T_f down to 0 °C and back to T_f. In other words, we used BS to measure $P_{FI,lim}$. When a FI is heated or cooled, starting from T_f, $w^{mono}(T)$ follows a linear quasi-isochore. Under this regime, the FI walls respond elastically to the stress that accumulates as the temperature departs from T_f, and $w^{mono}(T_h)$ remains unchanged. However, once $\Delta T > \Delta T_{lim}$ and $P_{FI,lim}$ is reached, the FI changes shape in an irreversible way. Beyond this limit, the walls deform in a plastic mode, and $w^{mono}(T)$ follows a parabolic trend. The temperature at which $P_{FI,lim}$ is reached is notably underlined by $w^{mono}(T)$ deviating from the elastic straight line. Thus, a FI that has not reequilibrated during the thermal cycle should present $w^{mono}(T)$ matching the linear theoretical speed of sound of a FI deforming elastically, and yield T_xs before and after cycle both close to T_f.

The results, presented in Figure 3.8, first confirm the size-related resistance to collapse. On the one hand, in small FIs, $w^{mono}(T)$ follows an elastic trend and yield T_xs before and after cycle close to each other and close to T_f (Figure 3.8A and B). On the other hand, in large FIs, $w^{mono}(T)$ deviates from the elastic path through cooling down and T_x is lower after thermal cycle (Figure 3.8C and D). We also investigated the mechanical behavior of two very close FIs of different size (Figure 3.8E). This last case clearly shows that the vicinity of FIs triggers

and enhances plasticity, as both FIs, whatever their size, show a trend strongly deviating from the elastic path, and yield a T_x much lower than T_f after cycle.

After converting ΔT into pressure and applying a factor 1.5 to the measured $P_{FI,lim}$ to get the host yield stress (Equation (3.1)), we plot the yield stresses versus size determined in this work along with data from the literature (Figure 3.9). In particular, we use the data of Zou and Spolenak (2013), who performed uniaxial compression experiments on monocrystalline NaCl micro-pillars of sizes ranging from 0.25 to 4 µm. We fit a power law to their data, which we extrapolate. It turns out our results fall perfectly on this extrapolated fit. The fact that other authors' yield stress data obtained on millimetric samples also match very well this fit bolsters its extrapolation up to sizes larger by 3 orders of magnitude. Therefore, we have shown the following fit is valid for the range 0.25 µm to 4.10^3 µm:

$$Y_s = (135\text{MPa})\frac{d}{(1\mu\text{m})}^{-0.64}, \tag{3.3}$$

with Y_s the yield stress of NaCl (MPa) and d the dimension of the surface on which the pressure is applied (i.e. the diameter for a circular section and the side for a square section). Dividing by the aforementioned factor 1.5, we get:

$$P_{FI,lim} = (90\text{MPa})\frac{l}{(1\mu\text{m})}^{-0.64}, \tag{3.4}$$

with l the side of the square FI. Considering a gradient 1 MPa $°C^{-1}$ inside FIs, typical for NaCl-H_2O FIs (this is further detailed in Chapter 4), we get:

$$\Delta T_{lim} = (90\text{K})\frac{l}{(1\mu\text{m})}^{-0.64}, \tag{3.5}$$

with ΔT_{lim} the amount of overheating/overcooling from T_f that can be applied before reaching $P_{FI,lim}$. Note that the data from Zou and Spolenak (2013) is the yield flow at 5% strain, which is very similar to the yield stress since the stress-strain curve in their experiments is very flat once yield stress is reached (i.e. samples in their experiments undergo little strain hardening). As an additional check, we selected the lowest value for each of their micro-pillar size and fitted a power-law; we observed that the resulting curve was in very good agreement with the one fitted in Figure 3.9.

3.4.3 Are natural halite FIs more resistant to collapse ?

It is sometimes stated that reequilibration after cooling does not occur in natural halite FIs (Satterfield et al., 2005a; Speranza et al., 2013). Indeed, Roberts and Spencer (1995) results match closely the brine temperature. T_hs in Benison and Goldstein (1999) were all reproducible within 1 °C, and exhibited a narrow distribution and no correlation between T_h and size in each FIA. In some other studies though, a negative T_h-size trend is identified in some sample groups (e.g. Zhang et al. 2017; Sun et al. 2017). T_h reproducibility runs (i.e. the re-measurement of FIs T_h after reiterated cooling nucleations), when performed by authors (Roberts and Spencer 1995; Lowenstein et al. 1998; Zhang et al. 2015, 2017), usually show a decrease of $T_{h,mean}$ between

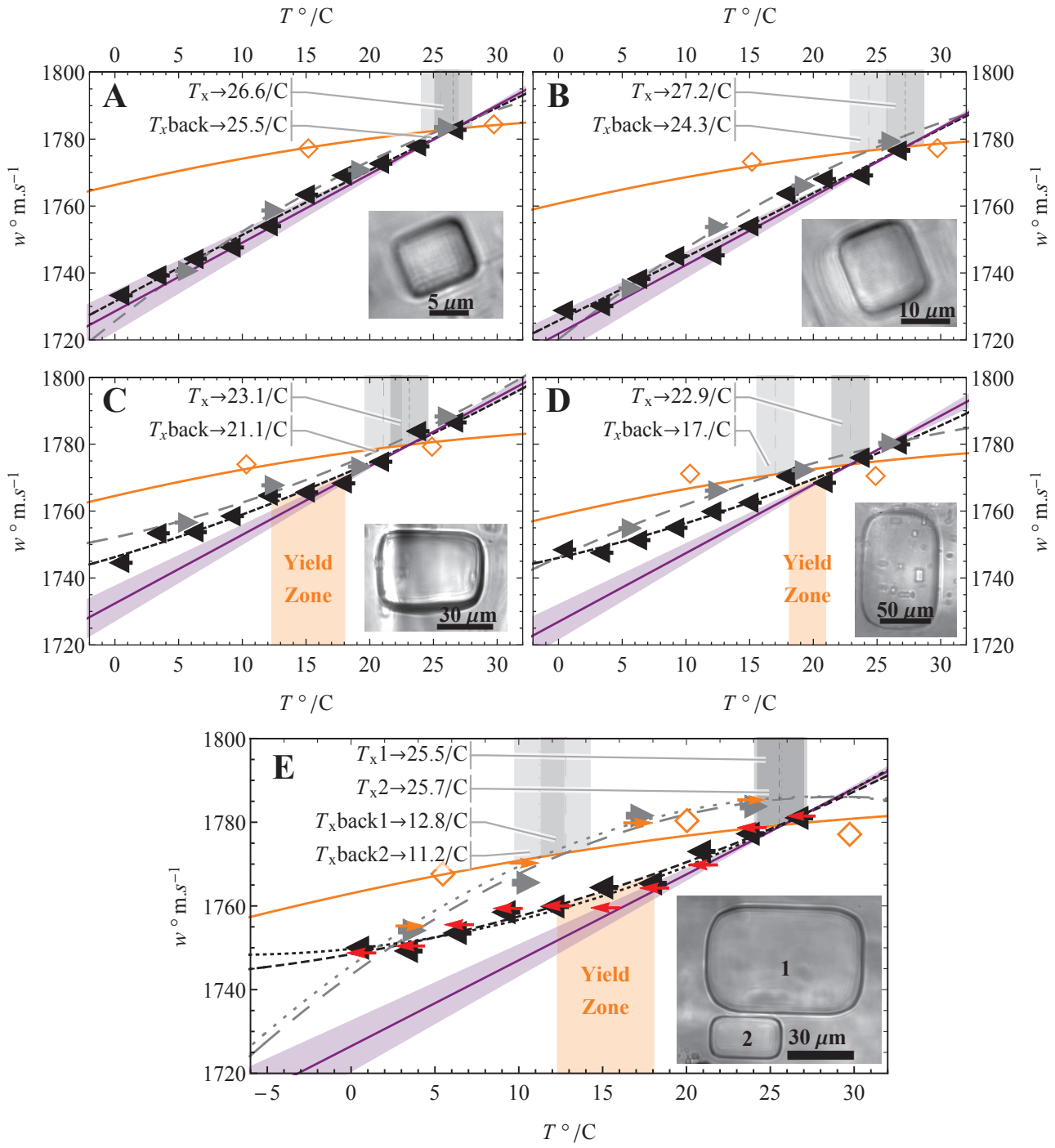

Figure 3.8: ***Reequilibration limit of various FIs revealed by BS.*** *Samples from SyntHal24.6. 4 FIs of increasing size (A to D) and 2 neighboring FIs (E). $w^{mono}(T)$ measured during cooling to 0 °C (left-pointing black triangles fitted by black dashed parabola) and then during heating from 0 °C (right-pointing gray triangles fitted by gray dashed parabola). In E, data for FI2 during cooling and heating shown with left-pointing red and right-pointing orange arrows fitted by short-dash black and gray parabolas, respectively. After cavitation, we measured $w^{LVE}(T)$ (orange diamonds fitted with orange solid parabolas). Dot-dashed purple line: expected $w^{mono}(T)$ if deformation is elastic. Slope and error envelope of this line obtained by taking average and standard deviation of the slopes of all the measured non-reequilibrated and isolated FIs from SyntHal24.6 and SyntHal33$_{16}$. Vertical orange shaded area: yield zone. Uncertainty on each measurement slightly smaller than symbols. Note: for better accuracy, LVE values were fitted with the equation of the speed of sound in water saturated with NaCl (Millero et al., 1987; Sawamura et al., 2007), rescaled by a factor.*

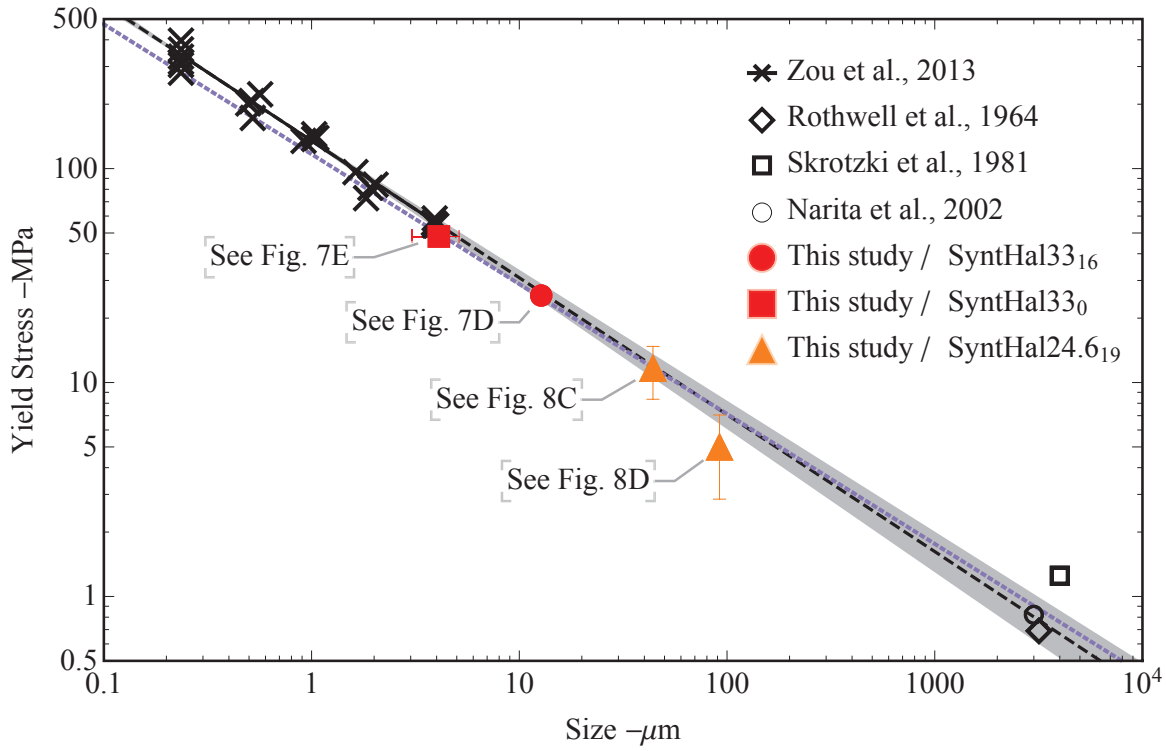

Figure 3.9: ***Pure NaCl single crystal yield stress as a function of size.*** *Data from Zou and Spolenak (2013) are shown by black crosses and fitted with a power-law (solid black line). Extrapolation of this power-law (black dashed line) matches well yield stress values obtained through compressive (Skrotzki and Haasen, 1981), bending (Rothwell and Greenler, 1964) and tensile (Narita et al., 2002) mechanical tests on millimetric [100]-oriented NaCl crystals. Note that when the data provided by authors is the critical resolved shear stress (CRSS), we multiplied it by 2, according to Schmid's law.*

the first run and the following ones (Lowenstein et al. 1998; see compilation or literature reproducibility runs in Section 3.E). In a nutshell, it seems reequilibration in natural halite FIs occurred in some studies and not in others, even though inclusions median size is rather comparable from one study to another. In the following section we discuss the potential causes for such a discrepancy.

Surface tension issues. As soon as a bubble nucleates in a FI, the stress is released, and the risk for FI walls to collapse disappears. Moreover, all FIs do not nucleate a bubble simultaneously, nor at the same temperature -therefore, nor the same tension. Indeed, nucleation is a thermally activated process: for the new phase to appear, the system must overcome an energy barrier E_b (Debenedetti, 1996; Volmer and Weber, 1926). This barrier results from the competition between the energy gain corresponding to the creation of a volume of the new phase, and the energy cost corresponding to the interface between the two phases. Adapting the equations of the Classical Nucleation Theory (Debenedetti, 1996; Caupin and Herbert, 2006) to the case of microthermometry experiments, we get a nucleation rate that is proportional to $V_{\mathrm{FI}}.\tau.e^{[-\gamma^3/(P_{\mathrm{FI}}^2.k_{\mathrm{B}}.T_{\mathrm{Min}})]}$, with T_{Min} the cooling temperature in the freezer or in the cooling stage, τ the time spent by the halite sample at T_{Min}, V_{FI} the volume of the FI, k_{B} the Boltzmann constant, P_{FI} the FI internal negative pressure and γ the surface tension of the inclusion fluid. We see that the main parameter controlling bubble nucleation is by far γ. We calculate that the probability $\frac{1}{2}$ of homogeneous nucleation of a bubble in a saturated NaCl-H_2O FI

requires an additional ~30 MPa of tension compared to a pure water FI of equivalent size, even though the former has a surface tension only higher by ~14% compared to the latter - at 25 °C, 82 mN m^{-1} and 72 mN m^{-1} respectively (Allen et al., 2009). As the surface tension of chloride salts solutions depends rather linearly on the chlorinity with an approximate increase of 2 mN m^{-1} per additional molar of chlorine (Weissenborn and Pugh, 1996), we would expect FIs of halites from hyper-saline bodies that have a chlorinity even higher than that of saturated NaCl-H_2O, such as the Dead Sea (Krumgalz et al., 2002), to require a very strong internal tensile stress for bubble nucleation. More generally, the vast majority of electrolytes tend to increase the surface tension of brines alike. These range from halide salts to sulfate salts and include carbonate salts (Pegram and Record, 2007). Conversely, acids tend to decrease the surface tension of water (Allen et al., 2009; Álvarez et al., 1997). Interestingly T_hs in (Benison and Goldstein, 1999), namely one of the studies on which suspicions of FIs reequilibrations are the smallest, were obtained in very acid FIs in halite from the Permian red bed deposits of the US midcontinent. It was suggested that hyper-saline lakes from this period and region could have had pH < 0 (Benison, 2013). Moreover, 10-20% of the FIs had nucleated a bubble at $-10\,°C$ in their study, which is much better than our synthetic samples (5% of the FIs had nucleated at $-20\,°C$ in our case). Thus, we surmise that the very low pH of their FIs might have made possible the nucleation of bubbles at a milder T_{Min}, thereby preventing FIs to be subjected to an excessive tensile stress. Note that in this paragraph we only consider the case of homogeneous bubble nucleation. In reality, most bubbles nucleate at less negative pressures, through a process called “heterogeneous nucleation”. Heterogeneous nucleation is less quantitatively constrained, and depends on additional factors such as the amount of impurities of the liquid and the roughness of the contact with the solid surface.

T_f - T_{Min}. The difference between T_f and T_{Min} determines the maximal tension FIs are subjected to, unless bubble nucleation occurs at $T > T_{Min}$. Most studies use a very similar range $-20\,°C < T_{Min} < -15\,°C$, with the mildest $T_{Min} = -10\,°C$ found in Benison and Goldstein (1999). Thus, the maximum tension FIs underwent is mainly dependent on T_f: the higher T_f, the higher ΔT and the stronger the tensile stress at T_{Min}.

Composition. In this study, we estimate a gradient of ~1 MPa $°C^{-1}$ in NaCl-H_2O FIs. However, this gradient is likely to be different for other compositions. This would have an impact on the reequilibration of FIs. For instance, a FI with a gradient 0.5 MPa $°C^{-1}$ would withstand temperature excursions twice as large as NaCl-H_2O FIs before reequilibrating. This question is tackled in the next chapter.

Host lattice impurities content. Contrary to synthetic NaCl-H_2O brines that precipitate pure NaCl crystals, natural brines are complex aqueous solutions containing many different cations and anions. These ions can co-precipitate with halite, substituting Na^+ or Cl^- and therefore remaining as impurities in the crystal lattice. Some having fairly high partition coefficient like K^+ or Br^- may amount up to several hundreds of ppm (McCaffrey et al., 1987). Here though, we are particularly interested in the co-precipitation of divalent cations, such as Ca^{2+}, Mn^{2+} or Sr^{2+}. Due to low partition coefficients and/or low concentration in the parent brine, these ions might

never exceed a few tens of ppm in the crystal lattice: indeed, Herut et al. (1998) found Ca^{2+} and Mn^{2+} contents in Dead Sea halite ranging from 4.7 to 8.8 ppm and from 18.5 to 22.4 ppm respectively while Blamey and Brand (2019) measured Sr^{2+} contents ranging from 4 to 35 ppm in halite from various locations. However, these low contents might be enough to affect significantly the stress at which FIs yield. Indeed, a divalent ionic impurity induces a charge-compensating defect or vacancy in the NaCl crystal lattice, which in turn affects the mobility of dislocations and ends up increasing the material yield stress. We found the following NaCl strengthening as a function of impurity content in the literature: yield stress increases by a factor 1.4 and 2 with 26 and 53 ppm of Eu^{2+} (Orozco and Agulló-López, 1986), 2.5 and 4 with 54 and 91 ppm of Ca^{2+}, respectively (Skrotzki and Haasen, 1981), 7 with 128 ppm of Sr^{2+} (Skrotzki and Haasen, 1981), and 4.5 with 150 ppm of Mn^{2+} (Orozco and Agulló-López, 1986). In theory, the yield stress of ionic crystals should increase linearly with the square root of the divalent cation concentration, though experiments might sometimes yield other trends (Mitchell and Heuer, 1977; Skrotzki and Haasen, 1981). Another unknown is the interplay between strengthening behaviors of impurities on the one hand and size on the other hand, though one study recently showed through comparing doped and pure KCl that impurities hardening doesn't affect the size effect (Zou and Spolenak, 2015). We surmise that the impurities content of halite crystals could play a role in the resistance of FIs to reequilibration.

3.4.4 Proposed "good practices" for thermometry on halite

Based on our findings and that of previous workers, we suggest the following practices and cautions when performing thermometry on halite FIs (see also Figure 3.6):

1) **Avoiding large ΔT.** For samples kept at atmospheric pressure (i.e. close to 0 MPa), an excessive internal pressure inside FIs is responsible for reequilibration. Thus, anyone working on halite FIs should take care that crystals experience the narrowest temperature range as possible, from sampling to measurement. Drilling campaigns during peak summer or winter should be avoided, and samples should be stored in an air-conditioned room. The thermal history from deposit to sampling (e.g. burial temperature) should also be constrained within the realms of possibility.

2) **Selection of small inclusions.** Through implementing Equation (3.4) with an estimate of ΔT, it is possible to estimate the FI size below which reequilibration is unlikely to have happened. Note that Equation (3.4) applies to NaCl-H_2O FIs, with gradient 1 MPa $°C^{-1}$. It is possible that gradients are different in FIs with different composition, and should be the subject of another study. Plotting the $T_{h/x}$s as a function of FIs size is a necessary (but not sufficient) step to check FIs are not reequilibrated.

3) **Selection of isolated inclusions.** The concept of isolation presented in Section 3.4.1 is illustrated in Figure 3.7C and Figure 3.8E: a FI close to any other surface is more prone to plastic deformation. As regards our results and Equation (3.1), the limit $Iso_{FI} \geq 1$ is appropriate.

4) **Gaussian $T_{h/x}$ distribution in each FIA.** If the number of $T_{h/x}$s is statistically high enough, the normal

distribution of $T_{h/x}$s in one FIA should be checked, as non-Gaussian distributions are very likely to highlight reequilibration (Vityk and Bodnar, 1998). The closeness of $T_{h/x,mean}$ and $T_{h/x,median}$ can be used to check $T_{h/x}$ distributions are normal, as shown in Table 3.1.

5) **Narrow $T_{h/x}$ distribution in each FIA.** The contemporaneity in a FIA implies all FIs should yield close $T_{h/x}$s. In order to ascertain FIs had not reequilibrated since their entrapment, Goldstein (2001) proposed to check that 90% of the T_hs from one FIA do not deviate more than 10-15 °C, which corresponds to σ_{Th} = 3 °C and 4.6 °C, respectively. This statement, based on observations in FIs from different minerals and various P_f-T_f conditions, is often used in the literature to rule out reequilibration issues. However, we believe this cannot apply entirely to low T_f halite FIs. Fall and Bodnar (2018) reviewed a large amount of studies and showed that highly saline FIs trapped in the monophasic state typically show a range in T_h lower than 5 °C. Similarly, from 222 T_hs in 58 FIAs in Benison and Goldstein (1999), we calculate an average σ_{Th} = 1.3 °C. It converts into a 4.3 °C range within a 90% confidence interval. We conclude that a T_h range significantly higher than 5 °C in a FIA either highlights reequilibration processes or shows a great variability in temperature conditions during entrapment. In the case of T_xs obtained with BS, one expects a larger spread as the instrumental error adds up to the "natural" error. Typically, $1.5 < \sigma_{Tx} < 2$°C in synthetic NaCl-H_2O FIs, but the distribution may be different for other chemistries. Analogously to T_h distributions, T_x distributions presenting σ_{Tx} significantly larger than expected may be due to reequilibration or temperature variability of the parent brine.

In addition to these 5 criteria applicable with both techniques, we add some other points that are specific to microthermometry:

6) **T_{Min} as high as possible.** As explained before, the colder the temperature, the higher the tension inside the monophasic FI and the higher the risk of FI reequilibration. However, the higher T_{Min}, the lower the probability to cavitate. Consequently, in order to apply the mildest cooling temperature sufficient to make FIs cavitate, we propose to slowly cool down the sample in the microscope stage until first cavitations occur, and then keep the sample at this threshold temperature for as long as necessary in the stage or in the freezer. For instance, in the case of our synthetic halites, -12 to −15 °C seems a good choice: out of 38 FIs whose cavitation temperature was checked, none cavitated above −12 °C, then 9 cavitated between −12 °C and −15 °C during the −5 °C min $^{-1}$ cooling ramp, and 8 others subsequently cavitated while stored for 2 days at −15 °C in the freezer. We do not expect all samples to show similar rates of cavitation, as this process is controlled by multiple parameters. The fluid surface tension is one of them, and depends on salinity (Weissenborn and Pugh, 1996) and pH (Allen et al., 2009).

7) **Correction of the Laplace pressure.** Because of the pressure differential between the vapour and the liquid (Young, 1805), FIs homogenize at $T_h < T_f$. This effect becomes more pronounced for small FIs: for pure water inclusions at T_f = 150 °C, Fall et al. (2009) calculate a T_h lower than T_f by 1 °C for 1000 µm^3 inclusions, by 3 °C for 10 µm^3 inclusions and by 5 °C for 1 µm^3 inclusions. We calculate a weaker

effect for NaCl-saturated aqueous FIs, with a correction of 0.3 °C for 1000 µm^3 inclusions, 0.9 °C for 10 µm^3 inclusions and 1.7 °C for 1 µm^3 inclusions. The effect can be quantitatively observed on our microthermometry results in Figure 3.7. See Section 3.C and Krüger et al. (2011) for more information on the correction of this effect.

8) **The exclusive use of $T_{h,max}$ unless the absence of reequilibration is demonstrated.** Our work confirms the observations of Lowenstein et al. (1998): in a sample cooled in the stage or in the freezer, only the highest T_h values match the brine temperature. All the other values indicate that FIs underwent shrinkage during the cooling process. Thus, unless the T_h distribution in each FIA is Gaussian, narrow and uncorrelated with FIs size as stated above, we strongly recommend to only keep $T_{h,max}$ for convincing paleotemperature reconstructions. One could argue that broad T_h distributions do not necessarily underline reequilibration but might rather be due to a short time variability of the brine temperature at the time of FIs entrapment, as stated in paragraph (5) of this section. However, unless authors do have quantitative information about temperature variability in the parent brine, the dilemma is impossible to untangle. In the case of the selection of $T_{h,max}$ as the only relevant T_h, one gets the maximum temperature of the brine during the FIA formation. For instance, in the case of a FIA trapped within one day/one year in a shallow water body, $T_{h,max}$ provides information on the temperature around midday/summer, respectively. We see here how important it is to have a constraint on the timing of halite precipitation, in order to be able to give a temporal meaning to temperature information. Note that selecting $T_{h,max}$ implies a sufficient amount of T_hs per FIA, namely several dozens.

3.5 Brillouin spectroscopy, a precise and accurate thermometer

All the Brillouin thermometry measurements were performed on halite crystals with very well constrained synthesis temperature within ± 1 °C or ± 0.5 °C (SyntHal33 and SyntHal24.6, respectively), which improves upon previous halite thermometry studies (Roberts and Spencer, 1995; Lowenstein et al., 1998). Thence it is possible to compare precisely our results to T_f. Once restricted to small and isolated enough FIs, the Brillouin thermometry T_xs show a normal distribution. As populations show $1.5 < \sigma_{Tx} < 2$ °C, the ensuing uncertainty on each individual T_x as a proxy for T_f is ± 1.5-2 °C (1-sigma confidence interval). Nonetheless, the average value converges towards T_f with a growing T_x population, and our experiments show that $T_{x,mean}$ matches T_f brackets to within a ~0.5 °C standard error (1-sigma). It implies $T_{x,mean}$ can be considered as a single accurate and precise T_f, and this works for any FIA from geological samples, provided the FIs in a same assemblage were all trapped at a same precise temperature. The main source of uncertainty in Brillouin thermometry is the instrumental error, which gives $0.1\% < \sigma_w < 0.15\%$. It results into a temperature uncertainty $1.5\,°C < \sigma_{Tx} < 2\,°C$ (See Appendices for more information on experimental uncertainty and estimated time needed to reach ± 0.5 °C uncertainty on T_f). Note that this conversion from σ_w to σ_{Tx} is valid for NaCl-H_2O compositions. Indeed, the composition controls the intersection angle between $w^{mono}(T)$ and $w^{LVE}(T)$, which in turn governs

the conversion ratio from w to T_x uncertainties. Thus, σ_{Tx} may be higher or lower depending on the FIs composition.

There are at least four upgrades that we see in the use of Brillouin thermometry instead of microthermometry:

- It is a way to avoid too large a ΔT and ensure T_x measurements from non-reequilibrated FIs. We calculate for a typical natural sample of $T_f = 25\,°C$ that has undergone $\Delta T \approx 20\,°C$ a size threshold $\approx$ 10-11 µm. Using microthermometry with $T_{Min} = -20\,°C$, this threshold would decrease down to 3 µm.

- It rehabilitates the use of the mean value instead of the maximum value. Selecting extrema in a histogram is always a delicate process, as one can never be sure that the selected minimum or maximum is not an outlier, or if additional measurements would increase the maximum value[1].

- It avoids the drawbacks that come up when scrutinizing a bubble homogenization. First, when approaching T_h in a small FI (< 10 µm), a bubble becomes difficult to observe; time-consuming methods like thermal cycling (Roberts and Spencer, 1995) become necessary for an accurate pinpointing of T_h. Secondly, calculating the Laplace pressure correction in halite FIs is a delicate task, as one has to know both the FI volume and composition, and be sure the literature provides the necessary empirical data to calculate the correction. This matter cannot be neglected for small FIs.

- It is a fast method that enables the user to get an accurate approximation of T_f within $1\,°C$ in one day. As it is based on the analysis of monophasic FIs, it makes the measurement of whichever FI possible, which is particularly convenient when it comes to analyze a FIA that only contains a few FIs.

3.6 Conclusions

In this study, we performed Brillouin spectroscopy and microthermometry to investigate the potential of halite fluid inclusions as temperature archives, and evaluate the ability of each of the two methods to reconstruct consistent paleotemperatures. These measurements were performed on lab-grown halite crystals synthetized at $24.6 \pm 0.5\,°C$ and $33 \pm 1\,°C$.

Our Brillouin thermometry measurements, along with Brillouin mechanical tests, enable us to highlight the T_x-size relation. We deduce reequilibration pressure thresholds ($P_{FI,lim}$) dependent on FI size, and plot them along with yield stress values of NaCl crystals found in solid mechanics literature. The power law we fit matches both the results of this study as well as published data, and allows us to propose an empirical equation linking $P_{FI,lim}$ to the size threshold above which FIs stretch/shrink in a plastic mode: $P_{FI,lim} = \left(l/(1\mu m)\right)^{-0.64}$ x (90 MPa). In the case of a NaCl-H_2O FI, where the P-T slope is 1 MPa $°C^{-1}$, we can thus link the threshold amount

[1] J. Mavrogenes, in Interactive Discussion of Spadin et al. (2015); available at https://www.clim-past-discuss.net/10/C2187/2015/cpd-10-C2187- 2015.pdf).

of overheating/overcooling to the FI size through: $\Delta T_{\text{lim}} = \left(l/(1\mu\text{m})\right)^{-0.64}$ x ($90\,^{\circ}\text{C}$). We also demonstrate that FIs close to other FIs or to the host surface by less than 2 radii have a lower yield stress.

Our microthermometry measurements yield broad T_{h} distributions, with only $T_{\text{h,max}}$ matching the brine temperature. After selection based on FIs size and isolation, the average T_{h} is 3.7 and $4.9\,^{\circ}\text{C}$ below T_{f}, respectively. The body of arguments we get through converging our data and that of previous authors, along with thorough considerations on the physical processes at stake when FIs undergo a cooling cycle, lead us to prompt authors to check the T_{h} distribution in each fluid inclusions assemblage, ensuring that the range of T_{h} values does not exceed $5\,^{\circ}\text{C}$ and that no T_{h}-size correlation exists. If not, we recommend to use only $T_{\text{h,max}}$ as a relevant paleoclimate indicator. We also recommend to slowly cool the sample in the stage down to the temperature at which the first bubbles nucleate, and use this temperature as T_{Min} for as long as necessary to nucleate a sufficient amount of bubbles, in a freezer or in the stage.

The Brillouin thermometry on halite FIs circumvents the biases and drawbacks of microthermometry, namely the Laplace pressure, the difficult observation of bubble homogenization in small FIs and the reequilibration of FIs due to overcooling. Our protocol consists in measuring the isochore of monophasic FIs and deducing their T_{x} from the intersection between the isochore and the liquid-vapour equilibrium curve. After selection based on FIs size and isolation, the average T_{x} for the two batches studied is 0.2 above and $1.1\,^{\circ}\text{C}$ below T_{f}, respectively, the T_{x} distribution is Gaussian and narrow, with a standard deviation $\sigma_{\text{Tx}} \leq 2\,^{\circ}\text{C}$. If the error was purely statistical, the standard error on the mean would be $\frac{\sigma_{\text{Tx}}}{N^{0.5}} = 0.4\,^{\circ}\text{C}$ in the present case. Our results thus demonstrate the advantage of the Brillouin technique over the previous approaches for much more accurate past temperature determinations. Brillouin spectroscopy provides a novel, faster, more precise and more accurate method for climatic reconstructions at diverse temporal and geographical scales.

3.7 Acknowledgements

We thank Yannick Bras for his help with measuring the refractive index of salt solutions and Dome Tanguy for fruitful discussions on solid mechanics. This work was supported by the project ARC 3 Environnement of the Region Rhone-Alpes through a 3-year PhD scholarship for the period 2015-2018.

Appendix

3.A LVE & iso-T_h plots

In this section the reader will find all the measurements that were used to get the Brillouin thermometry T_xs. $w^{mono}(T)$ and $w^{LVE}(T)$ data points and fitted parabolas of each FI are displayed in individual graphs. The error bars used in Figures 3.A.1 to 3.A.3 are one standard deviation on the speed of sound measurements, namely 0.1%. Such a standard deviation prevents us from drawing undisputable conclusions from the observation of one single graph, however, we draw the reader's attention on the fact that the iso-T_h of large FIs are statistically concave, compared to the average linear trend of the rest. This is due to the fact that large FIs stretch through the course of the experiment when heating from lowest to highest temperature of the 4 $w^{mono}(T)$ measurements. Note that we would expect the reverse shape (convex) for isochores measured from highest to lowest temperature, as exemplified in Figure 3.9.

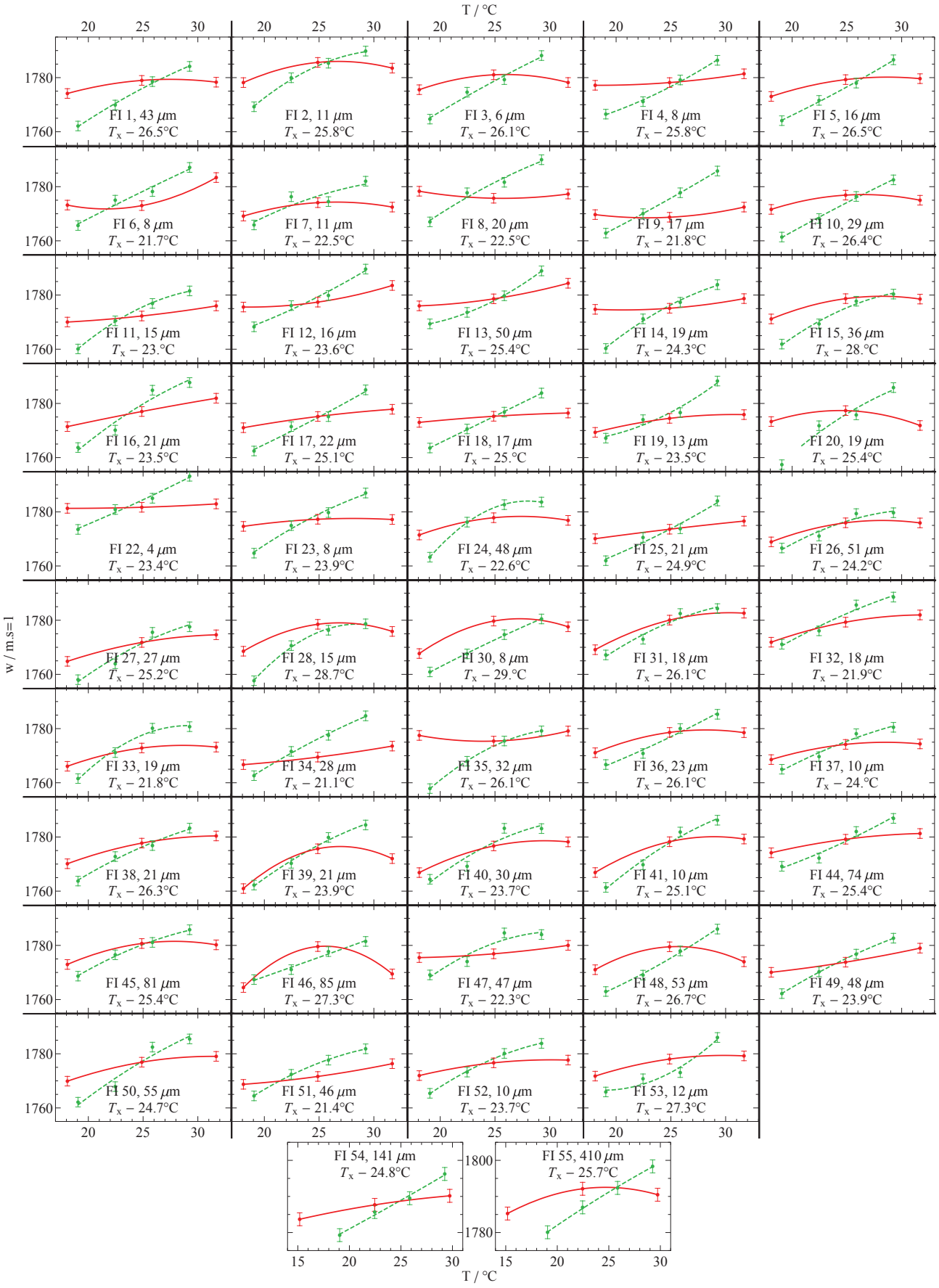

Figure 3.A.1: ***Individual LVE (red disks) and isochore (green disks) w measurements in SyntHal24.6$_{19}$ FIs.*** *Parabolas are fitted to the LVE data points (red solid curve) and the iso-T_h data points (green dashed curve). T_x is the temperature of intersection.*

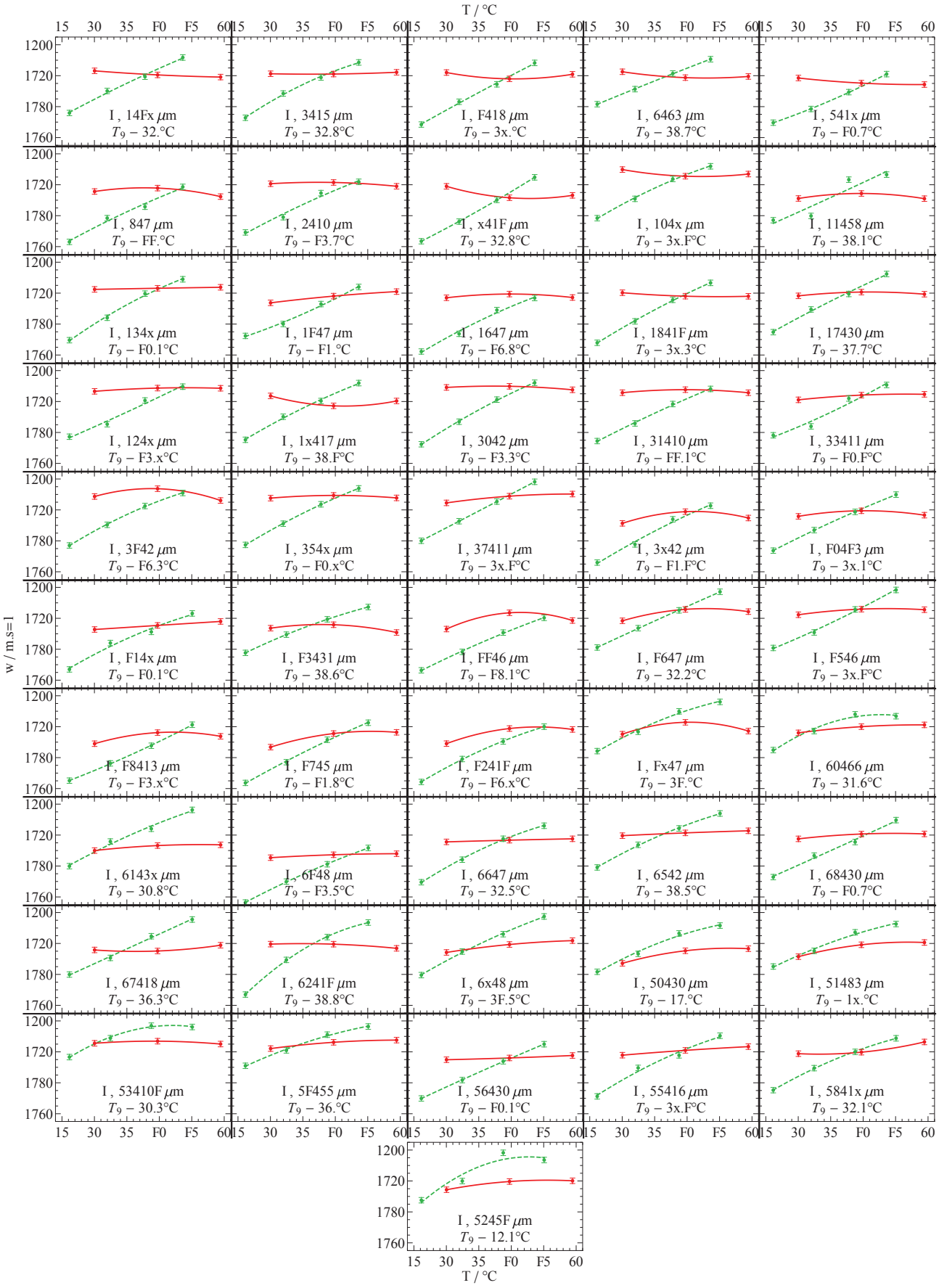

Figure 3.A.2: ***Individual LVE (red disks) and isochore (green disks) w measurements in SyntHal33$_{16}$ FIs.*** *Parabolas are fitted to the LVE data points (red solid curve) and the iso-T_h data points (green dashed curve). T_x is the temperature of intersection.*

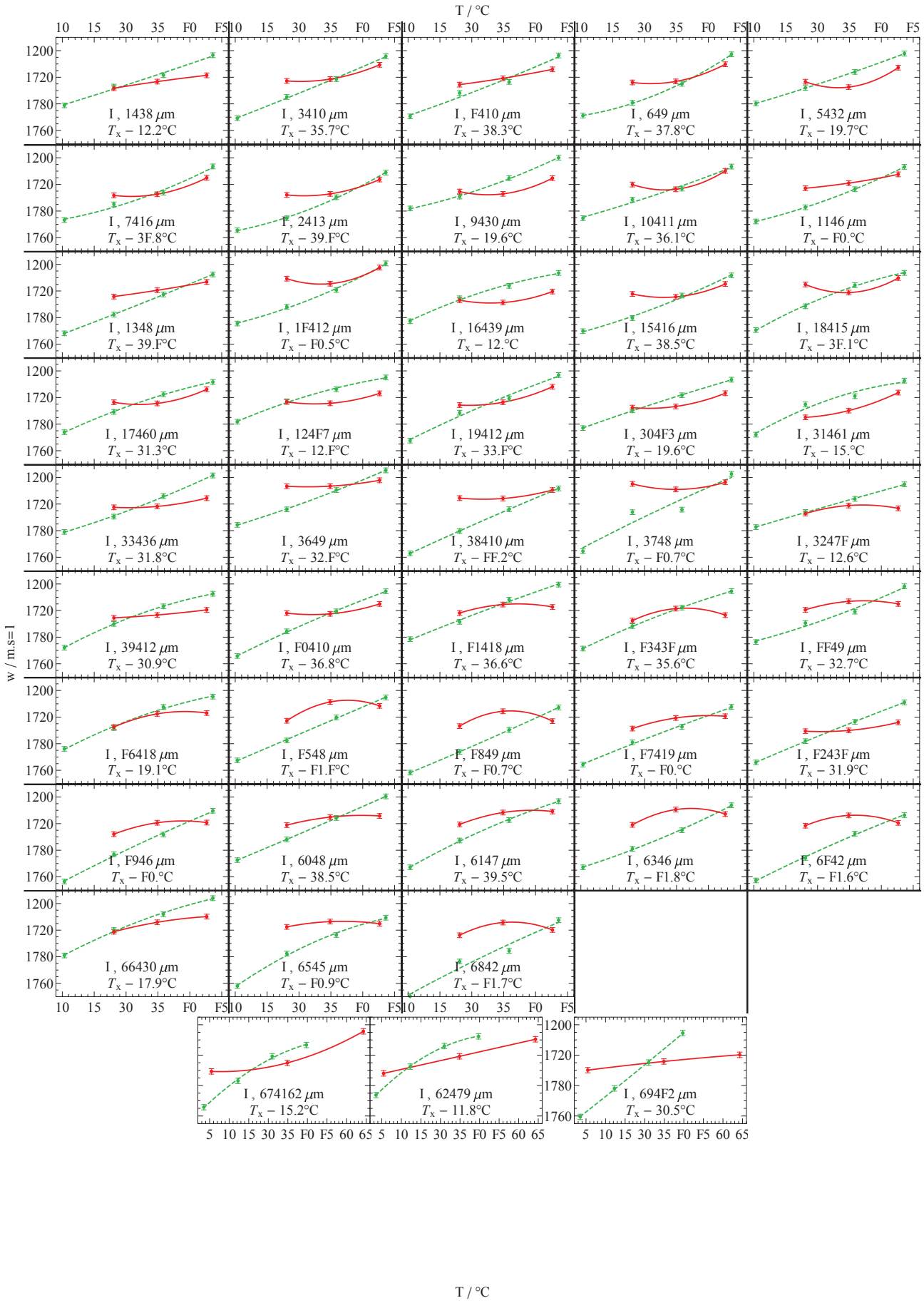

Figure 3.A.3: ***Individual LVE (red disks) and isochore (green disks) w measurements in SyntHal33$_0$ FIs.*** *Parabolas are fitted to the LVE data points (red solid curve) and the iso-T_h data points (green dashed curve). T_x is the temperature of intersection.*

3.B Experiments simulations

We ran a series of simulations to optimize the experimental protocol. These simulations, illustrated in Figure 3.B.1, consist in sampling at several T_i and T_j ($3 \leq \mathrm{i} \leq 4$ and $1 \leq \mathrm{j} \leq 4$) a large number N of random $w^{\mathrm{mono}}(T_\mathrm{i})$ and $w^{\mathrm{LVE}}(T_\mathrm{j})$ from Gaussian populations of standard deviation σ_w centered around the value yielded by the theoretical iso-T_h equation, ${w^{\mathrm{mono}}}_{\mathrm{theo}}(T)$, and the theoretical LVE equation, ${w^{\mathrm{LVE}}}_{\mathrm{theo}}(T)$, at temperatures T_i and T_j, respectively. ${w^{\mathrm{mono}}}_{\mathrm{theo}}(T)$ is the average iso-T_h obtained from SyntHal24.6$_{19}$ and SyntHal33$_{16}$ undamaged monophase FIs, and ${w^{\mathrm{LVE}}}_{\mathrm{theo}}(T)$ is the empirical equation of Millero et al. (1987) slightly extrapolated to saturation molality using the empirical equation of the saturation concentration of NaCl in water as a function of temperature from Sawamura et al. (2007). The temperature at which they interesect is T_f. In the following, we vary several parameters and investigate their influence on the T_x distribution. Some of them require a definition:

$$T_{\mathrm{range}} = \mathrm{Max}[T_\mathrm{i}] - \mathrm{Min}[T_\mathrm{i}] = \mathrm{Max}[T_\mathrm{j}] - \mathrm{Min}[T_\mathrm{j}], \tag{3.6}$$

and

$$T_{\mathrm{offset}} = \mathrm{Mean}[T_\mathrm{i}] - T_\mathrm{f} = \mathrm{Mean}[T_\mathrm{j}] - T_\mathrm{f}. \tag{3.7}$$

T_{range} is equal for *i* and *j* because we only simulate LVE and iso-T_h of equivalent temperature range. Unless we apply an offset only to the measurement temperatures of iso-T_h, in which case we write $\overset{\mathrm{Isochore}}{T_{\mathrm{offset}}}$, the temperature offset is the same for LVE and iso-T_h.

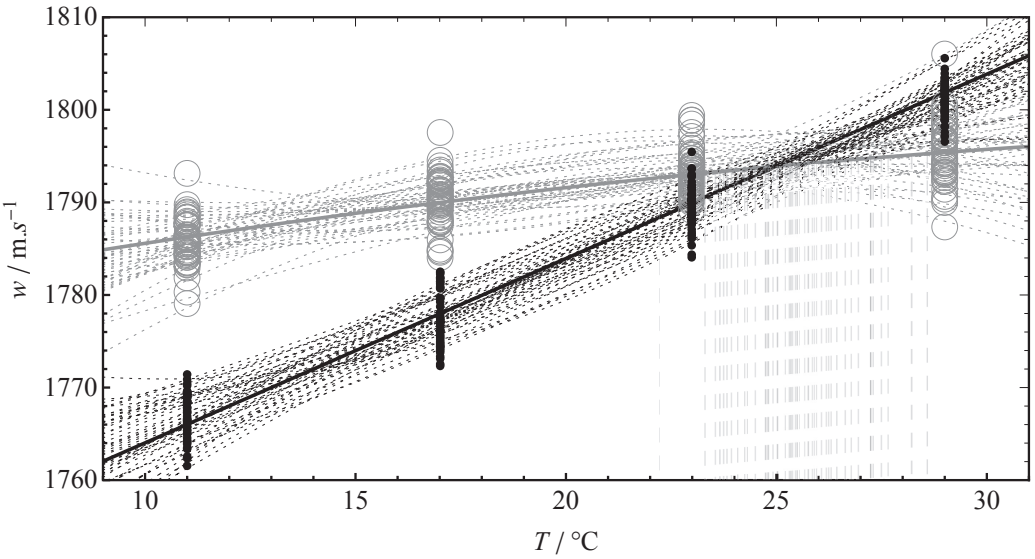

Figure 3.B.1: ***Example of T_x simulation.*** *In this case, we simulate the measurement of w^{mono} (black dots) and w^{LVE} (gray circles) on 50 FIs at 4 T_i and 4 T_j respectively, with an instrumental σ_w = 0.1%. T_f, 25 °C, is given by the intersection temperature between ${w^{mono}}_{theo}(T)$ and ${w^{LVE}}_{theo}(T)$ (solid black and gray lines, respectively). Parabolas are fitted to the w^{mono} and w^{LVE} data points (dotted black and gray lines, respectively). Each $w^{mono}(T)$-$w^{LVE}(T)$ pair intersects at a specific T_x (vertical dashed lines). Here, T_{range} = 18°C and T_{offset} = -5°C.*

What simulations teach us about the instrumental uncertainty In Figure 3.B.2, we show the results of a simulation that we ran to reproduce the Brillouin thermometry experiments on SyntHal24.6$_{19}$ FIs. We choose $\sigma_w = 0.145\%$ so that the T_x distribution obtained by the simulation presents a standard deviation comparable to our experimental T_x standard deviation, namely $\sigma_{T_x} = 1.9°C$ in the case of parabolas fitted to 3 $w^{LVE}(T_j)$ and 4 $w^{mono}(T_i)$. σ_w deduced from the simulations is higher than the usual 0.1% assumed in this work. A 0.1% σ_w shoud result in a $\sigma_{T_x} = 1.4°C$. The reason for this discrepancy is the machine stability. The reproducibility measurements shown in the previous chapter (Figure 2.6) imply that the correction for the machine drift brings an uncertainty inferior to 0.05%, which is negligible in the face of the short-term instrumental error 0.1%. However, the spectroscope might behave in a less stable way on some other days, drifting in a way that may be less easy to fit. Additionally, the drift might be accounted for with a lower quality when experiments are led on a short duration with fewer reference measurements done. For instance, SyntHal24.6$_{19}$ FIs from FI 1 to FI 25 were measured within one single day for which the reference measurements showed an easy fitted trend; these FIs T_x distribution show $\sigma_{T_x} = 1.7°C$. On the other hand, SyntHal24.6$_{19}$ FIs from FI 26 to FI 53 were measured on the course of several days, some of which were short days with a little amount of reference measurements and/or days with a reference trend uneasy to fit; these FIs T_x distribution show $\sigma_{T_x} = 2.1°C$. SyntHal33$_{16}$ FIs selected according to isolation and size, for which we didn't run simulations, have a T_x distribution with $\sigma_{T_x} = 1.7°C$. All in all, these variations in terms of σ_{T_x} show that our instrumental uncertainty σ_w lies between 0.1% and 0.15%.

Number of *w* measurements per FI and fit In addition to the constraints it brings on the uncertainties, the simulation provides us with valuable information on the statistical outputs we should expect in our experiments, depending on the number of data points measured per FI and on the way these data points are fitted. First, we notice that all of the 10 different combinations proposed in Figure 3.B.2 bring no bias as regards the estimation of T_f: $T_{x,mean}$ always approaches T_f within 0.02°C. We did not try to fit lines to the LVE data points, as it would make no sense, since we know the theoretical LVE is not linear. The result would be a systematic bias towards lower T_x. Second, the simulated T_x distribution tells us that we should expect a Gaussian distribution in our experiments. Third, we observe that i) fitting linear instead of parabolic isochores, ii) increasing the number of data points per FI and iii) fitting the theoretical trend to the LVE instead of a parabola, all lead to a narrower T_x distribution. In detail:

i) adjusting lines on the isochore data points instead of parabolas makes σ_{T_x} decrease by 0.1°C;

ii) measuring 4 $w^{mono}(T_i)$ and 4 $w^{LVE}(T_j)$ makes σ_{T_x} decrease by 0.3°C compared to 3+3 data points;

iii) fitting the theoretical equation to a 3 or 4 points LVE instead of a parabola makes σ_{T_x} decrease by 0.25-0.3°C.

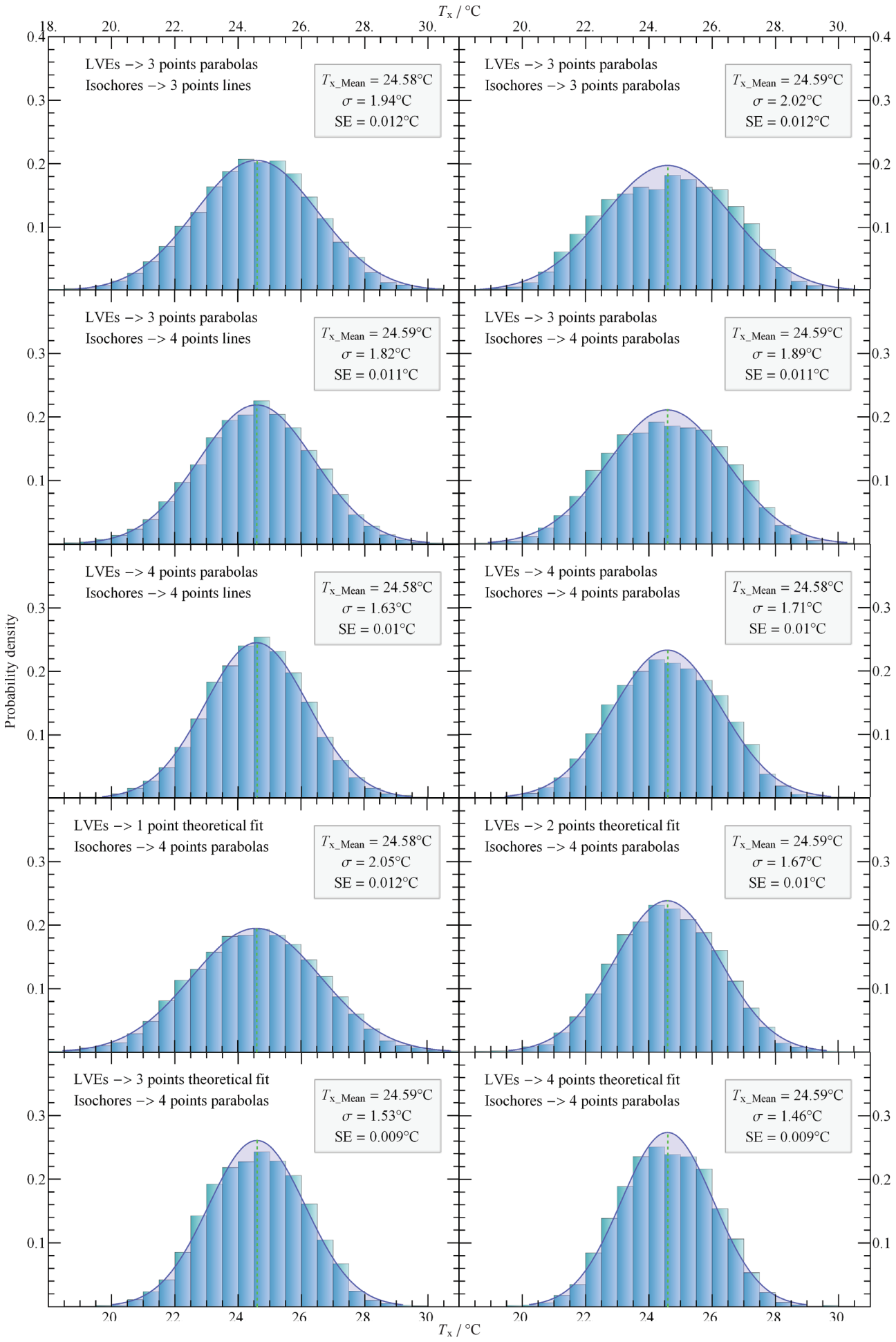

Figure 3.B.2: ***Test of the impact of various protocols on the T_x distribution through simulation..***

In Table 3.B.1, we summarize the statistics outputs for each of the 10 simulated combinations. Depending on σ_{T_x} obtained with the simulation, we calculated the number of FIs needed to reach a 0.5°C standard error on $T_{x,mean}$, and deduced the experimental time required. From the perspective of optimizing the ratio of precision of T_f estimation upon the experimental time, it comes out one would rather measure 4 $w^{LVE}(T_j)$ and 4 $w^{mono}(T_i)$ per FI, and fit a line to the $w^{mono}(T_i)$ data points (provided that the iso-T_h expected trend is linear). In the specific case when the theoretical $w^{LVE}(T)$ equation is known in advance, one can even better optimize through measuring 4 $w^{mono}(T_i)$, 3 $w^{LVE}(T_j)$ and adjust the theoretical equation to the latter.

LVE: *j*/fit - Isochore: *i*/fit	σ_{T_x}(°C)	**N**	**Experimental time (min)**
3/parabola - 3/line	1.94	17	510
3/parabola - 4/line	1.82	15	525
4/parabola - 4/line	1.63	12	480
3/parabola - 3/parabola	2.02	18	540
3/parabola - 4/parabola	1.89	16	560
4/parabola - 4/parabola	1.71	13	520
1/theoretica - 4/parabola	2.05	18	450
2/theoretica - 4/parabola	1.67	13	390
3/theoretica - 4/parabola	1.53	11	385
4/theoretica - 4/parabola	1.46	10	400

Table 3.B.1: ***Estimation of the time and number of FIs (N) required to reach a one sigma standard error on $T_{x,mean}$ of 0.5°C, depending on the number of data points per FI (i and j) and the fits used.*** *Here, we assume obtaining one w measurement takes 5 minutes. Calculations are based on a Student's t-distribution. Corresponding histograms for each case are shown in Figure 3.B.2.*

In this study however, we chose to fit parabolas to the isochores in order to comply with the curved trend of the FIs that were under reequilibration. For the sake of presenting results in the most generalizable case, we also decided not to fit the equation of $w^{LVE}_{theo}(T)$, albeit known in the simple case of a NaCl-H_2O saturated solution. The reader can find in Figure 3.B.3 a comparison of the T_x distributions yielded by our experiments on SyntHal24.6_{19} samples when various combinations are tested.

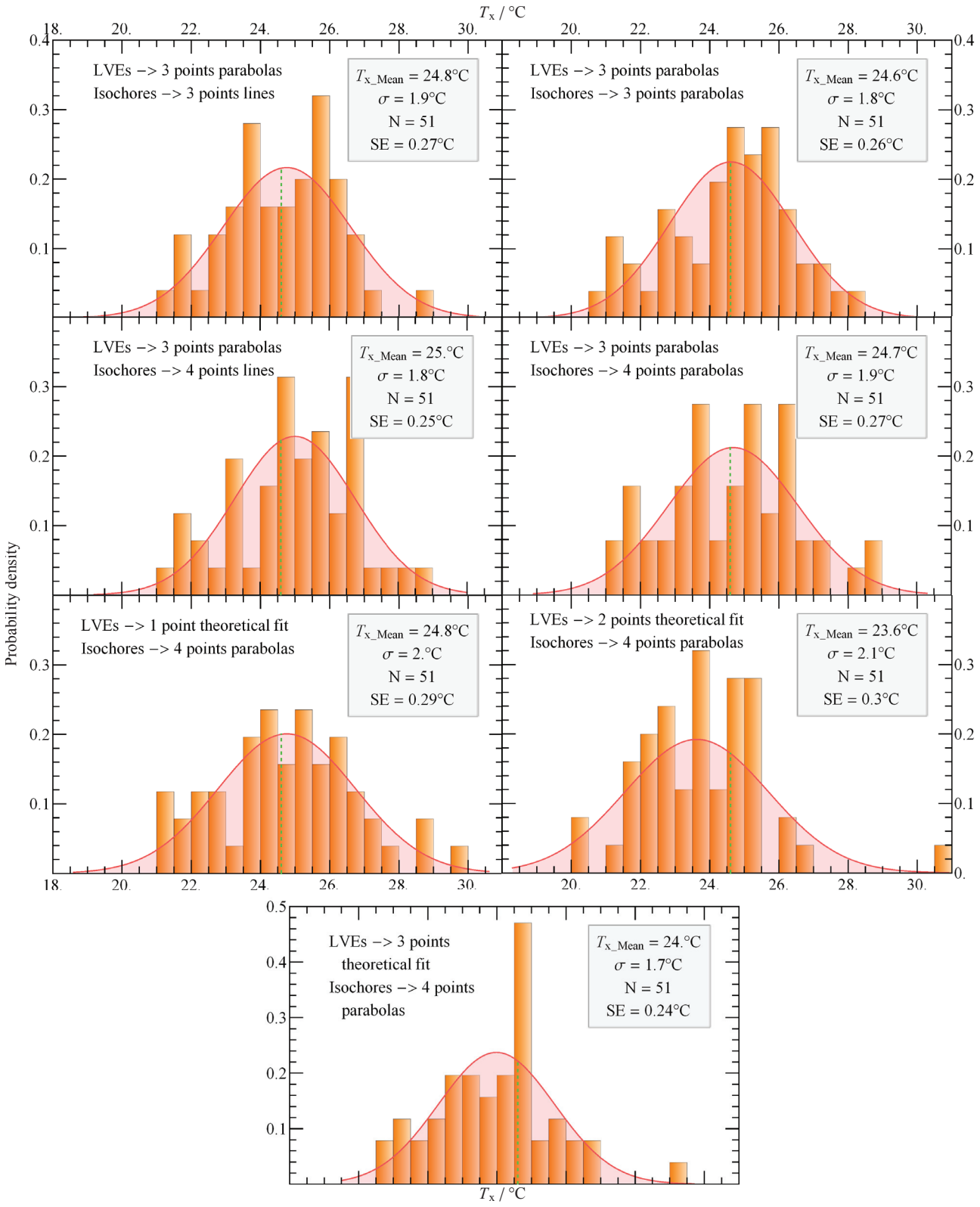

Figure 3.B.3: ***T_x histograms of SyntHal24.6$_{19}$ with various quantity of data points and methods of fit.*** *The green dashed line stands for T_f.*

T_{offset} and $T_{offset}^{Isochore}$ In Figure 3.B.4, we show the influence of T_{offset} on the T_x distribution. We observe that $T_{x,mean}$ remains very close to T_f and σ_{T_x} is small as long as the temperature range of measurements (here, T_{range} = 18°C) encompasses T_f. On the other hand, when T_f is on the limit (T_{offset} = -9 or 9°C) or out of the range

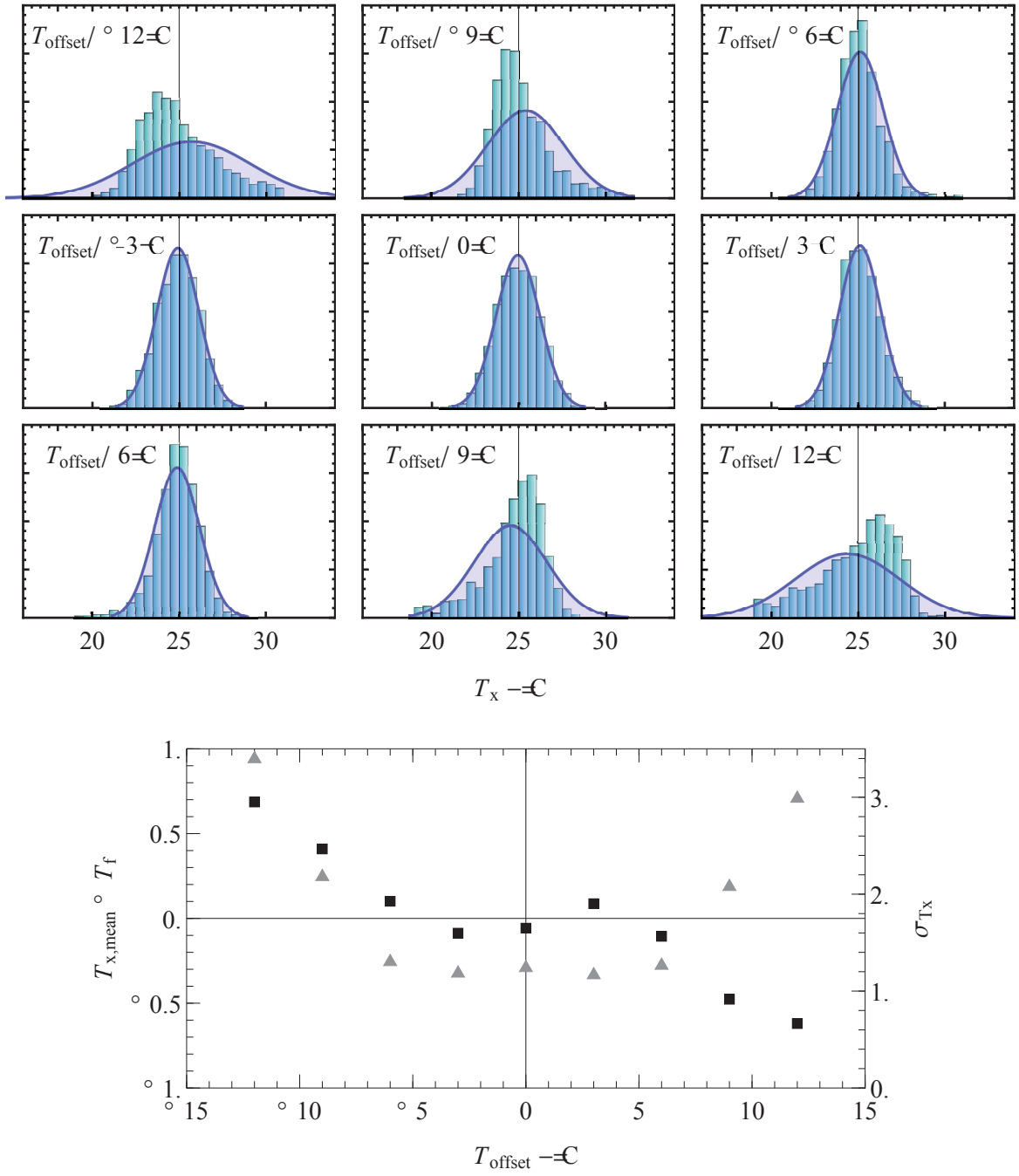

Figure 3.B.4: ***The infuence of T_{offset} on the T_x distribution.*** *$T_{x,mean}$ - T_f (black squares) and σ_{T_x} (gray triangles) are plotted as a function of T_{offset}. N = 2000, T_{range} = 18°C, T_f = 25°C. Protocol used: LVE 4/parabola and Isochore 4/parabola.*

of measurements (T_{offset} = -12 or 12°C), then $T_{x,mean}$ gets away from T_f and σ_{T_x} increases frankly. Also, as illustrated in Figure 3.B.5, it seems that applying different measurement temperatures to the isochores and the LVEs has no impact. Indeed, we observe that the influence of $T_{offset}^{Isochore}$ on the T_x distribution is very comparable to that of T_{offset}.

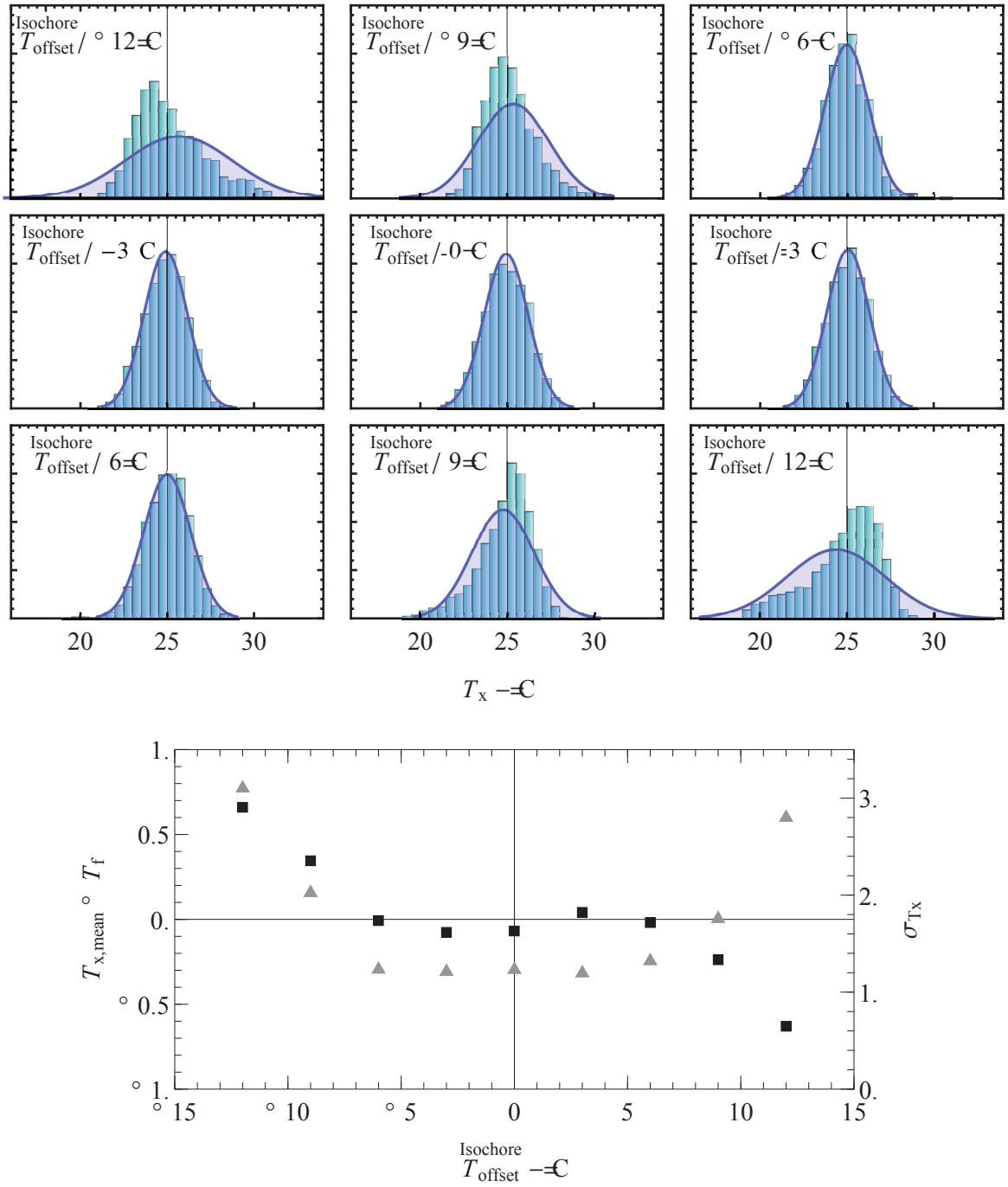

Figure 3.B.5: ***The infuence of $T_{offset}^{Isochore}$ on the T_x distribution.*** *$T_{x,mean}$ - T_f (black squares) and σ_{T_x} (gray triangles) are plotted as a function of T_{offset}. N = 2000, T_{range} = 18°C, T_f = 25°C. Protocol used: LVE 4/parabola and Isochore 4/parabola.*

T_{range} We observe in Figure 3.B.4 that T_{range} has no impact on $T_{x,mean}$ and σ_{T_x} if T_{offset} = 0°C. It remains true when T_{offset} is non-zero, provided T_f is encompassed in the temperature range of measurements. When this requirement is not fulfilled, then $T_{x,mean}$ isn't close to T_f anymore and σ_{T_x} increases, and this is all the more true as T_{range} is small.

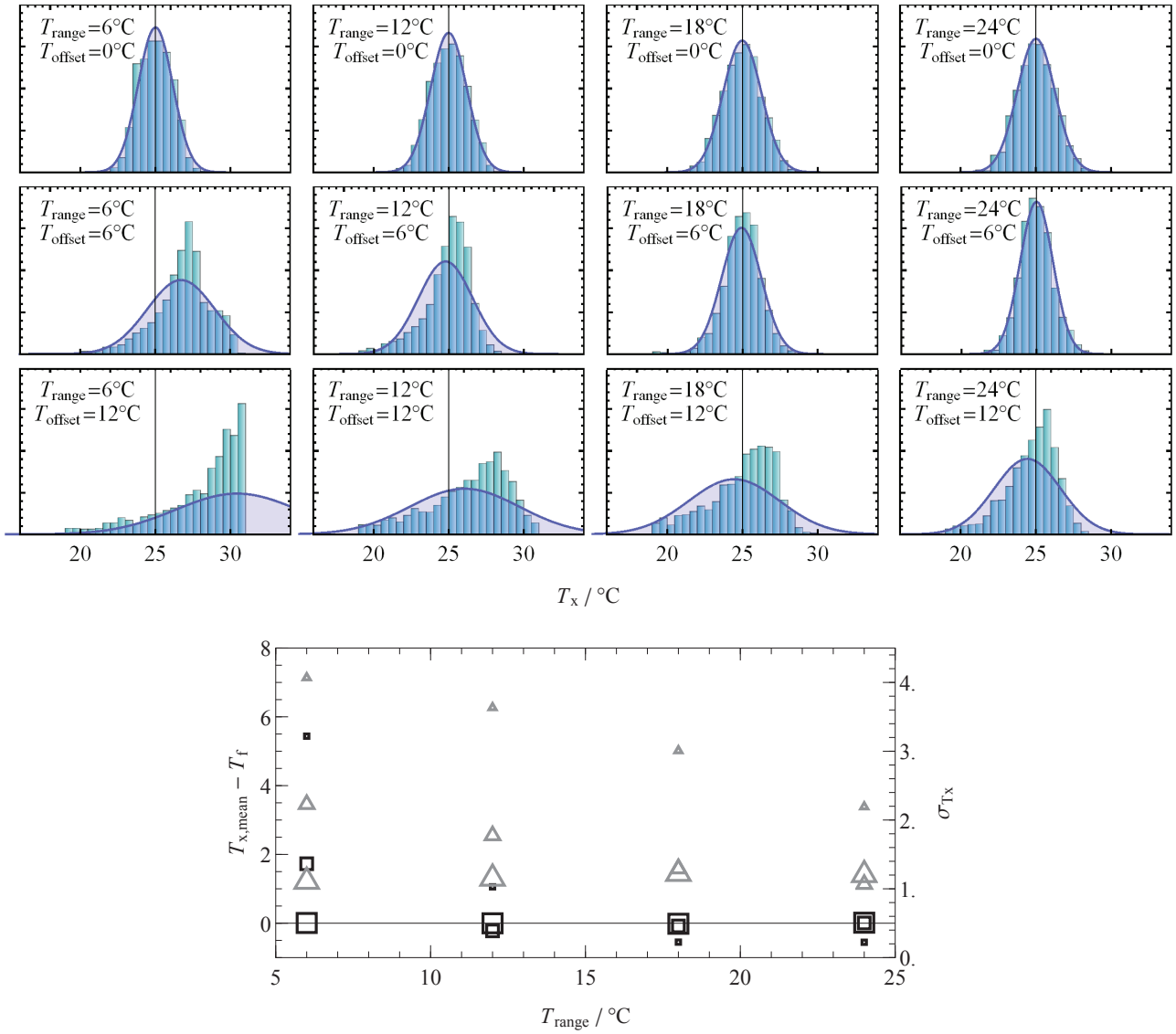

Figure 3.B.6: ***The influence of T_{range} on the T_x distribution.*** *$T_{x,mean}$ - T_f (black squares) and σ_{T_x} (gray triangles) are plotted as a function of T_{offset}. Large, medium and small symbols represent 0, 6 and 12°C T_{offset} respectively. N = 2000, T_f = 25°C. Protocol used: LVE 4/parabola and Isochore 4/parabola.*

Simulating Brillouin experiments shows that:

1. the instrumental uncertainty σ_{T_x} is sometimes higher than 0.1% and can reach 0.15%;
2. the most accurate, precise and fast method is to measure w^{mono} and w^{LVE} at 4 temperatures each;
3. fitting lines narrows the T_x distribution compared to parabolas and should therefore be preferred provided the theoretical trend is expected to be linear;
4. the optimal protocol is to fit the theoretical LVE and iso-T_h trends to the data, provided they are well constrained;
5. the measurement temperatures range, T_{range}, has little influence on the T_x distribution provided it is large enough to encompass T_f;
6. the measurement temperatures offset, T_{offset}, has little influence on the T_x distribution as long as T_f is encompassed in the measurement temperatures range.

3.C What σ_{T_x} tells us about T_f

We have seen that σ_{T_x} is typically in the range 1.5°C to 2°C in the case of NaCl-H_2O FIs. Basically, since we have shown $0.1\% < \sigma_w < 0.15\%$, provided one knows $w^{LVE}{}_{theo}(T)$ and $w^{mono}{}_{theo}(T)$ [2], one should be able to simulate σ_{T_x} for a specific sample. If the measured σ_{T_x} is significantly higher than the simulated σ_{T_x}, then it highlights a non-instrumental uncertainty. This can be the case when one measures a group of FIs that were not all trapped at the same temperature. In Figure 3.C.1, we show the results of a simulation in which we modelled two equal-size groups of FIs of respective entrapment temperature T_f1 and T_f2. They both have a T_x distribution that shows $\sigma_{T_x}1 = \sigma_{T_x}2 = 2°C$. We observe that the overall σ_{T_x} depends on the difference ΔT_f between T_f1 and T_f2. It is equal to $\sigma_{T_x}1 = \sigma_{T_x}2 = 2°C$ when ΔT_f is small, and increases with ΔT_f. For instance, we show that two groups of FIs trapped at temperatures different by 5°C would yield an overall $\sigma_{T_x} \simeq 3°C$. This statistical constraint can prove very useful when reconstructing paleo-environmental lake conditions, as the limnogeologist doesn't necessarily know at first the timing of halite precipitation and the amplitude of temperature changes in the paleo-waterbody.

3.D Correction of the Laplace pressure effect

FIs homogenize at a temperature lower than T_f, because of the pressure differential between the vapor and the liquid. This pressure differential, called Laplace pressure, is described by the Young-Laplace equation:

$$\Delta P = \frac{2\gamma}{r}, \tag{3.8}$$

where $\gamma$is the surface tension and r the bubble radius. This pressure difference implies that the bubble reaches a critical radius r_c under which it is not stable anymore. This critical radius writes as follows:

$$r_c = \frac{2\gamma}{(\frac{dP}{dT}_{iso} - \frac{dP}{dT}_{LVE})(T_{h,nom} - T_{h,obs})}, \tag{3.9}$$

where $\frac{dP}{dT}_{iso}$ is the fluid isochore slope, $\frac{dP}{dT}_{LVE}$ the liquid-vapor equilibrium curve slope, $T_{h,nom}$ represents the nominal homogenization temperature and $T_{h,obs}$ is the observed homogenization temperature. As to the bubble volume in function of temperature, it only depends on the FI volume and density of the fluid through the following equation:

$$V_{vap} = V_{FI} - \frac{V_{FI}.\rho_{liq}(T_{h,nom})}{\rho_{liq}(T)} \tag{3.10}$$

[2] These equations depend on the chemistry of the FIs. The current knowledge in the thermodynamics of highly saline multi-electrolyte brines doesn't allow us to calculate the speed of sound in brines as a function temperature, pressure and composition. However, these equations can be constrained empirically. Indeed, once the worker has measured a sufficient amount of w^{mono} and w^{LVE} in halite samples from a specific lake, he/she should be able to fit a parabolic or linear equation to both groups of data, and use these two equations to fit each individual LVE and iso-T_h.

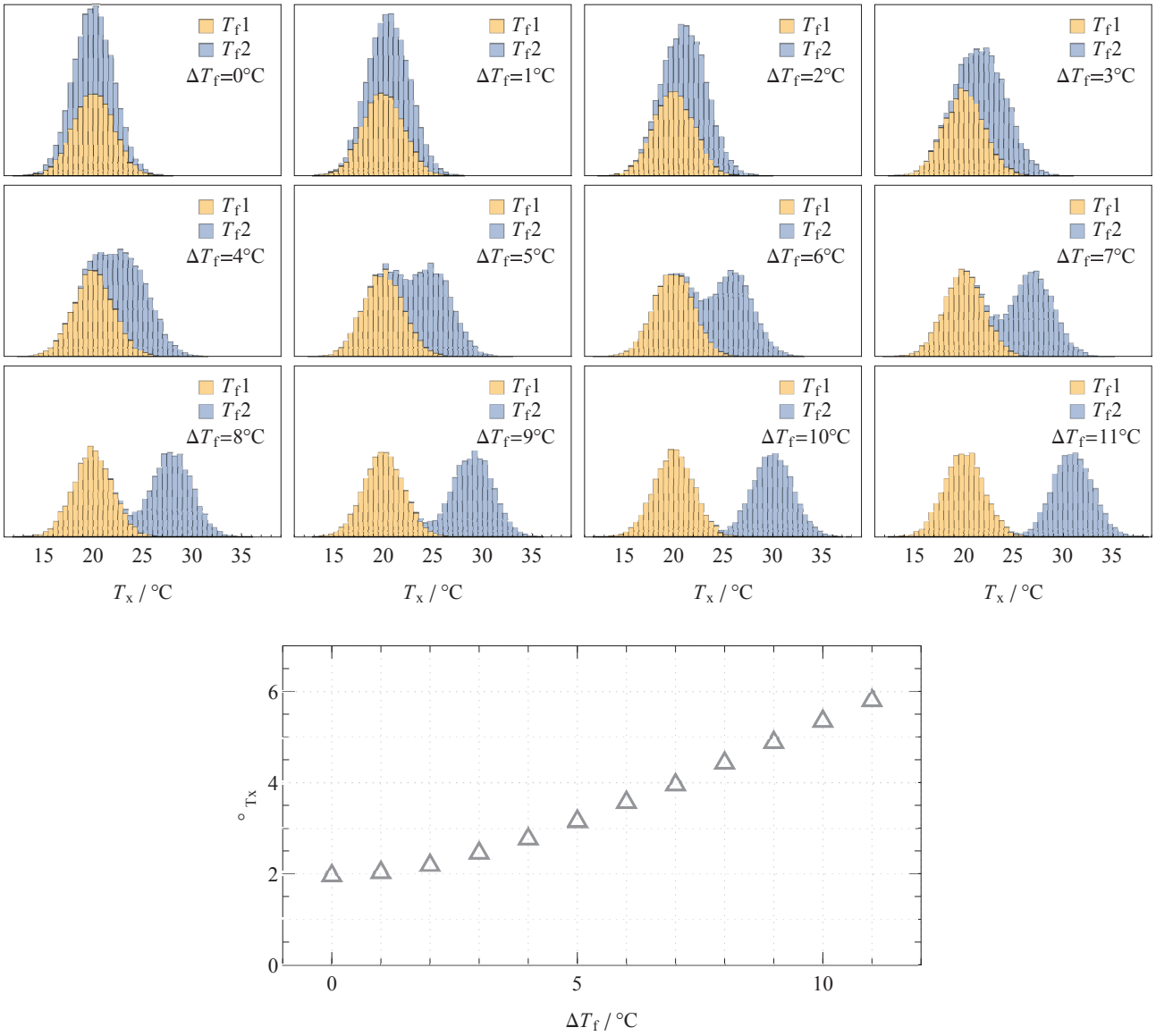

Figure 3.C.1: ***The consequence of mixing two groups of FIs on the overall distribution.*** *The group of FIs trapped at T_f1 = 20°C and the group of FIs trapped at T_f2 have $\sigma_{T_x1} = \sigma_{T_x2}$ = 2°C.*

where V_{vap} is the bubble volume, V_{FI} the FI volume and ρ_{liq} the density of a NaCl-H_2O fluid saturated with respect to NaCl. Then the bubble radius writes:

$$r_{vap} = \sqrt[3]{\frac{V_{vap}}{\frac{4}{3}\pi}} \tag{3.11}$$

Plotting r_c and r_{vap} as a function of temperature, one gets the temperature at which the bubble homogenizes, given by the intersection between the 2 curves. Here we give an example for NaCl-H_2O FIs saturated with respect to NaCl (Figure 3.D.1). For halite FIs with a complex composition, γ, $\frac{dP}{dT}_{iso}$ and $\frac{dP}{dT}_{LVE}$ are sometimes poorly constrained though. We refer the reader to Fall et al. (2009) and Marti et al. (2012) for a detailed explanation on T_h corrections, to Mao and Duan (2008), Zezin et al. (2014b) and Mao et al. (2017) for electrolytic solutions *P,V,T,x* properties, and to Weissenborn and Pugh (1996) and Pegram and Record (2007) for surface

tension experimental data of concentrated electrolytic solutions.

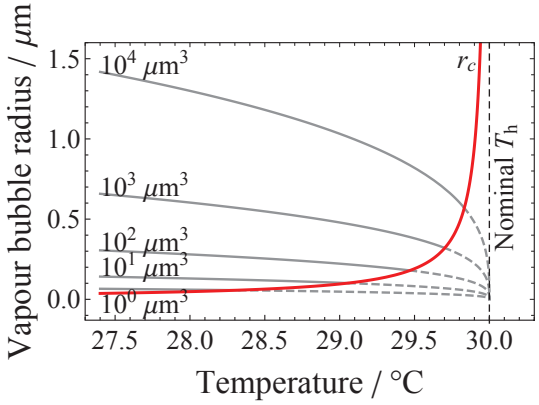

Figure 3.D.1: ***Bubble size and critical radius in halite FIs: how to correct for the Laplace pressure effect.*** *We show the relationship between the vapor bubble radius and temperature in NaCl-H_2O saturated fluid inclusions with volumes ranging from 1 to 10000 m^3 and having a nominal homogenization temperature of 30 °C. We also show the dependence of the critical radius on temperature. The intersections of the vapor bubble radius curves with the critical radius curve define the temperature of bubble collapse for the respective fluid inclusion volume.*

3.E Reproducibility runs in the literature

T_h reproducibility runs, that is, the re-measurement of FIs T_h after reiterated cooling nucleations, were performed by several authors. We collected the data provided by these studies and compared each time the mean T_h difference between the first run and the following ones. The results (Figure 3.E.1) show that T_hs always decrease from one run to another. Lowenstein et al. (1998) already noticed this behavior and recommended using the T_hs from the first run only. Yet still, nothing proves the first run is free from reequilibration. Quite the opposite, it is very likely that the first cooling nucleation leads to the strongest T_h decrease. Indeed, plastically deformed materials tend to strengthen through a mechanism called "strain hardening" (Taylor, 1934). As a material deforms plastically, its dislocations density dramatically increases; dislocations then get closer to each other and progressively impede the motion of one another. This higher dislocation density remains after unloading, resulting in the increase of the material yield stress. In the case of a halite FI, it implies that the plastic shrinkage strengthens the walls during a first cooling nucleation, leading to a lighter shrinkage during the next runs. It shows in repeated runs (Figure 3.E.1): the decrease in T_hs gets progressively smaller. Conversely, a good reproducibility of T_hs suggests that FIs have not reequilibrated from the first run: T_hs in Benison and Goldstein (1999) were all reproducible within 1 °C.

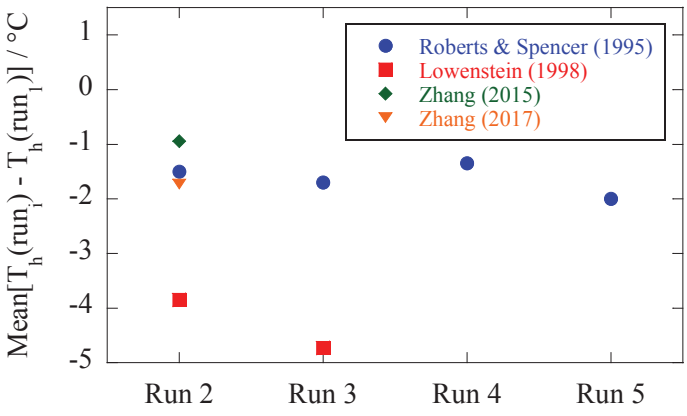

Figure 3.E.1: ***The impact of reproducibility runs on T_h.*** *Data from Roberts and Spencer (1995); Lowenstein et al. (1998); Zhang et al. (2015, 2017).*

CHAPTER 4

The Pressure inside Halite Fluid Inclusions: A Model to Predict Damages

ABSTRACT In the previous chapter, we have demonstrated the ability of Brillouin spectroscopy in restoring the potential of halite fluid inclusions (FIs) as temperature archives. Furthermore, using Brillouin spectroscopy as a mechanical sensor and comparing with data from the literature, we were able to establish an empirical equation that links the pressure FIs can sustain depending on their size. Knowing the pressure to temperature (*P*-*T*) dependence in the fluid inclusion, we can then determine the upper size limit for reliable thermometry measurements on FIs depending on the extrema temperatures (ΔT_{lim}) they have gone through. To make the calculation of this limit possible for a wide range of FI compositions, we have developed a model that applies to the Na-K-Mg-Ca-H_2O system, which we present in this chapter. The model, based on the Pitzer formalism and the Young mixing rule, calculates the density of multi-electrolyte brines as a function of temperature, pressure and salinity. Through predicting the volumetric and chemical responses of the fluid to a temperature change, along with the mechanical and chemical responses of the host crystal, the model then backcalculates the FI internal pressure. At the end of the chapter, we propose a selection of abaci that allow for the determination of FI size limit as a function of the entrapment temperature (T_{f}) and ΔT_{lim} for several FI compositions. In the future, extending the model to SO_4 and (H)CO_3 will allow the determination of pressure, and thus FI size limit, for all major types of FI compositions.

As highlighted in the previous chapter, knowing the pressure in FIs is of paramount importance to constrain the maximum temperature excursion ΔT_{lim} fluid inclusions can sustain as a function of their size. Estimating the size limit of undamaged FIs should be a preliminary step before performing thermometry measurements. And yet, to our knowledge, no study has proposed a way to address this issue so far. Although some rough estimations were led based on the knowledge on NaCl-H_2O physical properties (Roedder and Belkin, 1979), we have heard of no study that has looked at the interactions between fluid and halite host. Even more importantly, no study has ever addressed the dependence of pressure on the composition of FIs. And yet, the latter is extremely variable. Saline lakes that precipitate halite usually contain other major ionic components in addition to sodium and chlorine. Seawater derived saline lakes bear a fairly high amount of Mg^{2+} and SO_4^{2-} (McCaffrey et al., 1987). In continental settings, the hypersaline lakes composition is contingent to the rainwater, riverine, groundwater and hydrothermal inflows composition. In turn, the solutes content of these inflows is controlled by the bedrock mineralogy and the weatherability of each available mineral. We invite the reader to refer to the very scholarly compendiums on this matter by Eugster and Hardie (1978) and Hardie (1984), along with some works focused on brines compositions related to particular settings such as hydrothermal (Lowenstein et al., 1989; Hardie, 1990; Lowenstein and Risacher, 2009), diagenetic (Katz and Starinsky, 2009) or volcanic (Risacher and Fritz, 1991). Overall, the major elements found in saline lakes are Na-K-Mg-Ca-Cl-SO_4-(HCO_3+CO_3), with tremendous variations in each of these elements content from one lake to another; some examples that illustrate this diversity are given in Table 4.1.

In order to be able to predict the *P-T* behavior of natural brines trapped in halite, we need a complete model that takes into account the thermodynamic, mechanical and composition aspects. In this chapter we propose such a model, which applies to Na-K-Mg-Ca-H_2O compositions and takes into account FIs shape. Furthermore, we establish some rules of thumb that allow for the qualitative estimation of *P-T* trends for other chemistries. At the end of this section we provide abaci allowing for the determination of ΔT_{lim} as a function of FI size and T_{h} for some specific compositions.

4.1 Description of the model

4.1.1 Volumetric properties of hypersaline brines: a short review

Most fluids trapped inside metamorphic minerals are aqueous-electrolyte brines, essentially composed of water and Na, Ca or K chlorides. The homogenization temperature of biphasic fluids in such minerals is a lower bound for the entrapment temperature T_{f}. Knowing the entrapment pressure and the equation of the line of constant liquid-vapor homogenization temperature (iso-T_{h}, approximately equivalent to the "iso-density" or "isochore"; details on this terminology are given further) for the specific brine chemistry, one can determine the entrapment temperature T_{f}, namely the temperature of fluids circulation. As this piece of information is paramount in all fields related to metamorphic and economic geology, many studies have been carried to determine Pressure-Temperature-Volume-Composition (*PVTx*) properties of saline FIs. Before the 1960s, essentially all gas-free

Hypersaline lake, Location - *Inflow water type*[1]	**Na**	**K**	**Mg**	**Ca**	**Cl**	**SO_4**	**(H)CO_3**
[2]**Dead Sea**, Palestine - *Mixed D & S*	1.35	0.21	2.19	0.52	7.23	< 0.01	< 0.01
[3]**Bristol Dry Lake**, California - *D or H*	3.46	0.12	0.06	1.50	6.77	< 0.01	-
[4]**XiaoQaidam**, NE Tibet - *H*	5.43	0.04	0.19	0.01	4.39	0.81	-
[5]**Magadi**, Kenya - *M*	6.60	0.06	-	-	2.68	0.03	1.97
[6]**Salar Cachi Laguna**, Bolivia - *V*	4	0.91	< 0.01	< 0.01	1.61	0.37	2.5
[7]**Holocene Searles**, California - *V*	6.47	1.06	< 0.05	-	5.28	0.62	1.02
[8]**Assal**, Djibouti - *S*	4.03	0.12	0.46	0.06	5.23	0.05	-
[9]**Seawater at halite saturation** - *S*	5.00	0.11	0.58	< 0.01	5.67	0.21	-

Table 4.1: ***The diversity of hypersaline lakes compositions: some examples.***
All compositions in molal, apart from [3] in molar.
[1]Genetics of lake composition as defined by Hardie (1984). S: Seawater; D: Diagenetic; H: Hydrothermal; V: Volcanogenic; M: Meteoric.
[2]Average of major element compositions measured in the bottom layer (07/2015) by Sirota et al. (2016); SO_4 and (H)CO_3 from Klein-BenDavid et al. (2004).
[3]Hardie (1990).
[4]Vengosh et al. (1995).
[5]Average brine composition, Jones et al. (1977).
[6]Risacher and Fritz (1991).
[7]Fluid Inclusions Cryo-SEM data from the Upper Salt Unit, Early Holocene (Lowenstein et al., 2016).
[8]Sanjuan et al. (1990).
[9]Composition of seawater (sampled at Great Inagua Island, Bahamas) at evaporation degree 10.5, when reaching precipitation of the first halite crystal (McCaffrey et al., 1987).

aqueous inclusions were interpreted using *PVT* data for pure water (Kennedy, 1950; Kalyuzhnyy, 1960; Skinner, 1953), because of the lack of methods to get the FIs composition and the quasi inexistence of data on the *PVTx* properties of saline solutions. The 1960s saw the introduction of the first accurate cooling stage for measuring ice-melting temperatures of aqueous inclusions (Roedder, 1962b) along with the first application to interpret these data in terms of FIs salinity and composition (Roedder, 1963). It was also the time when Sourirajan and Kennedy (1962) published their classic paper on the *PTx* properties of the NaCl-H_2O system at elevated conditions of pressure and temperature. In 1975, Potter and Brown (1975) published a summary of *PVTx* data that allowed workers to estimate iso-density curves in the NaCl-H_2O system, and several works then extended the *P-T-x* range over which iso-T_h lines could be calculated, based on the measurement of T_h in NaCl-H_2O FIs synthetized inside quartz at known pressure and temperature conditions P_f and T_f, respectively (Knight and Bodnar, 1989; Bodnar, 1994; Bodnar and Vityk, 1994). Indeed, through fitting a straight line to a $\{T_h, P_h\}$ and $\{T_f, P_f\}$ pair of data points, the experimenter gets a valid approximation of the iso-T_h curve for a specific FI composition and T_h (Sterner and Bodnar, 1984; Bodnar and Sterner, 1985). The numerous linear iso-T_h obtained for different T_h and salinities gave rise to the possibility of fitting all the data to get an empirical polynomial equation suitable for the determination of the isochore over a very wide range of T_h and

salinities (50-700 °C and 0-40 NaCl mass%; Bodnar and Vityk 1994). The *PVTx* properties of other binary systems were also investigated with the same quartz synthetic FIs technique, and empirical fits were provided for the quaternary system NaCl-KCl-$CaCl_2$-H_2O (Zhang and Frantz, 1987). All these empirical fits offer the advantage of supplying isochore equations on a wide range of temperatures, pressures and salinities (typically up to 700 °C, 600 MPa and 40% solute mass fraction), hence their suitability for the study of saline brines trapped in geological conditions. These empirical fits, however, are based on a first-order approximation, that is, pressure is linearly dependent on temperature, hence the linear fits for isochores determination. This assumption is correct at high temperatures and at very elevated pressures of several kilobars (i.e. several hundreds of MPa); in the case of a halite FI though, which was trapped at surface temperature and undergoes much more moderate internal pressures, this assumption fails. In Figure 4.1, we show that the deviation from linearity is very strong at low temperatures. For instance, through comparing the isochores of pure water at 25 °C and ambient pressure obtained with the IAPWS-95 formulation (Wagner and PruSS, 2002)[1] to the isochores obtained with the empirical fit from Bodnar and Vityk (1994), we calculate that the latter yields $\frac{\mathrm{d}P}{\mathrm{d}T}$ 3.3 times steeper than the former. Similarly, for a salinity of 25% NaCl mass fraction at 25 °C, when comparing $\frac{\mathrm{d}P}{\mathrm{d}T}$ yielded by the empirical density EoS of Al Ghafri et al. (2012)[2] to Bodnar and Vityk's (1994) $\frac{\mathrm{d}P}{\mathrm{d}T}$, we calculate that the latter overestimates the slope by a factor almost 2 compared to the former. This non-linearity of the volumetric properties of aqueous solutions at Earth's surface conditions makes impossible the direct application of the empirical equations derived from the synthetic quartz inclusion technique to our goal of calculating the pressure inside halite FIs.

This led us to consider the use of the upstream *PVTx* variable from which the isochore is derived, namely density. Indeed, the definition of an isodensity is:

$$\left(\frac{\partial P}{\partial T}\right)_{\rho} = \frac{\alpha_{\mathrm{v}}}{\beta_{\mathrm{T}}} \tag{4.1}$$

with

$$\alpha_{\mathrm{v}} = -\frac{1}{\rho}\left(\frac{\partial \rho}{\partial T}\right)_{P} \tag{4.2}$$

and

$$\beta_{\mathrm{T}} = \frac{1}{\rho}\left(\frac{\partial \rho}{\partial P}\right)_{T}. \tag{4.3}$$

α_{v} ($°C^{-1}$) is the isobaric thermal expansion coefficient, β_{T} (MPa^{-1}) the isothermal compressibility and ρ ($kg.m^{-3}$) the density of the brine. Equations (4.1) to (4.3) show that knowledge of $\rho(T, P)$ is sufficient to obtain the isodensity. Two main options for obtaining $\rho(T, P)$ are available: i) purely empirical fits of density datasets, usually provided by experimenters along with their measurements data, and ii) semi-empirical models based on physically founded fits of volumetric properties datasets. As regards the first option, proposed equations rarely

[1] The International Association for the Properties of Water and Steam (IAPWS) provides, through its 1995 formulation, the international standard EoS for water's thermodynamic properties.

[2] The fit of Al Ghafri et al. (2012) provides an EoS with an accuracy better than 0.1% over the range 25-200 °C, 0-68 MPa and up to saturation molality.

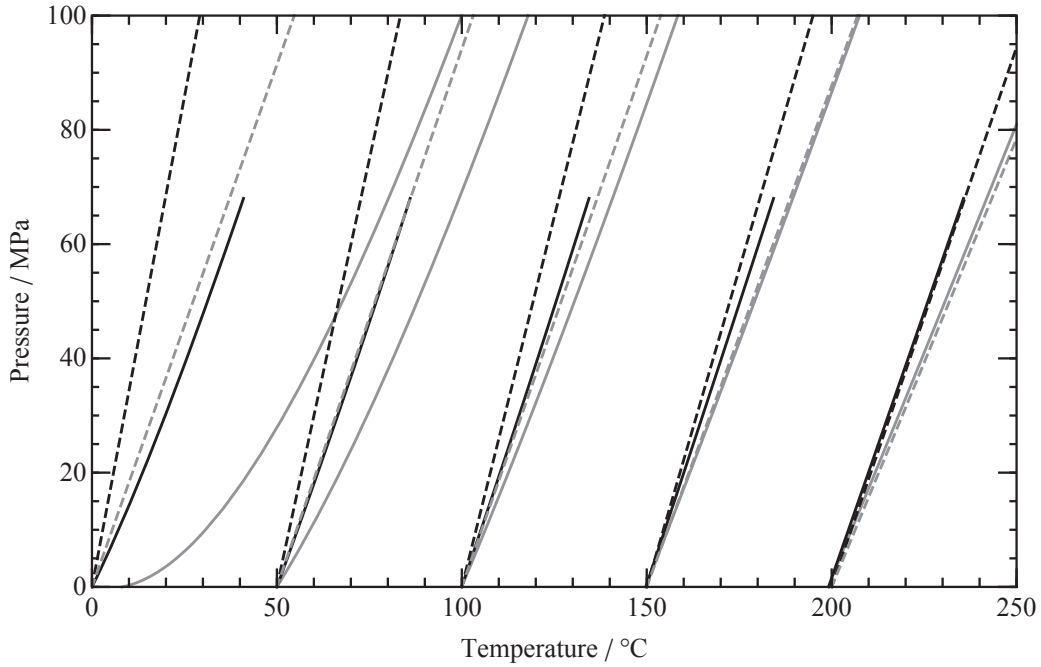

Figure 4.1: ***The inaccurate prediction of isochores by the quartz synthetic FI method at low P-T conditions.*** *Isochores for pure water (gray lines) and an aqueous binary solution with 25% mass fraction of NaCl (black lines) are plotted for different T_h (0, 50, 100, 150 and 200 °C). The isochores calculated with the equation provided by Bodnar and Vityk (1994; dashed lines) are compared with those obtained with the very well constrained density equations (solid lines) of the IAPWS-95 formulation for pure water (Wagner and Pruss, 2002) and of the empirical fit for the NaCl-H_2O system of Al Ghafri et al. (2012). The mismatch of the isochores at low temperature is obvious, and progressively disappears towards higher temperatures.*

span over a sufficiently wide pressure-temperature-molality (*PTm*) range, and fits are completely subjected to the accuracy of the single dataset. As to the second option, most of the predictive semi-empirical models are ion-interaction based, and tend to constrain the second and the third virial coefficients of the virial expansion EoS. The most famous and reputedly most accurate in characterizing concentrated brines is the Pitzer ion-interaction model (Pitzer, 1973, 1991), which has been developing and extending to an ever wider range of temperatures, pressures and compositions over the past 45 years. This model proposes equations for several properties of brines that stem from the differentiation of the excess Gibbs energy, such as the apparent molar heat capacity, the osmotic coefficient, the activity coefficient and, of utmost interest to us, the apparent molar volume V_{ϕ_j} ($cm^3.mol^{-1}$). The latter accounts for the change in volume of the brine when adding one mole of the solute j. It is related to density through:

$$V_{\phi_j} = \frac{1000(\rho_0 - \rho)}{m_j.\rho_0.\rho} + \frac{m_j.M_j}{m_j.\rho}, \tag{4.4}$$

with ρ_0 and ρ the density of pure water and of the brine respectively, m_j the molality of salt j in the solution,

and M_j the molar mass of j. V_{ϕ_j} is determined as follows in the Pitzer formalism:

$$V_{\phi_j} = \frac{V(m_{\mathrm{r}})}{m_{\mathrm{r}}} - \frac{v_{\mathrm{w}}}{m_{\mathrm{r}}} + (\nu_{\mathrm{ca}} + \nu_{\mathrm{an}})|z_{\mathrm{ca}} z_{\mathrm{an}}| \frac{A_V}{2.4} ln\Big[\frac{1 + 1.2I^{\frac{1}{2}}}{1 + 1.2I_{\mathrm{r}}{}^{\frac{1}{2}}}\Big] + 2\nu_{\mathrm{ca}}\nu_{\mathrm{an}} RT\Big\{m_j B_j^{\mathrm{V}}(m_j) - m_{\mathrm{r}} B_j^{\mathrm{V}}(m_{\mathrm{r}}) + \nu_{\mathrm{ca}} z_{\mathrm{ca}}\big(m_j^2 C_j^{\mathrm{V}}(m_j) - m_{\mathrm{r}}{}^2 C_j^{\mathrm{V}}(m_{\mathrm{r}})\big)\Big\}, \tag{4.5}$$

where ν_{ca} and ν_{an} are the stoichiometric numbers of cations and anions formed upon dissociation of the salt j, respectively, z_{ca} and z_{an} are the charges of the cation and anion, respectively, A_{V} is the Debye-Hückel limiting law coefficient for the apparent molar volume, v_{w} is the volume of 1 kg of water, I is the ionic strength, subscript r stands for a chosen reference solution concentration, and $V(m_{\mathrm{r}})$, B_j^{V} and C_j^{V} are pressure and temperature dependent adjustable parameters - the latter two being also molality dependent. These last three terms are generally obtained through fitting the published volumetric data of the chosen binary system. Therefore, the range of applicability and the accuracy of the Pitzer volumetric EoS for each binary system are dependent on the ranges and on the quantity of measurements available in the literature, respectively. As a matter of fact, as stated by Rowland et al. (2015), the fidelity of Pitzer fits is weighed against a high sensitivity to datasets gaps. For NaCl-H_2O, a parameterization for a wide *PT* range (0-300 °C, 0-100 MPa) and up to solubility molality was provided as soon as the 1980's with the EoS of S. Z. Rogers and S. Pitzer (1982), and extended and refined by Archer (1992). The latter is considered, still today, one of the must robust EoS applying to a concentrated binary system (Zezin and Driesner, 2017). As for other binary systems however, datasets have long remained scant. The recent advent of density measurements of other chloride salts on a large *PTm* range (e.g. Al Ghafri et al. 2012; Zezin et al. 2014a) made possible the Pitzer fit of the other major salt systems MgCl2, CaCl2 (Rowland and May, 2013), and KCl (Zezin and Driesner, 2017). As a result, EoS matching the three requirements for halite FIs pressure calculations, namely i) low temperature (~0 to 60 °C), ii) extremely high molalities and iii) pressures spanning over a range of several tens of MPa, have only become available in the last few years. In this work, we use the Pitzer EoS of Archer (1992) for NaCl-H_2O, Zezin and Driesner (2017) for KCl-H_2O and Rowland and May (2013) for MgCl2-H_2O and CaCl2-H_2O. They all span at least over the ranges 0-300 °C, 0.1-100 MPa and up to solubility molality. Comparisons with the empirical values of Al Ghafri et al. (2012) are found in Figure 4.A.1.

Saline lakes that precipitate halite usually contain other major ionic components. Overall, the major elements found in saline lakes are Na-K-Mg-Ca-Cl-SO_4-(H)CO_3, with tremendous variations of each of these elements content from one lake to another (see some examples in Table 4.1). Therefore, in order to be able to predict the *P-T* behavior of natural brines trapped in halite, we need to model the *PVTx* properties of multi-component solutions. The Pitzer formalism proposes a method for the calculation of volumetric properties of such brines (Krumgalz et al., 1995), making use of the B_j^{V} and C_j^{V} parameters characteristic of each salt j inside a more generalized variant of Equation (4.5). This type of Pitzer equation for multi-component brines can also comprise additional parameters $\Theta_{\mathrm{ca,ca}}$, $\Theta_{\mathrm{an,an}}$, $\Psi_{\mathrm{ca,ca,an}}$ and $\Psi_{\mathrm{an,an,ca}}$, which are the mixing terms arising due to possible interactions between any two like charged ions and between two like charged ions with an ion of

opposite charge. However, the use of such a highly detailed equation faces several obstacles. First, most available mixing terms Θ and Ψ were obtained at ambient pressure and 25 °C (Connaughton et al., 1989; Krumgalz et al., 1995), and therefore lack a trustworthy pressure and temperature dependence. Secondly, when tested by workers (Monnin, 1989), Θ and Ψ sometimes decreased the accuracy of density determination. Thirdly, all the single-solute parameters B_j^{V} and C_j^{V} used in the mixing equation have to have been obtained with the same fitting method for self-consistency (Monnin, 1989; Krumgalz et al., 2000; Rowland et al., 2015); in our case, parameters for binary systems come from different studies made by different authors, and therefore do not match this requirement. In the light of these limitations, we choose to model the *P-T-m* dependent volumetric properties of multi-component brines by using a simpler approach. Young and Smith (1954) propose a mere mixing rule to predict the mean apparent molar volume ${V^{\phi}}_{\mathrm{mean}}$ of multi-component aqueous electrolyte solutions, which writes:

$$ {V^{\phi}}_{\mathrm{mean}} = \sum_j \frac{m_j V_{\phi_j}}{\sum_j m_j}, \tag{4.6} $$

with $V_{\phi j}$ the apparent molar volume of binary aqueous electrolyte solution at the same ionic strength of total solution, determined with the Pitzer EoS for binary systems. If the molar volume is in $\mathrm{cm^3.mol^{-1}}$, we then express the density ρ of the multi-electrolyte aqueous solution as follows:

$$ \rho = \rho_{\mathrm{H2O}} \frac{1000 + \sum_j m_j \sum_j M_j m_j}{1000 + 10^{-3} \rho_{\mathrm{H2O}} {V^{\phi}}_{\mathrm{mean}} \sum_j m_j}, \tag{4.7} $$

with ρ and the density of pure water ρ_{H2O} in $\mathrm{kg.m^{-3}}$. Uncertainties that arise with this model are detailed in Section 4.3 and illustrated in Figures 4.A.2 and 4.A.3.

4.1.2 An iterative procedure accounting for brine and host behaviors

Knowing the *PVTx* properties of the aqueous solution is a prerequisite to calculate the pressure inside the FI. The brine volumetric EoSs are sufficient to calculate the iso-density *P-T* path of the FI. However, despite the many misuses of language, an iso-T_{h} is not exactly an iso-density nor an isochore. When the temperature decreases (increases), the pressure decreases (increases), both parameters leading to the thermal contraction (expansion) of the host and elastic shrinkage (expansion), respectively. These thermo-mechanical responses of a cavity wall are often mentioned in the literature (see for instance Landau et al. 1986; Zimmerman 1990; Pallares et al. 2016). Additionally, two other phenomena, negligible in most host crystals and therefore rarely addressed in the literature, cannot be neglected when it comes to halite: the temperature and pressure dependence of solubility $\frac{\mathrm{d}m_{\mathrm{sat}}}{\mathrm{d}T}$ and $\frac{\mathrm{d}m_{\mathrm{sat}}}{\mathrm{d}P}$, which induce FI volume changes $s_{\mathrm{V_T}}$ and $s_{\mathrm{V_P}}$, respectively. All these parameters, illustrated in Figure 4.2, are to be taken into account for an accurate pressure reconstruction model. We use the EoS for halite density (ρ_{NaCl}) given by Driesner (2007) to determine the thermal expansion coefficient of halite as a function of T.[3] To account for the elasticity of halite, we use the method of Zimmerman (1990) and treat the inclusion

[3] At 20 °C, the value is α_{V} = 1.15 10^{-4} $\mathrm{K^{-1}}$, and it varies by 5% from -20 to 40 °C.

as an ellipsoidal pore inside an infinite, isotropic medium. We choose a Poisson ratio $\nu = 0.203$ adapted for a force normal to the (100) plane of a NaCl crystal (calculated from Turley and Sines 1971) and the elastic stiffness coefficient C_{44} = 12.7 GPa (Hashin and Shtrikman, 1962) as the shear modulus G.[4] For an inclusion trapped at pressure-temperature conditions $\{T_f,\ P_f = 0\}$, the density $\rho(T, P)$ of the liquid at temperature T exerting a pressure $P < 0$ on the halite walls writes (Landau et al., 1986):

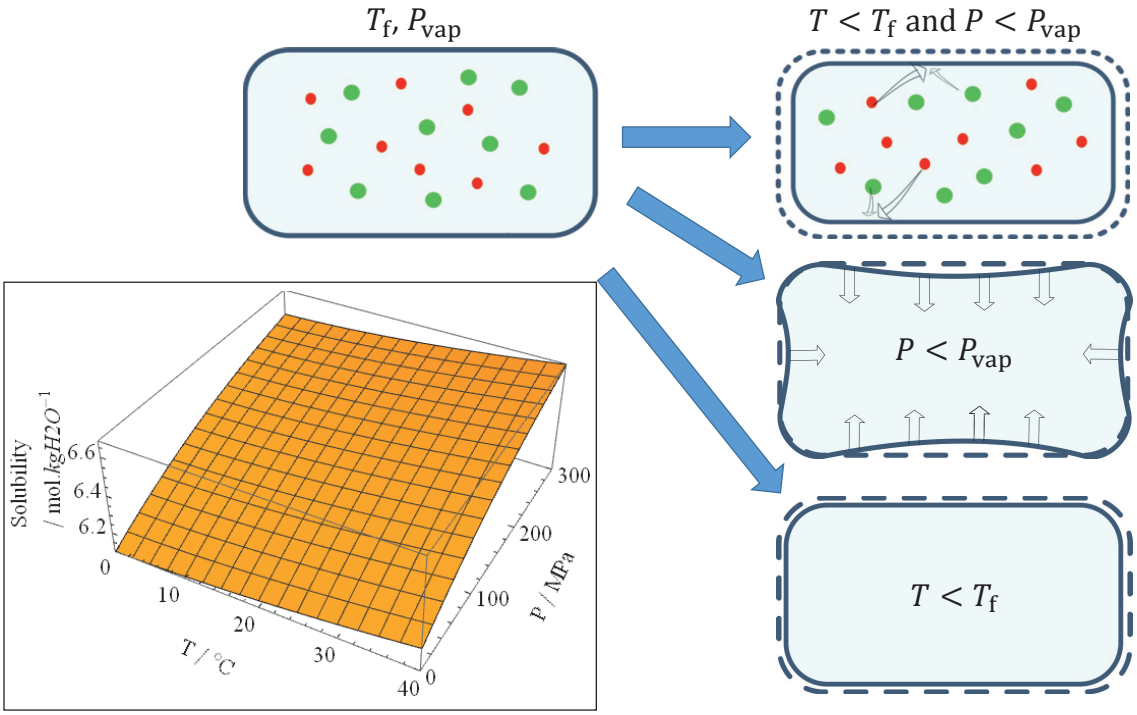

Figure 4.2: ***The three phenomena that deviate the halite FI from the isochore when moving away from T_h.*** *Halite is a compressible, thermally expandable and soluble crystal. When T decreases along with P, the FI host thermally contracts (bottom right FI), shrinks because of the FI centripetal stress (center right FI), and builds up with aggregating excess solutes (top right FI). Inset shows the solubility of NaCl in water as a function of T and P as measured by Sawamura et al. (2007). Note that a halite FI trapped at ambient conditions has a pressure P_{vap} (vapor pressure), that is, almost zero.*

$$\rho(T, P) = \rho(T_f, 0)[1 + \alpha_V(T - T_f) + C_{pp}P]^{-1} \tag{4.8}$$

C_{pp} is the pore compressibility (MPa^{-1}) and depends on the aspect ratio (AR) of the cavity, which we simplify as a spheroid (i.e. an ellipsoid with two equal semi-diameters $r_b = r_c$ and a third one, r_a, that is different; in such geometry, $AR = r_a/r_b$). When the spheroid has a prolate "rugby ball" shape ($AR > 1$), C_{pp} writes (Zimmerman, 1990):

$$C_{pp}(AR) = \frac{1 - 0.25 \exp \frac{1-AR}{3}}{G}, \tag{4.9}$$

[4]The choice of C_{44} as the shear modulus is the most adequate choice for a cubic system with a stress applied on (100) planes, as explained by Knowles and Howie (2015).

and when the ellipsoid has an oblate "penny" shape ($AR < 1$), C_{pp} writes:

$$C_{\text{pp}}(AR) = \frac{((1+3x)(1-2x(1-2\nu)+3AR^2)-2(1-2\nu)(1+2x))}{4G((1+3x)AR^2+(1+x)(\nu+x.\nu+x))}, \tag{4.10}$$

with

$$x = \frac{-1}{1-AR^2} + \frac{AR\arcsin(\sqrt[2]{1-AR^2})}{(1-AR^2)^{1.5}}. \tag{4.11}$$

To take into account the effect of salt precipitation/dissolution, we start with a simple mass balance (variables with subscript "f" are used for the initial conditions of FI formation):

$$\rho(T,P) = \frac{m}{V}, \tag{4.12}$$

m is the mass of the FI, and V its volume. We develop the denominator as follows:

$$V = V_{\text{f}} + \frac{m_{\text{NaCl}} - m_{\text{NaCl}_{\text{f}}}}{\rho_{\text{NaCl}}}, \tag{4.13}$$

with m_{NaCl} the mass of NaCl dissolved in the FI and ρ_{NaCl} the density of sodium chloride. We can express the mass of sodium chloride comparatively with the mass of water m_{H2O} as follows:

$$m_{\text{NaCl}} = \frac{x_{\text{M,NaCl}}.m_{\text{H2O}}}{1-x_{\text{M,tds}}} \tag{4.14}$$

with

$$m_{\text{H2O}} = V_{\text{f}}.\rho_{\text{f}}(1-x_{\text{M,tds,f}}). \tag{4.15}$$

$x_{\text{M,NaCl}}$ is the mass fraction of dissolved NaCl in the FI, and $x_{\text{M,tds}}$ is the mass fraction of total dissolved salts. Combining Equations (4.14) to (4.15) with Equation (4.13), we get:

$$V = V_{\text{f}} + \frac{V_{\text{f}}.\rho_{\text{f}}}{\rho_{\text{NaCl}}}\left(x_{\text{M,NaCl}}\left(\frac{1-x_{\text{M,tds,f}}}{1-x_{\text{M,tds}}}\right) - x_{\text{M,NaCl,f}}\right), \tag{4.16}$$

hence the volume ratio:

$$\begin{aligned} R_{\text{V}} &= \frac{V}{V_{\text{f}}} \\ &= 1 + \frac{\rho_{\text{f}}}{\rho_{\text{NaCl}}}\left(x_{\text{M,NaCl}}\left(\frac{1-x_{\text{M,tds,f}}}{1-x_{\text{M,tds}}}\right) - x_{\text{M,NaCl,f}}\right). \end{aligned} \tag{4.17}$$

The numerator of Equation (4.12) expands as follows:

$$\begin{aligned} m &= m_{\text{f}} + m_{\text{NaCl}} - m_{\text{NaCl}_{\text{f}}} \\ &= \rho_{\text{f}}.V_{\text{f}} + \rho_{\text{NaCl}}(V - V_{\text{f}}) \\ &= V_{\text{f}}(\rho_{\text{f}} + \rho_{\text{NaCl}}(R_{\text{V}} - 1)). \end{aligned} \tag{4.18}$$

Thus, incorporating Equations (4.16) and (4.18) into Equation (4.12), one gets :

$$\rho(T,P) = \frac{\rho_{\mathrm{f}} + \rho_{\mathrm{NaCl}}(R_{\mathrm{V}} - 1)}{R_{\mathrm{V}}}. \tag{4.19}$$

Densities are expressed in kg.m^{-3}, temperatures in °C and pressures in MPa. Note that $x_{\mathrm{M,tds}} = x_{\mathrm{M,NaCl}}$ in the NaCl-H_2O system. To calculate the pressure in a FI when conditions change from $\{T_{\mathrm{f}}, 0\}$ to $\{T, P\}$, we apply an iterative procedure. First (i), we only apply the temperature change, calculating $\rho(T, 0)$ with Equation (4.8) and (ii) feeding the result into Equation (4.19) instead of ρ_{f}. This first procedure amounts to assuming a perfectly incompressible cavity with (i) host thermal contraction/expansion and (ii) NaCl precipitation/dissolution in the fluid. The density found after this step enables us to (iii) get a first estimate of the pressure P_1 using the Pitzer density EoS. Now that we are done with reactions due to temperature change, (iv) we calculate the effect of a change in conditions from $\{T, 0\}$ to $\{T, P_1\}$ with Equation (4.8) to get a new estimate of the density once C_{pp} is taken into account. A new pressure P_2 is calculated with the EoS, which we use to recalculate the density with Equation (4.19), and so on iterating successively between Equations (4.8) and (4.19) until pressure varies less than 0.5%[5].

4.2 Results

To illustrate the rendering of the model and highlight its physical and geological implications, we investigate 3 case studies: lab-grown NaCl-H_2O FIs, Dead Sea-like FI compositions and Bristol Dry Lake-like FI compositions. The first case is interesting in the sense that it is the most simple and best-constrained, and thus allows for fine investigation of the thermo-mechanical processes at stake in halite FIs. Then, as most saline lakes contain other major solutes and cannot be approximated by a simple binary system, in the two following case studies we analyze the impact of multi-electrolyte brine chemistry on the *P-T* behavior of FIs, testing various compositions along an evaporation path. The comparison of the Dead Sea, Palestine, and Bristol Dry Lake, California, is of particular interest since it implies genetically close chemistries with, however, opposite Mg/Ca, the Dead Sea being Mg-rich and Bristol Dry Lake being Ca-rich (Table 4.1).

4.2.1 Case study #1: NaCl-H_2O lab-grown FIs

In the case of NaCl-H_2O FIs, the temperature and pressure dependent value of $x_{\mathrm{M,NaCl}}$ needed for the calculation of R_{V} (Equations (4.17) and (4.18)) is determined with the solubility empirical fit of Sawamura et al. (2007)[6]. Pressure at each iteration is calculated with the density EoS of Archer (1992).

Our calculations at T_{f} = 30 °C show that all the effects combined contribute to lower $\frac{\mathrm{d}P}{\mathrm{d}T}$ by more than 40%,

[5]More specifically, we undertake several compressibility iterations between each solubility iteration. In total, after 2 pressure solubility and 6 compressibility iterations, we reach a stable value to within 0.3%.

[6]This equation is defined in the range 0-40 °C, and 0-300 MPa. Comparing with the fit of Farelo et al. (1993) obtained on measurements at ambient pressure and higher temperature, we observe a very good agreement up to 60 °C, thus allowing extrapolation up to 60 °C. The quasi-linear dependence on pressure also allows for a safe extrapolation down to negative pressures of several tens of MPa.

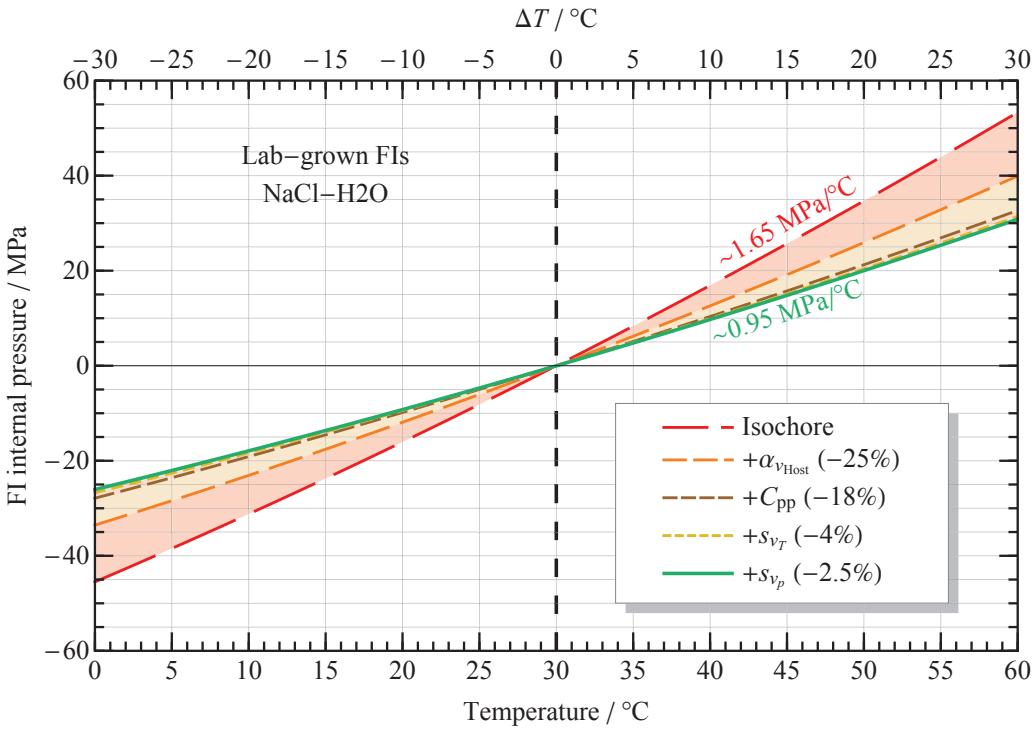

Figure 4.3: ***The effects of host thermal expansion, cavity compressibility and temperature and pressure dependence of solubility (s_{V_T} and s_{V_P}, respectively) on the P-T behavior of a FI trapped at T_f = 30 °C. Each plotted iso-T_h includes the effect indicated by the heading in the legend in addition to all the other effects that are above.***

from ~1.65 MPa/°C for the pure isochore down to ~0.95 MPa/°C (Figure 4.3). In detail, $\alpha_{V_{Host}}$ is the main factor, followed by C_{pp} and, very last, the temperature and pressure dependence of solubility s_{V_T} and s_{V_P}. Note that contributions of each effect displayed in the legend of Figure 4.3 are calculated in isolation, when each effect is considered as the only contribution.

The fact that the physical properties of the host crystal play such a role in the reducing of $\frac{dP}{dT}$ is inherent to halite, as this mineral is both highly expandable and rather soft. As a comparison, we calculate that the thermo-mechanical properties of a quartz host would only account for a -7% decrease of $\frac{dP}{dT}$ in the case of an identical fluid trapped at 30 °C[7]. The slight effect of the *P-T* dependence of solubility is explained by the fact that sodium chloride occupies a slightly larger volume as a solid than it does as a solute. Finally, we note a parabolic trend of the iso-T_h. This is due to halite thermal expansion, which depends on temperature, and to a lower α_V at low temperature. This results in slightly steeper iso-T_h at high T than at low T.

In Figure 4.4, we show the effect of the FI shape on the internal pressure. We observe that $AR > 1$ has a moderate effect on $\frac{dP}{dT}$, only some percents change. Basically, it was shown that a spheroid with $AR \to \infty$, *i.e.* a tube, has a finite compressibility $C_{pp_{tube}} = \frac{4}{3} C_{pp_{sphere}}$ (Zimmerman, 1990). On the other hand, $AR < 1$ has a prominent effect. For instance, a FI with $AR = 0.15$ has a compressibility $C_{pp} \approx 4C_{pp_{sphere}}$, which decreases the pressure in the FI by $\frac{1}{3}$. To sum up and express this matter in terms of halite FIs geometries, FIs with elongate cigar shape compress moderatly more than perfectly cubic ones, which results in pressures lower by

[7]Thermal expansion for quartz is found in Raz et al. (2002); elastic constants are found in Ohno et al. (2006). Note that in theory, if the host had a thermal expansion as low as that of the inclusion fluid, there would be no pressure building up in the FI.

some percents, while slabs are way more compressible than cubes and greatly alleviate pressure.

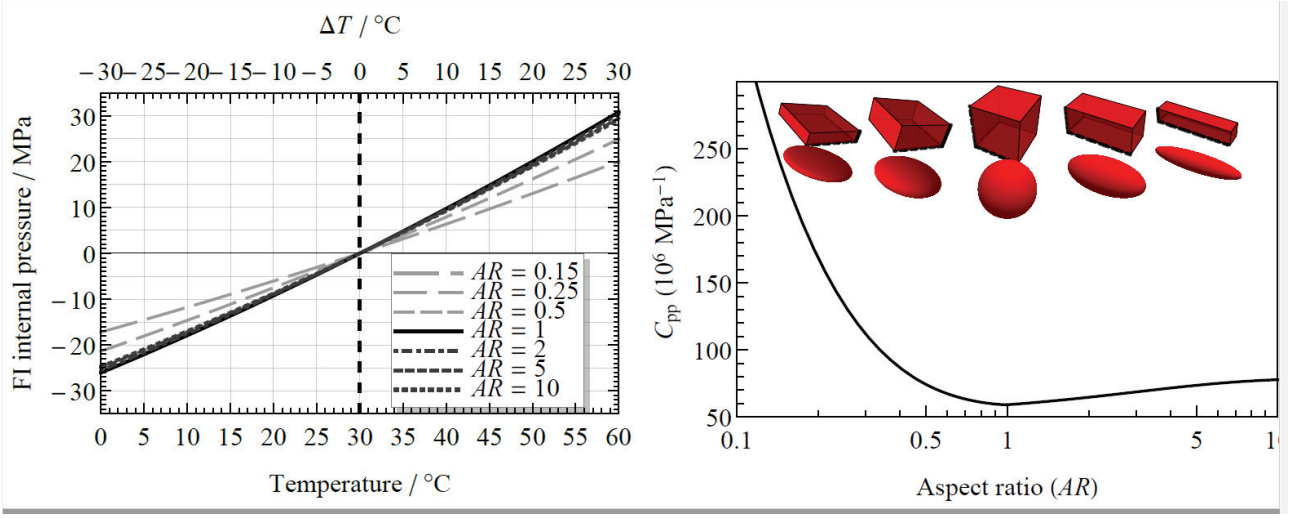

Figure 4.4: ***The effect of the FI aspect ratio.*** *The effect of the FI aspect ratio on the cavity compressibility (right panel) and on the internal pressure (left panel) is investigated. Here, we call "aspect ratio" the ratio of the size of one semi-diameter over the size of the two other equal semi-diameters. For instance, to a prolate spheroid of aspect ratio 2:1:1, we assign a value AR = 2, and to an oblate spheroid of aspect ratio 1/2:1:1, we assign a value AR = 0.5.*

4.2.2 Case study #2: Dead Sea FIs

The Dead Sea composition (see Table 4.1) derives from seawater, to which it was supposedly connected in the Pliocene through the Yizreel Valley (Zak, 1997). This seawater heritage accounts for the high amount of Na, Cl and Mg in the lake. Since its isolation from the Mediterranean Sea, the lake chemistry has changed profoundly though. Its Ca content raised at the expense of Mg through the progressive dolomitization of surrounding calcium carbonates, and its CO_3 and SO_4 content dropped down because of the deposit of large amouts of calcium carbonates and gypsum (Katz and Starinsky, 2009). The resulting composition is a Cl-Na-Mg-Ca-K lake, in descending order of molality.

We test several Dead Sea chemistries: the chemistry as it was measured in 1993 by Stein et al. 1997 (see composition in Table 4.2); the composition of the beginning of the Last Integlacial (132 ka BP), as measured by Kiro et al. (2017) applying the Cryo-SEM method (Ayora et al., 1994) to halite FIs; and 5 other compositions selected on the evaporation and dilution paths of the aforementioned Last Interglacial chemistry. The compositions along the evaporation and dilution paths are calculated using the Pitzer-based PhreeSCALE software (Lach et al., 2016), an upgraded version of PhreeQC (Parkhurst and Appelo, 2013). To account for the temperature dependent value of $x_{\mathrm{M,NaCl}}$ needed for the calculation of R_{V} (Equations (4.17) and (4.18)), we take $\frac{\mathrm{d}m_{\mathrm{sat}}}{\mathrm{d}T}_{\mathrm{DS}}$ = 0.017 molal.°C^{-1} measured by Gavrieli et al. (1989), valid for a current Dead Sea composition. We determine $\frac{\mathrm{d}m_{\mathrm{sat}}}{\mathrm{d}T}$ of the other Dead Sea-like compositions through multiplying $\frac{\mathrm{d}m_{\mathrm{sat}}}{\mathrm{d}T}_{\mathrm{DS}}$ by a factor. We define this factor as the ratio of a Dead Sea-like composition $\frac{\mathrm{d}m_{\mathrm{sat}}}{\mathrm{d}T}$ upon the current Dead Sea composition $\frac{\mathrm{d}m_{\mathrm{sat}}}{\mathrm{d}T}$, both calculated with PhreeSCALE. We proceed this way because the absolute $\frac{\mathrm{d}m_{\mathrm{sat}}}{\mathrm{d}T}$ calculated for a current Dead

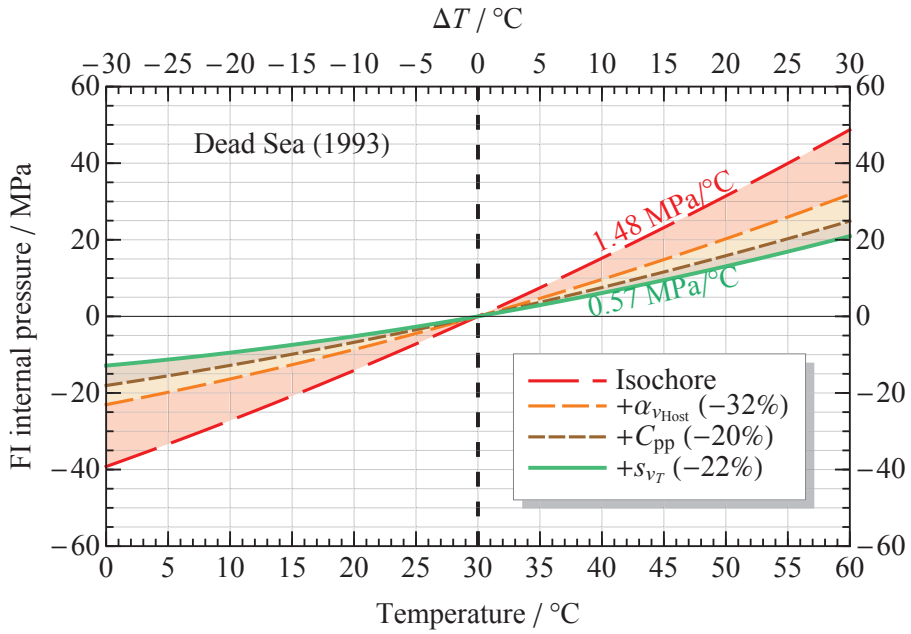

Figure 4.5: ***The effects of host thermal expansion, cavity compressibility and temperature dependence of solubility on the P-T behavior of a Dead Sea FI trapped at T_f =*** 30 °C***.*** *Each plotted iso-T_h includes the effect indicated by the heading in the legend in addition to all the other effects that are above.*

Sea composition by PhreeSCALE is much too low compared to the empirical value; we assume however the proportions between each calculated $\frac{dm_{sat}}{dT}$ are more trustworthy. Pressure at each iteration is calculated with the multi-component density EoS (Equations (4.6) and (4.7)). Note that we do not know $\frac{dm_{sat}}{dP}$ for a Dead Sea composition; therefore, it is not included in the following.

In Figure 4.5, we observe that the *P-T* slope in a Dead Sea FI is markedly more gentle than in a pure NaCl-H_2O FI, ~0.57 MPa/°C compared to ~0.95 MPa/°C, that is, 40% lower. In details, this is due to a more gentle isochore slope (-10% when compared to pure NaCl-H_2O) but also, interestingly, to a stronger contribution of α_V, C_{pp} and s_{V_T}. The much stronger contribution of the latter, in particular, is noticeable; this is explained by the fact that $\frac{dm_{sat}}{dT}_{DS} = 4\frac{dm_{sat}}{dT}_{NaCl\text{-}H_2O}$ at 30 °C.

To analyze more finely the factors governing the pressure inside halite FIs, we plot the *P-T* slope of several FIs trapped at 30 °C (Figure 4.6A), with chemistries reflecting several stages of a unique Dead Sea evaporation path (see Table 4.2 for compositions). When applying the same $\frac{dm_{sat}}{dT}_{DS}$ to all types of FIs, it comes out $\frac{dP}{dT}$ decreases along the first half of the evaporation path, and reaches a plateau at about the current Dead Sea degree of evaporation (~1240 kg.m^{-3}); afterwards, the *P-T* slope is constant up to carnallite saturation point. However, when assigning each composition a different and closer to reality estimate of $\frac{dm_{sat}}{dT}$, the trend is modified, with a noticeable increase of $\frac{dP}{dT}$ after a minimum value around 1240 kg.m^{-3}. The 4 terms governing the iso-T_h slope are investigated for each composition in Figure 4.6B. We see that FIs of the middle of the sequence show the lowest isochore slope; however, the main observable trend is the progressive increase in $\alpha_{V_{Host}}$ and C_{pp} contribution to $\frac{dP}{dT}$ lowering. This is further discussed in Section 4.3.

Dead Sea brine type*	**Na molal**	**K molal**	**Mg molal**	**Ca molal**	**Cl molal**	**Density kg.m^{-3}**	**$\frac{dm_{sat}}{dT}$ estimation molal.°C^{-1}*****
Dead Sea (1993)**	1.84	0.23	2.14	0.49	7.36	1235.0	**0.0170**
DSLowEem - 1	4.96	0.10	0.50	0.15	6.37	1205.2	0.0121
DSLowEem**	3.50	0.23	1.13	0.35	6.69	1216.3	0.0158
DSLowEem + 1	1.86	0.40	1.98	0.61	7.46	1239.8	0.0166
DSLowEem + 2	1.13	0.51	2.51	0.78	8.21	1260.7	0.0152
DSLowEem + 3	0.67	0.61	2.97	0.92	9.07	1282.7	0.0114
DSLowEem + 4	0.43	0.54	3.32	1.08	9.76	1299.9	0.0041
Bristol - 1	4.76	0.06	0.03	0.79	6.50	1214.2	0.0155
Bristol**	3.51	0.12	0.06	1.52	6.88	1231.0	0.0206
Bristol + 1	2.47	0.18	0.09	2.22	7.37	1250.0	0.0236
Bristol + 2	1.69	0.23	0.11	2.84	7.95	1270.0	0.0242
Bristol + 3	1.15	0.27	0.14	3.38	8.60	1290.1	0.0228
Bristol + 4	0.82	0.30	0.15	3.79	9.19	1307.1	0.0208

Table 4.2: ***Composition of Dead Sea and Bristol Dry Lake FIs used in this study.***
**"DSLowEem" stands for the early Last Interglacial composition of the Dead Sea (see text for details). "Bristol" stands for a typical Bristol Dry Lake brine composition. The appended negative/positive integer respectively stands for the step in the dilution/evaporation sequence with respect to the initial DSLowEem or Bristol composition.*
***The compositions are recalculated with PhreeSCALE from the ones found in the literature so it reaches perfect equilibrium with halite. See text for more details.*
****Bold value is $\frac{dm_{sat}}{dT}_{DS}$, measured empirically in the current Dead Sea by Gavrieli et al. (1989); all other $\frac{dm_{sat}}{dT}$ is obtained via multiplication of $\frac{dm_{sat}}{dT}_{DS}$ by a factor (see text for details).*

4.2.3 Case study #3: Bristol Dry Lake FIs

Bristol Dry Lake is a closed basin in the Mojave Desert, California, the center of which contains two small saline pans. The brines found in this area, of composition Cl-Na-Ca-K-Mg in descending order of molality (see Table 4.1), have a poorly constrained origin. The Na-Ca-Cl composition being very different from the composition of the known (H)CO_3-rich inflow waters, Lowenstein and Risacher (2009) hypothesized the existence of hot groundwaters enriched in Ca-Cl when coming into contact with the magma chamber of the neighbouring Amboy Crater. Indeed, such a Ca-chloridic chemistry is a typical feature in hydrothermal areas (Lowenstein et al., 1989; Hardie, 1990), where the calcium leaches out of Ca-feldspars and Ca-pyroxenes into hot hydrothermal brines. The fact that this type of chemistry is widespread amongst closed-basins brines makes the study of Bristol Dry Lake all the more relevant.

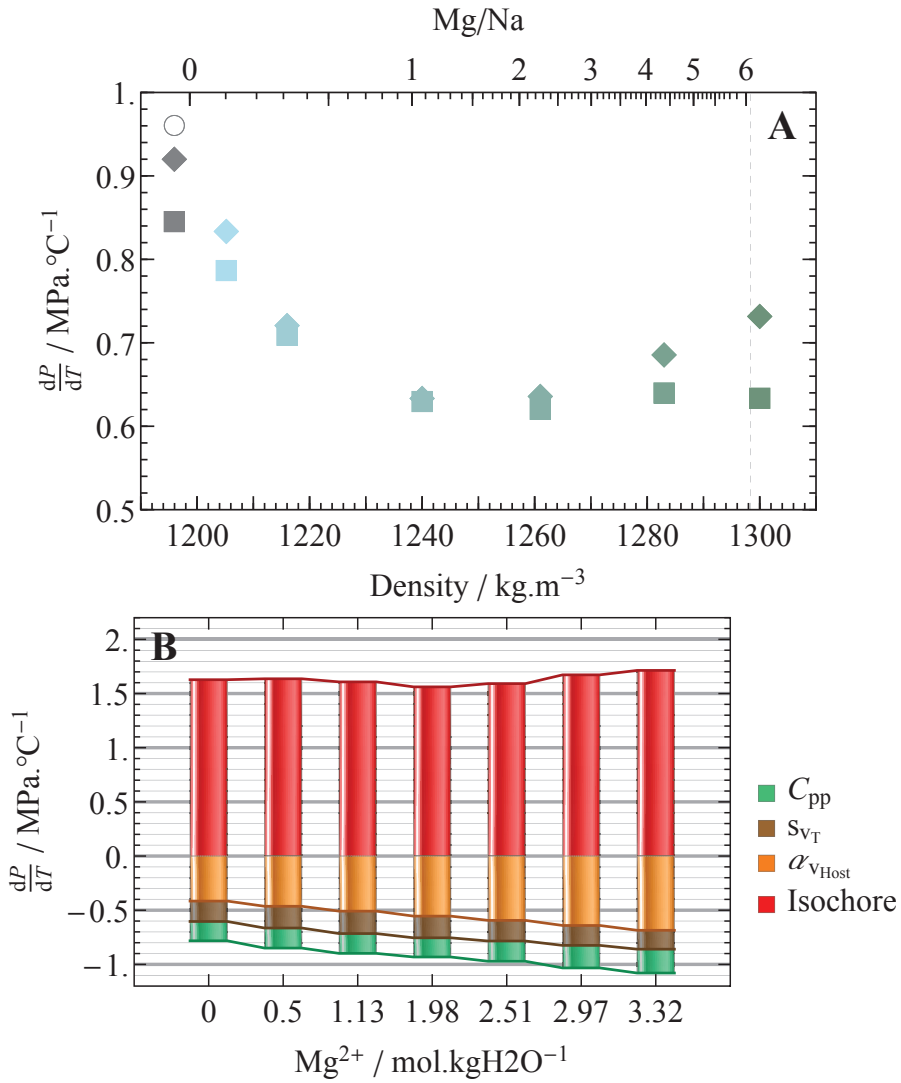

Figure 4.6: ***The pressure in Dead Sea FIs as a function of the evaporation degree.*** *(A) The iso-T_h P-T slope of a halite FI trapped at 30 °C is plotted as a function of brine density and Mg/Na molal ratio. The 6 blue datapoints correspond to different stages in the evaporation sequence of a Lower Eemian Dead Sea water (compositions described in Table 4.2), from most dilute (lighter blue) to most concentrated (darker blue). For comparison, the values for a pure NaCl-H_2O composition are also plotted (gray markers). The squares represent the value calculated with $\frac{dm_{sat}}{dT}_{DS}$. The diamonds represent the value calculated when a different $\frac{dm_{sat}}{dT}$ is applied for each chemistry (see Table 4.2). The empty circle is calculated when applying the NaCl-H_2O solubility EoS of Sawamura et al. (2007). (B) The pressure contribution of every factor is represented for each of the 7 compositions tested in the case of a constant $\frac{dm_{sat}}{dT}_{DS}$.*

We test several Bristol Dry Lake chemistries: the 1950s chemistry as reported by Hardie (1990), and 5 other compositions selected on the evaporation and dilution paths of the 1950s chemistry (see composition in Table 4.2). Compositions and $\frac{dm_{sat}}{dT}$ along the evaporation and dilution paths are calculated the same way as described for case study #2; $\frac{dm_{sat}}{dT}_{DS}$ is also taken as a basis for the calculation of $\frac{dm_{sat}}{dT}$. Pressure at each iteration is calculated with the multi-component density EoS (Equations (4.6) and (4.7)). Note that we do not know $\frac{dm_{sat}}{dP}$ for a Bristol Dry Lake composition; therefore, it is not included in the following.

In Figure 4.7, we observe that the isochoric *P-T* slope in a Bristol Dry Lake FI is slightly steeper than in a pure NaCl-H_2O FI trapped at 30 °C. Nonetheless, the iso-T_h *P-T* slope is slightly more gentle, ~0.87 MPa/°C

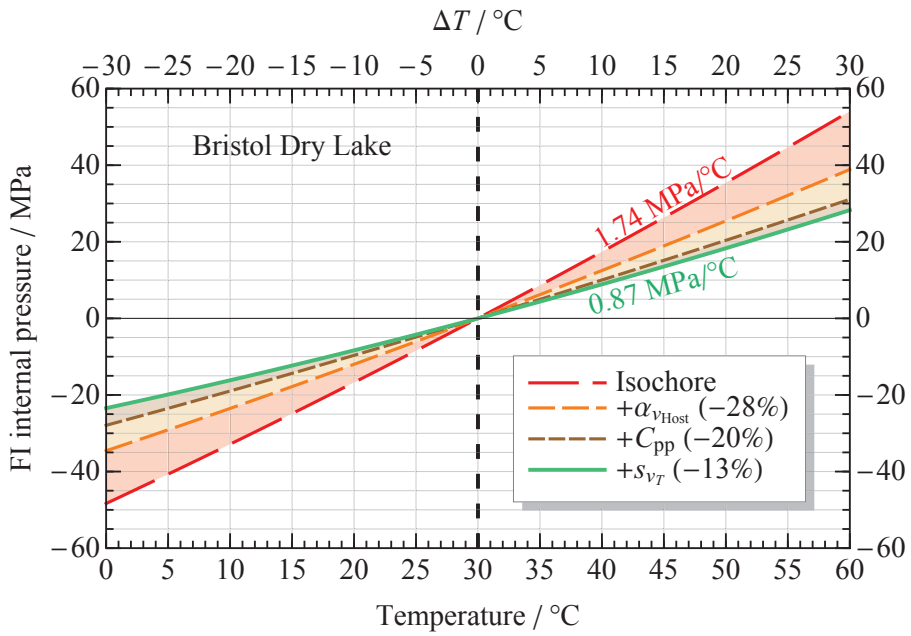

Figure 4.7: ***The effects of host thermal expansion, cavity compressibility and temperature dependence of solubility on the P-T behavior of a Bristol Dry Lake composition FI trapped at T_f =*** 30 °C***.*** *Each plotted iso-T_h includes the effect indicated by the heading in the legend in addition to all the other effects that are above.*

compared to ~0.95 MPa/°C, that is, 8% lower. The higher contribution of s_{V_T}, due to the high value of $\frac{dm_{sat}}{dT}$, is the only significant difference with a NaCl-H_2O FI.

In Figure 4.8A, we plot the $\frac{dP}{dT}$ calculated for several Bristol Dry Lake chemistries reflecting several stages of a unique Bristol Dry Lake evaporation path (see Table 4.2 for compositions). The first two compositions show comparable values of $\frac{dP}{dT}$ slightly lower than that of pure NaCl-H_2O. Then, beyond the current density of Bristol Dry Lake ~1230 kg.m^{-3}, the *P-T* slope increases linearly with density. The 4 terms governing the iso-T_h slope are investigated for each composition in Figure 4.8B. We see that the isochore slope increases all along the evaporation path. It is offset by a rather equivalent contribution of $\alpha_{V_{Host}}$ and C_{pp} to the lowering of $\frac{dP}{dT}$. In addition, the contribution of s_{V_T} almost disappears in the most concentrated FIs. In total, this results in the observed increase of the iso-T_h $\frac{dP}{dT}$ along the evaporation path. This is further discussed in Section 4.3.

4.3 Discussion

In Section 4.2, we have calculated the pressure in FIs as a function of temperature, T_h, composition and shape. In this section, in order to single out the contribution of each parameter and better discuss the processes involved, we propose to simplify the problem and look at $\frac{dP}{dT}$ at conditions close to $\{T_h, 0\}$. For this simpler approach, an analytic calculation can be made instead of the iterative approach. Indeed, the slope of the iso-density of a fluid at conditions $\{T, P\}$ corresponds to the simple ratio of the fluid thermal expansion upon the fluid isothermal compressibility at these specific conditions $\{T, P\}$, as shown in Equation (4.1). This equation can be generalized to the case of an iso-T_h that is not an iso-density, through taking the ratio of the sum of the

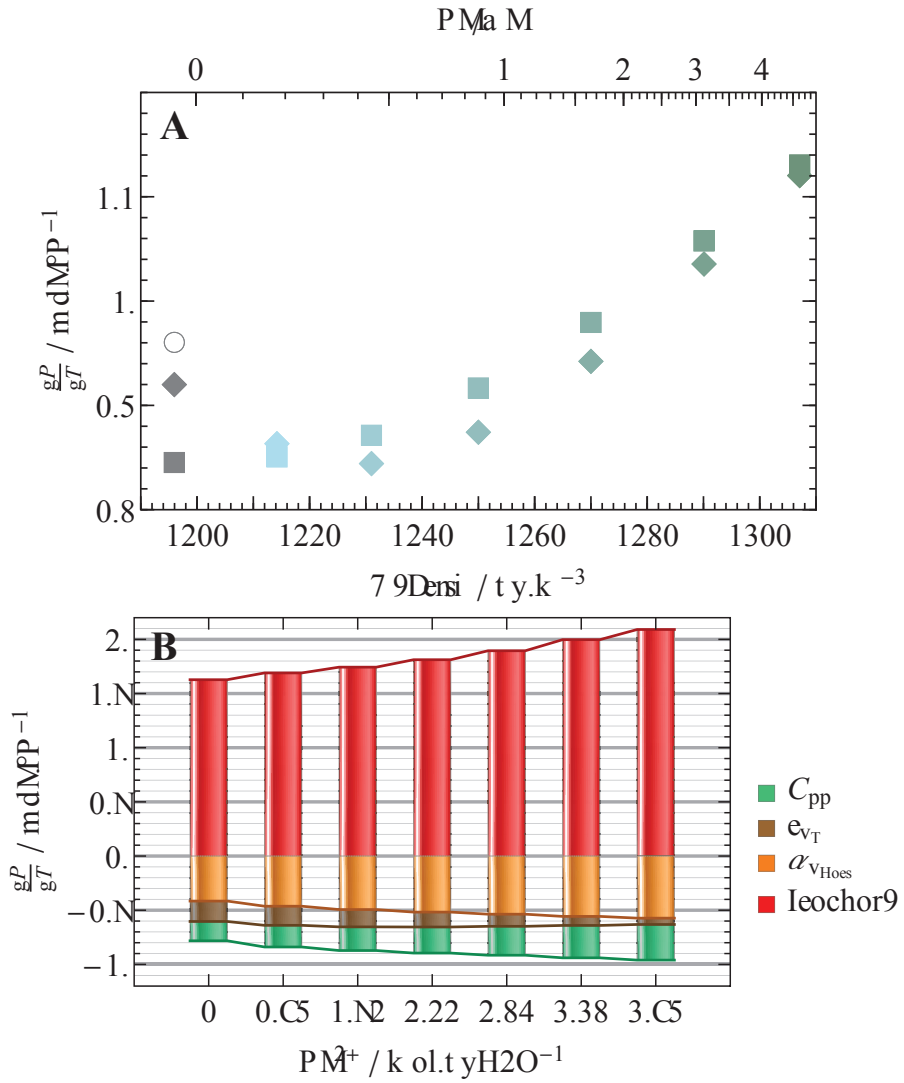

Figure 4.8: ***The pressure in Bristol Dry Lake FIs as a function of the evaporation degree.*** *(A) The iso-T_h P-T slope of a halite FI trapped at 30 °C is plotted as a function of brine density and Ca/Na molal ratio. The 6 blue datapoints correspond to different stages in the evaporation sequence of a Bristol Dry Lake brine (compositions described in Table 4.2), from most dilute (lighter blue) to most concentrated (darker blue). For comparison, the values for a pure NaCl-H_2O composition are also plotted (gray markers). The squares represent the value calculated with $\frac{dm_{sat}}{dT}_{DS}$. The diamonds represent the value calculated when a different $\frac{dm_{sat}}{dT}$ is applied for each chemistry (see Table 4.2). The empty circle is calculated when applying the NaCl-H_2O solubility EoS of Sawamura et al. (2007). (B) The pressure contribution of every factor is represented for each of the 7 compositions tested in the case of a constant $\frac{dm_{sat}}{dT}_{DS}$.*

coefficients α_{i} that contribute to the fluid expansion per temperature unit over the sum of the coefficients β_{j} that contribute to the fluid contraction per pressure unit, as follows:

$$\left(\frac{\partial P}{\partial T}\right)_{T_{\mathrm{h}}} = \frac{\sum_i \alpha_i}{\sum_j \beta_j}. \tag{4.20}$$

In the case of the halite FI and at conditions $\{T_{\mathrm{h}}, 0\}$, the iso-T_{h} slope thus writes:

$$\frac{\mathrm{d}P}{\mathrm{d}T} = \frac{\alpha_{\mathrm{v}} + s_{\mathrm{v_T}} - \alpha_{\mathrm{v_{Host}}}}{\beta_{\mathrm{T}} + C_{\mathrm{pp}}}. \tag{4.21}$$

s_{V_T}, in °C^{-1}, is the FI expansion due to the temperature dependence of NaCl solubility. We can expand s_{V_T} as follows:

$$s_{V_T} = \frac{dm_{sat}}{dT}\left(-\frac{1}{\rho}\left(\frac{\partial\rho}{\partial m_{NaCl}}\right)_{P,T} + 10^{-3} M_{NaCl}.x_{M,H_2O}.(1-\frac{\rho}{\rho_{NaCl}})\right), \tag{4.22}$$

with $\frac{dm_{sat}}{dT}$ in molal.°C, M_{NaCl} the molar mass of NaCl in kg.mol^{-1} and x_{M,H_2O} the mass fraction of water. $\frac{1}{\rho}\left(\frac{\partial\rho}{\partial m_{NaCl}}\right)_{P,T}$ accounts for the brine relative density change when adding 1 molal of NaCl, and the second term $10^{-3} M_{NaCl} x_{M,H_2O}(1-\frac{\rho}{\rho_{NaCl}})$ represents the FI relative volume change when transferring 1 molal of NaCl from its solid state on the FI wall to the solute state in the liquid. Comparing this analytic approach with the iterative approach around ambient pressure, we get identical results within the 0.3% uncertainty of the iterative method.

Equation (4.21) highlights the role of two types of contributions to the value of $\frac{dP}{dT}$ in halite FIs: the host thermo-mechanical properties and the fluid volumetric derivatives. The host influences the pressure inside the FI through its thermal expansion, which is invariant from one case to another, and the cavity compressibility, which depends on the FI shape. The fluid volumetric derivatives, α_v, β_T and s_{V_T}, all have a strong influence on $\frac{dP}{dT}$ and are highly dependent on the FI composition. All these factors should be constrained in the perspective of a good pressure estimation.

4.3.1 The pressure lowering due to shape

The issue of the mechanical interaction between an inclusion and its host was addressed by several authors. The simplest issue assuming a spherical inclusion in an isotropic infinite host was addressed early (Goodier, 1933; Eshelby John Douglas and Peierls Rudolf Ernst, 1959; Landau et al., 1986). Zimmerman (1990) developed an adapted formulation for the compressibility of spheroidal cavities. Zhang (1998) developed a formulation that includes the effect of a near host surface, as explained in Chapter 3. Several workers modeled with finite elements and compared with experiments the volume changes of the host as a function of the cavity shape (Burnley and Davis, 2004; Burnley and Schmidt, 2006; Mazzucchelli et al., 2018). Their work showed that the main factor that affects volume change when compared to a sphere is by far the aspect ratio, the presence of edges and corners (cuboids instead of spheroids) only having a secondary effect. Hence, in this thesis, we have assumed a spheroidal shape for FIs and used the formulation of Zimmerman (1990) to investigate the effect of the spheroid aspect ratio on the halite FI pressure. It comes out flatness ($AR < 1$) plays a predominant role in the lowering of pressure. We estimate the flatness effect can be "felt", *i.e.* induces a $\frac{dP}{dT}$ drop that exceeds our calculation uncertainty, when $AR < 0.5$ and $\frac{dP}{dT}$ is reduced by more than 5%. We calculate that when $AR < 0.13$, the cavity is even more compressible than the brine itself, which leads to $\frac{dP}{dT}$ lower by more than 50% compared to the spherical case[8]. On the other hand, we show that a tubular or cigar-shaped FI show $\frac{dP}{dT}$ lower by no more than 5% compared to the spherical case. However, the reader should keep in mind that this reducing of the

[8] In the case of a quartz host, we calculate that this would happen when $AR < 0.045$; elastic constants of quartz found in Heyliger et al. (2003).

pressure is not a guarantee of avoiding reequilibration. On the contrary, non-spherical geometries are more compressible because they have a non homogeneous deformation, some areas (faces) undergoing more flexure than others (edges and corners). This, in turn, should result in preferential plastic yielding of some specific parts.

In the perspective of improving our model, the issue of edges and corners should be addressed. Mazzucchelli et al. (2018) modeled the effect of aspect ratio on both spheroids and cuboids solid inclusions of quartz in pyrope and pyrope in diamond. From their models, we estimate that a cuboid should lead to a ~4% P drop compared to a spheroid of same aspect ratio. Yet, as their conditions are not the same as ours, this matter should be adressed with a 3D finite element modelling adapted to our case.

4.3.2 The link between fluid chemistry, fluid thermodynamic properties and the FI internal pressure

The 2 case studies we carried on multi-component brines show 2 opposite trends: as the Dead Sea FIs show $\frac{\mathrm{d}P}{\mathrm{d}T}$ always lower than in NaCl-H_2O FIs and all the lower as the evaporation degree is high, $\frac{\mathrm{d}P}{\mathrm{d}T}$ in Bristol Dry Lake FIs is equal to or higher than in NaCl-H_2O FIs and increases with the evaporation degree. To understand these opposite trends, we plot the three thermodynamic coefficients α_V, β_T and $s_{\mathrm{V_T}}$ that determine the value of $\frac{\mathrm{d}P}{\mathrm{d}T}$ (Equation (4.21)) as a function of temperature and for each of the compositions along the evaporation path of the Dead Sea and of Bristol Dry Lake (Figure 4.9, left and right panels respectively). On the whole, we observe that concentration tends to decrease the value of each of the three thermodynamic coefficients. Since it affects α_V and β_T the same way, Equation (4.1) shows it should not result in a strong modification of the isochore slope; and, indeed, we never observe large variations in the isochore slope (see Figures 4.6 and 4.8). However, we see in Equation (4.21) that the lower α_V and β_T, the stronger the role of the thermo-mechanical properties of the host in the reducing of the iso-T_h $\frac{\mathrm{d}P}{\mathrm{d}T}$. While this trend is moderate in the case of Bristol Dry Lake FIs, it is much stronger in the case of the Dead Sea FIs. This phenomenon explains the opposite influence that concentration have on Dead Sea and Bristol Dry Lake FIs. The former show α_V and β_T ever smaller in the face of $\alpha_{\mathrm{V_{Host}}}$ and C_pp along the evaporation path, leading to the decrease of $\frac{\mathrm{d}P}{\mathrm{d}T}$. The latter show values of α_V and β_T still high enough to drive the evolution of $\frac{\mathrm{d}P}{\mathrm{d}T}$; as β_T decreases more than α_V along the evaporation path, this leads to the increase of $\frac{\mathrm{d}P}{\mathrm{d}T}$. We also note that the value of $s_{\mathrm{V_T}}$ approaches 0 in highly concentrated brines.

The question that arises then is: can we draw generalizable conclusions on the dependence of the P-T slope on the composition of multi-component FIs from the example of the Dead Sea and Bristol Dry Lake ? Let's address this question by looking at each contribution of Equation (4.21) individually.

α_V We calculated punctual values of α_V from available density datasets of binary chloride, sulfate and carbonate salts aqueous solutions; we plot them as a function of molality in the left panel of Figure 4.10. From this graph, it comes out magnesium salts, either $MgCl_2$ or $MgSO_4$, have a null or negative effect on α_V, while all the other salts have a positive effect; we notice in particular the very strong effect of Na_2SO_4. Therefore, it

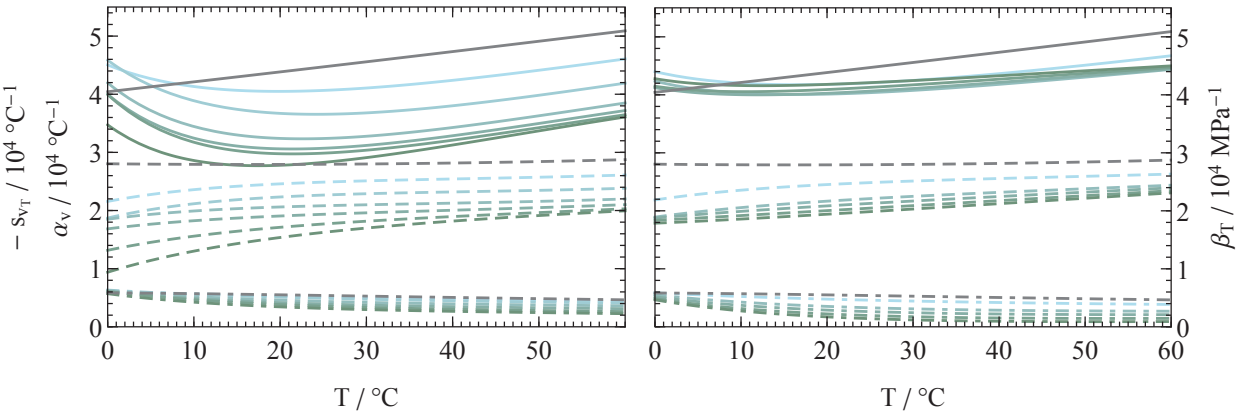

Figure 4.9: ***The effect of the brine composition and temperature on its thermodynamic properties.*** *α_V (solid lines), β_T (dashed lines) and s_{V_T} (dash-dotted lines) are calculated for the 6 Dead Sea compositions (left panel) and the 6 Bristol Dry Lake compositions (right panel) of the evaporation sequence presented in Table 4.2, from most dilute (lighter blue) to most concentrated (darker blue). The same physical properties in the case of a saturated NaCl-H_2O brine are also plotted for comparison (gray lines). Note that s_{V_T} is calculated with $\frac{dm_{sat}}{dT}_{DS}$ for every composition.*

seems magnesium is responsible for the low pressure in the Dead Sea FIs, and this should be generalized to all Mg-rich brines.

β_T As with α_V, we calculated punctual values of β_T from available density datasets of binary chloride, sulfate and carbonate salts aqueous solutions; we plot them as a function of molality in the right panel of Figure 4.10. We observe that the compressibility of each aqueous salt solution decreases linearly with the square root of molality. The trend is all the more pronounced as the solute in question has a high molar mass. On the whole, we thereby expect dense brines to be weakly compressible and to show higher $\frac{dP}{dT}$.

s_{V_T} and $\frac{dm_{sat}}{dT}$ s_{V_T} tends to lower $\frac{dP}{dT}$ (Equation (4.21)). On the other hand, both Dead Sea and Bristol Dry Lakes evaporation sequences show that the denser the brine, the lower s_{V_T}. This can be explained by the evolution of the term $\left(\frac{\partial \rho}{\partial m_{NaCl}}\right)_{P,T}$ in Equation (4.22). Indeed, solutes have a tendency to increase density. However, this salinity contraction is not linearly correlated to molality: the denser and more concentrated the aqueous solution, the weaker the contraction due to additional solute. We could imagine that $\left(\frac{\partial \rho}{\partial m_{NaCl}}\right)_{P,T}$ tends towards 0 in the case of extremely dense brines, and in this case the addition of new solute from the wall of the FI into the brine would increase pressure, opposite to what we have seen so far. As for $\frac{dm_{sat}}{dT}$, in both case studies #2 and #3, the values yielded by PhreeSCALE, albeit not in agreement with empirical values, show an increase of $\frac{dm_{sat}}{dT}$ in the first half of the evaporation path, followed by a decrease. This should be modelled with the appropriate softwares, for instance with EQL/EVP (Risacher and Clement, 2001), and/or measured *in-situ*.

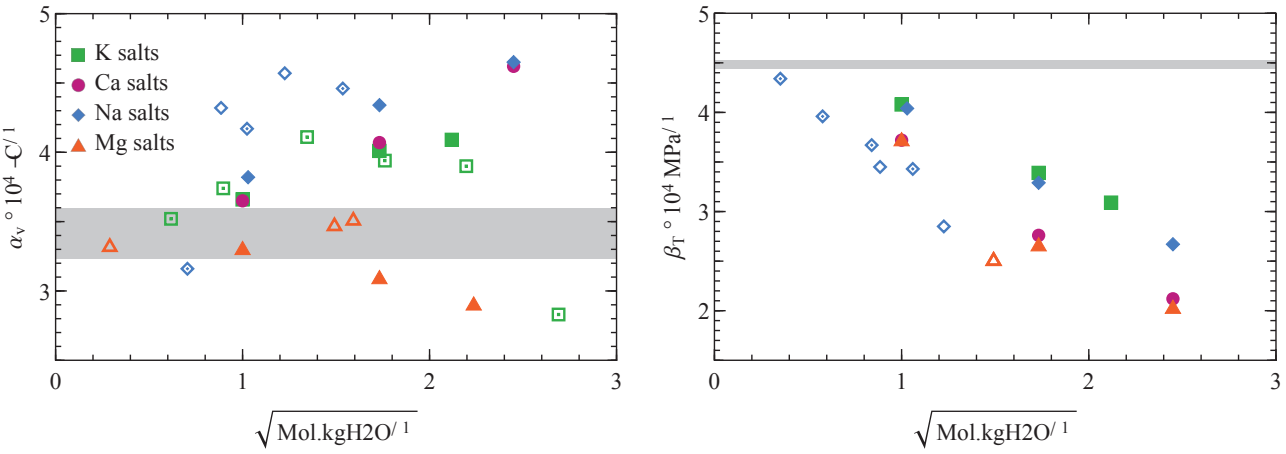

Figure 4.10: ***The effect of various solutes on binary aqueous solutions*** α_V ***and*** β_T**.** *α_V (left panel) and β_T (right panel) of chloride (filled symbols), sulfate (hollow symbols) and carbonate (hollow symbols with small dot) binary aqueous solutions are plotted as a function of the square root of each salt molality. All α_V values are calculated from literature density data at a temperature 32.5 °C < T < 34 °C and ambient pressure, apart from $\alpha_{V_{Na_2SO_4}}$ calculated at 37.5 °C. All β_T values are calculated from literature density data at a temperature 25 °C < T < 26.5 °C and ambient pressure, apart from $\alpha_{V_{Na_2CO_3}}$ calculated in the range 26-35.5 °C. NaCl, KCl, $MgCl_2$ and $CaCl_2$ data from Al Ghafri et al. (2012); Na_2SO_4 data from Al Ghafri et al. (2013); $MgSO_4$ data from Abdulagatov et al. (2007); Na_2CO_3 and K_2CO_3 α_V data from Knuutila et al. (2010); Na_2CO_3 β_T data from Abdulagatov et al. (2009). Pure water α_V and β_T values in the temperature range of the displayed data is also represented (gray strip).*

4.3.3 Uncertainties on the pressure calculations

To our knowledge, the Pitzer model for the thermodynamics properties of NaCl-H_2O of Archer (1992) proposes the most robust density EoS for this system. On the range 25-100 °C, 0.1-100 MPa and up to molality solubility, it is always in agreement with the experimental data of Al Ghafri et al. (2012) within better than 0.1% (see Figure 4.A.1). We also calculate deviations of the density derivatives α_V and β_T of about ~2% and ~5%, respectively. Consequently, we estimate the uncertainty on the pressure calculations in NaCl-H_2O FIs to be ~5%. It is noteworthy to add that we might overestimate the pressure in FIs by some ~4% due to the spheroid approximation. However, for a robust estimation of the uncertainty brought by FIs shape, this should be tested with 3D mechanical finite element modelling.

The Pitzer density EoS for aqueous KCl, MgCl2 and CaCl2 used in this study all compare favourably with experimental values in the range 25-100 °C, 0.1-100 MPa and up to solubility molality (Figure 4.A.1). The highest deviations are observed at high pressure for CaCl2-H_2O (up to 0.3%), and at high pressure and low temperature for MgCl2-H_2O (up to -0.2%). We calculate the maximum deviations on the density derivatives in the MgCl2-H_2O system; in particular, the deviation of α_V becomes very important at low T and high molality, hence we think it should be used with caution at ambient temperature. It certainly explains the low T retracing of α_V observed for Dead Sea compositions below ~20 °C in Figure 4.9.

Implementing these binary systems density models altogether in the mixing rule equation of Young and Smith (1954), one can constrain densities of hypersaline brines of ionic strength up to 8-10 molal typically

within better than 0.1% (Figure 4.A.2), and the density derivatives α_v and β_T within a few percents uncertainty (Figure 4.A.3). However, the deviation is higher than ~10% at very high ionic strengths. We thereby estimate that the uncertainty in FIs of ionic strength > 8 molal lies in the range 10-15%. Fortunately several datasets of volumetric properties of Dead Sea compositions are available in the literature; through comparing with these datasets, we can test the calculated multi-component densities and derivatives for this type of brine. We observe that our calculations underestimate both the Dead Sea compressibility and thermal expansion by about 10-15%. As both coefficients deviate in the same direction and with the same magnitude, we can infer that our uncertainty on the pressure calculation in Dead Sea FIs is markedly below 10%.

The increase of uncertainties towards very high concentrations is partly due to the limitations of Pitzer equations, but also to the shortcomings inherent to the mixing rule. Indeed, the latter implies the extrapolation of binary solutions density EoS to molalities beyond solubility. For this reason, we cannot extend our model to Na-sulfatic or Na-carbonatic brines, as these salts show lower solubilities than chlorides; the extrapolation would be all the stronger. Therefore, one of the further developments of our model would be to get a self-consistent set of Pitzer parameters in order to be able to calculate multi-component brines density and derivatives with the Pitzer formalism instead of using the current mixing rule. From then on, we could extend our model to sulphate and carbonate brines.

Lastly, we didn't take the $\frac{dm_{sat}}{dP}$ into account when modelling complex brines densities. It was quite negligible in the case of NaCl-H_2O system (~2.5%) but, just like temperature solubility revealed significant for a current Dead Sea composition, it could be that pressure solubility varies strongly with FI composition. This should be investigated more thoroughly in future developments of the model.

4.3.4 Model verification

The speed of sound w in a liquid is linked to its volumetric properties through:

$$w = \sqrt{\frac{1}{\beta_s \rho}}. \tag{4.23}$$

β_s, the isentropic compressibility of the liquid, equals:

$$\beta_s = \beta_T - \frac{{\alpha_V}^2 . T}{\rho . C_p} \tag{4.24}$$

with C_p the specific heat capacity of the brine. We can thus calculate w in a NaCl-H_2O monophase FI with the EoS of Archer (1992) by applying the pressure as determined with the present model, and compare with the speed of sound measured with Brillouin spectroscopy in monophase NaCl-H_2O FIs. If our model predicts well the temperature dependence of pressure in FIs, then the measured and calculated speed of sound in monophase FIs should show comparable $\frac{dw}{dT}$. In Figure 4.11 we observe that the temperature dependence of calculated speed of sound is in good agreement with the measurements, within the uncertainty. Note however that our

uncertainty on $\frac{dw}{dT}$ is high, as it depends on the density second order derivative with respect to temperature.

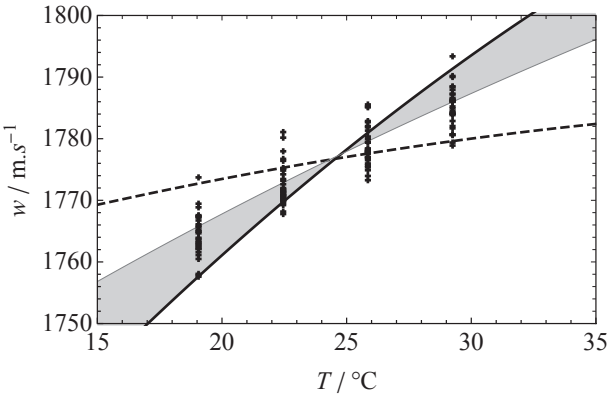

Figure 4.11: ***The speed of sound in monophase NaCl-H_2O FIs as measured with Brillouin spectroscopy and as calculated with our model.*** *Speed of sound w as calculated with the equation of state (EoS) of Archer (1992) and the pressure model, in a monophase FI (black solid line) and in a biphasic FI (black dashed line). w as calculated with the empirical fit of Al Ghafri et al. (2012) and the pressure model is also shown for a monophase FI (gray solid line); the filled area thereby represents the uncertainty on the calculation. Measured w of 33 isolated FIs from SyntHal24.6$_{19}$ is displayed (black crosses). Note that the curve of Al Ghafri and the measured w are rescaled with a factor 0.97093 and 1.00014, respectively, so that the value at 24.6 °C is equal to the value calculated with Archer EoS.*

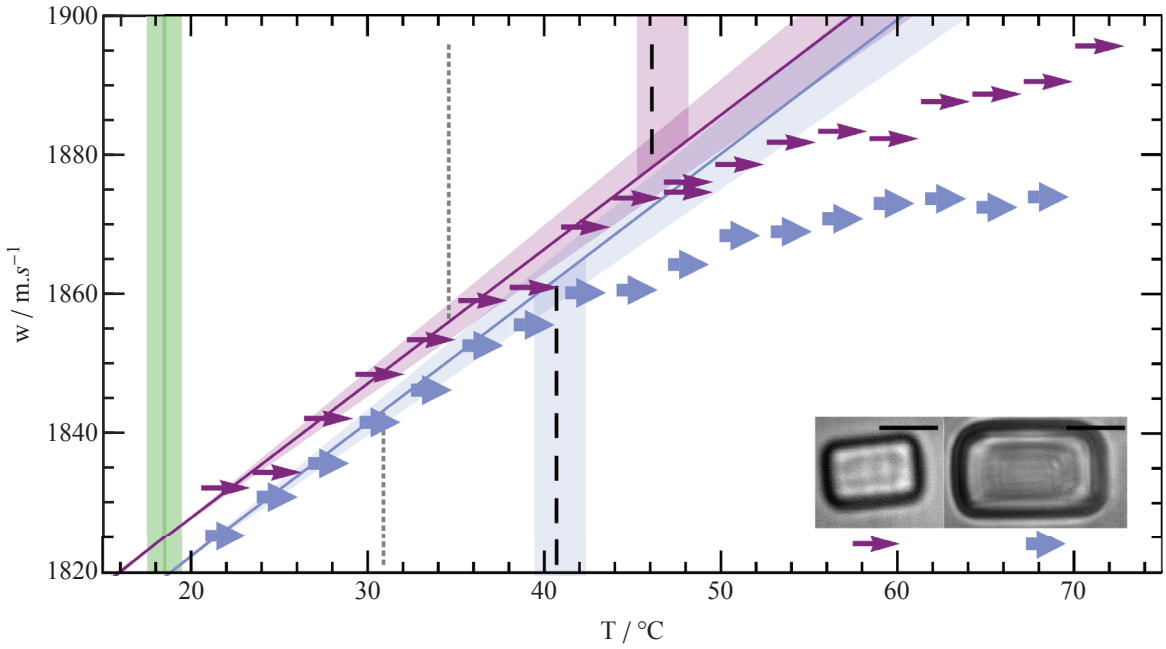

Figure 4.12: ***The agreement between calculated and observed ΔT_{lim} in Dead Sea FIs.*** *The small and medium FIs were both trapped at 18.5±1 °C (green vertical line with envelope). The speed of sound, measured stepwise along a heating path, deviates from the expected speed of sound of a FI deforming in the elastic mode (purple/blue solid lines) when the FI reaches yield stress (highlighted by purple/blue vertical strips). Based on the size-dependent elastic limit equation, Equation (3.4), vertical dotted gray lines indicate the expected yield stress if P-T slope is the same as in the NaCl-H_2O system, and black dashed lines indicate the yield we expect with the P-T slope calculated for a FI with current Dead Sea composition . Note: the slope of the elastic mode straight lines, 1.93 m.(s.°C)$^{-1}$, is the average slope obtained from speed of sound measurements in 49 FIs in halite crystals precipitated in the current Dead Sea (see Chapter 5). Size bar on pictures is 10 μm.*

The Brillouin yield stress tests (see Chapter 3) can provide us with a way to compare our pressure calculations on multi-component brines to experimental values. Thanks to the empirical equation Equation (3.4) developed in Chapter 3, we are able to know the pressure at which a FI of known size should yield. If T_f

and FI composition are also constrained, then we can use our pressure model to calculate the FI *P-T* path and determine ΔT_{lim}. When performing a Brillouin yield stress test, we should thereby be able to predict the temperature at which the plastic mode appears on the Brillouin speed of sound curve. To lead this experiment, we synthesized halite crystals by cooling a small amount of Dead Sea water sampled on the shores of Ein Gedi in 2017. In doing so, we make sure FIs do have a Dead Sea composition, and not an overconcentrated composition that would arise if synthesized by evaporation. The experiment illustrated in Figure 4.12 shows that indeed we are able to predict a temperature of yield stress within the uncertainties in the case of a Dead Sea FI.

Here are some rules of thumb emerging from the work led in this chapter, which can prove useful for any worker performing paleothermometry on halite fluid inclusions:

1. Mg-rich brines should produce halite FIs with a gentle *P-T* slope. This is the case of seawater-derived brines (Table 4.1), but also many other closed basin brines where diagenetic or hydrothermal inflows interact with dolomite or ultrabasic rocks (Eugster and Hardie, 1978; Hardie, 1984; Lowenstein and Risacher, 2009), like in Qaidam basin (Liu et al., 1997), Salar de Atacama (Lowenstein and Risacher, 2009), some lakes of British Columbia (Eugster and Hardie, 1978), lakes and salt pans of the Danakil area in Ethiopia (Holwerda and Hutchinson, 1968), lakes of the McMurdo Dry Valleys in Antarctica (Witherow and Lyons, 2011), to cite but a few.
2. Extremely dense and Mg-poor brines should produce high *P-T* slope FIs. This is the case, for instance, of sodium sulfate rich lakes, or soda lakes, that can reach densities > 1300 kg.m^{-3}. In this case, FIs selected for thermometry should be all the smaller.
3. Na-Cl dominated brines should have a $\frac{dP}{dT}$ comparable to pure NaCl system, that is, ~0.9-1 MPa/°C.
4. Flat FIs should be avoided, as they deform much more.

4.4 Conclusion

We have developed a model allowing the calculation of fluid inclusions internal pressure as a function of temperature, entrapment temperature, composition and shape. It uses the Pitzer formalism to calculate the density of the binary systems NaCl-H_2O, KCl-H_2O, $MgCl_2$-H_2O and $CaCl_2$-H_2O as a function of temperature, pressure and molality, and implements a mixing rule (Young's rule) to calculate the density of multi-electrolyte solutions. For a given composition and shape, the only free parameter is temperature, as pressure and NaCl saturation only modify as a response to temperature changes. The fluid inclusion is considered at mechanical and chemical equilibrium with the host; thus, through calculating the mechanical and chemical responses of the host to the volumetric and chemical changes in the fluid, the model backcalculates the pressure. The model is valid in the range 0-60°C, 0-100 MPa and ionic strength up to 10 molal. It has a 5% uncertainty in the case of NaCl-H_2O, and ~10% uncertainty in the case of more complex chemistries; the uncertainty increases

with concentration. It is supported by Brillouin spectroscopy measurements on NaCl-H_2O and Dead Sea fluid inclusions within the uncertainties. Through investigating three case studies, we have shown that:

- NaCl-H_2O fluid inclusions have a pressure-temperature (*P-T*) slope of ~0.95 MPa $°C^{-1}$ at 30 °C;
- Mg-rich fluid inclusions have a more gentle slope, about ~0.6 MPa $°C^{-1}$ in the case of the Dead Sea;
- Extremely dense magnesium-poor brines have a higher slope, about 1.1 MPa $°C^{-1}$ in the case of a Bristol Dry lake FI concentrated to 1300 kg m^{-3};
- These aforementioned composition-dependent trends in *P-T* slopes can be generalized to compositions not studied here, as highlighted by the trends in the volumetric properties of chloride, sulfate and carbonate solutions found in the literature;
- Flat fluid inclusions deform much more than cuboids, while elongated cigar shapes do not behave very differently from cuboids;

The model is especially intended to paleoclimatologists performing Brillouin thermometry on halite fluid inclusions, as it can be used to estimate the size limit of fluid inclusions as a function of their composition. It should be further extended to include sulfates and carbonates.

4.5 Abaci

In this section we provide *P-T* graphs plotting the calculated pressure in FIs as a function of T and T_f, along with the calculated reequilibration pressure for FIs ranging from 2 to 100 μm using the empirical equation Equation (3.4). We show the case of NaCl-H_2O FIs in Figure 4.13, current Dead Sea FIs in Figure 4.14, Lower Eemian Dead Sea FIs in Figure 4.15 and Bristol Dry Lake FIs in Figure 4.16. The compositions used for pressure calculations are NaCl-H_2O, Dead Sea (1993), DSLowEem and Bristol (see Table 4.2). Each isochore is labeled with its T_f value. For the NaCl-H_2O system, density and solubility EoS are well constrained on all 0-60 °C range. For the other compositions, *P-T* curves are plotted with dashed lines when $T_f < 20$ °C, to highlight the increase in uncertainty for this range of T_f, as observed in Figure 4.9.

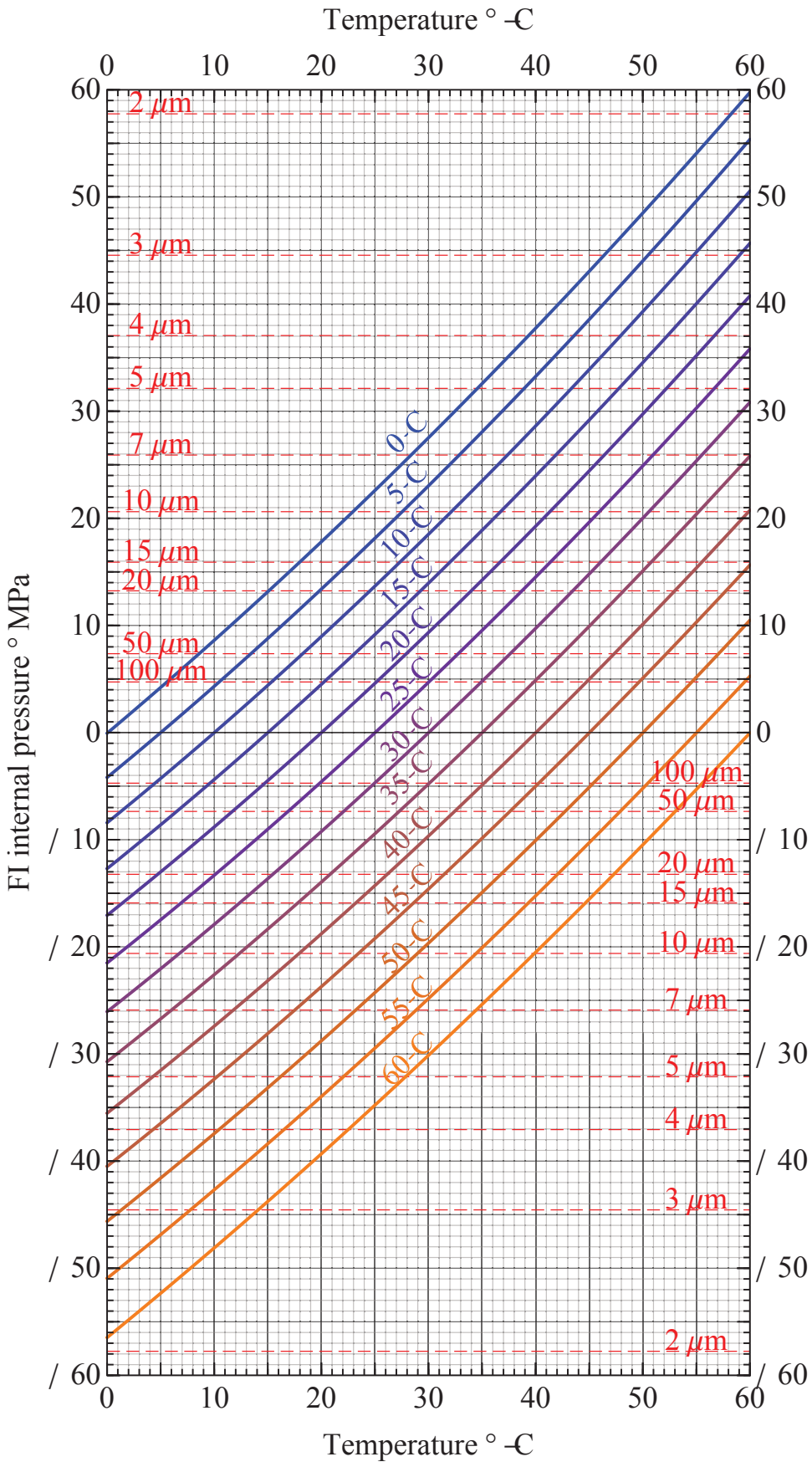

Figure 4.13: ***The elastic limit as a function of FI size and T_f in NaCl-H_2O system.*** *See text for details.*

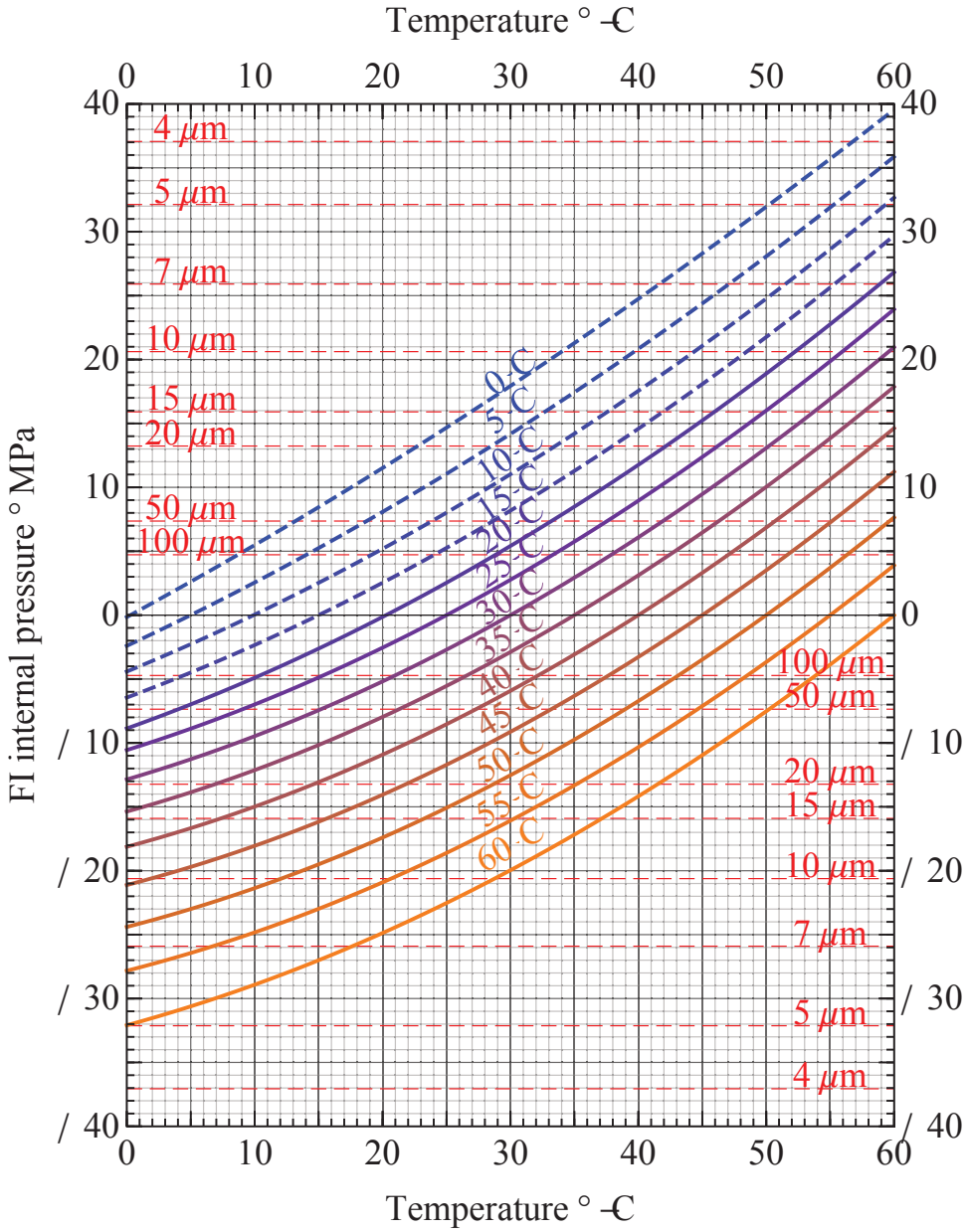

Figure 4.14: ***The elastic limit as a function of FI size and T_f for a current Dead Sea composition.*** *See text for details.*

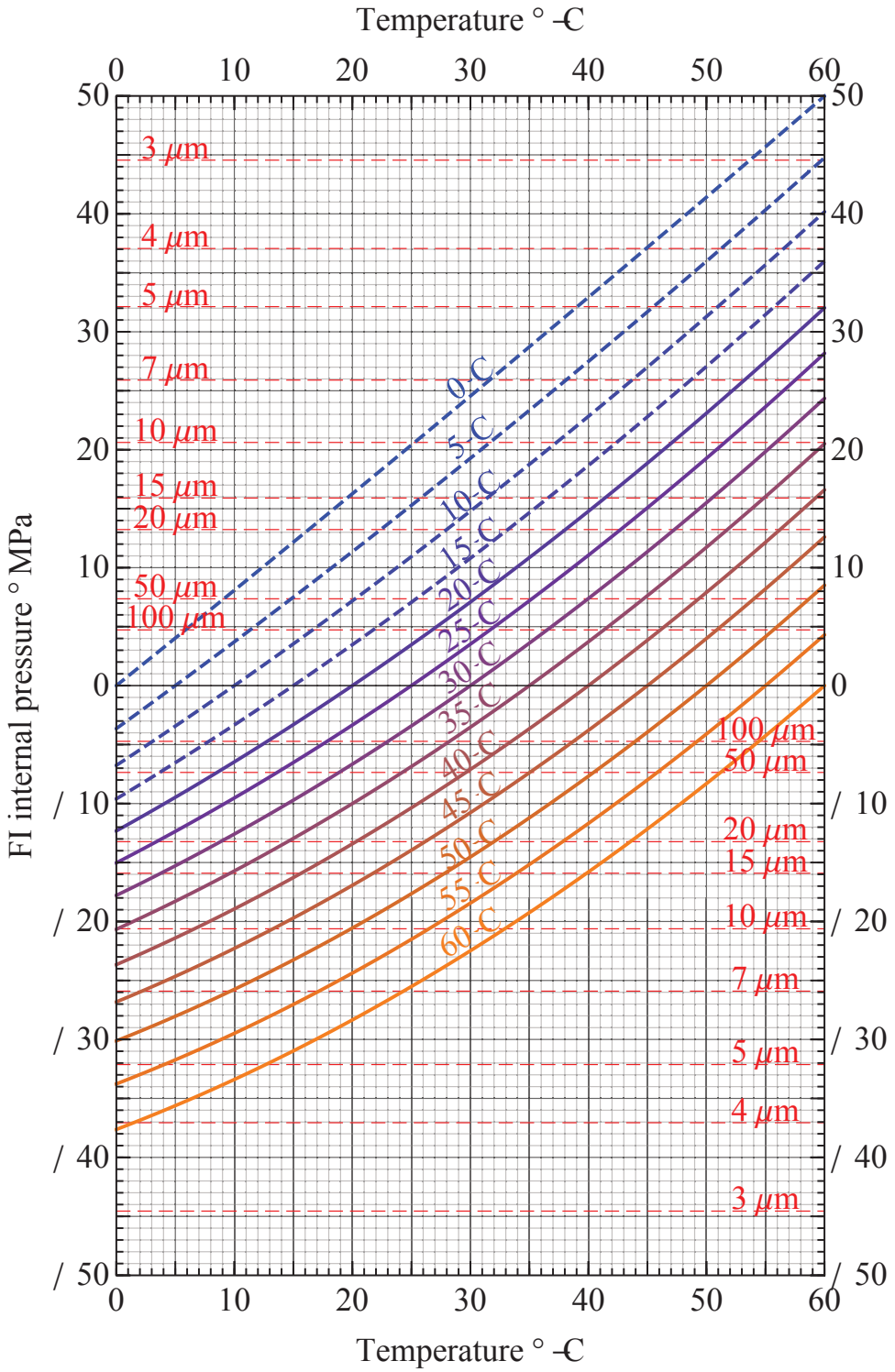

Figure 4.15: ***The elastic limit as a function of FI size and T_f for a Lower Eemian Dead Sea composition.*** *See text for details.*

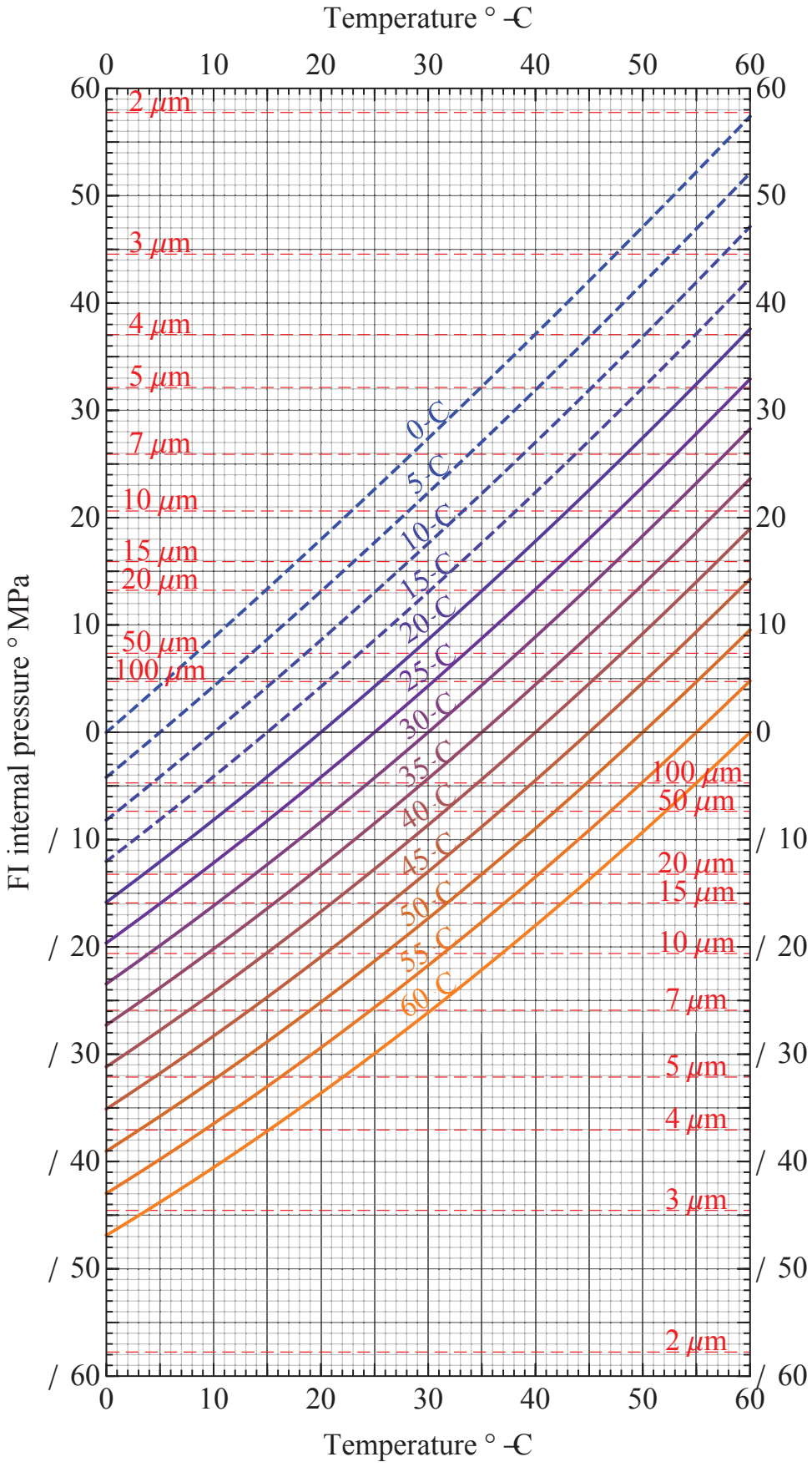

Figure 4.16: ***The elastic limit as a function of FI size and T_f for a Bristol Dry Lake composition.*** *See text for details.*

Appendix

4.A Comparison of the calculated density and thermodynamic derivatives to literature data

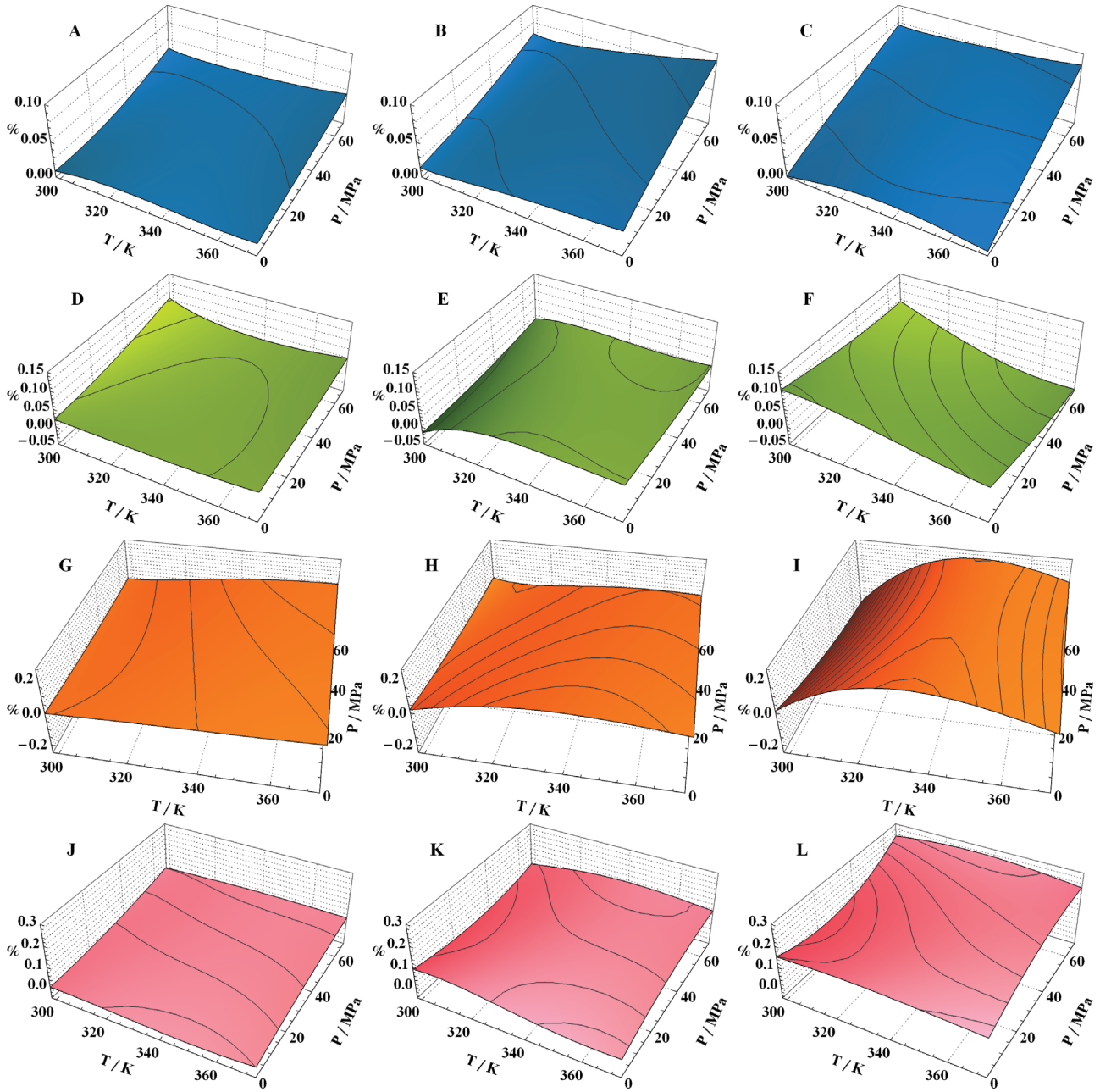

Figure 4.A.1: ***Deviation of the density EoS of Archer (1992) from the empirical fit of Al Ghafri et al. (2012) as a function of temperature, pressure and molality.*** *First line: NaCl-H_2O; second line: KCl-H_2O; Third line: MgCl2-H_2O; Fourth line: CaCl2-H_2O. First column: 1 molal; second column: 3 molal; Third column: (C) 6 molal, (F) 4.5 molal, (I) 5 molal and (L) 6 molal. Spacing of contour lines: 0.025%*

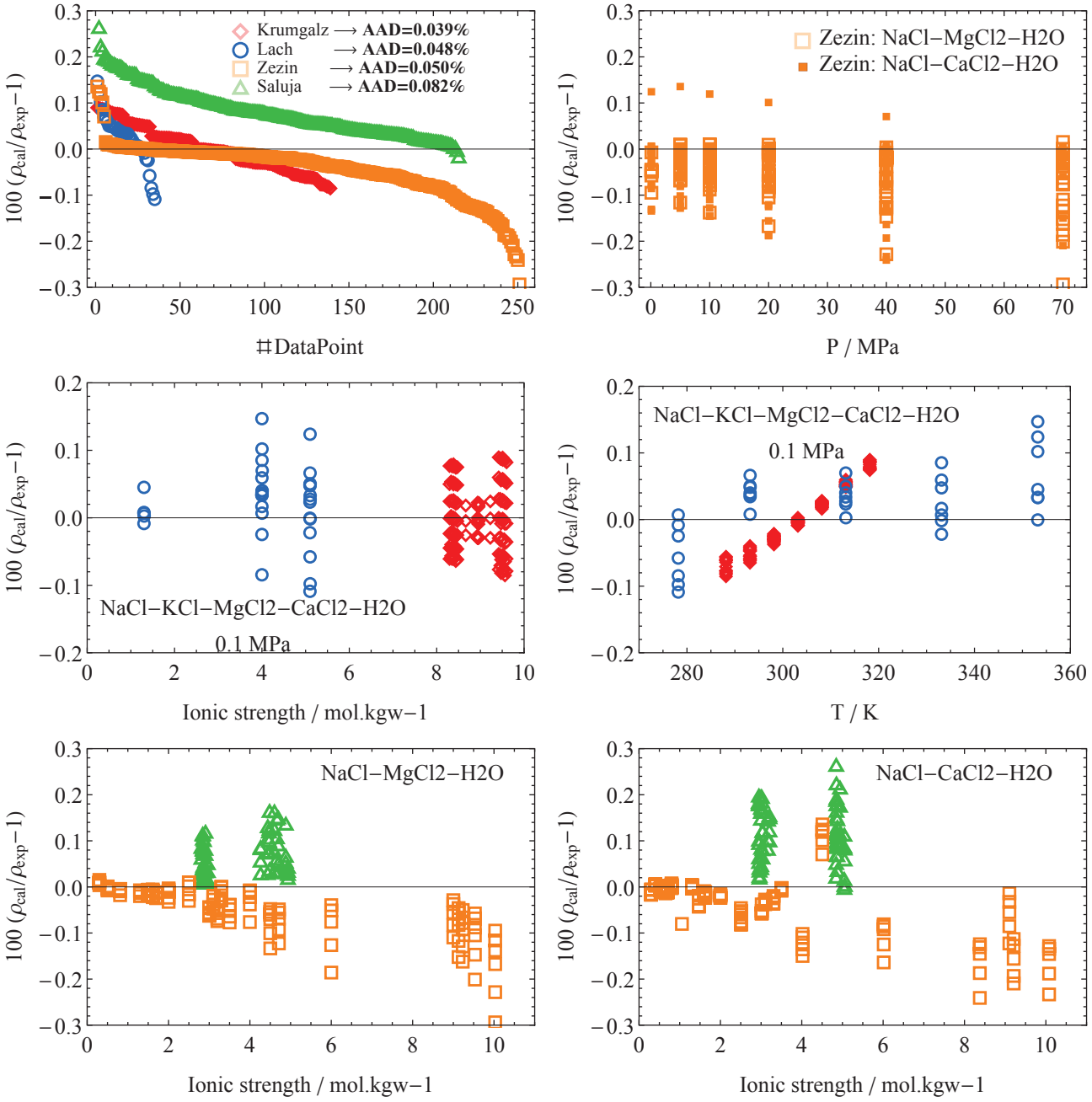

Figure 4.A.2: ***Deviation of calculated density of multi-component brines from experimental data, as a function pressure, temperature and ionic strength.*** *AAD, Average Absolute Deviation of this model from experimental data, writes:* $AAD = \frac{\rho_{calc}}{\rho_{exp}} - 1$. *Krumgalz and Millero (1982); Krumgalz et al. (1992): density experimental data of various Dead Sea waters; P-T-I ranges: 0.1 MPa, 15-45 °C, 8.3-9.6 molal. Lach et al. (2017): density experimental data of Na-K-Mg-Ca-Cl aqueous solutions; P-T-I ranges: 0.1 MPa, 5-80 °C, 1.3-5.1 molal. Saluja et al. (1995): density experimental data of Na-Mg-Ca-Cl aqueous solutions; P-T-I: 0.6 MPa, 23-99 °C, 2.7-5.1 molal. Zezin et al. (2014b): density experimental data of Na-Mg-Ca-Cl solutions; P-T-I ranges: 0.1-70 MPa, 25 °C, 0.3-10.1 molal. Top left panel shows data points from first to last ("#DataPoint") in descending order of deviation value.*

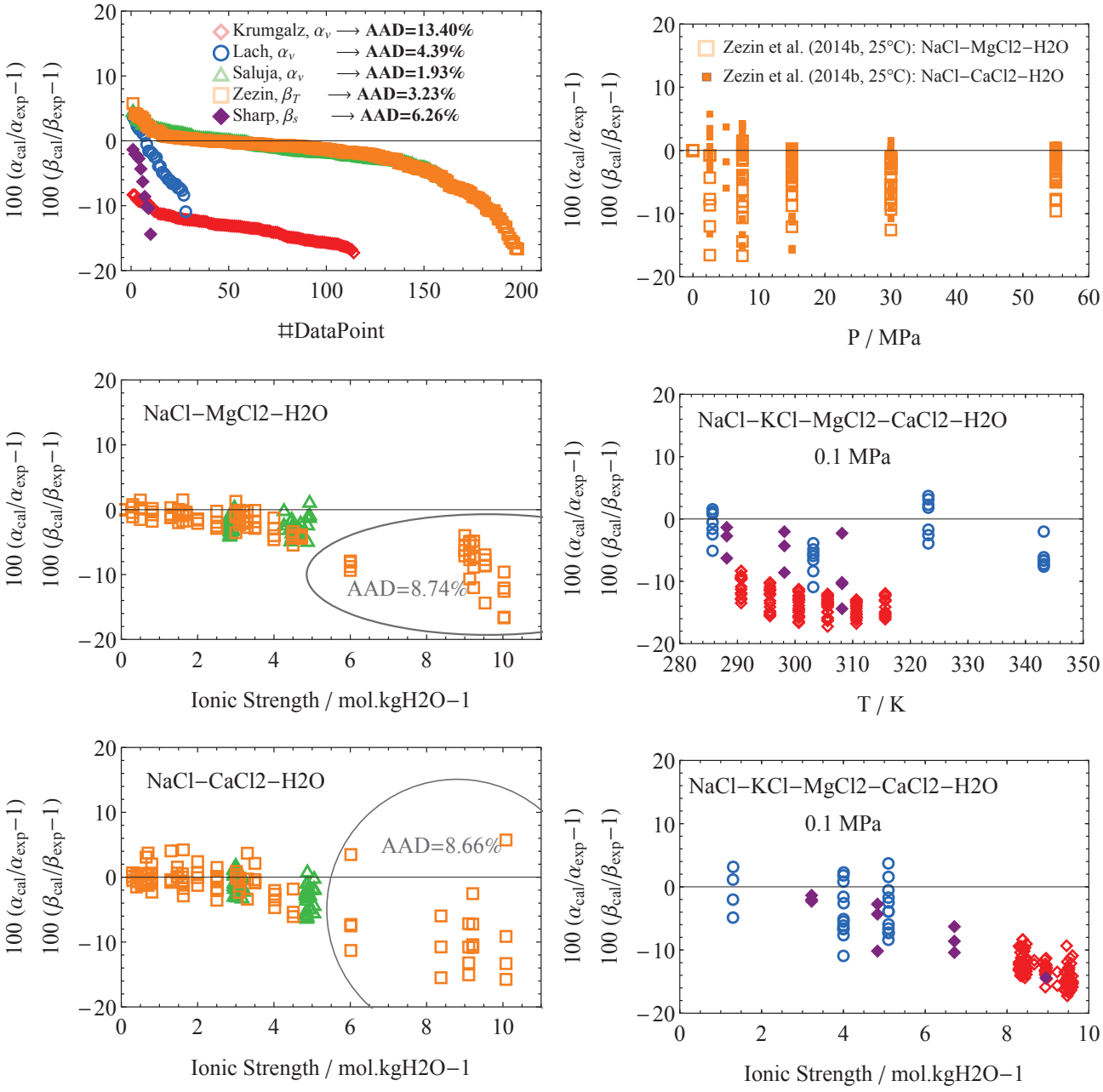

Figure 4.A.3: ***Deviation of calculated density first order derivatives of multi-component brines from experimental data, as a function pressure, temperature and ionic strength.*** *Krumgalz and Millero (1982); Krumgalz et al. (1992): thermal expansion experimental data of various Dead Sea waters; P-T-I ranges: 0.1 MPa, 17.5-42.5 °C, 8.3-9.6 molal. Lach et al. (2017): thermal expansion experimental data of Na-K-Mg-Ca-Cl aqueous solutions; P-T-I 0.1 MPa, 12.5-70 °C, 1.3-5.1 molal. Saluja et al. (1995): thermal expansion experimental data of Na-Mg-Ca-Cl aqueous solutions; P-T-I: 0.6 MPa, 36-86 °C, 2.7-5.1 molal. Zezin et al. (2014b): isothermal compressibility experimental data of Na-Mg-Ca-Cl solutions; P-T-I: 2.6-55 MPa, 25 °C, 0.3-10.1 molal (AAD of the most saline brines of this dataset is highlighted, as we noticed the uncertainty was higher for these specifically concentrated solutions that are of utmost interest to us).Sharp et al. (2015): isentropic compressibility of Dead Sea brines; P-T-salinity range: 0.1 MPa, 15-35 °C, 112-262.5 g/kg. Top left panel shows data points from first to last ("#DataPoint") in descending order of deviation value.*

CHAPTER 5

Temperature and hydrological variabilities during the Last Interglacial in the Eastern Mediterranean revealed by levels and deep water temperatures of the Dead Sea

ABSTRACT The optimum of the Last Interglacial (LIG, ~125,000 years before present) is documeted by speleothems, vegetation and lacustrine records as a period of increased moisture all over the Mediterranean region. And yet, the long core recovered by the Dead Sea Deep Drilling Project (DSDDP 5017-1) from the deep Dead Sea floor in 2011 exhibits its thickest halite sequence at this interval and was therefore described by several authors as an interval of extreme drought. To disentangle this conundrum and investigate regional climatic trends during the LIG, we sampled several tens of halite intervals from the core. The application of Brillouin thermometry to this record provides a unique quantification of temperature changes in this region during the Last Interglacial (LIG, ~135,000 to 115,000 years ago). Based on the recent discoveries made on the limnological regime of the current Dead Sea, we use the deep water temperature yielded by halite fluid inclusions (FIs) as a proxy for winter temperature. Furthermore, we show that Brillouin spectroscopy on halite FIs allows, at the same time, the quantification of the volume changes of the Dead Sea. Through comparing the calculated halite thicknesses inferred by the volume changes to the actual thickness of the halite sequences, we are in position (i) to quantify the evolution of the absolute level of the Dead Sea, (ii) to confirm that underwater halite focusing did operate in the past, and (iii) to constrain an average subsidence rate of 2.5 mm per year over the last 132,000 years for the northern basin (under 400 meters below sea level). Using the reconstructed lake level curve to quantify paleorainfall, we thus propose a complete temperature-precipitation reconstruction that enable us to outline a radically new narrative for the climate of the region during this period. We show that the LIG winter temperatures were mostly lower than today, and precipitation were much higher, albeit on a drying trend. Contrary to previous estimations, the region never experienced extreme drought during the LIG, and only reached conditions as dry as today towards the end of the period. The clear connections with the Mediterranean and the Atlantic exhibited by the record, along with the clear climatic trends observed, lead us to suggest a strong orbital forcing of the atmospheric circulation over this part of the globe, with a peak in drought and winter cold in phase with the maximum of autumn insolation. We explain this peculiar phasing by the inertia of oceans. A strong sea level pressure (SLP) gradient between the Azores High and the Icelandic Low is associated with a northward shift of the westerlies, hence dry and cold winters in the Eastern Mediterranean. The winter SLP gradient is itself controlled by the winter sea surface temperature (SST), which is forced by the autumn insolation due to a 2 to 3 months lag. We thus suggest that our record constitute an evidence for a millennial-scale North Atlantic Oscillation in phase with the October perihelion.

5.1 Introduction

The Dead Sea basin (DSB) is located along the boundary fault that separates the Arabian and African plates. The specific left-lateral transform motions along this faults system has progressively contributed to the deepening of the area through the last 15 million years (Ma), making the DSB the lowest elevation on the Earth surface (Garfunkel and Ben-Avraham, 1996). As such, it has become a vast collector of water and sediments, where no less than a 10 km-thick sedimentary infill has deposited since Miocene ages under the area where the Dead Sea (DS) lies nowadays (Brink and Flores, 2012). The diversity of these sediments is astounding, as elements leached out from rocks on the course of the Jordan river, dusts blown from the Sahara (Haliva-Cohen et al., 2012), concentrated hydrothermal brines circulating through the basin (Katz and Starinsky, 2009) and salt formations deposited in former periods later resurfacing as diapirs (Weinberger et al., 2006; Levy et al., 2018, 2019) have all ended up in the terminal lake. Depending on various driving forces and especially on climatic cycles, all these elements and particles have either built up or deposited. Alternations of facies recorded in the finely laminated sedimentary pile are just so many pages of the history of climate in the region (Ben Dor et al., 2019), all the more as the extreme concentration of the Dead Sea makes it an excellent drought sensor. Thus, the study of these sediments can provide invaluable information on the hydrology, key to the understanding of the past and future of humanity in this region. The strong connection of the southern Levant with Mediterranean and North Atlantic climates (Ziv et al., 2006) also makes it one of the few places that have recorded the evolution of moisture and temperature at an hemispheric scale.

The Dead Sea Deep Drilling Project (DSDDP; Stein et al. 2011; Neugebauer et al. 2014) organized for the first time in 2010/2011 a drilling campaign in the center of the immersed basin. The ~400m-long core that was drilled has thus offered a new insight into the climate of the last 220 ka. One of the greatest surprises that have arisen is the finding of very thick salt sequences that deposited during the Holocene (present Interglacial, PIG, ~11 ka-today) and the Last Interglacial (LIG, ~135-115 ka). Several authors have interpreted these sequences as evidences of extreme aridity (Neugebauer et al., 2014; Torfstein et al., 2015; Kiro et al., 2016, 2017; Torfstein, 2019). From this interpretation has emerged an inextricable conundrum (Bar-Matthews et al., 2019), as models (e.g. Kutzbach et al. 2014; Bosmans et al. 2015) and all other records in the region (e.g. Bar-Matthews et al. 2000, 2003; Vaks et al. 2006, 2010; Develle et al. 2011; Gasse et al. 2015) have depicted the LIG as a period of increased moisture that would have constituted a favourable climatic window for the African exodus of early modern humans (Vaks et al., 2007). In this work, we propose to address this issue through the study of the halite deposits of the LIG. We apply Brillouin spectroscopy on halite fluid inclusions (FIs) to measure the evolution of the temperature of the deep waters of the lake through time, which prove to be a good proxy for winter temperature. Furthermore, we develop and apply a new method that enables us to quantify the evolution of the lake concentration through time, which is a direct sensor of the relative volume changes of the lake. We use the relative volume changes as a constraint and simulate a wide variety of scenarii for the evolution of the absolute volume and level of the lake. Comparing the simulated thickness of deposited halite with the actual DSDDP

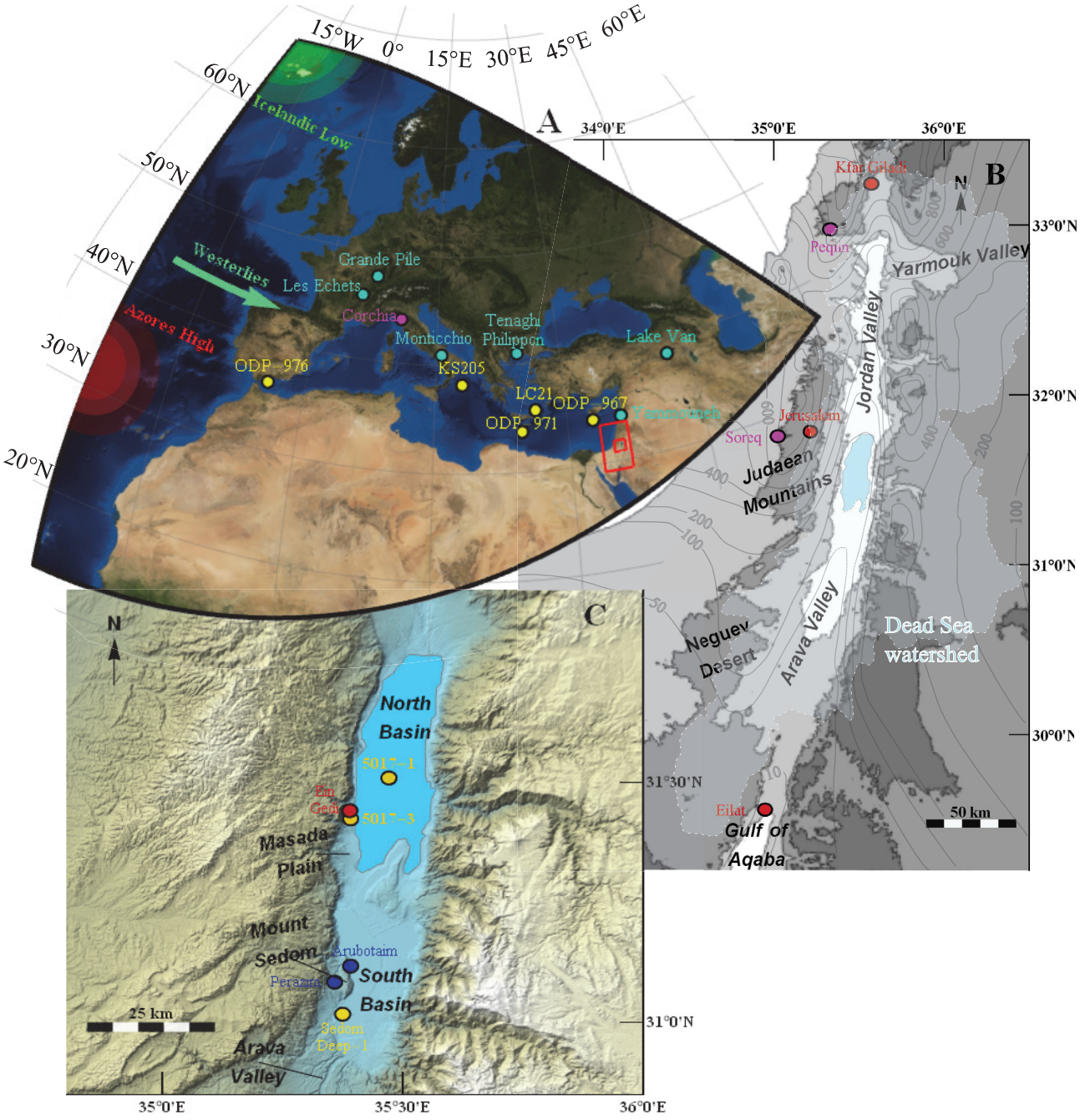

Figure 5.1: ***Location of the Dead Sea in the Mediterranean realm.*** *A: North Africa, Europe and the Near East, borderlands of the Mediterranean. Also shown, the area of minimum sea level pressure (Icelandic Low) and maximum sea level pressure (Azores High). B: The southern Levant and the Dead Sea watershed. Gray contour lines are isohyets, that is, they stand for precipitation amounts (mm yr^{-1}. C: The Dead Sea. Also indicated are the sites mentioned in the text. Light blue markers: pollen sites; yellow: boreholes; purple: cave speleothems; deep blue: outcrops; red: stations.*

record at several steps, we are able to point out the most likely scenario for the evolution of the lake and its basin. We use the reconstructed lake level curve to quantify the paleorainfall in the central Levant, which is by far the most active part of the watershed in contributing to the lake level (see Figure 5.1), through applying the method of Morin et al. (2019). This method proves particularly accurate for periods of halite precipitation and annual overturning, during which the density of the lake is homogeneous and thus the yearly evaporation of the surface layer is well constrained. The quantification of temperature and hydrology thereby enables us to

assess the actual state of climate in the Levant during the LIG, and to scrutinize potential linkages with regional climatic trends.

5.2 Limnology of the Dead Sea

5.2.1 Mechanisms of stratification

The Dead Sea was a meromictic lake (i.e. permanently stratified) for at least 300 years (Stiller and Chung, 1984), with a strong density difference (25 to 50g.kg^{-1}) between the 30-40 m thick upper layer and the deeper water body (Steinhorn, 1985). The thermohaline structure of the lake changed in 1979, when a complete mixing occurred, following a decrease in lake level initiated in the 1920s and emphasized in the 1970s through the intensification of the use of water from the main tributaries, the Jordan and Yarmouk rivers (Steinhorn, 1985). Since 1983, the Dead Sea has been a monomictic lake: it has overturned every end of year and remained homogeneous all winter long (Anati et al., 1987; Gertman and Hecht, 2002; Sirota et al., 2016), with the exception of the three years consecutive to the particularly wet episode that followed the eruption of the Pinatubo in 1991 (Bookman et al., 2014). The lake remains homogeneous as long as the temperature of the air is cool. As of March, when the air temperature gets warmer, a 25 m-thick upper layer, the epilimnion, builds up upon the colder deeper layer, the hypolimnion. The stratification gets all the stronger as the temperature and density gradients sharpen all the way to mid-August. The subsequent cooling of the epilimnion after peak summer leads to the weakening of the density gradient and, finally, the layers mixing in December. This annual regime is maintained through time by the lake negative water balance: the current inflow of ~300.10^6 m^3/yr[1] (+0.5 m/yr) does not make up for the rate of evaporation (~-1.1 to -1.3 m/yr), which results in a level decrease of 0.6-0.8m/yr (Lensky et al., 2005). This decrease is amplified by the pumping achieved by The Dead Sea Works for the industrial production of salts, with a total annual level drop of 1 meter. The destabilisation of the stratification needs the epilimnion to be denser than the hypolimnion, and this requirement is only matched under dry and cold conditions; any freshening may decrease the density of the epilimnion enough to dismiss durably this requirement, as it happened after the wet episodes of 1980 and 1992. Thus, it appears the monomictic regime settles after a long-term and pronounced negative water balance, while the meromictic regime re-establishes immediately upon the onset of positive water balance.

5.2.2 Implications of the limnological regime on halite precipitation

Three mechanisms may lead to the saturation of a saline lake with respect to halite, in descending order of importance on a short timescale: (i) evaporation, through increasing ions concentration; (ii) cooling, as the ability of water to dissolve solutes positively depends on temperature; (iii) salting out, that is, a decrease of NaCl solubility due to an increase of other cations proportions compared to Na^+. In the first place, considering evaporation as the prevailing driver, one expects halite precipitation to occur only under monomictic conditions.

[1]To compare with an estimated 1600.10^6 m^3/yr in the middle of the 20th century (Bentor, 1961)

Indeed, the denser and saltier deeper layer cannot reach saturation under meromixis, as it is not subject to evaporation. Conversely, if the evaporating upper layer hits saturation, it necessarily becomes saltier and denser than the deeper layer, and ends up mixing with the rest. Facts supported theory at the onset of monomixis in 1979, as halite precipitation started simultaneously (Steinhorn, 1983). Since then, up to 0.1 m of halite has deposited on the lake floor every year.

A series of recent papers dramatically increased the understanding of the processes controlling halite saturation and deposition. Arnon et al. (2016) showed the major role of double-diffusive diapycnal fluxes (DD flux; Stern 1960) at the interface between the two layers, where the stabilizing temperature gradient is in competition with the destabilizing salinity gradient, leading to gravitational instabilities and downwards transfers of salt from epilimnion to hypolimnion. This process, which becomes significant as of mid-August, accounts for the continuous precipitation of salt at the bottom of the lake despite the isolation of the hypolimnion due to stratification. In turn, it also accounts for the undersaturation in the epilimnion from spring to autumn, despite the intense "production" of salinity with evaporation. Sirota et al. (2016, 2017) assessed the seasonality of halite saturation and precipitation in the two layers. They showed the whole water column was supersaturated with respect to NaCl from the beginning of autumn to the end of winter, due to cooling. During this period, small cumulate halite crystals, several hundreds of microns in size, precipitate in the whole lake and deposit on the bottom. With the onset of stratification in March, the warming epilimnion becomes undersaturated, and the hypolimnion is not supersaturated enough to nucleate halite crystals. Therefore, from March to beginning of September, halite only grows as coarse crystals directly on the bottom. We summarize these seasonal mechanisms in Table 5.1.

	Dec. to Feb.		Mar. to mid-Aug.		mid-Aug. to Sep.		Oct. to Nov.	
	Epi	Hypo	Epi	Hypo	Epi	Hypo	Epi	Hypo
Temperature	↘	↘↘	↗↗	↗	↘↘	↗↗	↘↘	↗↗
Saturation	++	++	-	+	-	+	+	+
Halite	Cum.	Cum.	Dissol.	Coarse	Dissol.	Coarse	~Cum.	Cum.
Water column	Mixed		Low DD		High DD		High DD	

Table 5.1: ***Seasonal characteristics of the Dead Sea.*** *Cum: cumulate halite nucleating in the water column; Coarse: coarse halite crystals growing on the lake floor; Epi: epilimnion; Hypo: hypolimnion; Dissol: dissolution; DD: Double-diffusive diapycnal flux (downward salt and heat fluxes).*

In addition to these annual considerations on halite precipitation, Sirota et al. (2018) developed a model for the pluriannual mechanisms of halite deposition at basinal scale. Based on their *in-situ* observations (Sirota et al., 2017) and considering that the sedimentary record on the Dead Sea margins (i.e. above 400 m below sea level) mainly lacks halite layers (Waldmann and , 2002) while the center of the basin presents thick halite layers (Kiro et al., 2016), they proposed a concept of halite focusing (Figure 5.2). In summer, the undersaturated

epilimnion dissolves the salt layers that it deposited in winter, thereby only the hypolimnetic lake floor remains covered with halite. Through retreating year after year, the lake leaves no salt deposits on the open margins, as all the salt is preferentially recycled and deposited on the deep lake floor. In the following, we call this model "underwater halite focusing".

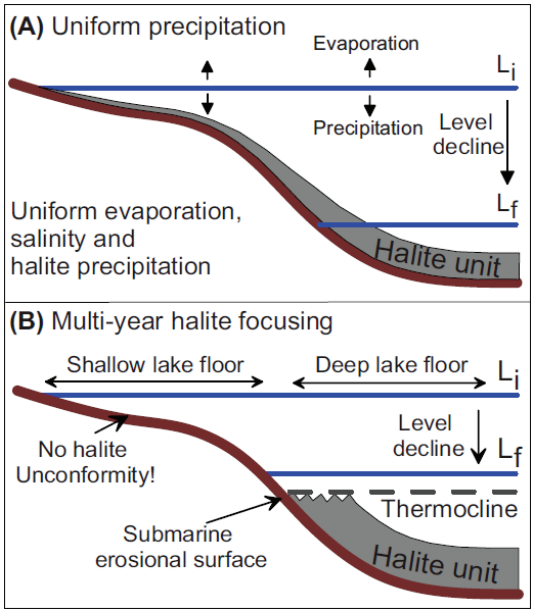

Figure 5.2: ***Schematic illustration of halite deposition in deep basins.*** *From Sirota et al. (2018). (A) Uniform precipitation. Evaporation surface area is equal to the accumulation halite surface area. As lake level (blue lines) declines, the submerged areas become smaller, resulting in thickening of the halite unit in the basin because of the longer accumulation interval there. (B) Multi-year halite focusing. Halite is deposited on the deep floor at a very high rate, at the expense of halite dissolution on the shallow lake floor. L_i and L_f are the initial and final levels of the halite deposition interval.*

5.2.3 What does the temperature we measure in bottom growth halite FIs mean ? Relations between hypolimnion and air temperatures

In this study, we determine the temperature of the Dead Sea hypolimnion through measuring the entrapment temperature T_f of FIs in bottom growth halite. In order to estimate air temperature variations from our data, we thus need to know the relation between the Dead Sea hypolimnion temperature and the temperature of the air. We gathered available hypolimnion temperature (Gertman et al., 2010; Arnon et al., 2016) and air temperature data (Figure 5.3). For the latter, data from the Dead Sea is sorely lacking. The U.S. National Oceanic and Atmospheric Administration (NOAA) provides worldwide air temperature data through the Global Historical Climatology Network (GHCN) database. The closest stations prividing sufficiently extensive data in the area are Tel-Aviv airport, close to the Mediterranean coast, and Eilat, at the northernmost tip of the Gulf of Aqaba,

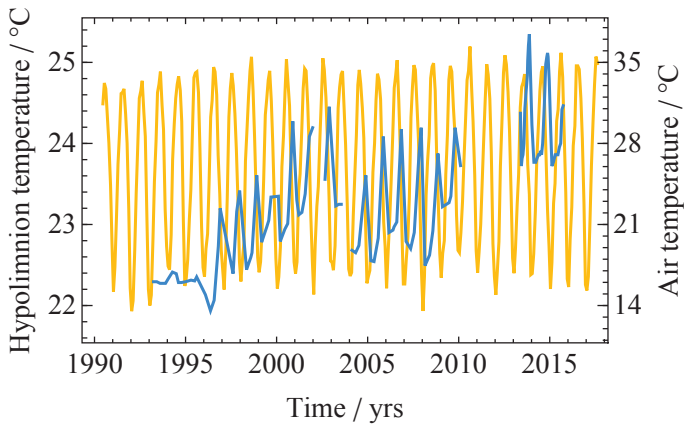

Figure 5.3: ***Hypolimnion temperature and air temperature through time.*** *Temperature of the Dead Sea hypolimnion (blue) and air temperature as measured in the nearby meterological station of Eilat (yellow).*

Red Sea. The Dead Sea and Eilat are connected through the Arava valley, and thus pertain to the same climatic area (Goldreich and Karni, 2001), while both are separated from the Mediterranean by the Judean Mountains. We thereby chose Eilat station.

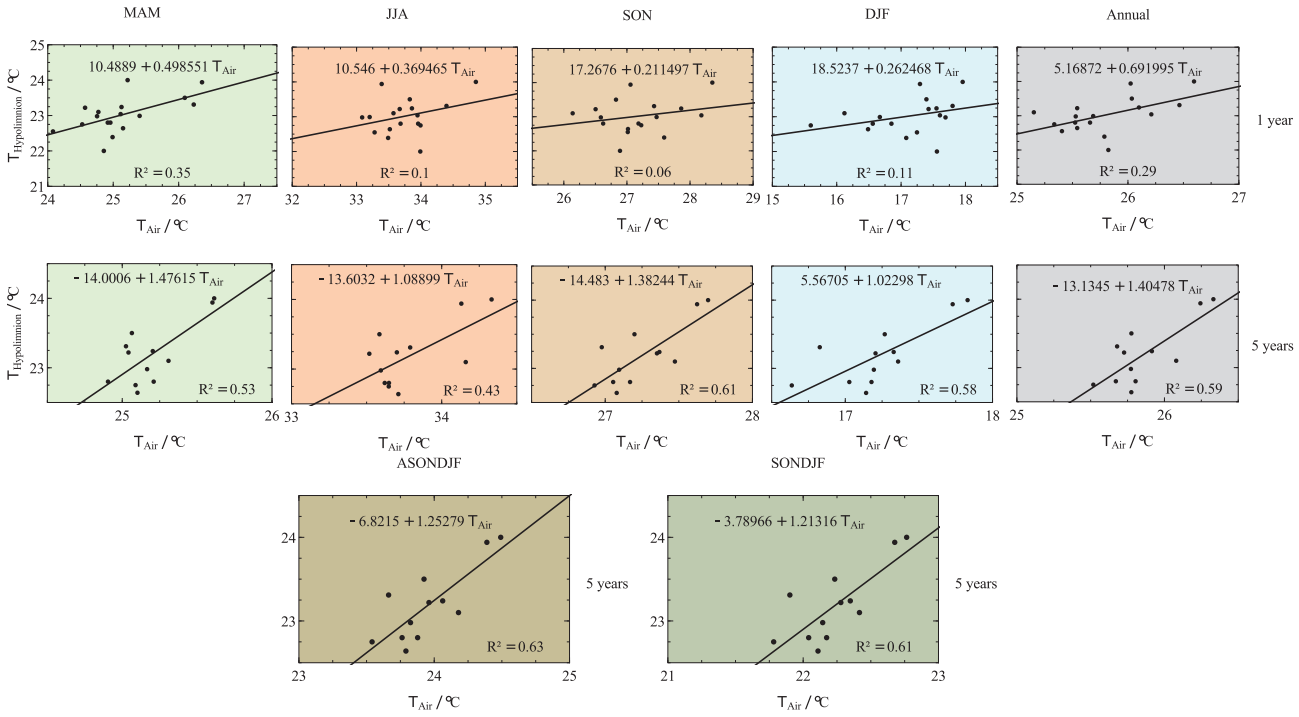

Figure 5.4: ***Correlation of the Dead Sea hypolimnion temperature with seasonal, annual and pluri-annual air temperature.*** *Hypolimnion average temperature during March-August period of year n (1996 to 2015). Annual 1 year and 5 years air temperature correspond to average air temperature from March (year n-1 and n-5) to February (year n), and seasonal 1 year and 5 years correspond to average air temperature during indicated months inside the same period, respectively.*

In Figure 5.4, we show the results of several linear regressions, which aim at testing the correlation between the temperature of the hypolimnion and the temperature of the air at various periods. Note that as the halite facies we use in this study, coarse crystals, precipitates during March through August, we use an average hypolimnion temperature for this period instead of a whole year average temperature. First, we observe that the temperature of the hypolimnion is poorly correlated with all seasonal and annual air temperature signals on the 1-year scale, although annual and spring average air temperatures show a coefficient of determination somewhat higher than the rest. Additionally, we observe that the amplitude of air temperature changes on the 1-year scale is much higher than the amplitude of hypolimnion temperature changes, as shown by the slope values systematically < 1. Correlations are much stronger on the 5-year scale, especially in the case of autumn, winter and annual average air temperatures. Lastly, we tested regressions on many other periods of the year on the 5-year scale, and found that average air temperature from August through February and from September through February show the highest coefficients of determination with hypolimnion temperature. Among the best correlations, winter (5 years) yields the slope closest to 1. To sum up, hypolimnion temperature is most directly linked to 5-year average winter air temperature, but the correlation is very good for a period extending

from late summer to February.

The observed seasonality of the connection between air and deep water temperatures in the Dead Sea can be very well explained by the seasonality of the lake thermo-haline structure and fluxes. From March to Mid-summer, the lake is strongly stratified, thus preventing thermal connection between the hypolimnion and the atmosphere. A thermal connection progressively establishes as DD fluxes strengthen during summer and autumn. The thermal connection peaks during winter mixing, when the thermal barrier between the atmosphere and deep waters completely disappears. Therefore, the temperature of the Dead Sea deep waters is apparently a good proxy for the 5-year averaged air temperature of the late summer to late winter period (SONDJF, or ASONDJF). The dominance of the cold season in this period would account for the Dead Sea hypolimnion temperature being currently ~2 °C lower than the mean annual air temperature. Note however that since the thermal connection strengthens progressively from August (and certainly even before) to November and becomes complete (slope = 1) in winter, we cannot infer a specific and well-defined period whose temperature would be mimicked by the hypolimnion. In the following, we use the hypolimnion temperature as a proxy for winter temperature.

5.3 Material

5.3.1 The Dead Sea Deep Drilling Project long core (DSDDP 5017-1)

The Dead Sea Deep Drilling Project (DSDDP) is an International Continental Scientific Drilling Program (ICDP)-funded drilling campaign performed during winter 2010-2011. The longest recovered sequence, 5017-1 (Figure 5.5), drilled by a rig in the center of the lake, reached a sediment depth 455 m below lake floor (blf). At this position in 2010, the floor of the lake was 297 m below lake level, hence the deepest part of the sequence lied at 752 m below lake level. With a ~89% core recovery, total length of the recovered sequence is ~406 m. The cores were first opened at GFZ, Potsdam, where several analyses were carried out and photographs were taken (Figure 5.5). Then they were transported to the final storage at MARUM core repository, Bremen, where they have been kept at 4 °C since then.

The lithology and measured ages allowed for the subdivision of 5017-1 into stratigraphic units. These units are defined and named following the typical stratigraphy recognized and described in the late Quaternary Dead Sea basin (Neev and Emery, 1967; Stein, 2001; Bookman et al., 2006): the Amora Unit (older than 135 ka, deeper than 320 m blf in DSDDP 5017-1), the Last Interglacial Samra Unit (135-75 ka, 320-199 m blf), the Last Glacial Lisan Unit (75-11 ka, 199-72 m blf) and the Holocene Zeelim Unit (11 ka to present, 72-0 m blf). These units display sharp lithological differences, which reflect profound changes in limnological conditions of the Dead Sea precursors (e.g., levels, structure and chemistry), largely affected by hydrological changes in their watersheds (Stein, 2001; Enzel et al., 2003). In their description of the long core sequence, Neugebauer et al. (2014) classified main lithologies as follows (Figure 5.5): (1) alternating aragonite and detritus (*aad*), mainly deposited during wet glacial intervals Lisan and Amora; (2) laminated detrital marl (*ld*), primarily

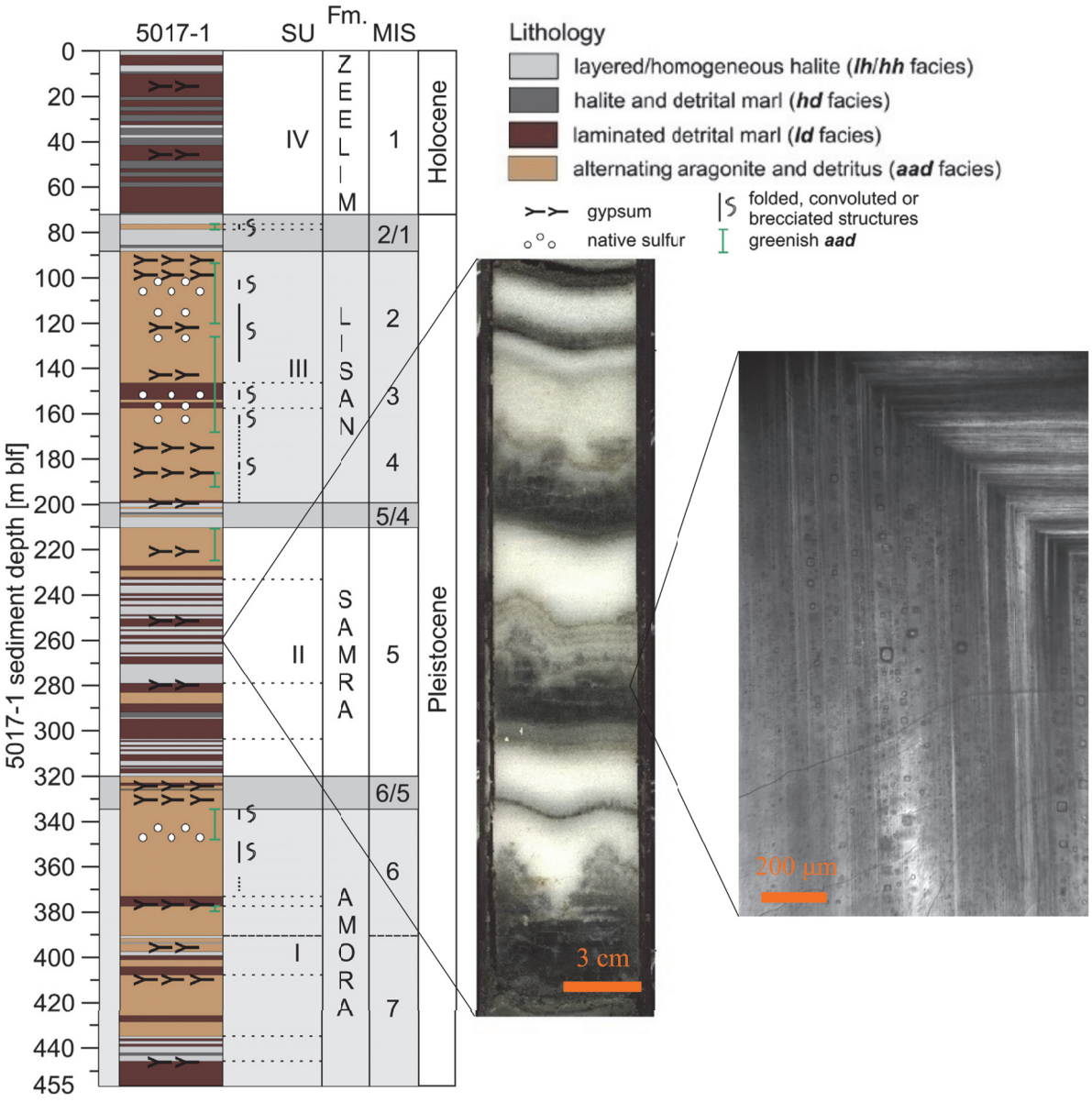

Figure 5.5: ***Lithological and stratigraphic profile of core 5017-1 recovered by DSDDP.*** *Profile from Neugebauer et al. (2014). SU: sediment unit, Fm.:sediment formations of the Dead Sea Group, MIS: marine isotope stage. In the center, photograph of an alternating cumulate/coarse halite section in core 5017-1-A-101. On the right, microscope photograph of a coarse halite crystal, showing a chevron structure with growth bands containing numerous FIs.*

encountered in interglacial intervals Samra and Zeelim; (3) halite, either alternating fine cumulate and coarse crystals (Figure 5.5) or cubic crystals scattered in mud, and exclusively occurring in interglacial intervals.

Age constraints on 5017-1 sequence were provided by Neugebauer et al. (2014) and Torfstein et al. (2015), using radiocarbon and U/Th on aragonite dating for sections younger and older than ~55 ka, respectively, along with lithological changes tied to dated key points in other regional records. We used these ages to construct the age model used in this study (Figure 5.6). Additionally, we implemented different sedimentation rates for halite (15 mm yr^{-1}, estimated from Palchan et al. (2017)) and non-halite deposits (rate adjusted so that it tallies with dating and halite rate; it yielded non-halite sedimentation rates comprised between 3 and 6 mm yr^{-1} during MIS5e).

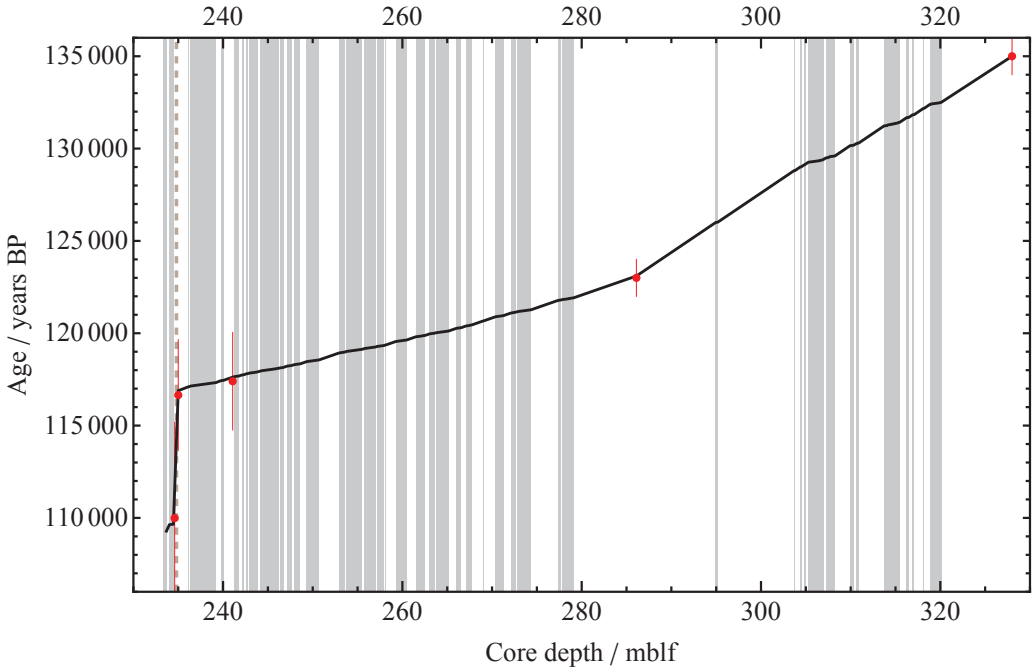

Figure 5.6: ***Age-depth model for the Last Interglacial in 5017-1.*** *Age data from Torfstein et al. (2015). See text for sedimentation rates. Gray vertical bars: halite layers; Dashed vertical line at 234.80 m blf: gravel deposit, marked by a sedimentary hiatus, interpreted as a mass waste deposit not well-recovered during the drilling (Neugebauer et al., 2014, 2016).*

5.3.2 Halite samples

In collaboration with Markus Schwab and Ina Neugebauer, researchers at GFZ, we went to MARUM where we collected the required cores, and transported them to GFZ to proceed to sampling. As most halite sections are consolidated, we had to proceed to saw most needed sections. We sampled 50 sections, including 41 in the Marine Isotope Stage 5e (MIS5e, 132-117 ka, 320-234 m blf). The 120 m-thick Last Interglacial Samra Unit comprises ~34 m of salt, including 31 m solely in MIS5e. Most of the salt sections are alternations of fine cumulate and coarse halite crystals. We mostly sampled coarse crystals inside these alternations. We mainly selected them in the middle of salt layers, and tried to avoid the bottom of layers as much as possible. This is because the appearance of a salt layer in the section may highlight a limnological transition in the lake, thus it is preferable to select crystals that precipitated several years after this transition, when the lake was likely to be at thermal equilibrium. Samples were then transported to the University of Lyon, where they were stored in the Brillouin spectroscopy room, which is air-conditioned to $21 \pm 1\,^{\circ}\mathrm{C}$. Estimated T_{Min} and T_{Max} undergone by samples are $4\,^{\circ}\mathrm{C}$ and $30\,^{\circ}\mathrm{C}$, respectively. For Brillouin spectroscopy experiments to be carried out, we extracted small pieces out of salt blocks using a chisel. Measured samples were smaller than 10 mm so they fit the temperature-controlled stage, thinner than 1 mm to ensure temperature difference with stage silver block $< 0.1\,^{\circ}\mathrm{C}$ and flat to ensure a good thermal contact. We made sure measured FIs were primary; in particular, we selected them in chevron and banded structures, as these are typical textures of primary halite growth (Figure 5.5).

5.4 Methods

The speed of sound w measured in halite FIs can be used to constrain both the temperature of the parent brine (Chapter 3) and the relative volume changes of the brine. In this section, we give details on the methodology developed to this end. We first explain the method developed to estimate relative volume changes R_v (Section 5.4.1.1) and how we convert these relative volume changes into absolute lake levels (Section 5.4.1.2). Then we give details of the methodology used for the reconstruction of bottom water temperatures (Section 5.4.2).

5.4.1 Method for lake level reconstruction

5.4.1.1 Determination of relative volume changes

Upon evaporating and increasing the concentration of solutes, a brine gets denser (Table 4.2) and less compressible (Figure 4.10). As shown in Equation (4.23), the speed of sound in a liquid is a function of the square root of the inverses of both its density (ρ) and compressibility (β). However, the decrease of β prevails compared to the increase of ρ[2], so well that one expects an increase of the speed of sound in the evaporating brine.

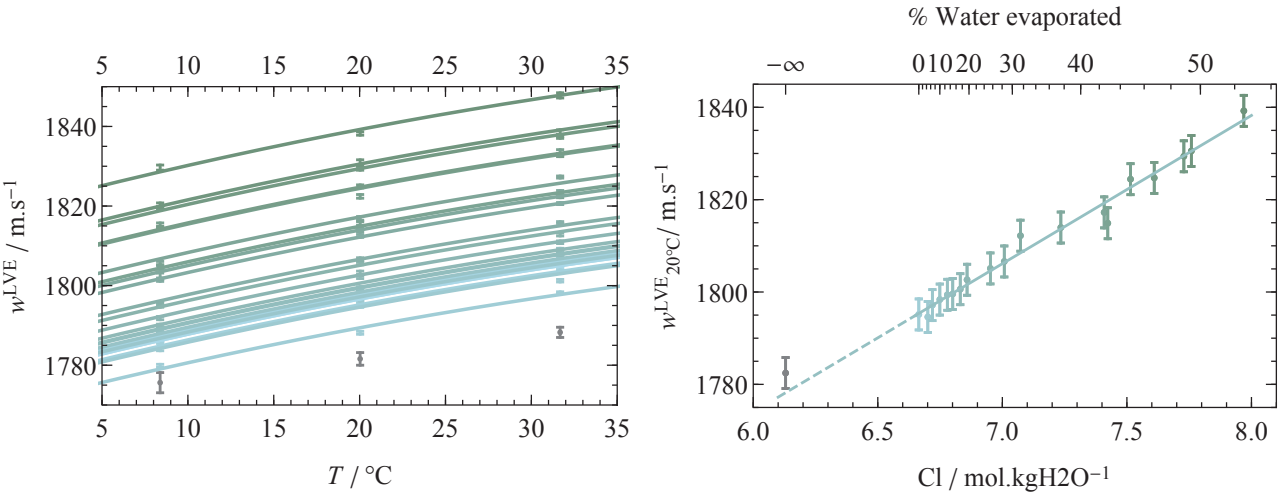

Figure 5.7: ***Calibration of the speed of sound at liquid-vapor equilibrium (w^{LVE}) as a function of the evaporation degree of a synthetic LIG Dead Sea-like brine.*** *Left Panel: w^{LVE} measured at 3 differents temperatures in droplets sampled from the evaporating brine, from initial chemistry (lightest blue) to most concentrated (darkest blue). Each data point is the average of 15 measurements; error bars are the standard error on the average. Same parabolic equation $1787.06 + 1.11198T - 0.00751608T^2$ fitted to each trio, rescaled by a factor. Right Panel: w value yielded by the fitted equation at 20 °C, for each sampled droplet, as a function of chlorinity (molal). Initial brine (lightest blue point) measured 5 times at 5 different days; error bars, identical for all data points, are the standard deviation on these 5 measurements. Note: on the two panels, values measured for pure H_2O saturated with NaCl displayed for comparison (grey points).*

In order to quantify the dependence of the speed of sound on the evaporation degree in a brine at liquid-vapor equilibrium (LVE), we prepared a 40 mL solution with the composition of Dead Sea as it was at the beginning of the LIG (as measured with Cryo-SEM in FIs from halite samples recovered at 319.7 m blf in

[2]In the case of a Dead Sea chemistry as it was at the beginning of the LIG, we calculate a 10.9% decrease of β_T and 2.8% increase of ρ when 50% of the water evaporates.

sequence 5017-1, Kiro et al., 2017; see composition DSLowEem in Table 4.2). We set the solution to evaporate in a beaker and sampled a droplet (~2 µL) every ~3 hours in a capillary. To avoid partial evaporation of the droplet, capillaries were rapidly sealed with wax in a wet atmosphere. To ensure saturation with respect to NaCl whatever the temperature, sampled droplets were at equilibrium with a halite crystal placed inside each capillary. After sealing, Brillouin measurements were performed straightway on each sampled droplet, at three different temperatures. A parabolic equation, obtained by fitting the whole dataset, was then adjusted to each w^{LVE} trio with a factor. Results are shown in Figure 5.7, left Panel.

Thereafter, we call $w^{\mathrm{LVE}}_{20\,^{\circ}\mathrm{C}}$ the value yielded at 20°C by the fit to each droplet trio of values. We tested the dependence of $w^{\mathrm{LVE}}_{20\,^{\circ}\mathrm{C}}$ on several parameters related to the evaporation degree, namely: i) the mass fraction of evaporated water $1 - R_{\mathrm{H2O}}$, ii) the brine density ρ, iii) the brine ionic strength I and iv) the brine chlorinity Cl (note that the water mass loss was measured with high-precision weighing scales at each sampling step while ρ, I and Cl were calculated with the program PhreeSCALE (Lach et al., 2016), a code allowing for the calculation of the volumetric properties of complex aqueous electrolyte solutions). While $w^{\mathrm{LVE}}_{20\,^{\circ}\mathrm{C}}$ showed an exponential dependence on $1 - R_{\mathrm{H2O}}$, the dependence on ρ, I and Cl proved well-fitted with a line. As the best fit was achieved with Cl, with $\chi^2 = 0.29$, in this work we use the equation obtained from the linear regression of $w^{\mathrm{LVE}}_{20\,^{\circ}\mathrm{C}}$ as a function of chlorinity:

$$w^{\mathrm{LVE}}_{20\,^{\circ}\mathrm{C_{Cal}}}(Cl) = 1581.37 + 32.1085Cl. \tag{5.1}$$

Fit to the data is shown in Figure 5.7, right Panel. Due to differences in correction factors (see Chapter 2), w obtained with Brillouin spectroscopy from identical brines in a capillary or in a halite inclusion are not the same. Therefore, the equation used in this work to relate the speed of sound measured in FIs at LVE to chlorinity is:

$$w^{\mathrm{LVE}}_{20\,^{\circ}\mathrm{C_{DSDDP}}}(Cl) = k.w^{\mathrm{LVE}}_{20\,^{\circ}\mathrm{C_{Cal}}}(Cl), \tag{5.2}$$

with k a constant factor determined as follows:

$$k = \frac{w^{\mathrm{LVE}}_{20\,^{\circ}\mathrm{C_{DSDDP}}}(Cl_{\mathrm{initial}})}{w^{\mathrm{LVE}}_{20\,^{\circ}\mathrm{C_{Cal}}}(Cl_{\mathrm{initial}})}, \tag{5.3}$$

with $w^{\mathrm{LVE}}_{20\,^{\circ}\mathrm{C_{DSDDP}}}(Cl_{\mathrm{initial}})$ the average speed of sound at 20 °C measured in FIs in the halite sample from early MIS5e halite layer located 319.7 m blf in sequence 5017-1 and $w^{\mathrm{LVE}}_{20\,^{\circ}\mathrm{C_{Cal}}}(Cl_{\mathrm{initial}})$ the speed of sound at 20 °C in the initial synthetic brine before evaporation. We calculate $k = 0.9920$.

The volume of the brine can be expressed as follows:

$$V = m_{\mathrm{H2O}}\frac{m_{\mathrm{tds}} + 1}{\rho}, \tag{5.4}$$

with m_{H2O} the mass of water in kg and m_{tds} the total molality of dissolved salts. Hence R_{v}, the ratio of V to

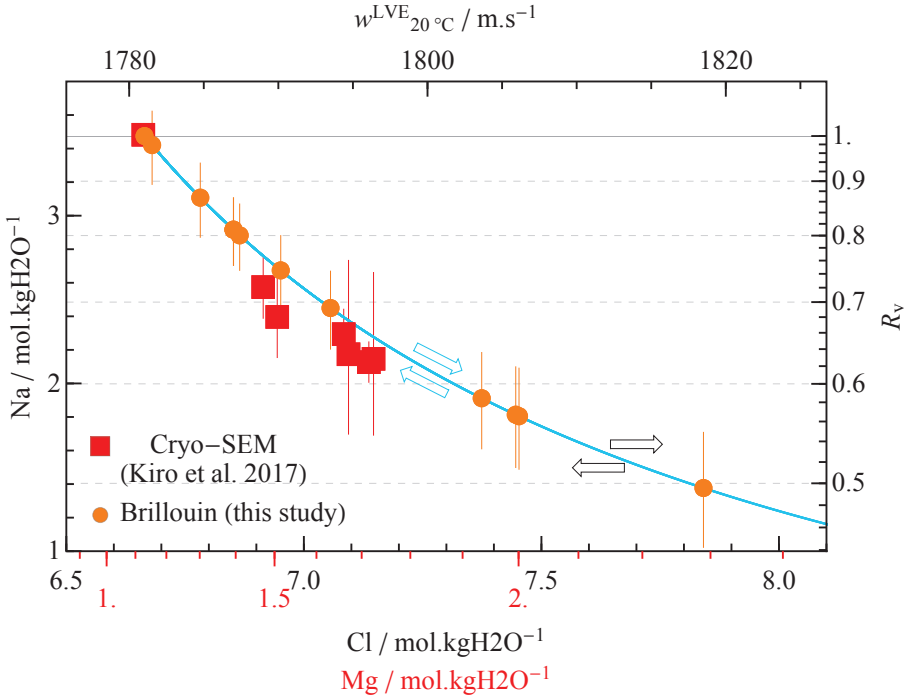

Figure 5.8: ***Na vs. Cl in Dead Sea halite FIs.*** *Blue line: evaporation curve calculated with PhreeSCALE with initial chemistry measured at 319.7 m blf in sequence 5017-1. Values of $w^{LVE}_{20\,°C}$, Mg molality and R_v are calculated according to Cl molality along the evaporation curve. Error bars: uncertainty on Mg content (Cryo-SEM) and $w^{LVE}_{20\,°C}$ (Brillouin) converted into an uncertainty on R_v; each error bar combines data point uncertainty and initial data point uncertainty (319.7 m blf). Note: Cryo-SEM values are recalculated with PhreeSCALE to reach saturation with halite, hence some discrepancies with values displayed in Kiro et al. (2017). Rightwards (leftwards) blue arrows show the path followed by the NaCl-saturated brine through the course of evaporation (dilution) at equilibrium with NaCl. Rightwards (leftwards) black arrows illustrate expected deviations from the evaporation curve if significant supply of $\frac{Na}{Cl}$ poorer (richer) external source.*

the initial volume of the brine at 0% evaporation V_{initial}:

$$R_v = R_{H2O}\frac{\rho_{\text{initial}}}{\rho}\frac{m_{\text{tds}}+1}{m_{\text{tds,initial}}+1}, \tag{5.5}$$

with R_{H2O} the mass fraction of non-evaporated water.

Along an evaporation path (Figure 5.8) and at a given temperature, at each evaporation step, there is only one solution for m_{tds}, ρ and Cl (and all other solutes molalities). Thus, we can determine m_{tds} and ρ in Equation (5.5) via Cl, itself linearly related to $w^{LVE}_{20\,°C}$ through Equation (5.2). Therefore, the speed of sound measured with Brillouin spectroscopy in biphasic halite FIs is a direct sensor of the relative volume changes in the paleo-lake. This stands in the case of an evaporating closed system, where halite that precipitates or dissolves comes from the lake itself, and all other solutes are conservative, which implies negligible supply of ions from external sources (e.g. rivers, springs and hydrothermal brines) during the studied period. This assumption is discussed in Section 5.6.1.

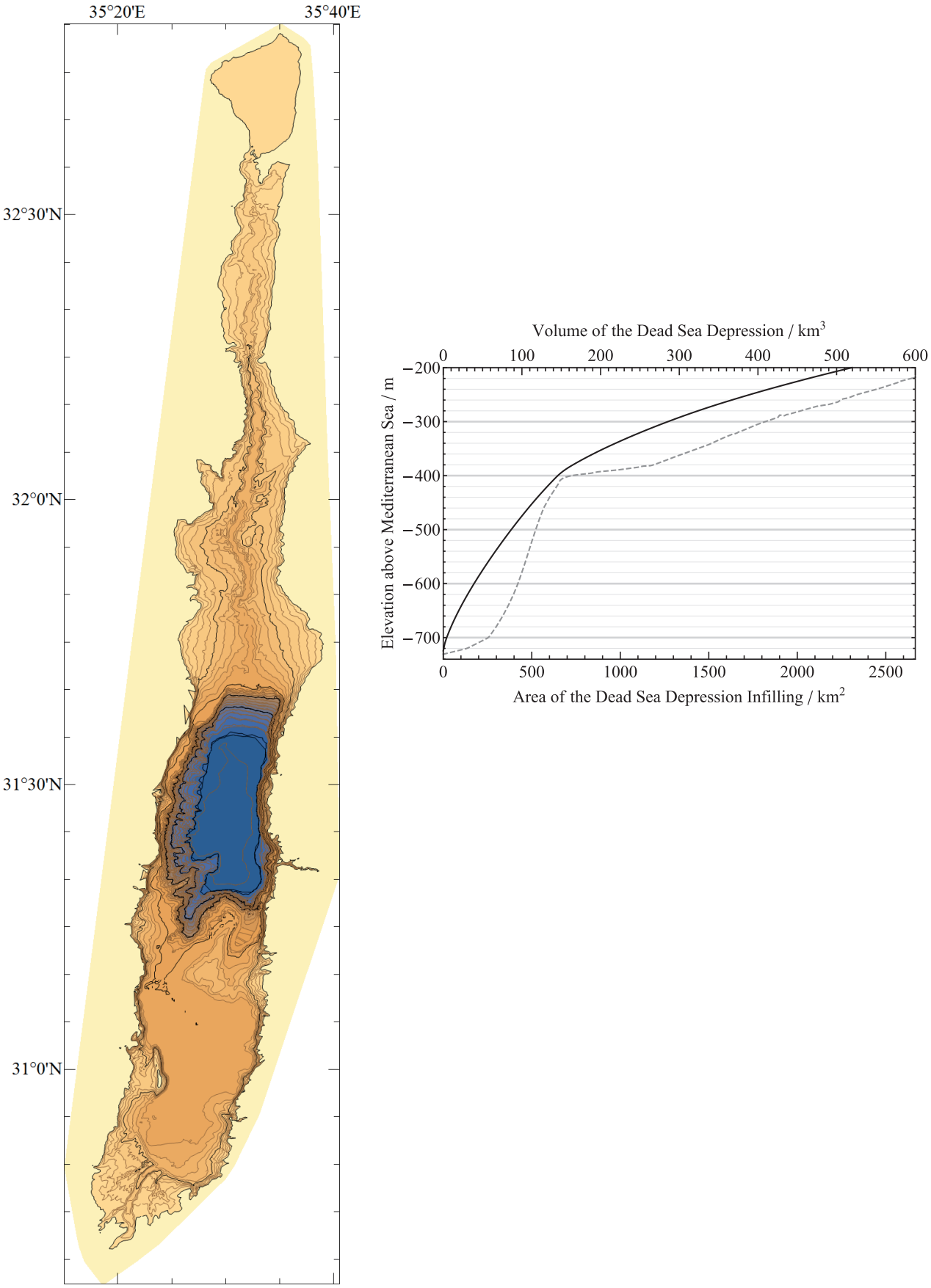

Figure 5.9: ***Hypsometry and bathymetry of the Dead Sea basin.*** *Left: Contour map of the Dead Sea basin. 20 m-spaced (light brown) and 100 m-spaced (black) contour lines span from 720 m bsl (center of the basin) to 200 m bsl (most external contour line). Right: Hypsometric area (dashed) and volume (solid) curves. DS today: 430 m bsl, 125 km^3, 600 km^2.*

5.4.1.2 Determination of absolute volume changes and lake levels

The Dead Sea is an endorheic basin, that is, it allows no outlflow to other external bodies of water. Below its spillway towards the Mediterranean through the Jezreel Valley, elevated 60.5 m above sea level, we can thus consider the DS basin as a mere water tank. From the elevation of the water body, one may calculate its area and volume, providing the shape of the basin is known. Such relations of level vs. volume or surface area are established through hypsometric and bathymetric curves, which consist in cumulative distribution functions of elevations above and below water surface, respectively. In other words, hypsometric curves show the area or volume of the water body that would be produced as the basin was filled up meter by meter from the bottom of the basin to a given elevation. Hall (1996) released such curves for the Dead Sea. Since a new bathymetric survey of the Dead Sea was achieved more recently (Sade et al., 2014), we recalculated the Dead Sea curves (Figure 5.9). Details on the method are found in Section 5.A.

Constraining the evolution of the level of the lake during the LIG based on our results on relative volume changes requires to know the initial volume - or, at least, the volume at some point during the period. Assuming a dynamic basin whose shape modifies through time with subsidence and sedimentation, one also needs to constrain the paleo-hypsometric curve. As existing constraints on lake level and volume during this period are scant and contradictory (see Waldmann et al. 2009; Kiro et al. 2017), and as the situation is even worse as to the subsidence of the basin over the last 130 ka, we proceed differently. Assuming the thickness of halite layers in DSDDP drill core is representative of the average thickness of halite layers deposited in the basin, it is possible to infer an initial lake volume and level. Indeed, at a given depth d in the sequence, the thickness of halite H_t [m] deposited above the initial depth $d_\mathrm{initial} = 319.7$ m blf writes:

$$\begin{aligned} H_\mathrm{t} &= \frac{H_\mathrm{v}}{S} \\ &= \frac{H_\mathrm{m}}{S}\frac{M_\mathrm{NaCl}}{\rho_\mathrm{NaCl}}, \end{aligned} \tag{5.6}$$

with H_v [m^3] the volume of deposited halite, H_m [mol] the amount of deposited halite and S [m^2] the surface area of the lake; the value of d_initial, 319.7 m blf, is the depth of the deepest halite crystal measured in this study. H_m is obtained as follows:

$$\begin{aligned} H_\mathrm{m} &= [Na]_\mathrm{initial} V_\mathrm{initial} - [Na].V \\ &= V_\mathrm{initial}\big([Na]_\mathrm{initial} - [Na].R_\mathrm{v}\big), \end{aligned} \tag{5.7}$$

with $[Na]$ [mol m^{-3}] the Na^+ concentration of the lake when halite layer located at depth d deposited. Combining Equations (5.6) and (5.7), we get:

$$H_\mathrm{t} = \frac{V_\mathrm{initial}}{S}\frac{\big([Na]_\mathrm{initial} - [Na]_\mathrm{f} R_\mathrm{v}\big) M_\mathrm{NaCl}}{\rho_\mathrm{NaCl}}. \tag{5.8}$$

As explained in previous Section 5.4.1.1, we get R_v with Brillouin spectroscopy and deduce $[Na]$ with Phree-SCALE. Thus, testing several values of initial lake level (i.e. testing several values of V_initial; S being then de-

duced with the hypsometric curve) for the calculation of H_t and comparing with the actual thickness observed in sequence 5017-1, we can infer a consistent initial lake level/$V_{initial}$. Although for a given halite thickness several scenarii may prove consistent, we bypass this hurdle through applying the method to each of the section we measured with Brillouin spectroscopy. Indeed, a thick layer may result either from the evaporation of x% of a great volume of brine in a basin with steep slopes or of x% of a smaller volume of brine experiencing strong halite focusing, in a basin where a vast flat area is covered with the epilimnetic shallow part of the lake (see Figure 5.2); on the other hand, in a sequence of halite layers with various thicknesses and for which R_v is constrained at several depths, the likely unique imprint of a specific lake decline through the complex basin may be deciphered. We also test several subsidence rates between 0 and 4.5 m ka^{-1}. An average subsidence rate > 4.5 m ka^{-1} is very unlikely as, with an average sedimentation rate of 2.4 m ka^{-1} over the last 130 ka as deduced from sequence 5017-1, it would imply that the main basin did not exist at the beginning of the LIG. Note that we only apply the subsidence rate to the lake floor with elevation below -400 m, that is, the northern basin for which average sedimentation rate is known. As for the rest of the basin, as it was not underwater all the time, sedimentation and subsidence were certainly highly variable through space and time, thus it is safer to consider this part of the basin has been at equilibrium (sedimentation rate = subsidence rate) for the last 130 ka. We also test several halite deposition scenarii:

- no halite focusing, which implies S in Equation (5.8) is the average surface area of the lake between initial stand and final stand, S_{Mean};
- subaerial halite focusing as assumed by Kiro et al. (2017), that is, halite previously deposited on dry margins is dissolved by rainfalls and runoff, thus returning to the lake; it implies S is the surface area at final stand, S;
- underwater halite focusing as described by Sirota et al. (2018), which implies S is the surface area of the thermocline at final stand, $S_{thermocline}$;

In total, testing (i) initial lake levels from 200 to 400 m bsl every 5 m, (ii) subsidence rates from 0 to 4.5 m ka^{-1} every 0.5 m ka^{-1} and (iii) 3 different values of S, we explore 1230 scenarii for each section measured with BS.

For details on the several assumptions made, that is, the equality between sedimentation and subsidence above 400 m bsl, the representativeness of 5017-1 sediments thickness as an average sediments thickness for the northern basin and the paleo-thermocline depth, we refer the reader to Section 5.6.1

5.4.2 Method for the reconstruction of temperatures

The method to reconstruct paleotemperatures using Brillouin spectroscopy is described in Chapter 3. For each section, we measured ~20-25 FIs. FIs were selected according to the isolation criterion ($Iso_{FI} > 1$) and had a size below the threshold given by Equation (3.4) (with P calculated as described in Section 4.1). We measured w^{LVE} at 3 temperatures and w^{mono} at 3 or 4 temperatures for each FI. Each FI w^{mono} trio/quartet and w^{LVE}

trio were fitted with a line and with an empirical parabola, respectively. The aforesaid parabolic equation was obtained through fitting the whole dataset, that is, all measured w^{LVE} from all sections as a function of temperature. This fitting method, also applied to the synthetic brine as described in Section 5.4.1.1, is a way to reduce significantly σ_{Tx}. Thus, it yields more accurate and more precise results, provided one makes sure this fit is adapted to each section (see Figure 5.C.1). Note that, for each section, the average equation $w^{\mathrm{LVE}}(T)$ at 20 °C provides $w^{\mathrm{LVE}}_{20\,^{\circ}\mathrm{C}}$, used for the reconstruction of relative volume changes as described in Section 5.4.1.1.

In a fluid inclusions assemblage (FIA) trapped at atmospheric pressure, the average T_{x} ($T_{\mathrm{x,mean}}$) approaches precisely and accurately the entrapment temperature T_{f}, as illustrated in Figure 3.1 and comprehensively detailed in Chapter 3. However, as the Dead Sea is the deepest saline lake in the world, the water column exerts a pressure of several megapascals on halite crystals growing on the lake floor. Therefore, a correction term ΔT_{P} must be added to $T_{\mathrm{x,mean}}$ to account for the high pressure entrapment:

$$T_{\mathrm{f}} = T_{\mathrm{x,mean}} + \Delta T_{\mathrm{P}}, \tag{5.9}$$

where

$$\begin{aligned} \Delta T_{\mathrm{P}} &= \frac{\beta_{\mathrm{T}} - \beta_{\mathrm{T_{Host}}}}{\alpha_{\mathrm{v}} - \alpha_{\mathrm{v_{Host}}}} P_{\mathrm{bottom}} \\ &= \frac{\beta_{\mathrm{T}} - \beta_{\mathrm{T_{Host}}}}{\alpha_{\mathrm{v}} - \alpha_{\mathrm{v_{Host}}}} \big(L - F\big)\rho. \end{aligned} \tag{5.10}$$

P_{bottom} [MPa] is the pressure at the bottom of the lake. L and F [m] are the level of the lake surface and the level of the lake floor, determined as explained in Section 5.4.1.2. The brine density ρ [kg m^{-3}], the isothermal compressibility of the fluid β_{T} [MPa^{-1}] and the thermal expansion of the fluid α_{v} [°C^{-1}] are calculated with the model presented in Chapter 4, implementing the ionic contents determined in PhreeSCALE via Cl, itself linearly related to $w^{\mathrm{LVE}}_{20\,^{\circ}\mathrm{C}}$ through Equation (5.2). The isothermal compressibility $\beta_{\mathrm{T_{Host}}}$ and thermal expansion $\alpha_{\mathrm{v_{Host}}}$ of the NaCl host are calculated with the NaCl density equation of Driesner (2007).

5.5 Results

In the following, we will first present the DS volumes and levels reconstruction, and will show the results of the temperatures reconstruction in a second phase. A summary of various parameters and results for each halite section measured in this work can be found in Table 5.2.

Depth in core m blf	$w_{20\,°C}^{LVE}$ **m s^{-1}**	**Na* molal**	**K* molal**	**Mg* molal**	**Ca* molal**	**Cl* molal**	ρ*** kg m^{-3}**	R_{H2O}*	R_v*	$H_{t\,calc}$ ** **m**	**Volume *** km^3**	**Lake elevation *** m bsl**	**Floor elevation *** m bsl**	$T_{x,mean}$ °C	ΔT_P*** °C	T_f °C
319.71	1781.1	3.47	0.23	1.13	0.35	6.66	1218.0	1	1	0	311	285	719	15.7	3.9	19.6
313.94	1781.5	3.42	0.24	1.15	0.36	6.68	1218.5	0.979	0.978	0.55	304	288	716	16.3	3.8	20.1
307.96	1784.8	3.11	0.26	1.30	0.40	6.78	1221.8	0.868	0.868	3.69	270	307	714	8.5	3.7	12.2
306.68	1787.0	2.91	0.28	1.39	0.43	6.85	1224.0	0.810	0.810	5.52	252	317	713	16.0	3.7	19.7
304.40	1787.4	2.88	0.29	1.41	0.44	6.86	1224.4	0.801	0.800	5.84	249	318	712	15.6	3.7	19.2
277.81	1790.2	2.67	0.31	1.52	0.47	6.95	1227.0	0.746	0.745	7.86	232	328	703	18.8	3.5	22.3
273.92	1787.0	2.92	0.28	1.39	0.43	6.85	1224.0	0.811	0.810	5.49	252	315	701	16.7	3.6	20.3
264.57	1793.5	2.45	0.33	1.63	0.51	7.06	1230.2	0.693	0.692	10.05	215	337	694	13.5	3.4	16.9
259.85	1803.6	1.91	0.39	1.94	0.60	7.37	1239.6	0.584	0.584	17.20	182	360	691	14.8	3.3	18.0
255.05	1806.1	1.80	0.41	2.00	0.62	7.45	1241.9	0.565	0.565	20.48	176	364	687	12.8	3.2	16.1
248.14	1805.9	1.81	0.41	2.00	0.62	7.45	1241.7	0.566	0.567	19.97	176	362	682	-	-	-
238.65	1818.5	1.38	0.47	2.29	0.71	7.84	1252.8	0.493	0.496	31.28	154	379	676	-	-	-

Table 5.2: ***Summary of measured and calculated values for each halite section.***

**Calculated with PhreeSCALE and Equation (5.2).*

***Calculated thickness of halite deposited above 319.7 m blf*

****In the case of scenario #1 (Initial elevation 285 m bsl and subsidence rate 2.5 m ka^{-1}).*

5.5.1 Lake levels

Results of the relative DS volume changes are presented in Figure 5.10, left Panel. We clearly observe a decrease in lake volume through the period from 320 to 240 m blf, interrupted during the 25 m-thick detritus interval (304 to 279 m blf), which amounts to -50% at the top of the sequence. From the 1230 lake level decline scenarii that we ran based on measured R_v (see Figures 5.B.1 to 5.B.3), we display the 10 best matching scenarii in Table 5.3. It comes out all best scenarii but one ran on the basis of underwater halite focusing, and all but two considered a subsidence rate comprised between 2 and 3 m ka^{-1}. Apart from the two outliers accounting very low/very high subsidence (#2 and #8, respectively) and no halite focusing (#2), all scenarii suggest an initial lake level comprised between 295 and 255 m blf. Amongst all, the best scenario as regards both matching occurrences and required model tolerance increase is by far #1. It suggests an initial lake level of 285 m blf, a subsidence rate of 2.5 m ka^{-1} and assumes underwater halite focusing. In Figure 5.10, right Panel, we show the calculated cumulated halite thickess along the core in the case of scenario #1 and compare the results with observed halite thickness. In the following, we use subsidence and initial lake level suggested by scenario #1.

Best scenarii	**#1**	**#2**	**#3**	**#4**	**#5**	**#6**	**#7**	**#8**	**#9**	**#10**
Initial lake elevation (m bsl)	285	330	280	290	250	295	265	335	255	260
Subsidence rate (m ka^{-1})	2.5	1	2.5	3	2	3	2	4	2	2
Halite focusing/ Type*	Yes/ U.w.	No	Yes/ U.w.	Yes/ U.w.	Yes/ U.w.	Yes/ U.w.	Yes/ U.w.	Yes/ U.w.	Yes/ U.w.	Yes/ U.w.
Matching occurrences	10/11	9/11	9/11	9/11	9/11	8/11	8/11	8/11	9/11	9/11
Required tolerance increase**	1.07	1.13	1.16	1.19	1.20	1.21	1.21	1.22	1.22	1.22

Table 5.3: ***The 10 best fitting scenarii.*** *1230 lake decline scenarii simulated, including 41 initial levels from 200 to 400 m bsl, 10 subsidence rates from 0 to 4.5 m ka^{-1} and 3 different halite deposition processes (*underwater(U.w.)/subaerial/no halite focusing).*
***Scenarii ranked in descending order of likelihood, according to required tolerance increase of the model, that is, how large a factor is to be applied to error bars so predicted and observed halite thicknesses agree for all 11 data points.*

Reconstructed Dead Sea levels during MIS5e are shown in Figure 5.11. To assess approximate lake levels during salt-free wetter intervals, we used the magnesium content of pore fluids measured by Levy et al. (2017) as a proxy for R_v. The concentration of this conservative element depends linearly on the lake volume. As pore fluids reflect the chemistry of the bottom water body (with, however, some possible delay), it can be used to determine minimum R_v. Based on our absolute level constraints, we can thereby convert these values in absolute minimum lake levels. For comparison, we also plot the other estimations made for this period by other

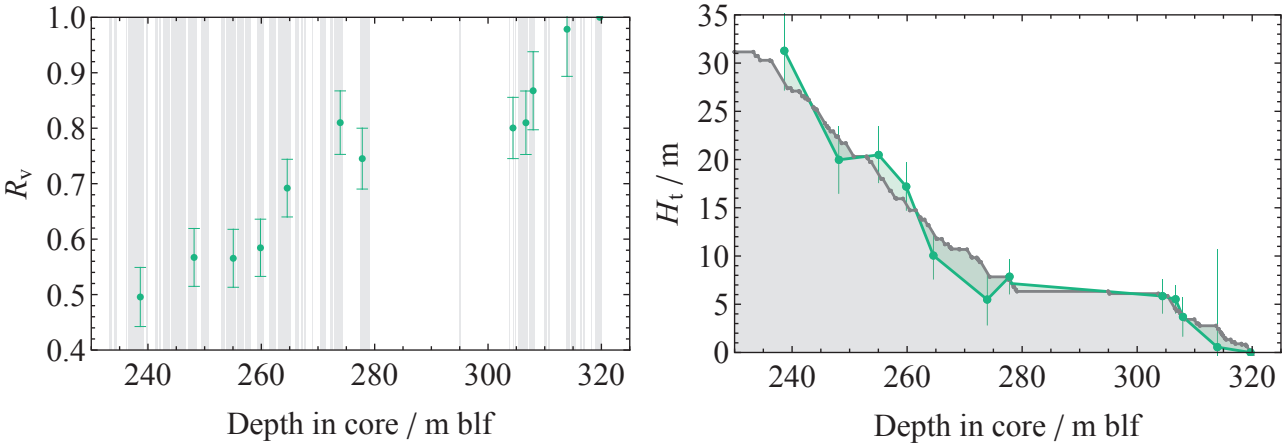

Figure 5.10: ***Relative volume changes and deduced best scenario of halite deposition.*** *Left: Volume changes relative to initial lake volume at the moment of deposition of sample located 319.7 m blf. Error bars: same as in Figure 5.8. Vertical gray bars represent halite layers. Right: Observed (thick gray line) vs. calculated with Equation (5.8) (green points) cumulative halite thickness above 319.7 m blf in the case of best scenario of lake level decline (#1, $L_{initial}$ = 285 m blf and subsidence rate 2.5 m ka^{-1}; see Table 5.2). Error bars: error on R_v (same as in Figure 5.8) converted in halite thickness error, and combined with estimated PhreeSCALE calculation uncertainty ~10%.*

authors. Interestingly, punctual independent estimations of the lake level during this period strongly support our reconstruction. The reconstructed curve shows a 3-phases pattern:

- from 134 to 129 ka, the lake faces a decline faster than -10 m ka^{-1}, starting higher than 260 m bsl down to 320 m bsl;
- from 129 to ~124 ka, halite precipitation and lake recession stop synchronously; from 129 to 126 ka, the lake probably does not rise much above 320 m bsl, since it deposits halite at 126 ka, which shows it remains close to saturation; after 126 ka, it rises up to at least 310-300 m bsl;
- from ~124 ka to 117 ka, the lake recedes again with a rate higher than -10 m ka^{-1}, hitting halite saturation at around ~122 ka.

Note that we cannot constrain precisely the age of maximum level for the period 122-129 ka. The start of lake recession at ~124 ka is associated with an uncertainty of 2 ka. This reconstruction and its implications are further discussed in Section 5.6.

5.5.2 Temperatures

In Figure 5.12, we show all the T_x values obtained in halite coarse crystals of the MIS5e period. We also show measurements carried out on contemporary coarse crystals from the top of sequence 5017-1. The latter precipitated shortly after the wet winter 1991-1992 (characterized by a mud laminae), when permanent stratification set in for several years, thereby ensuring very stable hypolimnion temperature (Beyth et al., 1993; Gertman and Hecht, 2002). Narrow error bars allow us to observe an excellent agreement between monitored temperature and $T_{x,mean}$.

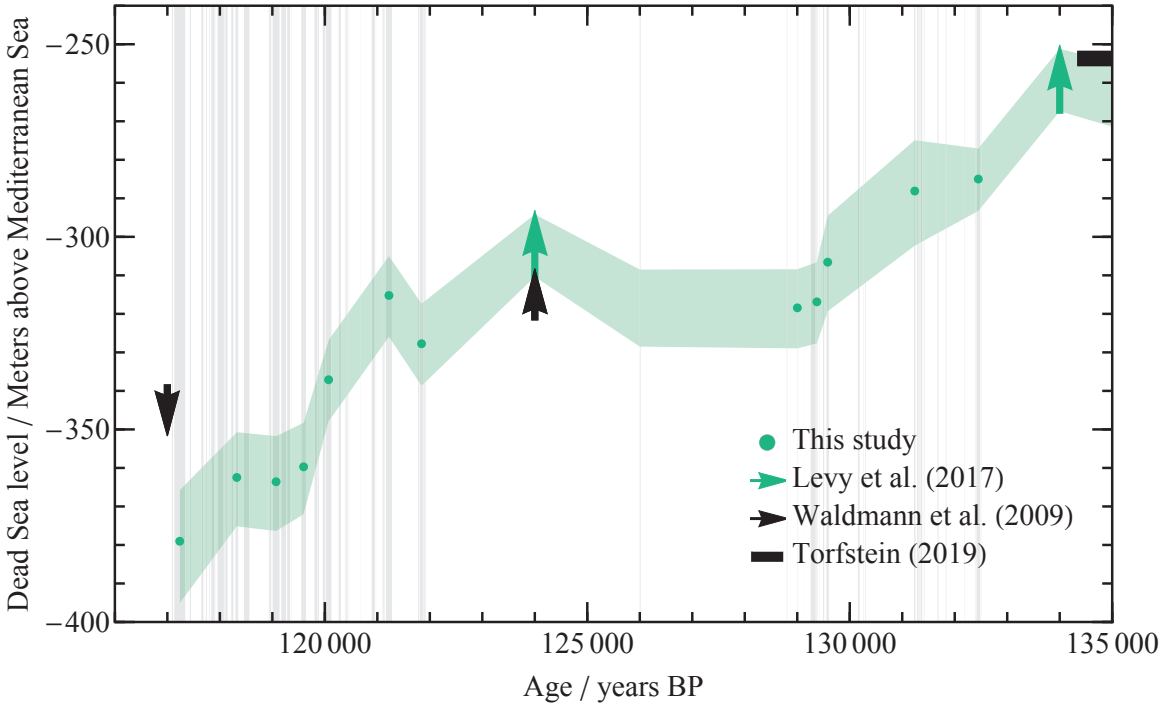

Figure 5.11: ***Last Interglacial Dead Sea levels reconstruction.*** *Blue markers: levels reconstructed in this study using our measurements and data from Levy et al. (2017). Black markers: independent estimations. Downwards arrows: lower than; upwards arrows: higher than. Mg^{2+} content measured in 5017-1 pore fluids (Levy et al., 2017) is used as a proxy for relative volume changes through the equation $R_v = \frac{Mg^{2+}_{initial}}{Mg^{2+}}$ (Kiro et al., 2017); pore fluids reflect the chemistry of the deep water body which during meromictic periods is not equal to the whole chemistry, the upper layer being fresher; thus, lake levels inferred by pore fluids chemistry are minimum elevations; note that observed delays between pore fluid and deep lake chemistries might induce high age uncertainty (> 1000 ka). Data from Waldmann et al. (2009) are based on stratigraphic observations in Arava Valley; we discarded observations from Masada Plain, where subsidence is much stronger than assumed by the authors (Lisker et al., 2009); note that as datings are approximate we slightly modified ages so that lowstand and highstand concur with 5017-1 stratigraphy (from ~116 ka to 117 ka and from ~120 ka to 124 ka, respectively). Value from Torfstein (2019): mean elevation for most MIS6, based on correlation of Dead Sea levels and global climate records. Gray vertical bands: halite deposits.*

The evolution of the Dead Sea hypolimnion temperature through MIS5e, shown in Figure 5.13, can be splitted into two phases. From 132.5 to 129 ka, the temperature of the deep layer remained stable around 20 °C, albeit a sharp drop punctuates the record at 129.6 ka. As the thick mud parting prevents any temperature measurement during the period from 129 to 122 ka, we can just assume it increased up to the highest temperature on record at 122 ka. From 122 to 119 ka, temperatures then decrease rapidly at a rate of 2 °C ka^{-1}. We further discuss this temperature reconstruction along with its implications in Section 5.6.

5.6 Discussion

5.6.1 Validity of assumptions

This work is based on several strong assumptions that need support. Here we discuss these hypotheses, their support and the extent of their validity.

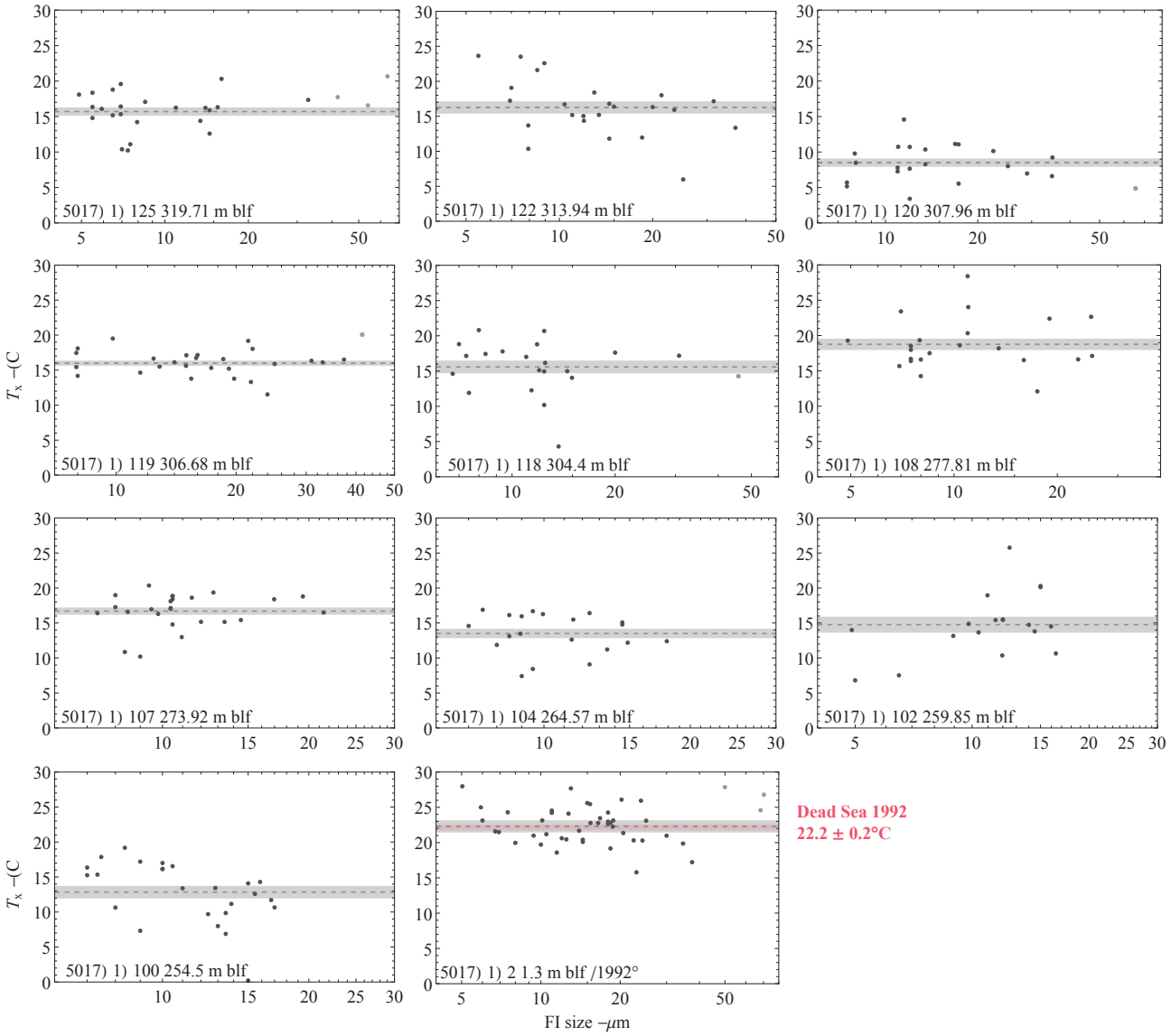

Figure 5.12: ***T_xs obtained in FIs of each section.*** *Gray horizontal bars: average T_x ($T_{x,mean}$); thickness indicates standard error on the mean. Lighter gray data points are discarded from the calculation of the mean because of the size of the FI. In addition to MIS5e measurements, measurements on a crystal sampled from core top (5017-1-2) are shown; crystal growth is estimated to date back to 1992, based on Kiro et al. (2016) age model. Note that all T_x values are non-corrected for pressure, except 5017-1-2 for which the pressure correction term $\Delta T_P = 3.7$°C is added to each T_x value for easier comparison with monitoring temperature.*

The Last Interglacial Dead Sea as a semi-closed system The reconstruction of relative volume changes assumes that the DS is a closed system with respect to solutes, that is, there is no significant external source of ions, all halite that precipitates or dissolves coming from the initial stock in solution. Only pure water goes in (e.g. riverine discharge and runoff) and out of (evaporation) the system. This assumption is obviously wrong in the long term, since ions in any non-marine hypersaline lake are brought by rivers and springs. Its validity therefore relies on the timescale considered. Kiro et al. (2017) demonstrated that the chemistry of Dead Sea FIs plotted well on a single evaporation curve, as can be seen in Figure 5.8. Levy et al. (2018) measured δ^{37}Cl in 5017-1 pore fluids and showed that values followed a Rayleigh distillation curve for the period 132-116 ka,

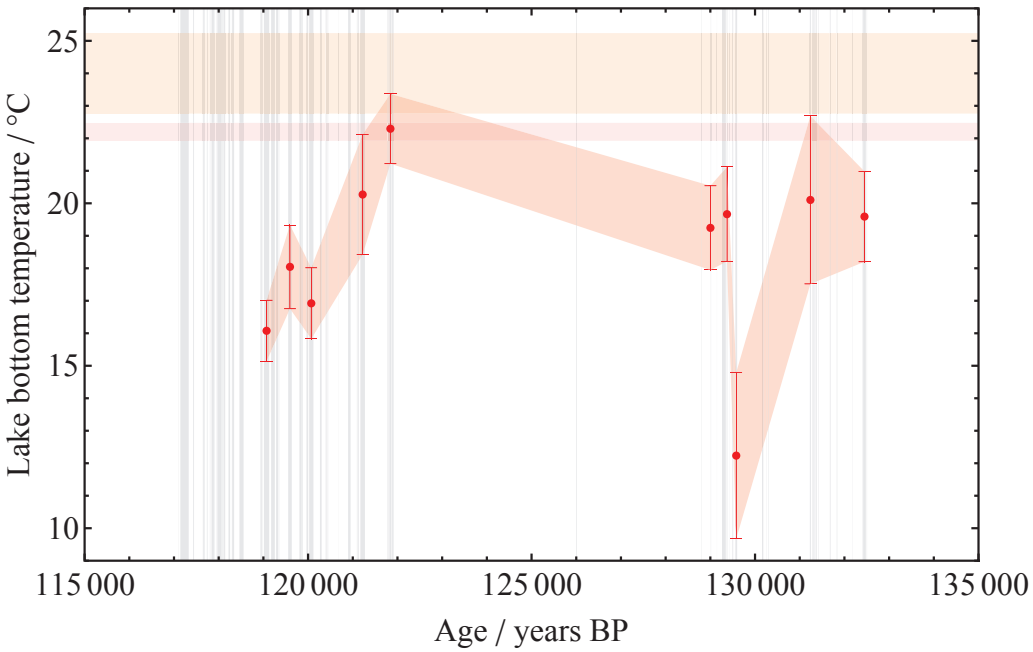

Figure 5.13: ***Evolution of Dead Sea deep layer temperature during MIS5e.*** *Vertical gray bands: halite deposits. Horizontal red band: temperature in 1992, which can be considered as a good estimate for 20th century hypolimnion temperature[a]. Horizontal orange band: Range of hypolimnion temperatures for the period 2010-2019. Error bars: combination of the standard error on $T_{x,mean}$ and the mean deviation of w^{LVE} measurements from the empirical parabolic fit.*

[a]Compilation of deep layer temperature measurements for the past 60 years can be found at https://isramar.ocean.org.il/isramar2009/DeadSea/LongTerm.aspx

thus evidencing the minor role of external sources during MIS5e. Our data also suggest a minor influence of external sources during MIS5e, since $w^{\mathrm{LVE}}_{20\,^{\circ}\mathrm{C}}$ values are very comparable before and after the 7,000 year-long halite free episode. However, current NaCl fluxes are estimated around ~1.4 Tg yr^{-1} (~50/50 Jordan and springs; Bentor 1961) which, if applied to the 16,000-year-long MIS5e period, amounts to 22,400 Tg or 15.9 meters of salt in a basin of 650 km^2 surface area. This would account for 50% of deposited salt during the period. This discrepancy is explained by the fact that current fluxes are not truly external. Indeed, during high stands like the Last Glacial Lisan period a portion of the solutes is stored in the western shores aquifer (Weber et al., 2018) and in sediments (Stein et al., 1997; Katz and Starinsky, 2009). These stocks are then recycled during low stands, when the Jordan washes away part of its bed sediments and brines discharge back into the Dead Sea. This process must be particularly enhanced today, as the lake level has rapidly declined all century long and is amongst lowest ever recorded. In the long term, the average NaCl flux to the lake is very likely much lower than today.

As a matter of fact, we can infer rough external fluxes estimates from the current NaCl stock. No salt sequences dating back to the last 220 ka were found in cores drilled in the southern basin (Salhov et al., 1994) nor in outcrops (Torfstein et al., 2009; Waldmann et al., 2009)[3]. This means that halite has always focused in

[3]The exception is the early Holocene (~11ka) ~15 m-thick salt sequence found in 5017-1 and in all cores drilled in the western margins and in the northern part of the southern basin (Yechieli et al., 1993; Migowski et al., 2006; Stein et al., 2010), which is an evidence for a larger area of halite deposition for this period. It is uneasy to estimate the deposition area of this halite sequence, and

the northern basin. Defining the northern basin as the area encircled by the contour line 400 m bsl, it implies that the 68 meters of salt deposited since 220 ka BP cover a 650 km^2 area, hence 96,000 Tg of NaCl. Adding the 10,000 Tg of NaCl dissolved in the DS in 2010 when 5017-1 sequence was drilled, we calculate a total 106,000 Tg halite stock. Starting with a zero stock (i.e. an empty Dead Sea), we deduce a maximum value for the average NaCl flux from external sources ~0.49 Tg yr^{-1} over the last 220 ka. As the Dead Sea was not empty at this initial time and presented a much higher NaCl concentration than today (4.9 mol.kgH_2O^{-1} as measured by Kiro et al. (2017) in FIs from the deepest halite layer found in 5017-1), it certainly started depositing halite at a higher stand than today. Considering the lake reached halite saturation around 300 m bsl at this time, we calculate a 73,000 Tg initial stock, which suggests only 33,000 Tg out of the current 106,000 Tg would originate from external sources, indicating an average NaCl flux 0.15 Tg yr^{-1} over the last 220 ka. This value, albeit strongly dependent on the guess for the initial volume of the lake at 220 ka BP, is in good agreement with the 0.24 Tg yr^{-1} estimation of Levy et al. (2018) based on the evolution of pore fluids chlorine and magnesium concentrations. To sum up, external contributions to the ~3 Tg yr^{-1} precipitated in the Dead Sea during MIS5e (31.5 meters of salt over a 650 km^2 area deposited within 15,000 years) should amount to 5% (0.15 Tg yr^{-1}) to 8% (0.24 Tg yr^{-1}). Note that sodium and chlorine are the prevailing ions in the sources contributing to the Dead Sea composition, therefore the annual flux of any other ion is lower than the flux of NaCl.

Basinwide representativeness of sediments thickness in 5017-1 A recent geophysical 3D mapping of the Dead Sea northern basin shed light on its architecture (Coianiz et al., 2019c). It has revealed quite heterogeneous sedimentary thicknesses over the whole basin, with thinner deposits close to the western margin and thicker ones in the so-called “Arnon Sink”, in the southeastern part of the basin. It has also shown that the 5017-1-A borehole is located in an area where the thickness of sediments is close to an average. It is thus a good support of our assumption that the sediments thickness in 5017-1 is representative of the average sediments thickness over the northern basin.

Constant thermocline depth In this work we set the thermocline depth to 25 m below lake level, which is the current value (e.g. Sirota et al. 2016). Through testing 52 tropical and temperate lakes of various sizes Kling (1988) demonstrated the good linear relation between the logarithm of the thermocline depth and the logarithm of the lake surface area. Applying the regression equation to the Dead Sea, we find that doubling its area deepens its thermocline by only 3 meters. This weak difference bolsters the use of a constant thermocline depth.

Higher basin at equilibrium Our results point towards a deep basin (i.e. the northern basin) at equilibrium between sedimentation (2.4 m ka^{-1}) and subsidence (2.5 ± 0.3 m ka^{-1}) on average over the last 130 ka. However, this result is based on the assumption that the hypsometric curve above 400 m bsl has remained unchanged.

as on the other hand we may also overestimate the extent of other salt sequences, we assume it is safer to consider that salt always deposited in the same 650 km^2 depocenter.

In other words the basin floor lying above 400 m bsl, for which sedimentation rate is highly variable through time and space due to irregular immersion, is assumed at equilibrium on average during this period. Coianiz et al. (2019b, c) showed that the relation between sedimentation and subsidence was not direct, the latter depending mainly on the load applied to the basin floor and, to a lesser extent, on tectonics. Therefore, the main driver is the lake level. A high water column squeezes the sedimentary infill, leading to mud compaction and salt flow, and deposits mud at a slow pace. On the other hand, a low lake level releases pressure on the sedimentary stack and is likely to deposit thick salt sequences (at least during the decline phase), which is consistent with the current halt of subsidence and the very high Holocene sedimentation rate. Therefore one should not expect equilibrium in the short-term. In the longer term however, over several 10,000 years, this remains an open question, as constraints on late Quaternary subsidence are scant. Through dating stromatolites in caves unaffected by subsidence on the western side of the fault escarpment, Lisker et al. (2009) estimated the elevation of the Last Glacial Dead Sea, which they compared with estimations made on outcrops of equivalent age on the eastern side of the fault by Bartov et al. (2002) and Waldmann and (2002). The comparison revealed a subsidence rate comprised between 2 and 2.2 m ka^{-1} over the last 75 ka for the Masada Plain and the Perazim Valley, located on the southwestern shores of the northern basin and on the western part of the southern basin, respectively. Core 5017-3 (Coianiz et al., 2019a), drilled south of Ein Gedi on the Masada Plain shoreline, reveals a sedimentation rate of ~1.8 $\pm$ 0.2 m ka^{-1}over the last 56 ka, very close to the subsidence rate estimated by Lisker et al. (2009) for this area. After decompaction correction and using datation made by Torfstein et al. (2009), Brink and Flores (2012) estimate a sedimentation rate of ~2.2 m ka^{-1} over the last 420 ka in borehole Sedom Deep-1, in the southwestern part of the southern basin, also very close to the subsidence rate estimated by Lisker et al. (2009) in Perazim Valley. Hence, the comparison of the few sedimentation and subsidence estimations available support the equilibrium hypothesis for both the southern basin and Masada Plain. Further constraints are needed to support this statement for the whole higher basin, especially in the Jordan Valley where no estimation of the kind is available to our knowledge.

5.6.2 A coherent picture of the Last Interglacial Dead Sea and of its interplay with the basin

The results of the numerous scenarii we run to simulate the deposition of 5017-1 LIG thick halite sequence fermly support the observations of Sirota et al. (2018) on the modern Dead Sea: underwater halite focusing is the prevailing process of halite deposition. The lower rates of lake decline in the past compared to the current human-induced rate certainly contributed to make this process even more effective, explaining the complete absence of halite in the sedimentary record of the Dead Sea margins and conversely accounting for the very thick salt sequences in 5017-1. This concept sheds new light on the rare halite sequences present on the margins: the lake thermocline very likely did not drop below these sequences at the time of deposition. Conversely, marginal sedimentary records lacking a halite layer present in the deep basin highlight a decline of the thermocline below the elevation of the salt hiatus. This concept is likely to have affected any halite deposit in any saline lake over the world. For instance, it may bring a new insight into the processes that led to the

Messinian Salinity Crisis 5.5 Million years ago, when extremely thick accumulations of salt deposited on the deep floor of the Mediterranean.

Our simulations also allow us to determine for the first time an average subsidence rate for the deep basin over the past 130 ka. The value of 2.5 $\pm$ 0.3 m ka^{-1} [4] is close to, though logically higher than, values estimated for the western margins and the southern basin. It should be noted that this subsidence rate does not include the compaction of sediments, contrary to the value of Lisker et al. (2009).

Our results bring about a radically novel framework for the evolution of the lake level during the LIG, with an average elevation much higher than the Holocene Dead Sea (370-410 m bsl, leaving aside man-induced recent decline; see Bookman (Ken-Tor) et al. 2004; Bartov et al. 2007). The strength of the reconstruction relies on the consideration of underwater halite focusing, which strongly reduces the quantity of possible scenarii. In particular, the thickening of the salt sequence towards the end of the period anchors the final lake level to the elevation of the basin shoulder around 380 m bsl. The reconstruction reconciles the stratigraphy of core 5017-1 and level estimations made on marginal outcrops by Waldmann et al. (2009). It also justifies the late MIS5e clastic deposits observed in the southern basin outcrops of Perazim (Waldmann et al., 2007) and Arubotaim Cave (Torfstein et al., 2009): in the case of a southern basin elevated 400 m bsl as today and a lake level of 380 m bsl, these locations would have constituted shallow epilimnetic floors where halite could not durably deposit and which coarse detritus could reach. Finally, it is also consistent with the 130-120 ka outburst of subsidence noticed by Coianiz et al. (2019c), the occurrence of which requires a higher mass load. Indeed, the -10% drop of the water column from MIS6/5 transition to mid-MIS5e, as reconstructed in our work, was compensated by a ~+5% increase of its density and 40 m-thick additional sedimentary load that we can convert into a +20% mass, hence a net +15% mass applied to the central basin floor. The study of the long core drilled by the DSDDP previously led other authors to infer considerably more dramatic lake declines. Based on the thickness of the salt sequence, on top of which lies a gravel layer interpreted as a beach deposit, and on the evidence of a sedimentary hiatus as revealed by datings (see Figure 5.6), Torfstein et al. (2015) came to the conclusion that the Dead Sea underwent complete dessication during MIS5e, although Neugebauer et al. (2016) later interpreted the gravel layer as a mass waste deposit whose fine-grained components was washed out during drilling process. Based on the magnesium content of pore fluids (Levy et al., 2017) and on the sodium, chlorine and magnesium content measured in halite FIs, Kiro et al. (2017) modelled a lake decline from 320 to 490 m bsl required to account for the observed salt thickness. The large discrepancy between their model and the one proposed here rely on our considering underwater halite focusing and comparing predicted vs. observed halite thickness at several intervals.

Due to the potential 5 to 8% contribution of external sources to the thickness of deposited halite (see Section 5.6.1), we might overestimate the initial lake level by about 10 meters. The lake level curve could be adjusted when better constraints on the external sources arise.

[4] The uncertainty is the resolution of our method, stemming from the 0.5 m ka^{-1} interval applied in the simulations.

5.6.3 The LIG in the Levant: Mediterranean and North Atlantic signatures

Interglacials are usually defined on the basis of a climate as warm as, or warmer than, the present Interglacial (PIG; Kukla et al. 2002b). Usually in phase with enhanced insolation in relation with strong planetary orbital forcings (e.g. Kukla et al. 1981), these episodes experience extreme variabilities, especially at their onset and decline. For instance, the precession minimum of the Early Holocene (11-10 ka), albeit lower in amplitude compared to the LIG, was strong enough for a humid vegetation-covered Sahara to establish at 14.8 ka (Ritchie et al., 1985) and disappear at 5.5 ka, both appearance and demise occurring on a very abrupt centennial to decadal timescale (deMenocal et al., 2000). These non-linear sharp feedbacks to a gradual forcing are intriguing and do not always meet consistent explanations. In this scope, the LIG focuses particular attention as it is the most recent of these warm intervals (PIG excepted) and occurred during a constructive interference of precession, obliquity and eccentricity (Berger and Loutre, 1991). The latter phasing is expected to have caused all the more abrupt climatic shifts, leading some authors to name it a "super-interglacial" (e.g. Turney and Jones 2010), thereby promoting it as a potential analogue of the future climate. To date, a vast amount of work has been achieved to constrain the chronology and the amplitude of the LIG in the marine and polar realms (e.g. McManus et al. 1994; Shackleton et al. 2003; Kandiano et al. 2004; Andersen et al. 2004; Martrat et al. 2007; Denton et al. 2010; Leduc et al. 2010; Jacobel et al. 2016; Deaney et al. 2017). As polar ice sheets are driving forces of the global climate and constitute, along with oceans, excellent archives of planetary climate variability (Bond et al., 1993; Petit et al., 1999; Jouzel et al., 2007), the timeline of events and their amplitude across the world are now quite well constrained. On the other hand, the climatic variability of the continental counterpart is comparatively poorly understood, because lands offer much less continuous records while they display a much more heterogeneous response to climate variability. One of the main features of the LIG, the intensification (and geographical extension) of the African monsoon, has been thoroughly investigated in the geological record. It was shown that presently desert locations north of a 15°N line could present steppic to mixed forest vegetation at times of summer perihelion up to a latitude of 23°N in Africa (Jolly et al., 1998; Palchan and Torfstein, 2019) and maybe even ~25°N in Arabia (Fleitmann et al., 2003, 2004; Rosenberg et al., 2013; Enzel et al., 2015; Parton et al., 2018). These wetter conditions coeval with increased orbital summer insolation are well reproduced by Global Climate Models (GCMs), which show a northward shift of the Intertropical Convergence Zone (ITCZ) associated with summer perihelion, bringing significant rainfall (> 100 mm yr^{-1}) up to the northern Red Sea (e.g. Prell and Kutzbach 1987; Herold and Lohmann 2009; Kutzbach et al. 2014). North of this humidity boundary, and especially in the Mediterranean, models predict summer aridity and warmth. And yet, an overwhelming body of evidence suggest an increase in Mediterranean moisture perfectly synchronous with the African Monsoon. A proeminent sapropel (S5), i.e. a layer of sediments with elevated concentration of organic carbon that contrast with surrounding organic poor sediments (Rohling et al., 2015), is found in the Eastern Mediterranean sedimentary record and dated 128.3-121 ka (Grant et al., 2012). This kind of lithology is explained by a freshening of the marine upper layer, reinforced salinity gradient and resulting strengthening

of the stratification, leading to bottom layer anoxia and conservation of organic matter (Rossignol-Strick et al., 1982). This mechanism requires an increased supply of fresh water. In a precursor work, Rossignol-Strick (1985) showed that these deposits correlate with orbital high indices of insolation and African monsoon, and proposed the strengthening of the Nile river summer floods as the main source of additional fresh water in the Mediterranean. Nevertheless, synchronous with the sapropels fuelled by an indirect source of moisture, other evidences point toward a direct enhancement of moisture in the Mediterranean. Speleothems in the eastern and northern borderlands of the Mediterranean show increased precipitation covering the period ~129-122 ka (Bar-Matthews et al., 1999, 2000, 2003; Drysdale et al., 2005). Pollen records highlight the decline of steppic taxa and appearance of arboreal taxa (especially deciduous oak) as of 128.5-127 ka BP in Iberia (Sánchez Goñi et al., 1999), southern Italy (Brauer et al., 2007), northern and central Greece (Tzedakis et al., 2003, 2006), Lebanon (Develle et al., 2011; Gasse et al., 2015) or Turkey (Litt et al., 2014). These forests were first interpreted as indicators of increased summer precipitation (e.g. Rossignol-Strick and Paterne 1999), but Tzedakis (2007) questioned this interpretation and pointed out the significant amount of rainfall (800-1200 mm yr^{-1}, Rossignol-Strick and Paterne 1999) required for the presence of the deciduous oak, making the summer option dubious. More recently, combined palynological, mineralogical and paleontological study of records from Tenaghi Philippon (Milner et al., 2012, 2016) revealed the seasonality of precipitation, pointing out arid and warm summers followed by wet winters. While modellers usually focus on the impact of summer insolation peak during the LIG, Kutzbach et al. (2014) tested the impact of the coeval insolation minimum during winter. Their model predicted a substantial additional precipitation over the whole Mediterranean realm and the Middle East due to a southward shift and intensification of the Mediterranean stormtrack. Decoupling the precession and obliquity signals, Bosmans et al. (2015) showed that the LIG orbital pattern of precession minimum (i.e. summer perihelion/winter aphelion) and obliquity maximum both enhanced winter precipitation, albeit due to a stronger air-sea temperature difference inducing local convective precipitation rather than a more global shift in atmospheric circulation. Irrespectively of the local or western origin of the rain, both models support the synchronicity of Mediterranean winter moisture and precession peak suggested by records. To sum up, there is mounting evidence of an increased amount of precipitation over the Mediterranean region during the mid-LIG (~125 ka), synchronously with the enhanced monsoon over the tropics. However, while the tropical rainfall increase is linked to enhanced ocean-to-continent summer moisture transfer due to the peak in summer insolation, the increase in Mediterranean moisture probably bears a winter signature.

A contradiction to the narrative exposed above has emerged from the lithology of core 5017-1 drilled in the deep Dead Sea. The thick salt sequence observed at the bottom of the Samra Unit, coeval with MIS5e, has led authors to suggest an episode of extreme aridity (Neugebauer et al., 2014; Torfstein et al., 2015; Kiro et al., 2016, 2017; Torfstein, 2019). The suggested lake low stand, previously inferred by Waldmann et al. (2009) from stratigraphic observations on the lake margins, would have occurred during a period for which records north of the Dead Sea (Bar-Matthews et al., 2003), but also south of the Dead Sea (Vaks et al., 2006, 2010; Waldmann et al., 2010), show an increased moisture. To disentangle this apparent inconsistency (cf

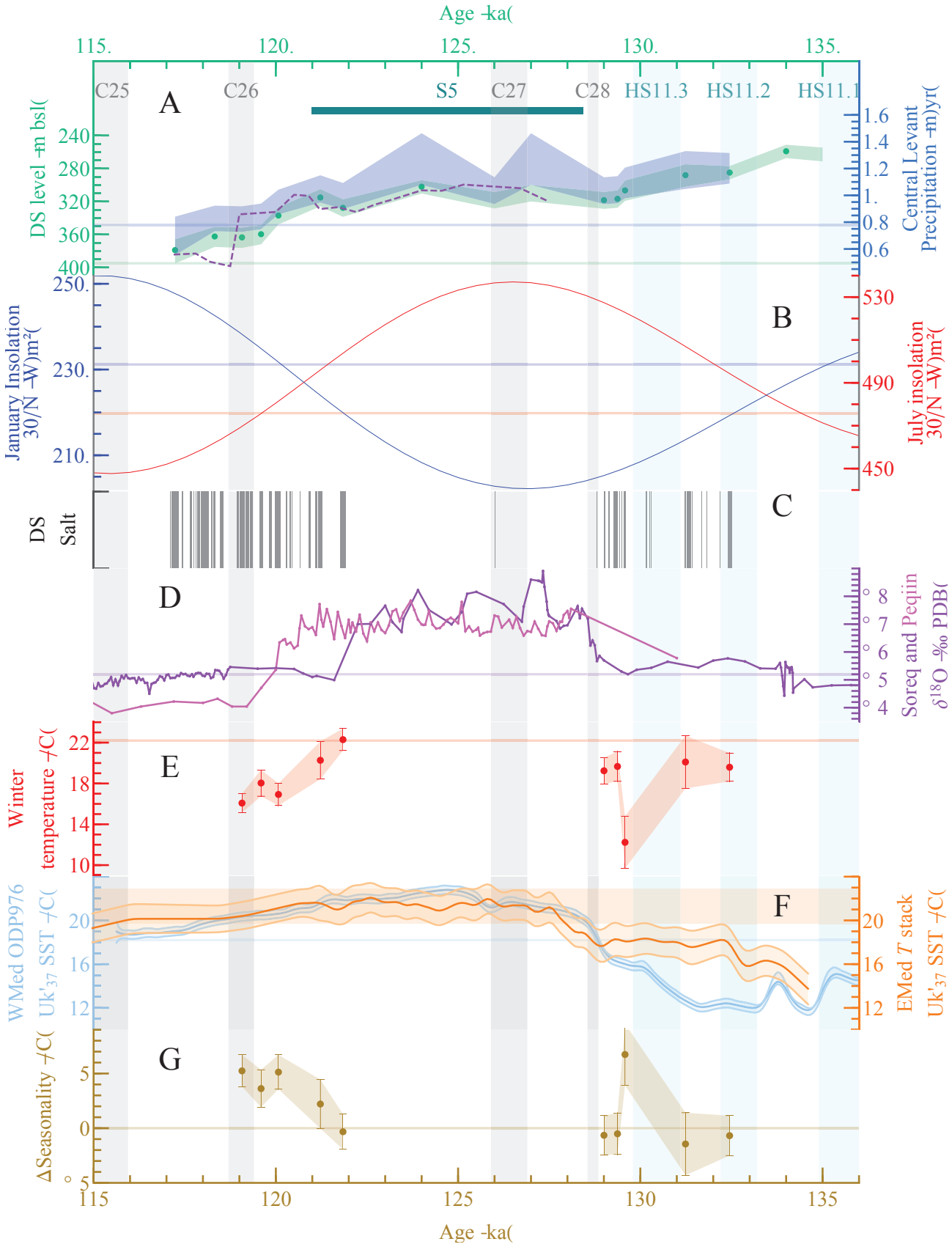

Figure 5.14

Bar-Matthews et al. 2019), Waldmann et al. (2010) and Torfstein et al. (2015) proposed two distinct sources of precipitation. The classical Mediterranean winter stormtrack would have kept on providing precipitation to the

Figure 5.14: ***Comparison of Dead Sea, North Atlantic and Mediterranean records.*** *A: Dead Sea levels as reconstructed in this study and deduced annual precipitation at Kfar Giladi station, north of the watershed; precipitation at Kfar Giladi calculated from Soreq speleothems $\delta^{18}O$ for comparison (see Section 5.D for details on precipitation calculations). B: 1st January and 1st July insolation at 30°N; data from Laskar et al. (2004). C: halite deposits in 5017-1-A. D: Soreq and Peqiin caves speleothems $\delta^{18}O$ (Bar-Matthews et al., 2003). E: Winter (~SONDJF) temperature as inferred from Dead Sea hypolimnion temperature measured in this study. F: West Mediterranean mean annual SST alkenone record as measured in core ODP976 off the Iberian coast, Alboran Sea (Martrat et al., 2014) and reassessed through a Monte Carlo analysis of chronological and SST uncertainties with a 0.2 ka Gaussian filter (Marino et al., 2015); East Mediterranean mean annual SST stack (Amies et al., 2019) obtained with Monte Carlo analysis of SST measured from alkenones in cores KS205, LC21 and ODP 967 and ODP 971 (Rohling et al., 2002, 2004; Marino et al., 2007). G: ΔSeasonality is the difference between annual and winter temperature compared to today, defined as $(EMedSST - DS\ hypolimnion T) - (EMedSST - DS\ hypolimnion T)_{late Holocene}$. Late Holocene value of Eastern Mediterranean SST is average over last 3 ka from Emeis et al. (2000), and late Holocene value for DS hypolimnion temperature is value of 1992. From A to G: vertical gray bands indicate North Atlantic ice-rafted events C28 to C25 (Chapman and Shackleton, 1999; Oppo et al., 2001, 2006; Mokeddem et al., 2014). Vertical blue bands: subdivisions 11.1 to 11.3 of Heinrich Stadial HS11 as in Tzedakis et al. (2018). Sapropel S5 as in Grant et al. (2012). Horizontal bands indicate late Holocene values, 20th century when available. Uncertainty envelopes: 1-sigma.*

central and northern Levant, but decreased its supply to the more southern Neguev desert and Dead Sea basin. In turn, southerly precipitation would have reached the southern Levant, accounting for the evidences of increased moisture such as the Neguev speleothems growth, the Arava travertines, the Red Sea corals calcification and the DSDDP 5017-1 129-122 ka thick mud layer. The latter southerly precipitation would have been either a direct manifestation of the northward shift of the summer African Monsoon (Torfstein et al., 2015), or would have originated from the spring and autumn particular atmospheric conditions associated with the Red Sea trough (Waldmann et al., 2010). Our lake level reconstruction suggest another story: the Dead Sea never experienced extreme aridity during MIS5e, and only reached Holocene-like arid conditions at ~117 ka. Following the method of Morin et al. (2019), we propose a lake level-based quantitative precipitation reconstruction for the region that contributes most to the riverine discharge into the Dead Sea, that is, the northernmost part of the watershed in the central Levant (see Figure 5.14, and see Appendix Section 5.D for details on the method). It comes out the amount of precipitation was 50% higher than today at the onset of halite deposition at 132.5 ka. After a decrease down to slightly more than 1000 mm yr $^{-1}$, it increased again synchronously with sapropel S5. To keep up with a ~300 m bsl high stand, a minimum amount of ~1080 mm yr $^{-1}$ of precipitation in the northern catchment was then necessary, and up to ~1460 mm yr $^{-1}$ depending on the density of the upper layer in the then meromictic lake. In the case of a southerly source of precipitation, we can imagine that the required amount of precipitation would have been even higher since the southern watershed undergoes more intense evaporation, which is way too high compared to the most optimistic models predicting at most ~100 mm yr $^{-1}$ of additional precipitation. Our hydrological reconstruction thus discards the southern origin of moisture, and anchors the Dead Sea back into the Mediterranean and North Atlantic realms. It is consistent with the Mediterranean records detailed above, with the southward reduction of speleothem growth observed in the Neguev during MIS5e (Vaks et al., 2010), and with the North Atlantic Oscillation (NAO) influence inferred from the decadal pattern of successive halite layers (Palchan et al., 2017) and with the Mediterranean and North Atlantic strong

relation observed for the next phases MIS5d to MIS5a (Neugebauer et al., 2016) and the Last Glacial (Kolodny et al., 2005). Our findings emphasize a misconception that often arises when thick salt sequences are observed in stratigraphic units: salt equals dry. In reality, salt only means *drier*. A negative water balance is a requisite for reaching halite saturation, while the stock of NaCl in solution determines the threshold volume/lake level below which saturation is reached. The latter has evolved dramatically through the two last glacial/interglacial transitions, thus explaining why the (low) lake level at which saturation was reached during the Holocene is completely different from the (high) lake level at which it was reached in the previous interglacial. In the following, we detail the hydrological and temperature trends observed during each of the three observed phases and discuss them in the light of the regional climatic trends (Figure 5.14).

- The first period starts with a highstand at ~134 ka (the uncertainty on the age is high because of the diffusion issues linked with pore fluids chemistry) followed by a 5 ka decline. This decline is due to a gradual drop in precipitation from > 1200 mm yr^{-1} to 1030 mm yr^{-1}. In the meantime, while winter temperatures remained stable and quite high around ~19-20 °C, the 12 °C value at 129.6 ka suggests possible dramatic and abrupt temperature shifts. Similarly, the long periods of mud deposition centered at 129.9, 130.8 and 131.9 ka suggest sweeping fluctuations of water balance. Although the age model does not allow for centennial scale comparisons, this period is in phase with the deglaciation episode Heinrich Stadial 11 (HS11, 135 ± 1 ka to 130 ± 2 ka, Marino et al. 2015). Oceanic records suggest incursions of icebergs and large volumes of meltwater well into the Atlantic and even into the Mediterranean, in multiple short events lasting less than 1 ka (Sierro et al., 2005). During periods of ice breakup, it is suggested that meltwater pulses following icesheet collapse put a halt on the Atlantic circulation and induced dry and cold climate all over vast regions of the Northern Hemisphere (NH), followed by an abrupt increase in SST when the circulation re-establishes (Bond et al., 1993). Interestingly, some models predict a particularly strong air cooling and drying during the Eastern Mediterranean winters (Hostetler et al., 1999) in the first phase followed by a very strong heating effect during the second phase of SST increase, with an overall temperature amplitude > 5 °C. The temperature and precipitation trend observed in the Dead Sea record between 129.6 and 129 ka might thus highlight the last HS11 substage, and suggests a delay of several centuries between temperature and precipitation increases. Fluctuations of water balance between 132.1 ka and 129.6 ka were also observed in Central Italy (Regattieri et al., 2016), though not exactly in phase with the ones observed in 5017-1. The last halite layer at 128.8 ka probably records the end of Termination II (TII), in line with dates suggested by the other Mediterranean records (e.g. 127.2 ± 1.6 ka, Brauer et al. 2007; 127.5 ± 2.3, Tzedakis et al. 2003; 128 ± 1 ka, Bar-Matthews et al. 2003; 128.2 ± 0.9 ka, Zanchetta et al. 2015; 129 ± 1 ka, Drysdale et al. 2005; 129 ka, JiménezAmat and Zahn 2015).

- The second phase (129-122 ka) is in excellent agreement with the timing of high $\delta^{18}O$ in Soreq cave speleothems, and with S5 onset. For this period, we could not measure any temperature. Precipitation

were higher than 1080 mm yr^{-1} and lower than 1460 mm yr^{-1} (35% to 85% higher than today). The short event of halite deposition at 126 ka highlights a brief decrease of rainfall down to ~1030 $\pm$ 100 mm yr^{-1}. This episode is in phase with the Atlantic C27 ice rafting event (Oppo et al., 2001, 2006; Zhuravleva et al., 2017), documented in the Mediterranean as a brief incursion of aridity and cold (Frogley et al., 1999; Martrat et al., 2004). Tzedakis et al. (2018) performed a North Atlantic meltwater experiment with an Earth System model to simulate C27 event, setting a freshwater flux of 0.05 Sv (1 Sv = 10^6 m^3 s^{-1}) for a 400 years period. It resulted in a precipitation drop of no more than 10 mm yr^{-1} in the Eastern Mediterranean. If this order of magnitude holds, then it means the Dead Sea upper layer was very close to halite saturation during the whole MIS5e peak, so that a minor drop in rainfall could lead to halite precipitation. In this case, we should favour the lower bounds of the error envelope as the most likely amount of precipitation during the period 122-129 ka, that is, ~1080 mm yr^{-1}. The comparison with rainfall amounts reconstructed from Soreq speleothems $\delta^{18}O$ also points towards the lower bounds scenario. This is also consistent with models which predict an increase in winter precipitation in the Levant due to orbital forcings at 125 ka of no more than 50 mm yr^{-1} (Kutzbach et al., 2014; Bosmans et al., 2015).

- The third phase (122-117 ka) outlines significant aridification and cooling with precipitation decreasing down to 740 mm yr^{-1}, close to present-day values (< 800 mm yr^{-1}), and winter temperatures dropping at a rate of 2 °C ka^{-1}, about 3 to 5 times as fast as the rate of decline of mean annual SST in the Western (Martrat et al., 2014) and Eastern (Amies et al., 2019) Mediterranean. Note that since the Dead Sea reached the basin shoulder (380-400 m bsl) at 118-117 ka, the lower uncertainty on the surface area, hence on the precipitation, is important, therefore one must consider the possibility of very low rainfall at this time (500-600 mm yr^{-1}). In the Mediterranean, this period corresponds to a rather gradual decline of arboreal taxa, especially the oak (Brauer et al., 2007; Milner et al., 2016), albeit more pronounced in the Levant (Gasse et al., 2015).

Overall, the temperature, hydrology and stratigraphy record of MIS5e in the Dead Sea shows it is very well correlated with the North Atlantic and Mediterranean climates.

5.6.4 Evidence for a millennial scale Northern Atlantic Oscillation (NAO) ?

Hydrology and winter temperatures in the Levant as reconstructed in this study show rather monotonic trends: lake level/precipitation decrease through the period 132-118 ka, and thermal seasonality, defined as the difference between annual and winter temperatures, increases. The hydrological recession stops from 129 to 122 ka synchronously with sapropel S5 and with a midpoint lag of ~2 ka compared to the summer/winter insolation maximum/minimum centered at 127 ka. The latter delay has been observed at an Atlantic scale (Shackleton et al., 2003) and justified as a consequence of late meltwater pulses affecting the Atlantic and its circulation (Grant et al., 2016). However, even taking into account this lag, it seems solstice insolation has limited in-

fluence on the DS paleoclimatic record. Indeed, the precipitation increase coeval with sapropel S5 probably remained limited, and rainfall amounts were likely lower than at 132 ka (see Section 5.6.3 above).

In Figure 5.15, we show the precipitation in central Levant and temperature seasonality both measured in this study along with arboreal pollens percentage measured by Chen and Litt (2018) in core 5017-1, the latter being a proxy for precipitation. We also plot the autumn insolation and the winter sea level pressure (SLP) near the Azores. First, we observe that autumn insolation and SLP correlate very well. This surprising correlation was pointed out by Hall et al. (2005): winter SST is mainly forced by autumn insolation, as thermal inertia of oceans results in a 2 to 3 months delay. In turn, winter SSTs are positively correlated with winter SLP at Azores, with a consistent causality of the former to the latter, as an increasing number of studies have demonstrated over the last two decades (Rodwell et al., 1999; Kushnir et al., 2002; Gastineau et al., 2013; Smith et al., 2016). This lagged SST control on SLP led Hall et al. (2005) to suggest the existence of a millennial scale Northern Hemisphere Annular Mode (NAM), also called North Atlantic Oscillation (NAO) in Eurasia, which would be controlled by automnal insolation. As a matter of fact a striking resemblance of trends arises through comparing DS climatic trends with SLP. Dead Sea winters get all the colder compared to mean annual temperature as SLP increases, and the abundance of arboreal pollen increases and decreases synchronously with autumn insolation, peaking at 120 ka. This trend is expected in the case of strong positive NAO: records over the period 1950-2005 highlight anticorrelation between NAO and DS winter temperature and positive correlation with DS precipitation (see maps in Figure 5.15). The singular vegetation lag observed by Chen and Litt (2018) when comparing with all the other Mediterranean pollen records meets here an interesting and likely explanation: the Dead Sea is the only Mediterranean pollen site to be positively correlated with NAO with respect to precipitation. Conversely, the central Levant is negatively correlated with NAO with respect to precipitation, which would justify the decreases in precipitation and lake level from 132 to 118 ka. Interestingly also, current (late Holocene) SLP and autumn insolation are intermediate, and so are central Levant precipitation, thermal seasonality and arboreal pollen percentages.

Such an Atlantic teleconnexion was already proposed by Felis et al. (2004) who deduced a thermal seasonality 1.6 times as high as today from geochemical measurements on corals from the Gulf of Aqaba, in the northernmost Red Sea, dated at 121.9 $\pm$ 7 ka. Coupling the measurements with a GCM modelling, they deduced direct solar forcing could only account for one third of the observed seasonality increase, the rest being explained by the cold winters brought by Siberian winds under conditions of positive NAO. In line with this previous study, we therefore suggest the existence of a millennial scale NAO, which can be termed as “orbital NAO”. Contrary to the latter study however, the temporal resolution of our record lead us to point out a phasing with ~October insolation. This observation, supported by the model of Hall et al. (2005), lead us to advance an autumn perihelion forcing.

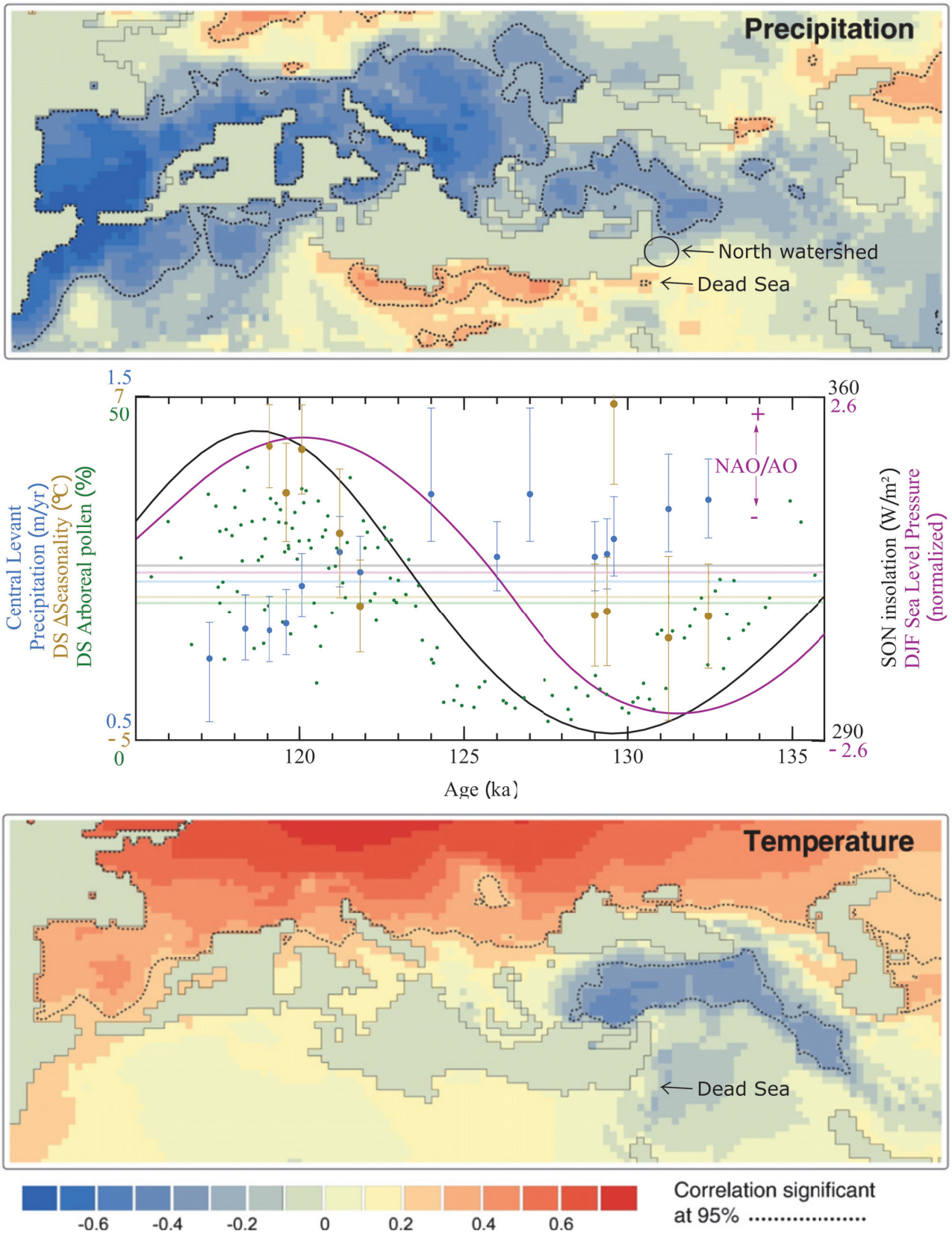

Figure 5.15: ***Correlation between Autumn insolation, Winter Sea Level Pressure at the Azores and climatic trends in the Levant during MIS5e.*** *Top and bottom maps (from López-Moreno et al. 2011): observed Pearsons correlation coefficients between winter (DJFM) NAO and winter precipitation and temperature for the period 1950-2005. Centre panel: Precipitation in central Levant (this study), temperature seasonality (annual - winter) in the DS compared to today (this study), and arboreal pollen as counted by Chen and Litt (2018) in core 5017-1, along with autumn (SON) insolation at 30°N (Laskar et al., 2004) and winter (DJF) normalized Sea Level Pressure calculated at the Azores high (Hall et al., 2005). Horizontal lines: late Holocene values.*

Such an orbital forcing on the atmospheric circulation has been abundantly documented for the Southern hemisphere sibling of NAO, the El Niño Soutern Oscillation (ENSO; e.g. Clement et al. 1999; Stott et al. 2002), but evidence may have lacked in the NH so far. If such a major phenomenon exists in the NH, then it should show a strong imprint in the paleoclimatic records of MIS5e, given the special precessional amplitude during this period. In Europe, North Africa and the Middle East, we can classify the area into four climatic NAO+ winter modes: (i) cold/dry (Anatolia, Northern Levant, southern Middle East), (ii) warm/wet (Northern Europe), (iii) warm/dry (northern Mediterranean border, Maghreb) and (iv) cold/wet (southeastern Mediterranean border). All these modes should be at their maximum at ~120 ka. In Northern Europe, the LIG has been documented as soon as the late 19th century, based on the recognition in the stratigraphy of vegetational and faunal evidence for a warm episode (Harting, 1874; Jensen and Milthers, 1928; Florschütz, 1930; Louman, 1934). This North European mild period, called the Eemian (Harting, 1874), has focused the work of many palynologists so well that a vast amount of palynological descriptions is available, albeit uneasy to correlate with the marine isotope stages. Such a correlation exists for the most classical cores however (e.g. Kukla et al. 2002a; Shackleton et al. 2002), and a date of 126-125 ka is usually ascribed to the onset of interglacial vegetation in northern and central Europe, that is, 2 ka later than in the Mediterranean. The european Eemian is subdivided within several substages bearing the name of the dominant vegetation component (Kukla et al., 2002b), the first arboreal one being *Corylus*-phase, corresponding to ~125 ka, and the next one being *Carpinus*-phase, corresponding to ~120 ka. Several authors propose probabilistic methods to assess quantitative precipitation and temperatures from the pollen assemblages. Among them, Guiot (1990) estimate winter temperatures higher than today by 0 to 2 °C from 124 to 115 ka at the French sites la Grande Pile and les Echets, Rousseau et al. (2006) estimate a peak in summer temperature at 125 ka and a peak in winter temperatures and precipitation at 120-119 ka, Zagwijn (1996) estimates a peak in summer temperatures (2 °C higher than present) during *Corylus*-phase and a peak in winter temperatures (3 °C higher than present) along with an increase in precipitation during *Carpinus*-phase in the Netherlands, and Aalbersberg and Litt (1998) also report a summer peak during *Corylus*-phase while winter temperatures peaked during *Carpinus*-phase based on an assessment of palaeobotanical, coleopteran and periglacial data from 106 sites in northern Europe. Overall, MIS5e climate in northern Europe is perfectly consistent with a prevailing summer insolation at 125 ka and a dominant positive NAO at 120 ka. This is reinforced by the fact that models agree with european climatic data at 125 ka (Kaspar et al., 2005; Otto-Bliesner et al., 2013) while they patently underestimate winter temperatures at 120 ka (Otto-Bliesner et al., 2013). Opposite to this European trend, a pollen record analyzed in a core drilled at lake Van (Pickarski et al., 2015), Turkey, shows a climatic optimum at 129 ka, and a deterioration from 126 ka with retreat of the mesophylous forest mainly highlighted by the progressive disappearance of *Carpinus* and *Ulma*. This deterioration peaks at 120 ka with the maximal abundance of *Pinus*, evidence of a dry and cold climate. This trend, opposite to the European one, is expected for this area with opposite NAO modes.

The above-mentioned European and Turkish records seemingly point out a winter climate in phase with autumn insolation and NAO at orbital scale, just like our results from the Dead Sea. If our theory reveals

true, then why GCMs do not reproduce such a trend ? This remains an open question. Chelton and Xie (2010) emphasized the prominent influence of models spatial resolution in reproducing accurately the ocean to atmosphere causal relation. This relation occurs at the mesoscale of 10s to 100s km, that is, the scale of eddies (Small et al., 2008). Yet, models that were used recently to investigate the LIG climatic trends typically used a grid with resolution coarser than 1° (Otto-Bliesner et al., 2013; Kutzbach et al., 2014; Bosmans et al., 2015). Furthermore, it was shown that a refined spatial grid was necessary but not sufficient to fully account for ocean to atmosphere relation (Bryan et al., 2010; Small et al., 2014). Through modelling the Kuroshio current, Ma et al. (2016b) showed that complex mesoscale feedbacks between oceanic eddies and atmosphere, usually overlooked by models, significantly increased the intensity of atmospheric jets when taken into account.

We suggest taking into account NAO modes could bring new insight into the temporal variabilities of the LIG across the Northern Hemisphere. The lag between the disappearance of forests in northern (~110 ka) and southern (~115 ka) Europe, so far justified by a difference in the response to the decrease in summer insolation (minimum at 115 ka; Tzedakis et al. 2003; Tzedakis 2005), could meet an additional explanation through the differences of climatic conditions establishing in these two regions in a period when the westerlies progressively trended southward along with decreasing NAO index. Trend discrepancies between speleothems $\delta^{18}O$ (Martrat et al., 2014) could also be analyzed in this new light. If this phenomenon is confirmed at hemispheric scale, it could have major consequences on the understanding we have on the routes followed by *Homo Sapiens* when exiting Africa some 120,000 years ago. It would also contribute to the debate on the mechanisms that have led the increase of NAO positive index for the last decades (e.g. Fyfe et al. 1999; Hu and Wu 2004), and thus allow for more robust predictions in regions of hydric stress like the Near-East, Middle-East and North Africa.

5.7 Conclusions

We have performed Brillouin spectroscopy measurements on fluid inclusions in halite layers of the Last Interglacial sequence of core 5017-1. Our results and their implications are multiple:

- We have developed a new method to estimate the evaporation degree of the Dead Sea. We have measured the speed of sound in a synthetic Dead Sea brine at successive evaporation steps, and shown that the speed of sound at liquid-vapour equilibrium depends linearly on the chlorinity of the solution. We have calculated the relative volume changes of the lake by implementing the speed of sound in biphasic fluid inclusions in the calibration equation. The volume of the lake decreased by ~50% from 132 ka to 118 ka.

- We have simulated multiple scenarii of lake decline and calculated the resulting thickness of halite at several evaporation steps for each scenario, which we compared with the actual thickness observed in core 5017-1. We used the relative volume changes and the hypsometric curve as constraints, let the basin subsidence (between 0 and 4.5 m ka^{-1}) and initial lake level (between 200 and 400 m bsl) as free parameters, and tested 3 different processes of halite deposition. Among the 1230 tested scenarii, it comes out one scenario especially yields halite thicknesses consistent with observations. This scenario

implies an initial lake level (when reaching halite saturation) at 285 m bsl at 132.5 ka, a subsidence rate of 2.5 m ka^{-1} and underwater halite focusing. We thus used these values, which we completed with some other relative volume change values for the sections devoid of salt (Levy et al., 2017), to reconstruct the evolution of the lake level during MIS5e.

- We have applied the method of Morin et al. (2019) and used lake levels to calculate paleo-rainfalls in the central Levant. Precipitation decreased from 1200 mm yr^{-1} at 132.5 ka down to 740 mm yr^{-1} at 118 ka, close to the current value (mean value for 1930-2015 of 779 mm yr^{-1}; 962 mm yr^{-1} in 1900). The gradual decrease in precipitation was interrupted by a 7 ka-long episode of increased precipitation corresponding to sapropel S5. During this specific period, precipitation were higher than 1080 mm yr^{-1} and lower than 1460 mm yr^{-1}, with some evidence pointing towards the likeliness of the lower bounds.

- The temperature of the Dead Sea proves to be a good proxy for winter temperatures (from september through february). Brillouin thermometry measurements show that winters were rather mild during MIS5e, close to late Holocene temperatures of ~22 °C. However, a sharp decrease in winter temperatures occurred at the end of MIS5e. We also observe the occurrence of very cold winters at ~129.6 ka, pointing out potential brief incursions of cold air masses during substages of Heinrich event HS11.

- Our results show the strong connection of the Dead Sea with North Atlantic and Mediterranean climates during MIS5e. Furthermore, we show that the trends of temperature seasonality and precipitation along with the evolution of forests are consistent with a millennial-scale North Atlantic Oscillation (NAO) switching from negative to positive mode from 132 to 118 ka. In the case of an autumnal insolation control on NAO, as expected due to oceans thermal inertia, such a trend is expected. Therefore we surmise that a millennial-scale NAO with highest (lowest) index at autumn (spring) perihelion controls the northern hemisphere climate, adding up to the better-documented influence of summer insolation at precessional scale.

Appendix

5.A Construction of the hypsometric curve

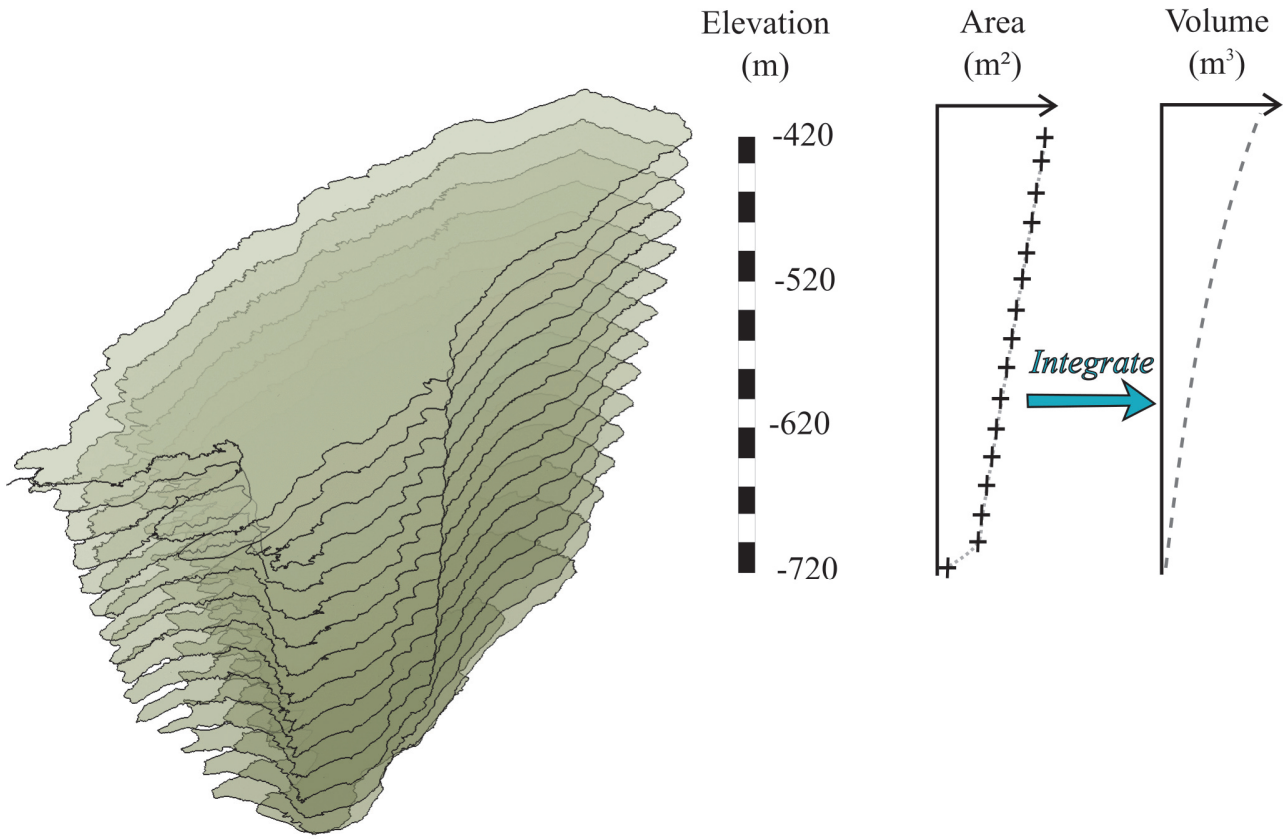

Figure 5.A.1: ***Method used for the construction of the Dead Sea hypsometric curve.*** *The stack of horizons corresponds to the series of 16 polygons obtained from the 20m-spaced contour lines -720m to -420m of the northern Dead Sea basin (i.e. the currently filled basin). Each polygon represents the surface of the lake if the level were equal to the elevation of the contour line. Elevation is exaggerated 100 times.*

Hypsometric curves of basins show the surface area and volume of an infilling water body depending on its elevation in the basin. We obtained the equation linking surface area to Dead Sea elevation through calculating the surface area of polygons defined by contour lines (Figure 5.A.1), and interpolated from minimum elevation of the basin (~-720m) to the spilway elevation at +60.5m. The volume curve is obtained by integrating the surface area equation. For the lower basin (-720 to -420m) we used 20m-spaced contour lines provided by John K. Hall, who kindly produced these data for us using the 5m-resolution multibeam bathymetric data obtained with the 2007 ship survey (Sade et al., 2014). For the currently dry higher basin (-420 to +60.5m), we produced 5m-spaced contour lines using 200m-resolution elevation data obtained with the Geographic Information System of *Mathematica v12*. At the junction between our two sets of data, at 420 m bsl, we noticed a ~9m elevation error.

5.B Scenarii of lake level decline and predicted halite thickness

5.C Agreement between measured LVE speeds of sound and fit

5.D Calculating rainfall amounts

The level of the Dead Sea is controlled by 2 parameters, the inflow (i.e. rivers discharge) and the outflow (i.e. evaporation) of water. The Dead Sea watershed spreads over extremely diverse hydrological regions, from beyond 33°N where MAP exceeds 800 mm yr^{-1} down to ~29°N where MAP is lower than 50 mm yr^{-1}. Therefore the rivers from the North, Jordan and Yarmouk, constitute the overwhelming proportion of the yearly water input. At equilibrium, the volume of water leaving the lake each year through evaporation equates to the annual discharge, to the extent that the value of the two parameters constrain the surface of the lake, ergo the level of the lake. The level of the Dead Sea thereby constitutes a hydrological monitor. In this work, we use the paleo-level of the Dead Sea to quantify rainfall amounts based on the work of Morin et al. (2019). In the following, we briefly describe the method.

The amount of evaporated water per year and unit area in the Dead Sea E, determined by applying a linear regression to evaporation estimations for Dead Sea surface density ranging from 1170 to 1330 kg m^{-3} ($R^2 = 0.85$; $RMSD = 0.09$m yr^{-1}; see Figure 5.D.1A), is:

$$E = -0.00472[(\text{m m}^3)/(\text{yr kg})^{-1}].\rho + 6.98[\text{m yr}^{-1}]. \tag{5.11}$$

MAP is very well correlated to annual discharge to the lake in all stations located Northwest of the watershed. As the best correlation is found for station Kfar Giladi ($R^2 \approx 0.8$), located in Central Levant far North in the watershed, the following linear regression relates volumetric discharge to the Dead Sea D [m^3 yr^{-1}] to the rainfall amount in this northern part of the watershed P_r[mm yr^{-1}]:

$$D = 2.48.10^6[\text{m}^3\ \text{mm}^{-1}].P_r - 0.55.10^9[\text{m}^3\ \text{yr}^{-1}]. \tag{5.12}$$

We constrain E in Equation (5.11) implementing density values shown in Table 5.2. We constrain D multiplying E by the surface area of the lake, and subsequently determine P_r through Equation (5.12). As the lake was monomictic during phases of halite precipitation, density estimations for the whole lake apply to the density of the surficial layer, thus ensuring relatively precise estimations. Conversely, determining P_r during periods of meromixis goes with increased uncertainties, as illustrated by a larger error envelope for the period ~125 ka. For this specific period, MAP and lower uncertainty are determined for a homogeneous lake, as the chemistry of the deep layer as determined with pore fluids chemistry is the maximum possible concentration for the upper layer. We then determined the upper uncertainty by assigning surficial waters a density of 1131 kg m^{-3}, which is the density of brines flowing out Ein Qedem spring and reckoned as a good proxy for the upper layer during

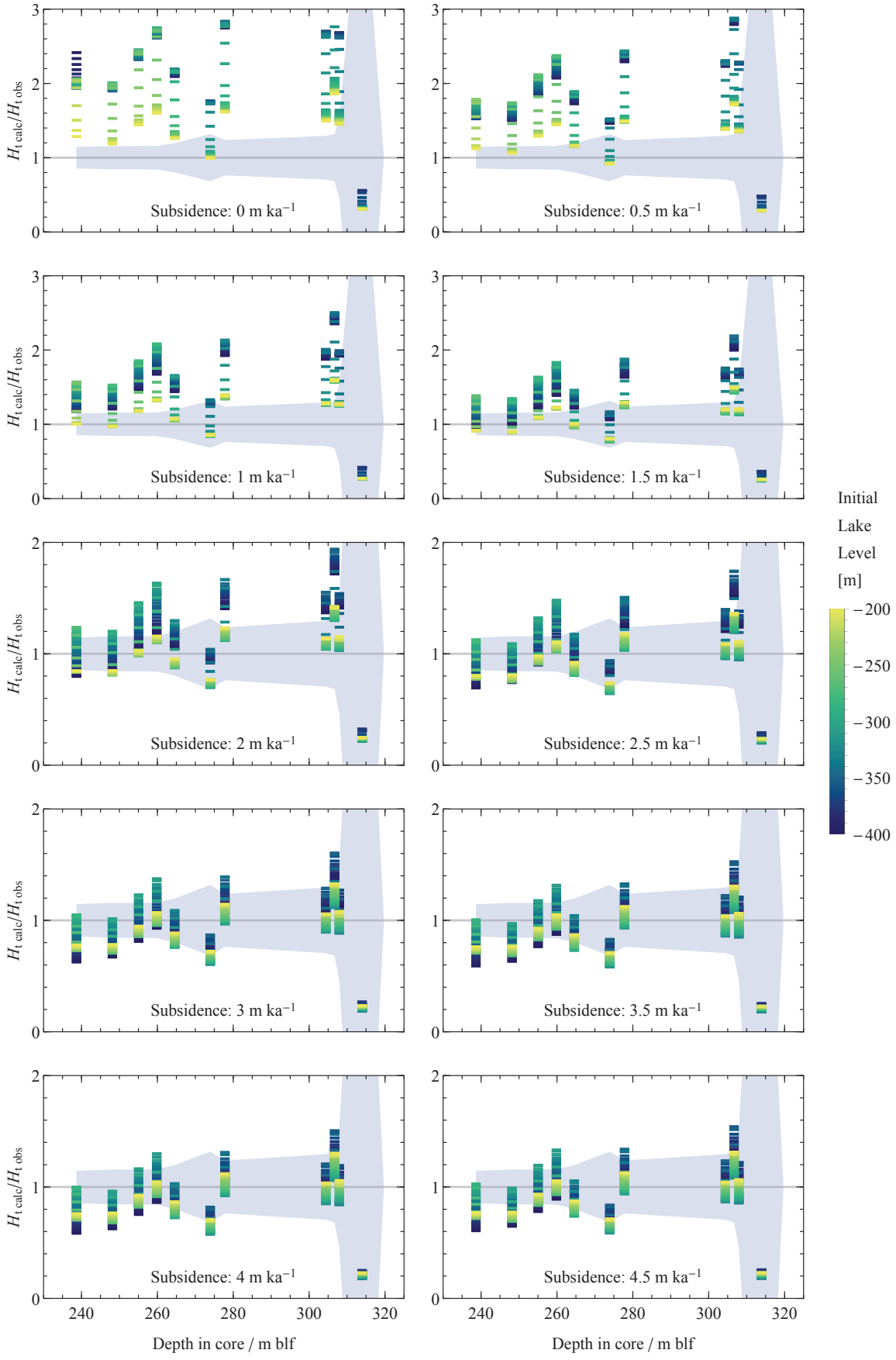

Figure 5.B.1: ***Scenarii of lake level decline and predicted vs. observed halite thickness: underwater halite focusing.*** *$H_{t\,calc}$ is the halite thickess calculated with Equation (5.8), and $H_{t\,obs}$ is the halite thickess observed in 5017-1. A data point located within the gray error envelope is considered consistent with observed halite thickness.*

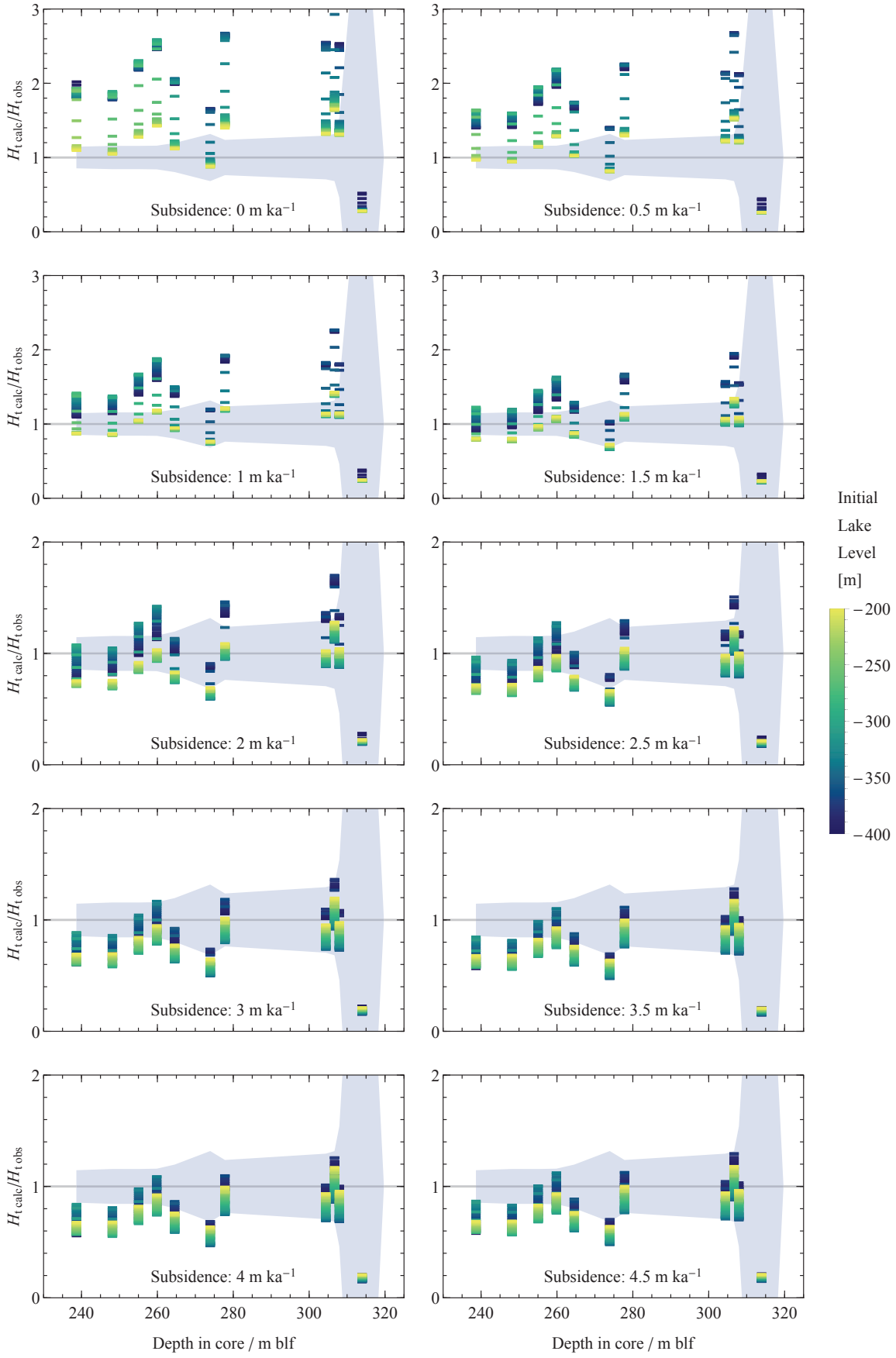

Figure 5.B.2: ***Scenarii of lake level decline and predicted vs. observed halite thickness: subaerial halite focusing.*** *A data point located within the gray error envelope is considered consistent with observed halite thickness.*

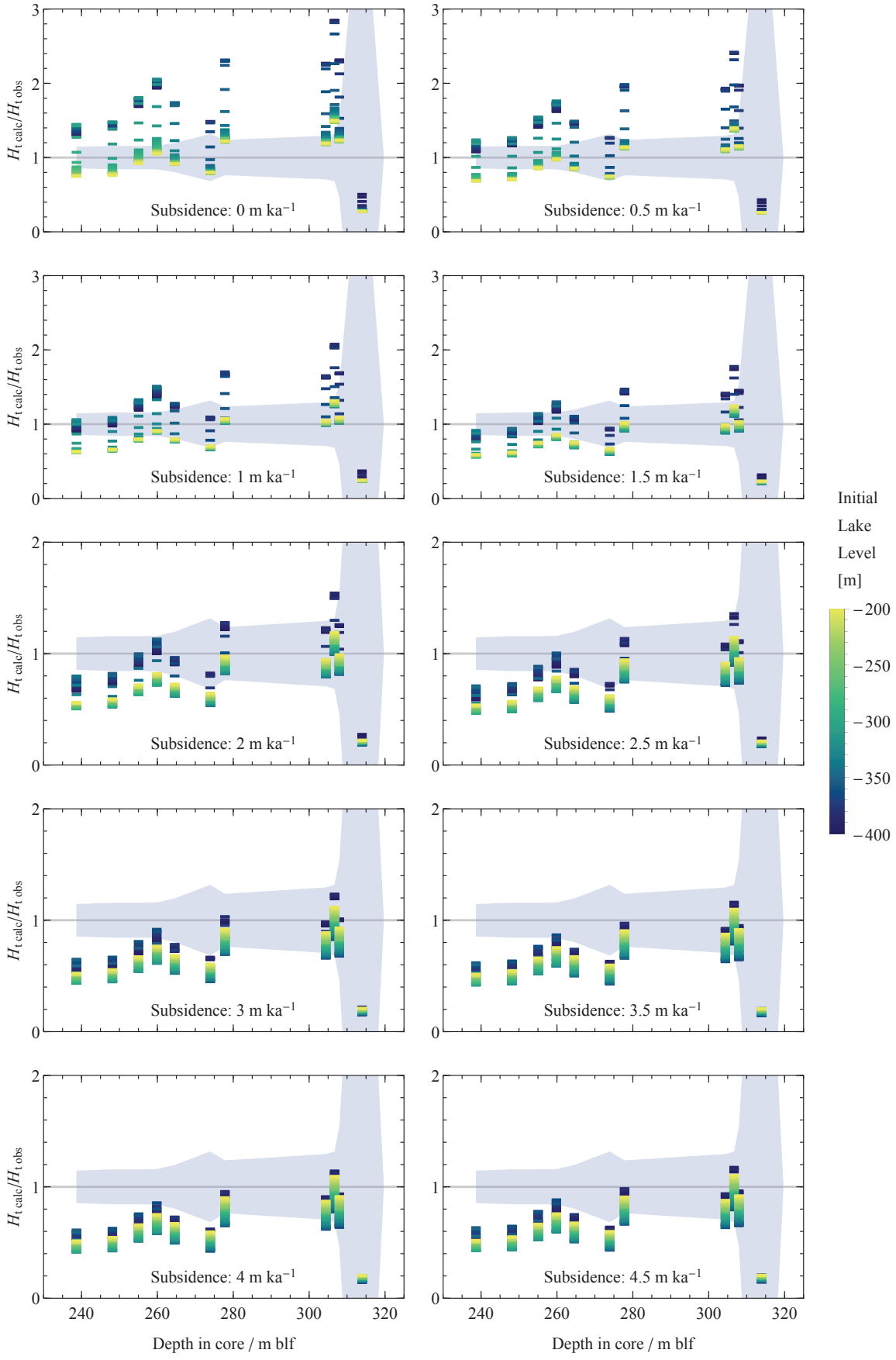

Figure 5.B.3: ***Scenarii of lake level decline and predicted vs. observed halite thickness: no halite focusing.*** *A data point located within the gray error envelope is considered consistent with observed halite thickness.*

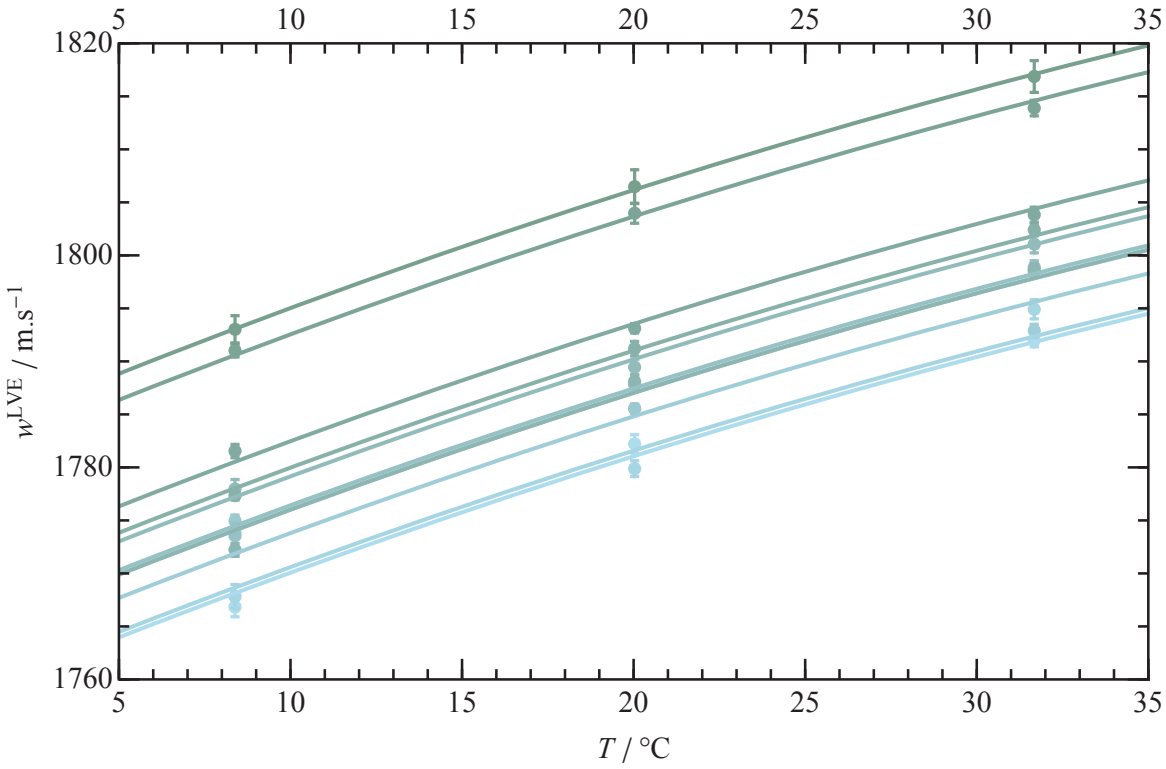

Figure 5.C.1: ***Average LVE curves obtained in the 11 sections used for the temperature reconstruction.*** *Each data point is the mean w^{LVE} value obtained from ~20 FIs. Error bars: standard error on the mean. Same parabolic equation fitted to each section trio of data point, rescaled with a factor. This equation was obtained by fitting a parabola to all the data points from all sections together. The fact that this global parabolic equation fits well each section shows that it can be used to fit w^{LVE} of each individual FI.*

Lisan meromictic period (Weber et al., 2018). Since Lisan was a much more prolonged period of meromixis compared to meromixis at 125 ka, we regard the density of the Lisan upper layer as a safe minimum value for the upper layer at 125 ka. Note that lake elevation during this period is also a minimum value, however we do not assign higher level estimations for the determination of the upper MAP uncertainty. Indeed, the outcrop showing the highest paleo-elevation of 310 m bsl at 125 ka, as shown in Waldmann et al. (2009), displays a 30 cm-thick sequence deposited during this period, compared to a 1 m-thick sequence on the second highest outcrop located 2 meters below in the same area (Arava Valley). This sudden sequence thinning points towards a very close paleo-shoreline, hence the lake level probably did not exceed much 310 m bsl at this time. Overall, a ~30 kg m^{-3}/20 m error on the density/level brings a 100 mm yr^{-1} error on the precipitations amount.

MAP estimates from $\delta^{18}O$ values of Soreq cave as displayed in Figure 5.14A are derived from paleorainfall $\delta^{18}O$ estimates through the equation (Bar-Matthews et al., 2003):

$$\delta^{18}O(rainfall) = -3.25[\text{mm yr}^{-1}] - 0.00508P_{r-Soreq}. \tag{5.13}$$

As Soreq is only 15 km away from Jerusalem, we regard rainfall in both locations as equal. In order to compare MAP estimates at Kfar Giladi inferred from Dead Sea levels and Soreq MAP, we then converted $P_{r-Soreq}$ into MAP at Kfar Giladi station using an inter-station precipitation linear regression (Morin et al., 2019):

$$P_{r-KfarGiladi} = 0.9004P_{r-Jerusalem} + 300.1[\text{mm yr}^{-1}]. \tag{5.14}$$

Lastly, we corrected values of the sapropel S5 period (128.3-121 ka) for a 1‰reservoir effect, accounting for the more depleted Mediterranean waters compared to late Holocene times (Grant et al., 2012). As R^2 for Equation (5.14) is not so high (0.54; see Figure 5.D.1C) and our way of taking into account the source effect is simplistic, quantitative values of MAP inferred from Soreq speleothem $\delta^{18}O$ must be considered with caution.

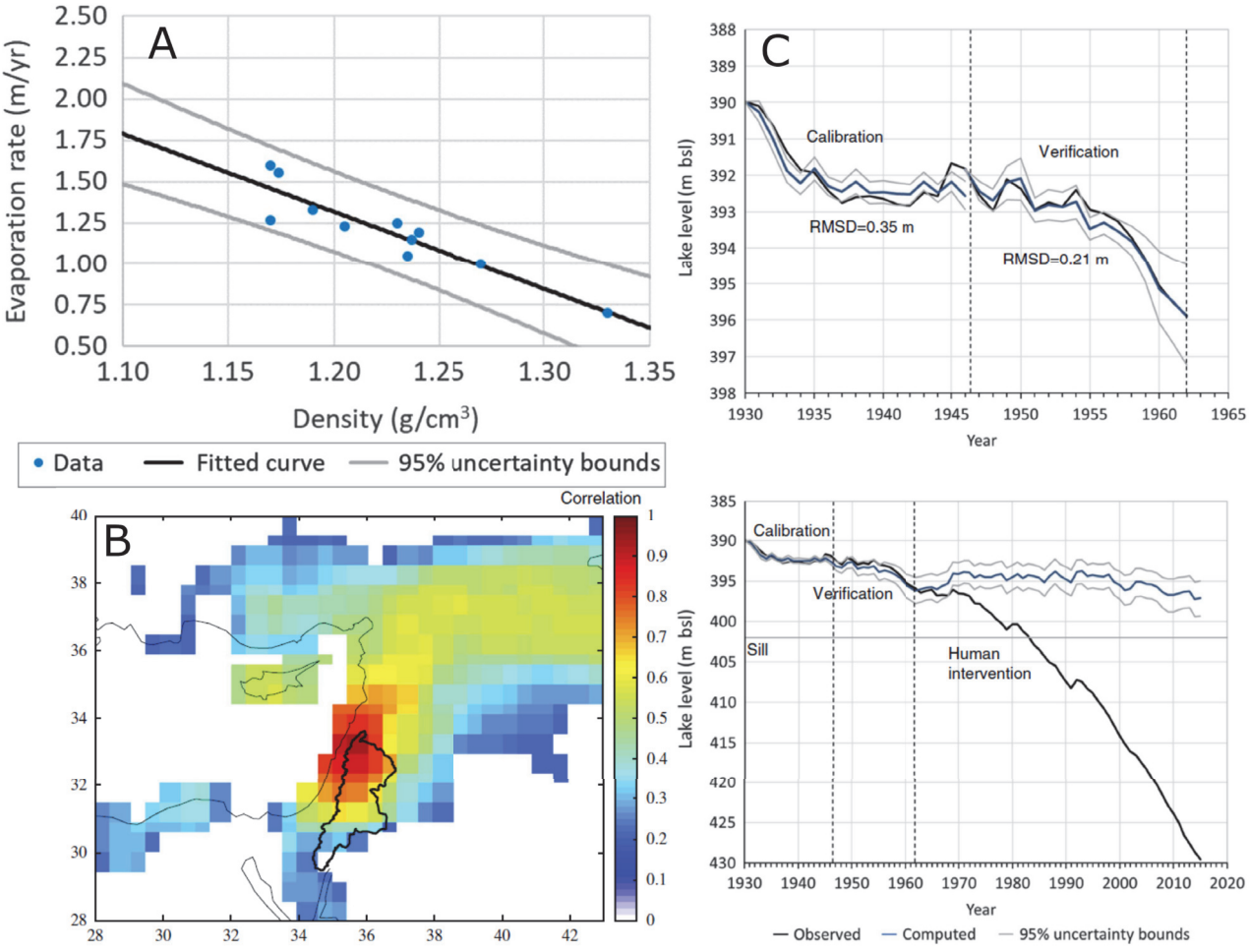

Figure 5.D.1: ***Method for the determination of MAP from Dead Sea levels (from Morin et al. 2019).*** *Panel A: linear regression of evaporation rates as a function of Dead Sea surface density. Panel B: Correlation of annual precipitations with annual precipitations at Kfar Giladi station. Panel C: Illustration of method calibration and verification. Model fits observations within uncertainty. Note that in Morin et al. (2019) an additional calibration is needed between level and surface density since the Dead Sea was not holomictic during calibration period. In our case, the determination of the density is more straightforward since we overwhelmingly apply the method to monomictic periods.*

CHAPTER 6

Conclusions and Prospects

In the following, we present a brief summary of the main advances achieved during this thesis, which we arrange by category of issue. Each section is coupled with a series of prospects.

Brillouin thermometry

We have developed a new paleothermometer that takes advantage of the information conveyed by the inelastic backscattering of light from halite fluid inclusions (FIs) to determine the entrapment temperature (T_f). It is the first technique ever to bypass the limitations associated with the FI bubble, as it constrains the curve of equal homogenization temperature (iso-T_h curve, generally termed "isochore") through speed of sound (w) measurements in the all-liquid FI. The main source of error is the instrumental uncertainty on the speed of sound σ_w, comprised between 0.1 and 0.15%, which converts into an uncertainty σ_{Tx} on the fluid inclusion's temperature of intersection of the iso-T_h and liquid-vapor equilibrium (LVE) curve, T_x, comprised between 1.5 and 2°C in the case of NaCl-H_2O FIs (1-sigma uncertainty). We overcome this rather large uncertainty, which can be different for other compositions, through measuring several FIs. In the case of a water body with stable temperature during the entrapment of the fluid inclusions assemblage (FIA), the average T_x ($T_{x,mean}$) can thus be identified as T_f, and the standard error on the mean be considered as the uncertainty on T_f. In samples synthetized in the lab at T_f of 24.6±0.5°C and 33.0±1°C, we have obtained $T_{x,mean}$ of 24.8±0.4°C and 31.9±0.4°C, respectively. In a sample that grew at 22.2±0.2°C on the deep floor of the Dead Sea, we have obtained 22.3±0.4°C after addition of a correction term to account for the pressure at the bottom of the Dead Sea. Our method thus proves accurate and precise, and presents the advantages of making possible the measurement of FIs down to ~3μm. The protocol is rather fast, as it allows the determination of a mean temperature with uncertainty ±1°C (2-sigmas) within 1 to 2 days.

Prospects:

- The uncertainty σ_{Tx} is inversely related to the angle of the intersection between the speed of sound iso-T_h and speed of sound LVE curves. Thus, it depends on the composition of the FI. So far, we have been unable to predict which will be the uncertainty for a given composition. We will know more through accumulating data of various samples from different saline lakes with different compositions. For instance, σ_{Tx} of FIs from the Dead Sea is twice as large as σ_{Tx} from NaCl-H_2O FIs. We suspect the magnesium content could be a major contributor in reducing the slope of the speed of sound iso-T_h, and therefore in reducing the intersection angle and increasing the uncertainty.

Brillouin thermometry proved successful on quartz (El Mekki-Azouzi et al., 2015) and on halite FIs, therefore we have every reason to think that it will work on any other mineral:

- Lacustrine gypsum would be a prominent candidate, as it would greatly extend the spatial applicability of the technique, and would be a way to complete the hatched stratigraphic pattern of halite. This is the subject of a currently running PhD project in our group.
- Cave calcite would be another excellent candidate, as caves temperature is acknowledged as a good proxy for mean annual air temperature. Moreover, as the content in heavy oxygen isotope of speleothems depends on both the cave temperature and the amount of precipitation, an independent constraint on the former would enable one to constrain the latter. Coupled Brillouin thermometry and oxygen isotope geochemistry could enable the worker to lead complete temperature-precipitation assessments. Based on Figure 4d in El Mekki-Azouzi et al. (2015), which shows that the uncertainty tends to infinity at 4°C in pure water, and the gain in precision made possible during this thesis, we estimate that we could perform paleothermometry with satisfactory precision ($\sigma_{\mathrm{Tx}} < 4°\mathrm{C}$) for any $T_{\mathrm{f}} >$ 9-10°C.

Constraining the pressure, deformation and damage in halite fluid inclusions

The present work has led to decisive advances in the understanding of halite fluid inclusions. We have developed a brand new method to measure the temperature away from T_{f} at which the halite FI starts "reequilibrating", that is, starts deforming in a non-reversible manner and definitely loses its initial density. Based on our results and on data from the literature, we have thus been in position to establish an empirical equation that predicts the reequilibration pressure: $P_{\mathrm{FI,lim}} = (90\mathrm{MPa})\frac{l}{(1\mu\mathrm{m})}^{-0.64}$. For a FI with *P-T* slope 1 MPa °C^{-1}, which is approximately the case of NaCl-H_2O FIs, this converts to the reequilibration temperature away from T_{f}: $\Delta T_{\mathrm{lim}} = (90\mathrm{K})\frac{l}{(1\mu\mathrm{m})}^{-0.64}$, with l the average side of a rectangular halite FI. In a more general case, estimating ΔT_{lim} requires knowing the *P-T* slope. For this reason, we have developed a model adapted for FIs with composition in the NaCl-KCl-$MgCl_2$-$CaCl_2$-H_2O system. Based on the Pitzer formalism, implementing the Young's mixing rule and accounting for the mechanical response of the FI's walls, the model calculates the *P-T* slope of FIs as a function of temperature, T_{h}, composition and shape. The model has an uncertainty on pressure of ~5% on NaCl-H_2O FIs and ~10% on other compositions, with a level of uncertainty increasing with the FI ionic strength, and is supported by experiments. Coupled with the empirical equation of pressure reequilibration, it makes possible the calculation of a paleothermometry "safety limit" in FI size depending on the temperature extrema the sample was subjected to. As an example, Dead Sea FIs present a ΔT_{lim} 40% larger compared to NaCl-H_2O FIs of comparable size.

Prospects:

- The use of Brillouin spectroscopy as a sensor of FIs reequilibration point could be extended to any type of FI composition and any type of host crystal. In detail, we could provide empirical equation for the reequilibration of calcite and gypsum FIs. Furthermore, we could synthetize halite crystals with lattice

impurities such as Ca^{2+} or Sr^{2+} in order to test the hypothetical strengthening effect of divalent cations on the FI walls.

- The model of pressure calculation could be extended to carbonates and sulfates, which would make the worker able to determine a FI size safety limit for any usual composition found in nature. For this, to comply with self-consistency, we need a homogeneous set of Pitzer parameters that is fitted the same way for all binary systems and which would cover the pressure, temperature and molality ranges of halite FIs.

The Dead Sea and its basin We have used the speed of sound in biphasic FIs as a proxy for relative volume changes of the Last Interglacial Dead Sea. Through comparing the calculated cumulated thickness of halite in 1230 different scenarii of lake decline -with initial level, subsidence rate and mode of halite deposition as variables- to the actual thickness along the sequence, we were able to identify a scenario that clearly outruns all the others. This scenario involves an initial lake level -at halite saturation- of 285 m below sea level (bsl), an average subsidence rate for the northern basin of 2.5 meters per 1,000 years over the last 132,000 years, and an operational underwater halite focusing as observed in the current Dead Sea by Sirota et al. (2016, 2017). Based on this scenario, we have reconstructed the Dead Sea level and its evolution during the Last Interglacial, which reveals much higher than suggested by previous studies, with a lowstand around 380 m bsl at the end of the period, that is, not lower than the Holocene average stand. Our lake level reconstruction reconciles the stratigraphy of core 5017-1 with observations on outcrops and estimations made on the evolution of the mass load on the basin floor.

Prospects:

- Our calculation of 0.15 Tg yr^{-1} for the average NaCl flux from external sources over the last 220,000 years, as well as the 0.24 Tg yr^{-1} suggested by Levy et al. (2018) for the last Glacial, support our assumption that the 3 Tg yr^{-1} of halite that deposited on the Dead Sea floor during the LIG mainly originate from the lake itself. Additional constraints are needed to better understand the evolution of the external flux, since the current value of 1.4 Tg yr^{-1} highlights a strong variability of this flux. This variability seems to be linked to the evolution of the lake level: the unprecedented speed in the drop of the Dead Sea level today is associated with an increased discharge from springs. Numerical hydrological models that take into account the aquifers of the Dead Sea and their interplay with the lake stands, along with constraints on the composition of the brines that circulate in the basin, could help us better understand the variability of the NaCl external flux.

- The Holocene lake stands are well constrained. It could be interesting to apply the method developed in this thesis to the Holocene halite sequences of core 5017-1, and compare the reconstructed lake level curve to the available one. The difference between the two curves could help better constrain the NaCl external flux.

Eastern Mediterranean climate and general atmospheric circulation Based on the correlation found between the Dead Sea hypolimnion temperature and the 5-year average air temperature of the period from September to February, we use the entrapment temperature measured in halite FIs as a proxy for winter temperature. We use the method of Morin et al. (2019) to infer paleo-precipitation in the central Levant from the Dead Sea level. This method is especially accurate in the cases when the Dead Sea is monomictic and saturated with respect to NaCl, as the density of the surface water is well constrained during these periods. Thus we are in position to propose a complete winter temperature-precipitation reconstruction for the LIG. We find no temperature significantly higher than the 20th century value of ~22°C. We show that winters were rather mild at the beginning of the LIG. We observe a strong decrease in winter temperature of ~2 °C ka^{-1} starting, at the latest, around 122 ka. We also show that precipitation were much higher than today during most of the LIG. It progressively declined from 1200 mm yr^{-1} at 132 ka down to 740 mm yr^{-1} at 118 ka. Although the uncertainty for the period spanning from 129 to 122 ka, coeval with the African Humid Period and sapropel S5, is higher, we can estimate precipitation were higher than 1080 mm yr^{-1} and lower than 1460 mm yr^{-1}. Our reconstruction reconciles the Dead Sea with estimations of increased moisture in other levantine sites during the LIG. Also, we recognize an Atlantic signature in the record, mainly highlighted by the occurrence of the 126 ka C27 dry event and a likely incursion of cold air masses possiby related to a substage of Heinrich stadial HS11 at ~129.6 ka. Furthermore, we suggest that the temperature and precipitation trends observed in the record, along with the Dead Sea pollen record, are in phase with autumn insolation and winter sea level pressure, and are thus consistent with an orbital North Atlantic Oscillation (NAO) sliding from negative mode at 132 ka to positive mode at 120 ka.

Prospects:

- In order to refine the observed trends, additional halite sections should be measured in the Last Interglacial sequence.
- The Holocene part of core 5017-1 bears many halite sequences, which would allow for a similar temperature-precipitation reconstruction. This could be the occasion to verify if a similar phasing with the autumn insolation is found; the latter reaches its maximum around 6 ka during the Holocene with, however, a much lower amplitude than during the LIG.
- In the light of our hypothesis of an orbital NAO forced by autumn insolation, we should check other records of the Northern Hemisphere that date back to the LIG and for which a winter temperature and precipitation quantification is available.

Bibliography

Aalbersberg, G. and Litt, T. (1998). Multiproxy climate reconstructions for the Eemian and Early Weichselian. Journal of Quaternary Science, 13(5):367–390.

Cited p. 153.

Abdulagatov, I. M., Azizov, N. D., and Zeinalova, A. B. (2007). Viscosities, densities, apparent and partial molar volumes of concentrated aqueous MgSO4 solutions at high temperatures and high pressures. Physics and Chemistry of Liquids, 45(2):127–148.

Cited p. 105.

Abdulagatov, I. M., Azizov, N. D., and Zeinalova, A. B. (2009). Density, Apparent and Partial Molar Volumes, and Viscosity of Aqueous Na2co3 Solutions at High Temperatures and High Pressures. Zeitschrift für Physikalische Chemie, 221(8):963–1000.

Cited p. 105.

Affek, H. P., Bar-Matthews, M., Ayalon, A., Matthews, A., and Eiler, J. M. (2008). Glacial/interglacial temperature variations in Soreq cave speleothems as recorded by clumped isotope thermometry. Geochimica et Cosmochimica Acta, 72(22):5351–5360.

Cited p. 18.

Al Ghafri, S., Maitland, G. C., and Trusler, J. P. M. (2012). Densities of Aqueous $MgCl_2$(aq), $CaCl_2$(aq), KI(aq), NaCl(aq), KCl(aq), $AlCl_3$(aq), and (0.964 NaCl + 0.136 KCl)(aq) at Temperatures Between (283 and 472) K, Pressures up to 68.5 MPa, and Molalities up to 6 mol·kg^1. J. Chem. Eng. Data, 57(4):1288–1304.

Cited p. 31, 88, 90, 105 et 107.

Al Ghafri, S. Z., Maitland, G. C., and Trusler, J. P. M. (2013). Densities of $SrCl_2$(aq), Na_2SO_4(aq), NaHCO3(aq), and Two Synthetic Reservoir Brines at Temperatures between (298 and 473) K, Pressures up to 68.5 MPa, and Molalities up to 3 mol·kg^1. J. Chem. Eng. Data, 58(2):402–412.

Cited p. 105.

Allen, H. C., Casillas-Ituarte, N. N., Sierra-Hernández, M. R., Chen, X., and Tang, C. Y. (2009). Shedding light on water structure at airaqueous interfaces: ions, lipids, and hydration. Phys. Chem. Chem. Phys., 11(27):5538–5549.

Cited p. 62 et 64.

Allen, J. R. M., Brandt, U., Brauer, A., Hubberten, H.-W., Huntley, B., Keller, J., Kraml, M., Mackensen, A., Mingram, J., Negendank, J. F. W., Nowaczyk, N. R., Oberhänsli, H., Watts, W. A., Wulf, S., and Zolitschka, B. (1999). Rapid environmental changes in southern Europe during the last glacial period. Nature, 400(6746):740–743.

Cited p. 10.

Alonso, R. N., Jordan, T. E., Tabbutt, K. T., and Vandervoort, D. S. (1991). Giant evaporite belts of the Neogene central Andes. Geology, 19(4):401–404.

Cited p. 45.

Álvarez, E., Vázquez, G., Sánchez-Vilas, M., Sanjurjo, B., and Navaza, J. M. (1997). Surface Tension of Organic Acids + Water Binary Mixtures from 20 ŕC to 50 ŕC. J. Chem. Eng. Data, 42(5):957–960.

Cited p. 62.

Ambaum, M. H. P., Hoskins, B. J., and Stephenson, D. B. (2001). Arctic Oscillation or North Atlantic Oscillation? J. Climate, 14(16):3495–3507.

Cited p. 6.

Amies, J. D., Rohling, E. J., Grant, K. M., RodríguezSanz, L., and Marino, G. (2019). Quantification of African Monsoon Runoff During Last Interglacial Sapropel S5. Paleoceanography and Paleoclimatology, 0(0).

Cited p. 148 et 150.

Anand, P., Elderfield, H., and Conte, M. H. (2003). Calibration of Mg/Ca thermometry in planktonic foraminifera from a sediment trap time series. Paleoceanography, 18(2).

Cited p. 16.

Anati, D. A., Stiller, M., Shasha, S., and Gat, J. R. (1987). Changes in the thermo-haline structure of the Dead Sea: 19791984. Earth and Planetary Science Letters, 84(1):109–121.

Cited p. 122.

Andersen, K. K., Azuma, N., Barnola, J.-M., and Bigler, M. (2004). High-resolution record of Northern Hemisphere climate extending into the last interglacial period. Nature, 431(7005):147–151.

Cited p. 8 et 145.

Archer, D. G. (1992). Thermodynamic Properties of the NaCl+H_2O System. II. Thermodynamic Properties of NaCl(aq), NaCl·$2H_2O$(cr), and Phase Equilibria. Journal of Physical and Chemical Reference Data, 21(4):793–829.

Cited p. 90, 94, 105, 106 et 107.

Arnon, A., Selker, J. S., and Lensky, N. G. (2016). Thermohaline stratification and double diffusion diapycnal fluxes in the hypersaline Dead Sea. Limnology and Oceanography, 61(4):1214–1231.

Cited p. 123 et 124.

Ayora, C., Garcia-Veigas, J., and Pueyo, J.-J. (1994). X-ray microanalysis of fluid inclusions and its application to the geochemical modeling of evaporite basins. Geochimica et Cosmochimica Acta, 58(1):43–55.

Cited p. 96.

Bakker, P., Masson-Delmotte, V., Martrat, B., Charbit, S., Renssen, H., Gröger, M., Krebs-Kanzow, U., Lohmann, G., Lunt, D. J., Pfeiffer, M., Phipps, S. J., Prange, M., Ritz, S. P., Schulz, M., Stenni, B., Stone, E. J., and Varma, V. (2014). Temperature trends during the Present and Last Interglacial periods a multi-model-data comparison. Quaternary Science Reviews, 99:224–243.

Cited p. 19.

Bar-Matthews, M., Ayalon, A., Gilmour, M., Matthews, A., and Hawkesworth, C. J. (2003). Sealand oxygen isotopic relationships from planktonic foraminifera and speleothems in the Eastern Mediterranean region and their implication for paleorainfall during interglacial intervals. Geochimica et Cosmochimica Acta, 67(17):3181–3199.

Cited p. 18, 120, 146, 148, 149 et 163.

Bar-Matthews, M., Ayalon, A., and Kaufman, A. (2000). Timing and hydrological conditions of Sapropel events in the Eastern Mediterranean, as evident from speleothems, Soreq cave, Israel. Chemical Geology, 169(1):145–156.

Cited p. 120 et 146.

Bar-Matthews, M., Ayalon, A., Kaufman, A., and Wasserburg, G. J. (1999). The Eastern Mediterranean paleoclimate as a reflection of regional events: Soreq cave, Israel. Earth and Planetary Science Letters, 166(1):85–95.

Cited p. 146.

Bar-Matthews, M., Keinan, J., and Ayalon, A. (2019). Hydro-climate research of the late quaternary of the Eastern Mediterranean-Levant region based on speleothems research A review. Quaternary Science Reviews, 221:105872.

Cited p. 120 et 147.

Barker, S., Chen, J., Gong, X., Jonkers, L., Knorr, G., and Thornalley, D. (2015). Icebergs not the trigger for North Atlantic cold events. Nature, 520(7547):333.

Cited p. 10.

Barker, S., Knorr, G., Edwards, R. L., Parrenin, F., Putnam, A. E., Skinner, L. C., Wolff, E., and Ziegler, M. (2011). 800,000 Years of Abrupt Climate Variability. Science, 334(6054):347–351.

Cited p. 9.

Bartlein, P. J., Anderson, K. H., Anderson, P. M., Edwards, M. E., Mock, C. J., Thompson, R. S., Webb, R. S., Webb III, T., and Whitlock, C. (1998). Paleoclimate simulations for North America over the past 21,000 years: features of the simulated climate and comparisons with paleoenvironmental data. Quaternary Science Reviews, 17(6-7):549–585.

Cited p. 17.

Bartlein, P. J., Harrison, S. P., Brewer, S., Connor, S., Davis, B. A. S., Gajewski, K., Guiot, J., Harrison-Prentice, T. I., Henderson, A., and Peyron, O. (2011). Pollen-based continental climate reconstructions at 6 and 21 ka: a global synthesis. Climate Dynamics, 37(3-4):775–802.

Cited p. 17.

Bartov, Y., Enzel, Y., Porat, N., and Stein, M. (2007). Evolution of the Late PleistoceneHolocene Dead Sea Basin from Sequence Statigraphy of Fan Deltas and Lake-Level Reconstruction. Journal of Sedimentary Research, 77(9):680–692.

Cited p. 144.

Bartov, Y., Stein, M., Enzel, Y., Agnon, A., and Reches, Z. (2002). Lake Levels and Sequence Stratigraphy of Lake Lisan, the Late Pleistocene Precursor of the Dead Sea. Quaternary Research, 57(1):9–21.

Cited p. 143.

Ben Dor, Y., Neugebauer, I., Enzel, Y., Schwab, M. J., Tjallingii, R., Erel, Y., and Brauer, A. (2019). Varves of the Dead Sea sedimentary record. Quaternary Science Reviews, 215:173–184.

Cited p. 120.

Bencivenga, F., Cimatoribus, A., Gessini, A., Izzo, M. G., and Masciovecchio, C. (2009). Temperature and density dependence of the structural relaxation time in water by inelastic ultraviolet scattering. J. Chem. Phys., 131(14):144502.

Cited p. 31.

Benison, K. C. (2013). Acid saline fluid inclusions: examples from modern and Permian extreme lake systems. Geofluids, 13(4):579–593.

Cited p. 62.

Benison, K. C. and Goldstein, R. H. (1999). Permian paleoclimate data from fluid inclusions in halite. Chemical Geology, 154(1-4):113–132.

Cited p. 46, 62, 64 et 83.

Bentor, Y. K. (1961). Some geochemical aspects of the Dead Sea and the question of its age. Geochimica et Cosmochimica Acta, 25(4):239–260.

Cited p. 122 et 141.

Berger, A. (1978). Long-term variations of daily insolation and Quaternary climatic changes. Journal of the atmospheric sciences, 35(12):2362–2367.

Cited p. 11.

Berger, A. and Loutre, M. F. (1991). Insolation values for the climate of the last 10 million years. Quaternary Science Reviews, 10(4):297–317.

Cited p. 12, 13, 22 et 145.

Beyth, M., Gavrieli, I., Anati, D., and Katz, O. (1993). Effects of the December 1991-May 1992 floods on the Dead Sea vertical structure. Israel J. Earth Sci., 42(1):45–48.

Cited p. 138.

Birks, H. J. B. (1995). Quantitative palaeoenvironmental reconstructions. Statistical modelling of Quaternary science data. Technical Guide, 5:161–254.

Cited p. 17.

Bjerknes, J. (1964). Atlantic Air-Sea Interaction. In Landsberg, H. E. and Van Mieghem, J., editors, Advances in Geophysics, volume 10, pages 1–82. Elsevier.

Cited p. 3.

Blamey, N. J. F. and Brand, U. (2019). Atmospheric gas in modern and ancient halite fluid inclusions: A screening protocol. Gondwana Research, 69:163–176.

Cited p. 45 et 63.

Bodnar, R. J. (1994). Synthetic fluid inclusions: XII. The system H_2O-NaCl. Experimental determination of the halite liquidus and isochores for a 40 wt% NaCl solution. Geochimica et Cosmochimica Acta, 58(3):1053–1063.

Cited p. 87.

Bodnar, R. J. and Bethke, P. M. (1984). Systematics of stretching of fluid inclusions; I, Fluorite and sphalerite at 1 atmosphere confining pressure. Economic Geology, 79(1):141–161.

Cited p. 58.

Bodnar, R. J., Binns, P. R., and Hall, D. L. (1989). Synthetic fluid inclusions-VI. Quantitative evaluation of the decrepitation behaviour of fluid inclusions in quartz at one atmosphere confining pressure. Journal of Metamorphic Geology, 7(2):229–242.

Cited p. 58.

Bodnar, R. J. and Sterner, S. M. (1985). Synthetic fluid inclusions in natural quartz. II. Application to PVT studies. Geochimica et Cosmochimica Acta, 49(9):1855–1859.

Cited p. 87.

Bodnar, R. J. and Vityk, M. O. (1994). Interpretation of microthermometric data for H_2O-NaCl fluid inclusions. In De Vivo, B. and Frezzotti, M. L., editors, Fluid Inclusions in Minerals : Methods and Applications, pages 117–130. Blacksburg, VA: Virginia Tech.

Cited p. 87 et 88.

Bond, G., Broecker, W., Johnsen, S., McManus, J., Labeyrie, L., Jouzel, J., and Bonani, G. (1993). Correlations between climate records from North Atlantic sediments and Greenland ice. Nature, 365(6442):143–147.

Cited p. 10, 145 et 149.

Bond, G., Heinrich, H., Broecker, W., Labeyrie, L., McManus, J., Andrews, J., Huon, S., Jantschik, R., Clasen, S., and Simet, C. (1992). Evidence for massive discharges of icebergs into the North Atlantic ocean during the last glacial period. Nature, 360(6401):245.

Cited p. 10.

Bookman, R., Bartov, Y., Enzel, Y., and Stein, M. (2006). Quaternary lake levels in the Dead Sea basin: two centuries of research. SPECIAL PAPERS-GEOLOGICAL SOCIETY OF AMERICA, 401:155.

Cited p. 126.

Bookman, R., Filin, S., Avni, Y., Rosenfeld, D., and Marco, S. (2014). Possible connection between large volcanic eruptions and level rise episodes in the Dead Sea Basin. Quaternary Science Reviews, 89:123–128.

Cited p. 122.

Bookman (Ken-Tor), R., Enzel, Y., Agnon, A., and Stein, M. (2004). Late Holocene lake levels of the Dead Sea. GSA Bulletin, 116(5-6):555–571.

Cited p. 144.

Bosmans, J. H. C., Drijfhout, S. S., Tuenter, E., Hilgen, F. J., Lourens, L. J., and Rohling, E. J. (2015). Precession and obliquity forcing of the freshwater budget over the Mediterranean. Quaternary Science Reviews, 123:16–30.

Cited p. 120, 146, 150 et 154.

Boyle, E. A. and Keigwin, L. (1987). North Atlantic thermohaline circulation during the past 20,000 years linked to high-latitude surface temperature. Nature, 330(6143):35.

Cited p. 14.

Braconnot, P., Harrison, S. P., Kageyama, M., Bartlein, P. J., Masson-Delmotte, V., Abe-Ouchi, A., Otto-Bliesner, B., and Zhao, Y. (2012). Evaluation of climate models using palaeoclimatic data. Nature Climate Change, 2(6):417–424.

Cited p. 19.

Brauer, A., Allen, J. R. M., Mingram, J., Dulski, P., Wulf, S., and Huntley, B. (2007). Evidence for last interglacial chronology and environmental change from Southern Europe. PNAS, 104(2):450–455.

Cited p. 146, 149 et 150.

Brennan, S. T., Lowenstein, T. K., and Cendón, D. I. (2013). The major-ion composition of Cenozoic seawater: The past 36 million years from fluid inclusions in marine halite. American Journal of Science, 313(8):713–775.

Cited p. 45.

Brink, U. S. t. and Flores, C. H. (2012). Geometry and subsidence history of the Dead Sea basin: A case for fluid-induced mid-crustal shear zone? Journal of Geophysical Research: Solid Earth, 117(B1).

Cited p. 120 et 143.

Broecker, W. S. (1966). Absolute dating and the astronomical theory of glaciation. Science, 151(3708):299–304.

Cited p. 12.

Broecker, W. S. (1998). Paleocean circulation during the last deglaciation: a bipolar seesaw? Paleoceanography, 13(2):119–121.

Cited p. 10 et 15.

Broecker, W. S. and van Donk, J. (1970). Insolation changes, ice volumes, and the O^{18} record in deep-sea cores. Reviews of Geophysics, 8(1):169–198.

Cited p. 8.

Bryan, F. O., Tomas, R., Dennis, J. M., Chelton, D. B., Loeb, N. G., and McClean, J. L. (2010). Frontal Scale AirSea Interaction in High-Resolution Coupled Climate Models. J. Climate, 23(23):6277–6291.

Cited p. 4 et 154.

Bunker, A. F. (1976). Computations of Surface Energy Flux and Annual AirSea Interaction Cycles of the North Atlantic Ocean. Mon. Wea. Rev., 104(9):1122–1140.

Cited p. 3.

Burnley, P. C. and Davis, M. K. (2004). Volume Changes In Fluid Inclusions Produced By Heating And Pressurization: An Assessment By Finite Element Modeling. The Canadian Mineralogist, 42(5):1369–1382.

Cited p. 102.

Burnley, P. C. and Schmidt, C. (2006). Finite element modeling of elastic volume changes in fluid inclusions: Comparison with experiment. American Mineralogist, 91(11-12):1807–1814.

Cited p. 54 et 102.

Cacho, I., Grimalt, J. O., Canals, M., Sbaffi, L., Shackleton, N. J., Schönfeld, J., and Zahn, R. (2001). Variability of the western Mediterranean Sea surface temperature during the last 25,000 years and its connection with the Northern Hemisphere climatic changes. Paleoceanography, 16(1):40–52.

Cited p. 22.

Capron, E., Govin, A., Stone, E. J., Masson-Delmotte, V., Mulitza, S., Otto-Bliesner, B., Rasmussen, T. L., Sime, L. C., Waelbroeck, C., and Wolff, E. W. (2014). Temporal and spatial structure of multi-millennial temperature changes at high latitudes during the Last Interglacial. Quaternary Science Reviews, 103:116–133.

Cited p. 18.

Caumon, M.-C., Dubessy, J., Robert, P., and Tarantola, A. (2013). Fused-silica capillary capsules (FSCCs) as reference synthetic aqueous fluid inclusions to determine chlorinity by Raman spectroscopy. European Journal of Mineralogy, 25(5):755–763.

Cited p. 41.

Caupin, F., Arvengas, A., Davitt, K., Azouzi, M. E. M., Shmulovich, K. I., Ramboz, C., Sessoms, D. A., and Stroock, A. D. (2012). Exploring water and other liquids at negative pressure. Journal of Physics: Condensed Matter, 24(28):284110.

Cited p. 53.

Caupin, F. and Herbert, E. (2006). Cavitation in water: a review. Comptes Rendus Physique, 7(9-10):1000–1017.

Cited p. 53 et 61.

Chapman, M. R. and Shackleton, N. J. (1999). Global ice-volume fluctuations, North Atlantic ice-rafting events, and deep-ocean circulation changes between 130 and 70 ka. Geology, 27(9):795–798.

Cited p. 148.

Cheddadi, R. and Bar-Hen, A. (2009). Spatial gradient of temperature and potential vegetation feedback across Europe during the late Quaternary. Climate Dynamics, 32(2-3):371–379.

Cited p. 17.

Chelton, D. B., Esbensen, S. K., Schlax, M. G., Thum, N., Freilich, M. H., Wentz, F. J., Gentemann, C. L., McPhaden, M. J., and Schopf, P. S. (2001). Observations of Coupling between Surface Wind Stress and Sea Surface Temperature in the Eastern Tropical Pacific. Journal of Climate, 14(7):1479–1498.

Cited p. 4.

Chelton, D. B. and Xie, S.-P. (2010). Coupled ocean-atmosphere interaction at oceanic mesoscales. Oceanography, 23(4):52–69.

Cited p. 4 et 154.

Chen, C. and Litt, T. (2018). Dead Sea pollen provides new insights into the paleoenvironment of the southern Levant during MIS 65. Quaternary Science Reviews, 188:15–27.

Cited p. 151 et 152.

Cheng, H., Edwards, R. L., Broecker, W. S., Denton, G. H., Kong, X., Wang, Y., Zhang, R., and Wang, X. (2009). Ice Age Terminations. Science, 326(5950):248–252.

Cited p. 8.

Clark, P. U., Archer, D., Pollard, D., Blum, J. D., Rial, J. A., Brovkin, V., Mix, A. C., Pisias, N. G., and Roy, M. (2006). The middle Pleistocene transition: characteristics, mechanisms, and implications for long-term changes in atmospheric pCO_2. Quaternary Science Reviews, 25(23-24):3150–3184.

Cited p. 13.

Clark, P. U. and Pollard, D. (1998). Origin of the middle Pleistocene transition by ice sheet erosion of regolith. Paleoceanography, 13(1):1–9.

Cited p. 15.

Clement, A. C., Seager, R., and Cane, M. A. (1999). Orbital controls on the El Niño/Southern Oscillation and the tropical climate. Paleoceanography, 14(4):441–456.

Cited p. 153.

Coianiz, L., Ben-Avraham, Z., Stein, M., and Lazar, M. (2019a). Spatial and temporal reconstruction of the late Quaternary Dead Sea sedimentary facies from geophysical properties. Journal of Applied Geophysics, 160:15–27.

Cited p. 143.

Coianiz, L., Bialik, O. M., Ben-Avraham, Z., and Lazar, M. (2019b). Late Quaternary lacustrine deposits of the Dead Sea basin: high resolution sequence stratigraphy from downhole logging data. Quaternary Science Reviews, 210:175–189.

Cited p. 143.

Coianiz, L., Schattner, U., Lang, G., BenAvraham, Z., and Lazar, M. (2019c). Between plate and salt tectonicsNew stratigraphic constraints on the architecture and timing of the Dead Sea basin during the Late Quaternary. Basin Research, 0(0).

Cited p. 142, 143 et 144.

Collins, M., Minobe, S., Barreiro, M., Bordoni, S., Kaspi, Y., Kuwano-Yoshida, A., Keenlyside, N., Manzini, E., OReilly, C. H., Sutton, R., Xie, S.-P., and Zolina, O. (2018). Challenges and opportunities for improved understanding of regional climate dynamics. Nature Climate Change, 8(2):101–108.

Cited p. 4.

Connaughton, L. M., Millero, F. J., and Pitzer, K. S. (1989). Volume changes for mixing the major sea salts: Equations valid to ionic strength 3.0 and temperature 95ř C. Journal of Solution Chemistry, 18(11):1007–1017.

Cited p. 91.

Constantin, S., Bojar, A.-V., Lauritzen, S.-E., and Lundberg, J. (2007). Holocene and Late Pleistocene climate in the sub-Mediterranean continental environment: A speleothem record from Poleva Cave (Southern Carpathians, Romania). Palaeogeography, Palaeoclimatology, Palaeoecology, 243(3):322–338.

Cited p. 18.

Czaja, A., Robertson, A. W., and Huck, T. (2003). The role of Atlantic ocean-atmosphere coupling in affecting North Atlantic Oscillation variability. Geophysical Monograph-American Geophysical Union, 134.

Cited p. 7.

Dansgaard, W., Clausen, H. B., Gundestrup, N., Hammer, C. U., Johnsen, S. F., Kristinsdottir, P. M., and Reeh, N. (1982). A new Greenland deep ice core. Science, 218(4579):1273–1277.

Cited p. 9.

Dansgaard, W., Johnsen, S. J., Clausen, H. B., DahlJensen, D., Gundestrup, N., Hammer, C. U., and Oeschger, H. (1984). North Atlantic climatic oscillations revealed by deep Greenland ice cores. Climate processes and climate sensitivity, 29:288–298.

Cited p. 9.

Davis, B. A., Brewer, S., Stevenson, A. C., and Guiot, J. (2003). The temperature of Europe during the Holocene reconstructed from pollen data. Quaternary science reviews, 22(15-17):1701–1716.

Cited p. 21 et 22.

Deaney, E. L., Barker, S., and van de Flierdt, T. (2017). Timing and nature of AMOC recovery across Termination 2 and magnitude of deglacial CO_2 change. Nature Communications, 8:14595.

Cited p. 8 et 145.

Debenedetti, P. G. (1996). Metastable Liquids: Concepts and Principles. Princeton University Press, Princeton.

Cited p. 61.

deMenocal, P., Ortiz, J., Guilderson, T., Adkins, J., Sarnthein, M., Baker, L., and Yarusinsky, M. (2000). Abrupt onset and termination of the African Humid Period:: rapid climate responses to gradual insolation forcing. Quaternary Science Reviews, 19(1):347–361.

Cited p. 145.

Denton, G. H., Anderson, R. F., Toggweiler, J. R., Edwards, R. L., Schaefer, J. M., and Putnam, A. E. (2010). The last glacial termination. Science, 328(5986):1652–1656.

Cited p. 8, 15 et 145.

Develle, A. L., Gasse, F., Vidal, L., Williamson, D., Demory, F., Van Campo, E., Ghaleb, B., and Thouveny, N. (2011). A 250ka sedimentary record from a small karstic lake in the Northern Levant (Yammoûneh, Lebanon): Paleoclimatic implications. Palaeogeography, Palaeoclimatology, Palaeoecology, 305(1):10–27.

Cited p. 120 et 146.

Diamond, L. W. (2001). Review of the systematics of CO_2–H_2O fluid inclusions. Lithos, 55(1):69–99.

Cited p. 32.

Ditlevsen, P. D., Svensmark, H., and Johnsen, S. (1996). Contrasting atmospheric and climate dynamics of the last-glacial and Holocene periods. Nature, 379(6568):810–812.

Cited p. 8.

Dove, H. W. (1839). Über die geographische Verbreitung gleichartiger Witterungserscheinungen. Erste Abhandlung. Über die nicht periodischen Änderungen der Temperaturvertheilung auf der Oberfläche der Erde. Druckerei der Königlichen Akademie der Wissenschaften.

Cited p. 6.

Dove, H. W. (1840). Ueber die nicht periodischen Änderungen der Temperaturvertheilung auf der Oberfläche der Erde, in dem Zeitraume von 1789 bis 1838: Akad. Abhandlung. Reimer.

Cited p. 6.

Driesner, T. (2007). The system H_2O–NaCl. Part II: Correlations for molar volume, enthalpy, and isobaric heat capacity from 0 to 1000řC, 1 to 5000 bar, and 0 to 1 XNaCl. Geochimica et Cosmochimica Acta, 71(20):4902–4919.

Cited p. 91 et 135.

Driscoll, S., Bozzo, A., Gray, L. J., Robock, A., and Stenchikov, G. (2012). Coupled Model Intercomparison Project 5 (CMIP5) simulations of climate following volcanic eruptions. Journal of Geophysical Research: Atmospheres, 117(D17).

Cited p. 7.

Drysdale, R. N., Zanchetta, G., Hellstrom, J. C., Fallick, A. E., and Zhao, J.-x. (2005). Stalagmite evidence for the onset of the Last Interglacial in southern Europe at 129 ś 1 ka. Geophysical Research Letters, 32(24).

Cited p. 146 et 149.

Dunstone, N., Smith, D., Scaife, A., Hermanson, L., Eade, R., Robinson, N., Andrews, M., and Knight, J. (2016). Skilful predictions of the winter North Atlantic Oscillation one year ahead. Nature Geoscience, 9(11):809–814.

Cited p. 7.

Duplessy, J. C., Shackleton, N. J., Fairbanks, R. G., Labeyrie, L., Oppo, D., and Kallel, N. (1988). Deep-water source variations during the last climatic cycle and their impact on the global deepwater circulation. Paleoceanography, 3(3):343–360.

Cited p. 14.

Egede, H. (1745). A description of Greenland. London.

Cited p. 6.

Ekman, V. W. (1905). On the influence of the earth's rotation on ocean-currents. Arkiv för Matematik, Astronomi och Fysik, 2(11):1–53.

Cited p. 3.

El Mekki-Azouzi, M. (2010). Etude expérimentale de l'eau et de solutions aqueuses métastables : implications pour le milieu naturel. PhD thesis, Orléans.

Cited p. 33.

El Mekki-Azouzi, M., Tripathi, C. S. P., Pallares, G., Gardien, V., and Caupin, F. (2015). Brillouin spectroscopy of fluid inclusions proposed as a paleothermometer for subsurface rocks. Scientific reports, 5:13168.

Cited p. 25, 28, 29, 34, 46, 47 et 166.

Elderfield, H., Ferretti, P., Greaves, M., Crowhurst, S., McCave, I. N., Hodell, D. a., and Piotrowski, A. M. (2012). Evolution of ocean temperature and ice volume through the mid-Pleistocene climate transition. Science, 337(6095):704–709.

Cited p. 16.

Elderfield, H. and Ganssen, G. (2000). Past temperature and δ^{18}O of surface ocean waters inferred from foraminiferal Mg/Ca ratios. Nature, 405(6785):442.

Cited p. 16.

Emeis, K.-C., Struck, U., Schulz, H.-M., Rosenberg, R., Bernasconi, S., Erlenkeuser, H., Sakamoto, T., and Martinez-Ruiz, F. (2000). Temperature and salinity variations of Mediterranean Sea surface waters over the last 16,000 years from records of planktonic stable oxygen isotopes and alkenone unsaturation ratios. Palaeogeography, Palaeoclimatology, Palaeoecology, 158(3):259–280.

Cited p. 148.

Emiliani, C. (1955). Pleistocene Temperatures. The Journal of Geology, 63(6):538–578.

Cited p. 8 et 12.

Emiliani, C. and Geiss, J. (1959). On glaciations and their causes. Geologische Rundschau, 46(2):576–601.

Cited p. 12.

Enzel, Y., Kushnir, Y., and Quade, J. (2015). The middle Holocene climatic records from Arabia: Reassessing lacustrine environments, shift of ITCZ in Arabian Sea, and impacts of the southwest Indian and African monsoons. Global and Planetary Change, 129:69–91.

Cited p. 145.

Enzel, Y., Tor), R. B. K., Sharon, D., Gvirtzman, H., Dayan, U., Ziv, B., and Stein, M. (2003). Late Holocene climates of the Near East deduced from Dead Sea level variations and modern regional winter rainfall. Quaternary Research, 60(3):263–273.

Cited p. 126.

EPICA Community Members (2006). One-to-one coupling of glacial climate variability in Greenland and Antarctica. Nature, 444(7116):195–198.

Cited p. 10.

Eshelby John Douglas and Peierls Rudolf Ernst (1959). The elastic field outside an ellipsoidal inclusion. Proceedings of the Royal Society of London. Series A. Mathematical and Physical Sciences, 252(1271):561–569.

Cited p. 102.

Eugster, H. P. and Hardie, L. A. (1978). Saline Lakes. In Lerman, A., editor, Lakes: Chemistry, Geology, Physics, pages 237–293. Springer New York, New York, NY.

Cited p. 86 et 108.

Fall, A. and Bodnar, R. J. (2018). How Precisely Can the Temperature of a Fluid Event be Constrained Using Fluid Inclusions? Economic Geology, 113(8):1817–1843.

Cited p. 64.

Fall, A., Rimstidt, J. D., and Bodnar, R. J. (2009). The effect of fluid inclusion size on determination of homogenization temperature and density of liquid-rich aqueous inclusions. American Mineralogist, 94(11-12):1569–1579.

Cited p. 46, 64 et 82.

Farelo, F., Brachel, G. V., and Offermann, H. (1993). Solid-liquid equilibria in the ternary system NaCl-KCl-H_2O. The Canadian Journal of Chemical Engineering, 71(1):141–146.

Cited p. 31 et 94.

Felis, T., Lohmann, G., Kuhnert, H., Lorenz, S. J., Scholz, D., Pätzold, J., Al-Rousan, S. A., and Al-Moghrabi, S. M. (2004). Increased seasonality in Middle East temperatures during the last interglacial period. Nature, 429(6988):164–168.

Cited p. 19 et 151.

Fischer, H., Meissner, K. J., Mix, A. C., Abram, N. J., Austermann, J., Brovkin, V., Capron, E., Colombaroli, D., Daniau, A.-L., Dyez, K. A., Felis, T., Finkelstein, S. A., Jaccard, S. L., McClymont, E. L., Rovere, A., Sutter, J., Wolff, E. W., Affolter, S., Bakker, P., Ballesteros-Cánovas, J. A., Barbante, C., Caley, T., Carlson, A. E., Churakova (Sidorova), O., Cortese, G., Cumming, B. F., Davis, B. A. S., Vernal, A. d., Emile-Geay, J., Fritz, S. C., Gierz, P., Gottschalk, J., Holloway, M. D., Joos, F., Kucera, M., Loutre, M.-F., Lunt, D. J., Marcisz, K., Marlon, J. R., Martinez, P., Masson-Delmotte, V., Nehrbass-Ahles, C., Otto-Bliesner, B. L., Raible, C. C., Risebrobakken, B., Goñi, M. F. S., Arrigo, J. S., Sarnthein, M., Sjolte, J., Stocker, T. F., Alvárez, P. A. V., Tinner, W., Valdes, P. J., Vogel, H., Wanner, H., Yan, Q., Yu, Z., Ziegler, M., and Zhou, L. (2018). Palaeoclimate constraints on the impact of 2 řC anthropogenic warming and beyond. Nature Geoscience, 11(7):474–485.

Cited p. 18.

Fleitmann, D., Burns, S. J., Mudelsee, M., Neff, U., Kramers, J., Mangini, A., and Matter, A. (2003). Holocene Forcing of the Indian Monsoon Recorded in a Stalagmite from Southern Oman. Science, 300(5626):1737–1739.

Cited p. 145.

Fleitmann, D., Burns, S. J., Neff, U., Mudelsee, M., Mangini, A., and Matter, A. (2004). Palaeoclimatic interpretation of high-resolution oxygen isotope profiles derived from annually laminated speleothems from Southern Oman. Quaternary Science Reviews, 23(7):935–945.

Cited p. 145.

Florschütz, F. (1930). Fossiele overblijfselen van den plantengroei tijdens het Würmglaciaal en het Riss-Würminterglaciaal in Nederland. Proceedings Koninklijke Akademie van Wetenschappen (Amsterdam), 33:1043–1044.

Cited p. 10 et 153.

Frogley, M. R., Tzedakis, P. C., and Heaton, T. H. E. (1999). Climate Variability in Northwest Greece During the Last Interglacial. Science, 285(5435):1886–1889.

Cited p. 150.

Fyfe, J. C., Boer, G. J., and Flato, G. M. (1999). The Arctic and Antarctic oscillations and their projected changes under global warming. Geophysical Research Letters, 26(11):1601–1604.

Cited p. 154.

Ganopolski, A. and Calov, R. (2011). The role of orbital forcing, carbon dioxide and regolith in 100 kyr glacial cycles. Climate of the Past, 7(4):1415–1425.

Cited p. 15.

Garfunkel, Z. and Ben-Avraham, Z. (1996). The structure of the Dead Sea basin. Tectonophysics, 266(1):155–176.

Cited p. 120.

Gasse, F., Vidal, L., Van Campo, E., Demory, F., Develle, A.-L., Tachikawa, K., Elias, A., Bard, E., Garcia, M., Sonzogni, C., and Thouveny, N. (2015). Hydroclimatic changes in northern Levant over the past 400,000 years. Quaternary Science Reviews, 111:1–8.

Cited p. 120, 146 et 150.

Gastineau, G., DAndrea, F., and Frankignoul, C. (2013). Atmospheric response to the North Atlantic Ocean variability on seasonal to decadal time scales. Clim Dyn, 40(9):2311–2330.

Cited p. 7 et 151.

Gavrieli, I., Starinsky, A., and Bein, A. (1989). The solubility of halite as a function of temperature in the highly saline Dead Sea brine system. Limnology and Oceanography, 34(7):1224–1234.

Cited p. 96 et 98.

Genty, D., Blamart, D., Ouahdi, R., Gilmour, M., Baker, A., Jouzel, J., and Van-Exter, S. (2003). Precise dating of DansgaardOeschger climate oscillations in western Europe from stalagmite data. Nature, 421(6925):833–837.

Cited p. 10.

Gertman, I. and Hecht, A. (2002). The Dead Sea hydrography from 1992 to 2000. Journal of Marine Systems, 35(3):169–181.

Cited p. 122 et 138.

Gertman, I., Kress, N., Katsenelson, B., and Zavialov, P. (2010). Equations of state for the Dead Sea and Aral Sea: Searching for common approaches. Technical report, IOLR.

Cited p. 124.

Ghosh, P., Adkins, J., Affek, H., Balta, B., Guo, W., Schauble, E. A., Schrag, D., and Eiler, J. M. (2006). $^{13}C^{18}O$ bonds in carbonate minerals: a new kind of paleothermometer. Geochimica et Cosmochimica Acta, 70(6):1439–1456.

Cited p. 18.

Gillett, N. P., Graf, H. F., and Osborn, T. J. (2003). Climate change and the North Atlantic oscillation. Geophysical Monograph-American Geophysical Union, 134:193–210.

Cited p. 7.

Giraudi, C., Magny, M., Zanchetta, G., and Drysdale, R. N. (2011). The Holocene climatic evolution of Mediterranean Italy: A review of the continental geological data. The Holocene, 21(1):105–115.

Cited p. 22.

Goldreich, Y. and Karni, O. (2001). Climate and precipitation regime in the Arava Valley, Israel. Israel Journal of Earth Sciences, 50:53–59.

Cited p. 125.

Goldstein, R. H. (2001). Clues from Fluid Inclusions. Science, 294(5544):1009–1011.

Cited p. 64.

Goodier, J. N. (1933). Concentration of Stress around Spherical and Cylindrical Inclusions and Flaws. T. A. S. M. E., 55:39.

Cited p. 102.

Goy, C., Potenza, M. A., Dedera, S., Tomut, M., Guillerm, E., Kalinin, A., Voss, K.-O., Schottelius, A., Petridis, N., Prosvetov, A., Tejeda, G., Fernández, J. M., Trautmann, C., Caupin, F., Glasmacher, U., and Grisenti, R. E. (2018). Shrinking of Rapidly Evaporating Water Microdroplets Reveals their Extreme Supercooling. Physical Review Letters, 120(1):015501.

Cited p. 27.

Grant, K. M., Grimm, R., Mikolajewicz, U., Marino, G., Ziegler, M., and Rohling, E. J. (2016). The timing of Mediterranean sapropel deposition relative to insolation, sea-level and African monsoon changes. Quaternary Science Reviews, 140:125–141.

Cited p. 150.

Grant, K. M., Rohling, E. J., Bar-Matthews, M., Ayalon, A., Medina-Elizalde, M., Ramsey, C. B., Satow, C., and Roberts, A. P. (2012). Rapid coupling between ice volume and polar temperature over the past 150,000 years. Nature, 491(7426):744–747.

Cited p. 145, 148 et 163.

Greer, J. R. and Nix, W. D. (2006). Nanoscale gold pillars strengthened through dislocation starvation. Physical Review B, 73(24):245410.

Cited p. 58.

Guihou, A., Pichat, S., Nave, S., Govin, A., Labeyrie, L., Michel, E., and Waelbroeck, C. (2010). Late slowdown of the Atlantic Meridional Overturning Circulation during the Last Glacial Inception: New constraints from sedimentary (^{231}Pa/^{230}Th). Earth and Planetary Science Letters, 289(3):520–529.

Cited p. 8.

Guiot, J. (1990). Methodology of the last climatic cycle reconstruction in France from pollen data. Palaeogeography, Palaeoclimatology, Palaeoecology, 80(1):49–69.

Cited p. 153.

Haarsma, R. J., Roberts, M. J., Vidale, P. L., Senior, C. A., Bellucci, A., Bao, Q., Chang, P., Corti, S., Fukar, N. S., Guemas, V., Hardenberg, J. v., Hazeleger, W., Kodama, C., Koenigk, T., Leung, L. R., Lu, J., Luo, J.-J., Mao, J., Mizielinski, M. S., Mizuta, R., Nobre, P., Satoh, M., Scoccimarro, E., Semmler, T., Small, J., and Storch, J.-S. v. (2016). High Resolution Model Intercomparison Project (HighResMIP v1.0) for CMIP6. Geoscientific Model Development, 9(11):4185–4208.

Cited p. 4.

Haliva-Cohen, A., Stein, M., Goldstein, S. L., Sandler, A., and Starinsky, A. (2012). Sources and transport routes of fine detritus material to the Late Quaternary Dead Sea basin. Quaternary Science Reviews, 50:55–70.

Cited p. 120.

Hall, A., Clement, A., Thompson, D. W. J., Broccoli, A., and Jackson, C. (2005). The Importance of Atmospheric Dynamics in the Northern Hemisphere Wintertime Climate Response to Changes in the Earths Orbit. J. Climate, 18(9):1315–1325.

Cited p. 19, 151 et 152.

Hall, J. K. (1996). Digital topography and bathymetry of the area of the Dead Sea Depression. Tectonophysics, 266(1):177–185.

Cited p. 133.

Hann, J. (1890). Zur Witterungsgeschichte von Nord-Grönland, Westküste. Meteor. Zeitschrift, 7:109–115.

Cited p. 6.

Hardie, L. A. (1984). Evaporites; marine or non-marine? American Journal of Science, 284(3):193–240.

Cited p. 86, 87 et 108.

Hardie, L. A. (1990). The roles of rifting and hydrothermal $CaCl_2$ brines in the origin of potash evaporites; an hypothesis. Am J Sci, 290(1):43–106.

Cited p. 86, 87, 98 et 99.

Harting, P. (1874). De bodem van het Eemdal.Verslagen en Verhandelingen Koninklijke Academie van Wetenschappen. Technical Report 2e Reeks 8:282-290.

Cited p. 10 et 153.

Hashin, Z. and Shtrikman, S. (1962). A variational approach to the theory of the elastic behaviour of polycrystals. Journal of the Mechanics and Physics of Solids, 10(4):343–352.

Cited p. 92.

Hashizume, H., Xie, S.-P., Liu, W. T., and Takeuchi, K. (2001). Local and remote atmospheric response to tropical instability waves: A global view from space. Journal of Geophysical Research: Atmospheres, 106(D10):10173–10185.

Cited p. 4.

Hays, J. D., Imbrie, J., and Shackleton, N. J. (1976). Variations in the Earths orbit: pacemaker of the ice ages. Science, 194(4270):1121–1132.

Cited p. 12.

Hays, J. D., Saito, T., Opdyke, N. D., and Burckle, L. H. (1969). Pliocene-Pleistocene sediments of the equatorial Pacific: their paleomagnetic, biostratigraphic, and climatic record. Geological Society of America Bulletin, 80(8):1481–1514.

Cited p. 12.

Heinrich, H. (1988). Origin and Consequences of Cyclic Ice Rafting in the Northeast Atlantic Ocean During the Past 130,000 Years. Quaternary Research, 29(2):142–152.

Cited p. 9 et 10.

Heiri, O. and Lotter, A. F. (2005). Holocene and Lateglacial summer temperature reconstruction in the Swiss Alps based on fossil assemblages of aquatic organisms: a review. Boreas, 34(4):506–516.

Cited p. 18.

Heiri, O., Lotter, A. F., Hausmann, S., and Kienast, F. (2003). A chironomid-based Holocene summer air temperature reconstruction from the Swiss Alps. The Holocene, 13(4):477–484.

Cited p. 17.

Herold, M. and Lohmann, G. (2009). Eemian tropical and subtropical African moisture transport: an isotope modelling study. Clim Dyn, 33(7):1075–1088.

Cited p. 145.

Herut, B., Gavrieli, I., and Halicz, L. (1998). Coprecipitation of trace and minor elements in modern authigenic halites from the hypersaline Dead Sea brine. Geochimica et Cosmochimica Acta, 62(9):1587–1598.

Cited p. 63.

Heyliger, P., Ledbetter, H., and Kim, S. (2003). Elastic constants of natural quartz. The Journal of the Acoustical Society of America, 114(2):644–650.

Cited p. 102.

Hodell, D., Crowhurst, S., Skinner, L., Tzedakis, P. C., Margari, V., Channell, J. E. T., Kamenov, G., Maclachlan, S., and Rothwell, G. (2013). Response of Iberian Margin sediments to orbital and suborbital forcing over the past 420 ka. Paleoceanography, 28(1):185–199.

Cited p. 10.

Hodell, D., Lourens, L., Crowhurst, S., Konijnendijk, T., Tjallingii, R., Jiménez-Espejo, F., Skinner, L., Tzedakis, P. C., Abrantes, F., Acton, G. D., Alvarez Zarikian, C. A., Bahr, A., Balestra, B., Barranco, E. L., Carrara, G., Ducassou, E., Flood, R. D., Flores, J.-A., Furota, S., Grimalt, J., Grunert, P., Hernández-Molina, J., Kim, J. K., Krissek, L. A., Kuroda, J., Li, B., Lofi, J., Margari, V., Martrat, B., Miller, M. D., Nanayama, F., Nishida, N., Richter, C., Rodrigues, T., Rodríguez-Tovar, F. J., Roque, A. C. F., Sanchez Goñi, M. F., Sierro Sánchez, F. J., Singh, A. D., Sloss, C. R., Stow, D. A. V., Takashimizu, Y., Tzanova, A., Voelker, A., Xuan, C., and Williams, T. (2015). A reference time scale for Site U1385 (Shackleton Site) on the SW Iberian Margin. Global and Planetary Change, 133:49–64.

Cited p. 10.

Hodell, D. A., Turchyn, A. V., Wiseman, C. J., Escobar, J., Curtis, J. H., Brenner, M., Gilli, A., Mueller, A. D., Anselmetti, F., and Ariztegui, D. (2012). Late Glacial temperature and precipitation changes in the lowland Neotropics by tandem measurement of δ^{18}O in biogenic carbonate and gypsum hydration water. Geochimica et Cosmochimica Acta, 77:352–368.

Cited p. 18.

Hoerling, M., Eischeid, J., Perlwitz, J., Quan, X., Zhang, T., and Pegion, P. (2012). On the increased frequency of Mediterranean drought. Journal of Climate, 25(6):2146–2161.

Cited p. 7.

Holser, W. T. (1966). Bromide geochemistry of salt rocks. In Rau, J., editor, Second Symposium on Salt, volume 1, pages 248–275, Northern Ohio Geological Society, Cleveland.

Cited p. 45.

Holten, V., Qiu, C., Guillerm, E., Wilke, M., Ricka, J., Frenz, M., and Caupin, F. (2017). Compressibility anomalies in stretched water and their interplay with density anomalies. The journal of physical chemistry letters, 8(22):5519–5522.

Cited p. 27, 28, 34 et 47.

Holwerda, J. G. and Hutchinson, R. W. (1968). Potash-bearing evaporites in the Danakil area, Ethiopia. Economic Geology, 63(2):124–150.

Cited p. 108.

Hostetler, S. W., Clark, P. U., Bartlein, P. J., Mix, A. C., and Pisias, N. J. (1999). Atmospheric transmission of North Atlantic Heinrich events. Journal of Geophysical Research: Atmospheres, 104(D4):3947–3952.

Cited p. 149.

Hu, Z.-Z. and Wu, Z. (2004). The intensification and shift of the annual North Atlantic Oscillation in a global warming scenario simulation. Tellus A: Dynamic Meteorology and Oceanography, 56(2):112–124.

Cited p. 154.

Huber, C., Leuenberger, M., Spahni, R., Flückiger, J., Schwander, J., Stocker, T. F., Johnsen, S., Landais, A., and Jouzel, J. (2006). Isotope calibrated Greenland temperature record over Marine Isotope Stage 3 and its relation to CH_4. Earth and Planetary Science Letters, 243(3):504–519.

Cited p. 9.

Hurrell, J. and (Eds), N. S. (2018). The Climate Data Guide: Hurrell North Atlantic Oscillation (NAO) Index (station-based).

Cited p. 7.

Hurrell, J. W. (1995). Decadal Trends in the North Atlantic Oscillation: Regional Temperatures and Precipitation. Science, 269(5224):676–679.

Cited p. 4.

Hurrell, J. W., Kushnir, Y., Ottersen, G., and Visbeck, M. (2003). An overview of the North Atlantic oscillation. Geophysical Monograph-American Geophysical Union, 134:1–36.

Cited p. 5 et 7.

Hurrell, J. W. and Van Loon, H. (1997). Decadal variations in climate associated with the North Atlantic Oscillation. Climatic Change, 36(3):301–326.

Cited p. 6.

Imbrie, J., Berger, A., Boyle, E. A., Clemens, S. C., Duffy, A., Howard, W. R., Kukla, G., Kutzbach, J., Martinson, D. G., and McIntyre, A. (1993). On the structure and origin of major glaciation cycles 2. The 100,000–year cycle. Paleoceanography, 8(6):699–735.

Cited p. 14 et 15.

Imbrie, J., Boyle, E. A., Clemens, S. C., Duffy, A., Howard, W. R., Kukla, G., Kutzbach, J., Martinson, D. G., McIntyre, A., and Mix, A. C. (1992). On the structure and origin of major glaciation cycles 1. Linear responses to Milankovitch forcing. Paleoceanography, 7(6):701–738.

Cited p. 14.

Imbrie, J. and Kipp, N. G. (1971). A new micropaleontological method for quantitative paleoclimatology: application to a late pleistocene caribbean core. In Turekian, K. K., editor, The late Cenozoic glacial ages, pages 71–182. Yale University Press, New Haven, Conn.

Cited p. 16.

Ineson, S. and Scaife, A. A. (2009). The role of the stratosphere in the European climate response to El Niño. Nature Geoscience, 2(1):32.

Cited p. 7.

Ineson, S., Scaife, A. A., Knight, J. R., Manners, J. C., Dunstone, N. J., Gray, L. J., and Haigh, J. D. (2011). Solar forcing of winter climate variability in the Northern Hemisphere. Nature Geosci, 4(11):753–757.

Cited p. 7.

Jacobel, A. W., McManus, J. F., Anderson, R. F., and Winckler, G. (2016). Large deglacial shifts of the Pacific Intertropical Convergence Zone. Nat Commun, 7(1):1–7.

Cited p. 145.

Jensen, K. and Milthers, V. (1928). Stratigraphical and Paleontological Studies of Interglacial Fresh-water Deposits in Jutland and North West Germany.

Cited p. 10 et 153.

JiménezAmat, P. and Zahn, R. (2015). Offset timing of climate oscillations during the last two glacial-interglacial transitions connected with large-scale freshwater perturbation. Paleoceanography, 30(6):768–788.

Cited p. 149.

Johnsen, S. J., Clausen, H. B., Dansgaard, W., Fuhrer, K., Gundestrup, N., Hammer, C. U., Iversen, P., Jouzel, J., and Stauffer, B. (1992). Irregular glacial interstadials recorded in a new Greenland ice core. Nature, 359(6393):311.

Cited p. 10.

Johnsen, S. J., DahlJensen, D., Gundestrup, N., Steffensen, J. P., Clausen, H. B., Miller, H., MassonDelmotte, V., Sveinbjörnsdottir, A. E., and White, J. (2001). Oxygen isotope and palaeotemperature records from six Greenland ice-core stations: Camp Century, Dye-3, GRIP, GISP2, Renland and NorthGRIP. Journal of Quaternary Science, 16(4):299–307.

Cited p. 8.

Jolly, D., Prentice, I. C., Bonnefille, R., Ballouche, A., Bengo, M., Brenac, P., Buchet, G., Burney, D., Cazet, J.-P., Cheddadi, R., Edorh, T., Elenga, H., Elmoutaki, S., Guiot, J., Laarif, F., Lamb, H., Lezine, A.-M., Maley, J., Mbenza, M., Peyron, O., Reille, M., ReynaudFarrera, I., Riollet, G., Ritchie, J. C., Roche, E., Scott, L., Ssemmanda, I., Straka, H., Umer, M., Campo, E. V., Vilimumbalo, S., Vincens, A., and Waller, M. (1998). Biome reconstruction from pollen and plant macrofossil data for Africa and the Arabian peninsula at 0 and 6000 years. Journal of Biogeography, 25(6):1007–1027.

Cited p. 145.

Jones, B. F., Eugster, H. P., and Rettig, S. L. (1977). Hydrochemistry of the Lake Magadi basin, Kenya. Geochimica et Cosmochimica Acta, 41(1):53–72.

Cited p. 87.

Jouzel, J., Alley, R. B., Cuffey, K. M., Dansgaard, W., Grootes, P., Hoffmann, G., Johnsen, S. J., Koster, R. D., Peel, D., and Shuman, C. A. (1997). Validity of the temperature reconstruction from water isotopes in ice cores. Journal of Geophysical Research: Oceans, 102(C12):26471–26487.

Cited p. 16.

Jouzel, J., Masson-Delmotte, V., Cattani, O., Dreyfus, G., Falourd, S., Hoffmann, G., Minster, B., Nouet, J., Barnola, J. M., Chappellaz, J., Fischer, H., Gallet, J. C., Johnsen, S., Leuenberger, M., Loulergue, L., Luethi, D., Oerter, H., Parrenin, F., Raisbeck, G., Raynaud, D., Schilt, A., Schwander, J., Selmo, E., Souchez, R., Spahni, R., Stauffer, B., Steffensen, J. P., Stenni, B., Stocker, T. F., Tison, J. L., Werner, M., and Wolff, E. W. (2007). Orbital and millennial Antarctic climate variability over the past 800,000 years. Science, 317(5839):793–796.

Cited p. 8, 9, 10 et 145.

Juggins, S. (2013). Quantitative reconstructions in palaeolimnology: new paradigm or sick science? Quaternary Science Reviews, 64:20–32.

Cited p. 18.

Kah, L. C., Lyons, T. W., and Chesley, J. T. (2001). Geochemistry of a 1.2 Ga carbonate-evaporite succession, northern Baffin and Bylot Islands: implications for Mesoproterozoic marine evolution. Precambrian Research, 111(1-4):203–234.

Cited p. 45.

Kalyuzhnyy, V. A. (1960). Liquid Inclusions in Minerals as a Geologic Barometer. International Geology Review, 2(3):181–195.

Cited p. 87.

Kandiano, E. S., Bauch, H. A., and Müller, A. (2004). Sea surface temperature variability in the North Atlantic during the last two glacialinterglacial cycles: comparison of faunal, oxygen isotopic, and Mg/Ca-derived records. Palaeogeography, Palaeoclimatology, Palaeoecology, 204(1):145–164.

Cited p. 145.

Kanner, L. C., Burns, S. J., Cheng, H., and Edwards, R. L. (2012). High-Latitude Forcing of the South American Summer Monsoon During the Last Glacial. Science, 335(6068):570–573.

Cited p. 10.

Kaspar, F., Kühl, N., Cubasch, U., and Litt, T. (2005). A model-data comparison of European temperatures in the Eemian interglacial. Geophysical Research Letters, 32(11).

Cited p. 18 et 153.

Katz, A. and Starinsky, A. (2009). Geochemical History of the Dead Sea. Aquat Geochem, 15(1):159–194.

Cited p. 86, 96, 120 et 141.

Kennedy, G. C. (1950). Pneumatolysis and the liquid inclusion method of geologic thermometry. Economic Geology, 45(6):533–547.

Cited p. 87.

Kiro, Y., Goldstein, S. L., Garcia-Veigas, J., Levy, E., Kushnir, Y., Stein, M., and Lazar, B. (2017). Relationships between lake-level changes and water and salt budgets in the Dead Sea during extreme aridities in the Eastern Mediterranean. Earth and Planetary Science Letters, 464:211–226.

Cited p. 96, 120, 130, 131, 133, 134, 139, 140, 142, 144 et 146.

Kiro, Y., Goldstein, S. L., Lazar, B., and Stein, M. (2016). Environmental implications of salt facies in the Dead Sea. GSA Bulletin, 128(5-6):824–841.

Cited p. 120, 123, 140 et 146.

Klein-BenDavid, O., Sass, E., and Katz, A. (2004). The evolution of marine evaporitic brines in inland basins: The Jordan-Dead Sea Rift valley. Geochimica et Cosmochimica Acta, 68(8):1763–1775.

Cited p. 87.

Kling, G. W. (1988). Comparative transparency, depth of mixing, and stability of stratification in lakes of Cameroon, West Africa1. Limnology and Oceanography, 33(1):27–40.

Cited p. 142.

Knight, C. L. and Bodnar, R. J. (1989). Synthetic fluid inclusions: IX. Critical PVTX properties of NaCl-H_2O solutions. Geochimica et Cosmochimica Acta, 53(1):3–8.

Cited p. 87.

Knowles, K. M. and Howie, P. R. (2015). The Directional Dependence of Elastic Stiffness and Compliance Shear Coefficients and Shear Moduli in Cubic Materials. J Elast, 120(1):87–108.

Cited p. 92.

Knuutila, H., Juliussen, O., and Svendsen, H. F. (2010). Density and N_2O solubility of sodium and potassium carbonate solutions in the temperature range 25 to 80řC. Chemical Engineering Science, 65(6):2177–2182.

Cited p. 105.

Kolodny, Y., Stein, M., and Machlus, M. (2005). Sea-rain-lake relation in the Last Glacial East Mediterranean revealed by 18o-13c in Lake Lisan aragonites. Geochimica et Cosmochimica Acta, 69(16):4045–4060.

Cited p. 149.

Kovalevych, V., Paul, J., and Peryt, T. M. (2009). Fluid inclusions in halite from the Roet (Lower Triassic) salt deposit in Central Germany: evidence for seawater chemistry and conditions of salt deposition and recrystallization. Carbonates and evaporites, 24(1):45–57.

Cited p. 46.

Krüger, Y., García-Ruiz, J. M., Canals, n., Marti, D., Frenz, M., and Van Driessche, A. E. (2013). Determining gypsum growth temperatures using monophase fluid inclusionsApplication to the giant gypsum crystals of Naica, Mexico. Geology, 41(2):119–122.

Cited p. 25 et 58.

Krüger, Y., Marti, D., Staub, R. H., Fleitmann, D., and Frenz, M. (2011). Liquidvapour homogenisation of fluid inclusions in stalagmites: Evaluation of a new thermometer for palaeoclimate research. Chemical geology, 289(1-2):39–47.

Cited p. 25, 46, 50, 58 et 65.

Krüger, Y., Stoller, P., Rika, J., and Frenz, M. (2007). Femtosecond lasers in fluid-inclusion analysis: overcoming metastable phase states. European Journal of mineralogy, 19(5):693–706.

Cited p. 25 et 58.

Krumgalz, B. S., Magdal, E., and Starinsky, A. (2002). The evolution of a chloride sedimentary sequence-simulated evaporation of the Dead Sea. Israel Journal of Earth Sciences, 51(3/4):253–267.

Cited p. 62.

Krumgalz, B. S., Malester, I. A., Ostrich, I. J., and Millero, F. J. (1992). Heat capacities of concentrated multicomponent aqueous electrolyte solutions at various temperatures. J Solution Chem, 21(7):635–649.

Cited p. 116 et 117.

Krumgalz, B. S. and Millero, F. J. (1982). Physico-chemical study of Dead Sea waters: II. Density measurements and equation of state of Dead Sea waters at 1 atm. Marine Chemistry, 11(5):477–492.

Cited p. 116 et 117.

Krumgalz, B. S., Pogorelsky, R., and Pitzer, K. S. (1995). Ion interaction approach to calculations of volumetric properties of aqueous multiple-solute electrolyte solutions. J Solution Chem, 24(10):1025–1038.

Cited p. 90 et 91.

Krumgalz, B. S., Pogorelsky, R., Sokolov, A., and Pitzer, K. S. (2000). Volumetric Ion Interaction Parameters for Single-Solute Aqueous Electrolyte Solutions at Various Temperatures. Journal of Physical and Chemical Reference Data, 29(5):1123–1140.

Cited p. 91.

Kukla, G., Berger, A., Lotti, R., and Brown, J. (1981). Orbital signature of interglacials. Nature, 290(5804):295–300.

Cited p. 145.

Kukla, G. J., Beaulieu, J.-L. d., Svobodova, H., Andrieu-Ponel, V., Thouveny, N., and Stockhausen, H. (2002a). Tentative Correlation of Pollen Records of the Last Interglacial at Grande Pile and Ribains with Marine Isotope Stages. Quaternary Research, 58(1):32–35.

Cited p. 153.

Kukla, G. J., Bender, M. L., Beaulieu, J.-L. d., Bond, G., Broecker, W. S., Cleveringa, P., Gavin, J. E., Herbert, T. D., Imbrie, J., Jouzel, J., Keigwin, L. D., Knudsen, K.-L., McManus, J. F., Merkt, J., Muhs, D. R., Müller, H., Poore, R. Z., Porter, S. C., Seret, G., Shackleton, N. J., Turner, C., Tzedakis, P. C., and Winograd, I. J. (2002b). Last Interglacial Climates. Quaternary Research, 58(1):2–13.

Cited p. 145 et 153.

Kushnir, Y., Robinson, W. A., Bladé, I., Hall, N. M. J., Peng, S., and Sutton, R. (2002). Atmospheric GCM Response to Extratropical SST Anomalies: Synthesis and Evaluation. J. Climate, 15(16):2233–2256.

Cited p. 151.

Kutzbach, J. E., Chen, G., Cheng, H., Edwards, R. L., and Liu, Z. (2014). Potential role of winter rainfall in explaining increased moisture in the Mediterranean and Middle East during periods of maximum orbitally-forced insolation seasonality. Clim Dyn, 42(3):1079–1095.

Cited p. 18, 120, 145, 146, 150 et 154.

Lach, A., Ballerat-Busserolles, K., André, L., Simond, M., Lassin, A., Cézac, P., Neyt, J.-C., and Serin, J.-P. (2017). Experimental Data and Modeling of Solution Density and Heat Capacity in the $NaKCaMgClH_2O$ System up to 353.15 K and 5 molůkg^{1} Ionic Strength. J. Chem. Eng. Data, 62(10):3561–3576.

Cited p. 116 et 117.

Lach, A., Boulahya, F., André, L., Lassin, A., Azaroual, M., Serin, J.-P., and Cézac, P. (2016). Thermal and volumetric properties of complex aqueous electrolyte solutions using the Pitzer formalism The PhreeSCALE code. Computers & Geosciences, 92:58–69.

Cited p. 96 et 130.

Landau, L. D., Lifshitz, E. M., and Pitaevskii, L. P. (1984). Electrodynamics of continuous media. Pergamon Press, Oxford.

Cited p. 28.

Landau, L. D., Pitaevskii, L. P., Kosevich, A. M., and Lifshitz, E. M. (1986). Theory of Elasticity: Volume 7. Butterworth-Heinemann, Amsterdam, 3 edition edition.

Cited p. 91, 92 et 102.

Larson, L. M. (1917). The King's Mirror: (Speculum Regalae-Konungs Skuggsjá). American-Scandinavian Foundation.

Cited p. 6.

Laskar, J., Fienga, A., Gastineau, M., and Manche, H. (2011). La2010: a new orbital solution for the long-term motion of the Earth. Astronomy & Astrophysics, 532:A89.

Cited p. 11 et 12.

Laskar, J., Robutel, P., Joutel, F., Gastineau, M., Correia, A. C. M., and Levrard, B. (2004). A long-term numerical solution for the insolation quantities of the Earth. A&A, 428(1):261–285.

Cited p. 12, 148 et 152.

Last, W. M. (1993). Geolimnology of Freefight Lake: an unusual hypersaline lake in the northern Great Plains of western Canada. Sedimentology, 40(3):431–448.

Cited p. 45.

Leduc, G., Schneider, R., Kim, J. H., and Lohmann, G. (2010). Holocene and Eemian sea surface temperature trends as revealed by alkenone and Mg/Ca paleothermometry. Quaternary Science Reviews, 29(7):989–1004.

Cited p. 145.

Lensky, N. G., Dvorkin, Y., Lyakhovsky, V., Gertman, I., and Gavrieli, I. (2005). Water, salt, and energy balances of the Dead Sea. Water Resources Research, 41(12).

Cited p. 122.

Levy, E. J., Sivan, O., Antler, G., Lazar, B., Stein, M., Yechieli, Y., and Gavrieli, I. (2019). Mount Sedom salt diapir - Source for sulfate replenishment and gypsum supersaturation in the last glacial Dead Sea (Lake Lisan). Quaternary Science Reviews, 221:105871.

Cited p. 120.

Levy, E. J., Stein, M., Lazar, B., Gavrieli, I., Yechieli, Y., and Sivan, O. (2017). Pore fluids in Dead Sea sediment core reveal linear response of lake chemistry to global climate changes. Geology, 45(4):315–318.

Cited p. 137, 139, 144 et 155.

Levy, E. J., Yechieli, Y., Gavrieli, I., Lazar, B., Kiro, Y., Stein, M., and Sivan, O. (2018). Salt precipitation and dissolution in the late Quaternary Dead Sea: Evidence from chemical and 37cl composition of pore fluids and halites. Earth and Planetary Science Letters, 487:127–137.

Cited p. 120, 140, 142 et 167.

Li, J., Lowenstein, T. K., Brown, C. B., Ku, T.-L., and Luo, S. (1996). A 100 ka record of water tables and paleoclimates from salt cores, Death Valley, California. Palaeogeography, Palaeoclimatology, Palaeoecology, 123(1-4):179–203.

Cited p. 45.

Lisiecki, L. E. and Raymo, M. E. (2005). A Pliocene-Pleistocene stack of 57 globally distributed benthic δ^{18}O records. Paleoceanography, 20(1).

Cited p. 8, 9, 12 et 13.

Lisker, S., Vaks, A., Bar-Matthews, M., Porat, R., and Frumkin, A. (2009). Stromatolites in caves of the Dead Sea Fault Escarpment: implications to latest Pleistocene lake levels and tectonic subsidence. Quaternary Science Reviews, 28(1):80–92.

Cited p. 139, 143 et 144.

Litt, T., Pickarski, N., Heumann, G., Stockhecke, M., and Tzedakis, P. C. (2014). A 600,000 year long continental pollen record from Lake Van, eastern Anatolia (Turkey). Quaternary Science Reviews, 104:30–41.

Cited p. 146.

Liu, T. W., Xie, X., Polito, P. S., Xie, S.-P., and Hashizume, H. (2000). Atmospheric manifestation of tropical instability wave observed by QuikSCAT and tropical rain measuring mission. Geophysical Research Letters, 27(16):2545–2548.

Cited p. 3 et 4.

Liu, W. G., Xiao, Y. K., Wang, Q. Z., Qi, H. P., Wang, Y. H., Zhou, Y. M., and Shirodkar, P. V. (1997). Chlorine isotopic geochemistry of salt lakes in the Qaidam Basin, China. Chemical Geology, 136(3):271–279.

Cited p. 108.

Liu, W. T., Zhang, A., and Bishop, J. K. B. (1994). Evaporation and solar irradiance as regulators of sea surface temperature in annual and interannual changes. Journal of Geophysical Research: Oceans, 99(C6):12623–12637.

Cited p. 3.

Liu, Z., Otto-Bliesner, B. L., He, F., Brady, E. C., Tomas, R., Clark, P. U., Carlson, A. E., Lynch-Stieglitz, J., Curry, W., and Brook, E. (2009). Transient simulation of last deglaciation with a new mechanism for Bølling-Allerød warming. Science, 325(5938):310–314.

Cited p. 19 et 22.

Liu, Z., Zhu, J., Rosenthal, Y., Zhang, X., Otto-Bliesner, B. L., Timmermann, A., Smith, R. S., Lohmann, G., Zheng, W., and Timm, O. E. (2014). The Holocene temperature conundrum. PNAS, 111(34):E3501–E3505.

Cited p. 19, 20, 21 et 22.

Lo, L., Chang, S.-P., Wei, K.-Y., Lee, S.-Y., Ou, T.-H., Chen, Y.-C., Chuang, C.-K., Mii, H.-S., Burr, G. S., and Chen, M.-T. (2017). Nonlinear climatic sensitivity to greenhouse gases over past 4 glacial/interglacial cycles. Scientific reports, 7(1):4626.

Cited p. 15.

Lohmann, G. (2017). Atmospheric bridge on orbital time scales. Theor Appl Climatol, 128(3):709–718.

Cited p. 19.

Losey, A. B. and Benison, K. C. (2000). Silurian paleoclimate data from fluid inclusions in the Salina Group halite Michigan Basin. Carbonates and Evaporites, 15(1):28–36.

Cited p. 46.

Lotter, A. F., Birks, H. J. B., Hofmann, W., and Marchetto, A. (1997). Modern diatom, cladocera, chironomid, and chrysophyte cyst assemblages as quantitative indicators for the reconstruction of past environmental conditions in the Alps. I. Climate. Journal of Paleolimnology, 18(4):395–420.

Cited p. 17.

Louman, G. G. (1934). On the occurrence of interglacial (Risz-Würm) peat in Holland. KAWA.

Cited p. 10 et 153.

Lowenstein, T. K., Dolginko, L. A. C., and García-Veigas, J. (2016). Influence of magmatic-hydrothermal activity on brine evolution in closed basins: Searles Lake, California. GSA Bulletin, 128(9-10):1555–1568.

Cited p. 87.

Lowenstein, T. K. and Hardie, L. A. (1985). Criteria for the recognition of salt-pan evaporites. Sedimentology, 32(5):627–644.

Cited p. 45.

Lowenstein, T. K., Li, J., Brown, C., Roberts, S. M., Ku, T.-L., Luo, S., and Yang, W. (1999). 200 ky paleoclimate record from Death Valley salt core. Geology, 27(1):3–6.

Cited p. 46.

Lowenstein, T. K., Li, J., and Brown, C. B. (1998). Paleotemperatures from fluid inclusions in halite: method verification and a 100,000 year paleotemperature record, Death Valley, CA. Chemical Geology, 150(3-4):223–245.

Cited p. ix, xi, 25, 46, 53, 58, 59, 61, 65 et 83.

Lowenstein, T. K. and Risacher, F. (2009). Closed Basin Brine Evolution and the Influence of CaCl Inflow Waters: Death Valley and Bristol Dry Lake California, Qaidam Basin, China, and Salar de Atacama, Chile. Aquat Geochem, 15(1):71–94.

Cited p. 86, 98 et 108.

Lowenstein, T. K., Spencer, R. J., and Pengxi, Z. (1989). Origin of Ancient Potash Evaporites: Clues from the Modem Nonmarine Qaidam Basin of Western China. Science, 245(4922):1090–1092.

Cited p. 86 et 98.

López-Moreno, J. I., Vicente-Serrano, S. M., Morán-Tejeda, E., Lorenzo-Lacruz, J., Kenawy, A., and Beniston, M. (2011). Effects of the North Atlantic Oscillation (NAO) on combined temperature and precipitation winter modes in the Mediterranean mountains: Observed relationships and projections for the 21st century. Global and Planetary Change, 77(1):62–76.

Cited p. 152.

Lüthi, D., Floch, M. L., Bereiter, B., Blunier, T., Barnola, J.-M., Siegenthaler, U., Raynaud, D., Jouzel, J., Fischer, H., Kawamura, K., and Stocker, T. F. (2008). High-resolution carbon dioxide concentration record 650,000–800,000 years before present. Nature, 453(7193):379–382.

Cited p. 8, 9 et 14.

Lunt, D. J., Abe-Ouchi, A., Bakker, P., Berger, A., Braconnot, P., Charbit, S., Fischer, N., Herold, N., Jungclaus, J. H., Khon, V. C., Krebs-Kanzow, U., Langebroek, P. M., Lohmann, G., Nisancioglu, K. H., Otto-Bliesner, B. L., Park, W., Pfeiffer, M., Phipps, S. J., Prange, M., Rachmayani, R., Renssen, H., Rosenbloom, N., Schneider, B., Stone, E. J., Takahashi, K., Wei, W., Yin, Q., and Zhang, Z. S. (2013). A multi-model assessment of last interglacial temperatures. Climate of the Past, 9:699–717.

Cited p. 18.

Lunt, D. J., Foster, G. L., Haywood, A. M., and Stone, E. J. (2008). Late Pliocene Greenland glaciation controlled by a decline in atmospheric CO_2 levels. Nature, 454(7208):1102.

Cited p. 15.

Luterbacher, J., Dietrich, D., Xoplaki, E., Grosjean, M., and Wanner, H. (2004). European seasonal and annual temperature variability, trends, and extremes since 1500. Science, 303(5663):1499–1503.

Cited p. 17.

Ma, J., Xu, H., Dong, C., Lin, P., and Liu, Y. (2015a). Atmospheric responses to oceanic eddies in the Kuroshio Extension region. Journal of Geophysical Research: Atmospheres, 120(13):6313–6330.

Cited p. 4.

Ma, X., Chang, P., Saravanan, R., Montuoro, R., Hsieh, J.-S., Wu, D., Lin, X., Wu, L., and Jing, Z. (2015b). Distant Influence of Kuroshio Eddies on North Pacific Weather Patterns? Scientific Reports, 5:17785.

Cited p. 4.

Ma, X., Chang, P., Saravanan, R., Montuoro, R., Nakamura, H., Wu, D., Lin, X., and Wu, L. (2016a). Importance of Resolving Kuroshio Front and Eddy Influence in Simulating the North Pacific Storm Track. J. Climate, 30(5):1861–1880.

Cited p. 4.

Ma, X., Jing, Z., Chang, P., Liu, X., Montuoro, R., Small, R. J., Bryan, F. O., Greatbatch, R. J., Brandt, P., Wu, D., Lin, X., and Wu, L. (2016b). Western boundary currents regulated by interaction between ocean eddies and the atmosphere. Nature, 535(7613):533–537.

Cited p. 4 et 154.

Maloney, E. D. and Chelton, D. B. (2006). An Assessment of the Sea Surface Temperature Influence on Surface Wind Stress in Numerical Weather Prediction and Climate Models. J. Climate, 19(12):2743–2762.

Cited p. 4.

Mann, M. E., Zhang, Z., Hughes, M. K., Bradley, R. S., Miller, S. K., Rutherford, S., and Ni, F. (2008). Proxy-based reconstructions of hemispheric and global surface temperature variations over the past two millennia. Proceedings of the National Academy of Sciences, 105(36):13252–13257.

Cited p. 17.

Mantua, N. J., Hare, S. R., Zhang, Y., Wallace, J. M., and Francis, R. C. (1997). A Pacific Interdecadal Climate Oscillation with Impacts on Salmon Production*. Bull. Amer. Meteor. Soc., 78(6):1069–1080.

Cited p. 3.

Mao, S. and Duan, Z. (2008). The P,V,T,x properties of binary aqueous chloride solutions up to T= 573 K and 100 MPa. The Journal of Chemical Thermodynamics, 40(7):1046–1063.

Cited p. 82.

Mao, S., Peng, Q., Wang, M., Hu, J., Peng, C., and Zhang, J. (2017). The PVTx properties of aqueous electrolyte solutions containing Li^+, Na^+, K^+, Mg^{2+}, Ca^{2+}, Cl^- and SO_4^{2-} under conditions of CO_2 capture and sequestration. Applied Geochemistry, 86:105–120.

Cited p. 82.

Marcott, S. A., Shakun, J. D., Clark, P. U., and Mix, A. C. (2013). A Reconstruction of Regional and Global Temperature for the Past 11,300 Years. Science, 339(6124):1198–1201.

Cited p. ix, xi, 17, 19, 20 et 21.

Marino, G., Rohling, E. J., Rijpstra, W. I. C., Sangiorgi, F., Schouten, S., and Damsté, J. S. S. (2007). Aegean Sea as driver of hydrographic and ecological changes in the eastern Mediterranean. Geology, 35(8):675–678.

Cited p. 148.

Marino, G., Rohling, E. J., Rodríguez-Sanz, L., Grant, K. M., Heslop, D., Roberts, A. P., Stanford, J. D., and Yu, J. (2015). Bipolar seesaw control on last interglacial sea level. Nature, 522(7555):197–201.

Cited p. 148 et 149.

Marsicek, J., Shuman, B. N., Bartlein, P. J., Shafer, S. L., and Brewer, S. (2018). Reconciling divergent trends and millennial variations in Holocene temperatures. Nature, 554(7690):92.

Cited p. 21.

Marti, D., Krüger, Y., Fleitmann, D., Frenz, M., and Rika, J. (2012). The effect of surface tension on liquidgas equilibria in isochoric systems and its application to fluid inclusions. Fluid Phase Equilibria, 314:13–21.

Cited p. 25 et 82.

Martin, C. (2018). Reconstruction des températures continentales en Europe de l'Ouest à partir de l'étude des tétraéthers ramifiés dans les sédiments du lac de Saint-Front (Massif Central, France). PhD thesis, Aix-Marseille.

Cited p. 21.

Martrat, B., Grimalt, J. O., Lopez-Martinez, C., Cacho, I., Sierro, F. J., Flores, J. A., Zahn, R., Canals, M., Curtis, J. H., and Hodell, D. A. (2004). Abrupt Temperature Changes in the Western Mediterranean over the Past 250,000 Years. Science, 306(5702):1762–1765.

Cited p. 150.

Martrat, B., Grimalt, J. O., Shackleton, N. J., Abreu, L. d., Hutterli, M. A., and Stocker, T. F. (2007). Four Climate Cycles of Recurring Deep and Surface Water Destabilizations on the Iberian Margin. Science, 317(5837):502–507.

Cited p. 9 et 145.

Martrat, B., Jimenez-Amat, P., Zahn, R., and Grimalt, J. O. (2014). Similarities and dissimilarities between the last two deglaciations and interglaciations in the North Atlantic region. Quaternary Science Reviews, 99:122–134.

Cited p. 148, 150 et 154.

Mathew, R., Albright, J. G., Miller, D. G., and Rard, J. A. (1990). Isothermal diffusion coefficients for sodium chloride-magnesium chloride-water at 25 řC. 4. Solute concentration ratio of 1: 3. Journal of physical chemistry, 94(17):6875–6878.

Cited p. 37.

Mauri, A., Davis, B. A. S., Collins, P. M., and Kaplan, J. O. (2014). The influence of atmospheric circulation on the mid-Holocene climate of Europe: a datamodel comparison. Climate of the Past, 10(5):1925–1938.

Cited p. 21.

Mauri, A., Davis, B. A. S., Collins, P. M., and Kaplan, J. O. (2015). The climate of Europe during the Holocene: a gridded pollen-based reconstruction and its multi-proxy evaluation. Quaternary Science Reviews, 112:109–127.

Cited p. 21 et 22.

Mazzucchelli, M. L., Burnley, P., Angel, R. J., Morganti, S., Domeneghetti, M. C., Nestola, F., and Alvaro, M. (2018). Elastic geothermobarometry: Corrections for the geometry of the host-inclusion system. Geology, 46(3):231–234.

Cited p. 102 et 103.

McCaffrey, M. A., Lazar, B., and Holland, H. D. (1987). The evaporation path of seawater and the coprecipitation of Br (super -) and K (super +) with halite. Journal of Sedimentary Research, 57(5):928–937.

Cited p. 62, 86 et 87.

McManus, J. F., Bond, G. C., Broecker, W. S., Johnsen, S., Labeyrie, L., and Higgins, S. (1994). High-resolution climate records from the North Atlantic during the last interglacial. Nature, 371(6495):326–329.

Cited p. 145.

McManus, J. F., Francois, R., Gherardi, J.-M., Keigwin, L. D., and Brown-Leger, S. (2004). Collapse and rapid resumption of Atlantic meridional circulation linked to deglacial climate changes. Nature, 428(6985):834–837.

Cited p. 8.

McManus, J. F., Oppo, D. W., and Cullen, J. L. (1999). A 0.5-million-year record of millennial-scale climate variability in the North Atlantic. science, 283(5404):971–975.

Cited p. 10.

Meckler, A. N., Affolter, S., Dublyansky, Y. V., Krüger, Y., Vogel, N., Bernasconi, S. M., Frenz, M., Kipfer, R., Leuenberger, M., Spötl, C., Carolin, S., Cobb, K. M., Moerman, J., Adkins, J. F., and Fleitmann, D. (2015). Glacialinterglacial temperature change in the tropical West Pacific: A comparison of stalagmite-based paleothermometers. Quaternary Science Reviews, 127:90–116.

Cited p. 18 et 25.

Mekki-Azouzi, M. E. and Ramboz, C. (2019). Fluid Inclusions, Solid-Solid Transitions in Salt, Ceramics and Minerals to Calibrate the Microthermometric Stage. In Petrogenesis and Exploration of the Earth's Interior, pages 175–177. Springer.

Cited p. 32.

Meng, F., Ni, P., Schiffbauer, J. D., Yuan, X., Zhou, C., Wang, Y., and Xia, M. (2011). Ediacaran seawater temperature: Evidence from inclusions of Sinian halite. Precambrian Research, 184(1-4):63–69.

Cited p. 46.

Meng, F.-W., Ni, P., Yuan, X.-L., Zhou, C.-M., Yang, C.-H., and Li, Y.-P. (2013). Choosing the best ancient analogue for projected future temperatures: A case using data from fluid inclusions of middle-late Eocene halites. Journal of Asian Earth Sciences, 67:46–50.

Cited p. 46.

Migowski, C., Stein, M., Prasad, S., Negendank, J. F. W., and Agnon, A. (2006). Holocene Climate Variability and Cultural Evolution in the Near East from the Dead Sea Sedimentary Record. Quaternary Research, 66(3):421–431.

Cited p. 141.

Milankovitch, M. K. (1941). Kanon der Erdbestrahlung und seine Anwendung auf das Eiszeitenproblem. Royal Serbian Academy Special Publication, 133:1–633.

Cited p. 11.

Millero, F. J., Vinokurova, F., Fernandez, M., and Hershey, J. P. (1987). PVT properties of concentrated electrolytes. VI. The speed of sound and apparent molal compressibilities of NaCl, Na_2SO_4, $MgCl_2$, and $MgSO_4$ solutions from 0 to 100 řC. Journal of solution chemistry, 16(4):269–284.

Cited p. 37, 38, 60 et 73.

Milner, A. M., Collier, R. E. L., Roucoux, K. H., Müller, U. C., Pross, J., Kalaitzidis, S., Christanis, K., and Tzedakis, P. C. (2012). Enhanced seasonality of precipitation in the Mediterranean during the early part of the Last Interglacial. Geology, 40(10):919–922.

Cited p. 146.

Milner, A. M., Roucoux, K. H., Collier, R. E. L., Müller, U. C., Pross, J., and Tzedakis, P. C. (2016). Vegetation responses to abrupt climatic changes during the Last Interglacial Complex (Marine Isotope Stage 5) at Tenaghi Philippon, NE Greece. Quaternary Science Reviews, 154:169–181.

Cited p. 146 et 150.

Minobe, S., Kuwano-Yoshida, A., Komori, N., Xie, S.-P., and Small, R. J. (2008). Influence of the Gulf Stream on the troposphere. Nature, 452(7184):206–209.

Cited p. 4 et 7.

Mitchell, T. E. and Heuer, A. H. (1977). Solution hardening by aliovalent cations in ionic crystals. Materials Science and Engineering, 28(1):81–97.

Cited p. 63.

Mokeddem, Z., McManus, J. F., and Oppo, D. W. (2014). Oceanographic dynamics and the end of the last interglacial in the subpolar North Atlantic. PNAS, 111(31):11263–11268.

Cited p. 148.

Monnin, C. (1989). An ion interaction model for the volumetric properties of natural waters: Density of the solution and partial molal volumes of electrolytes to high concentrations at 25řC. Geochimica et Cosmochimica Acta, 53(6):1177–1188.

Cited p. 91.

Monnin, E., Indermühle, A., Dällenbach, A., Flückiger, J., Stauffer, B., Stocker, T. F., Raynaud, D., and Barnola, J.-M. (2001). Atmospheric CO_2 concentrations over the last glacial termination. Science, 291(5501):112–114.

Cited p. 14.

Morin, E., Ryb, T., Gavrieli, I., and Enzel, Y. (2019). Mean, variance, and trends of Levant precipitation over the past 4500 years from reconstructed Dead Sea levels and stochastic modeling. Quaternary Research, 91(2):751–767.

Cited p. 121, 148, 155, 158, 163, 164 et 168.

Moron, V. and Gouirand, I. (2003). Seasonal modulation of the El NiñoSouthern Oscillation relationship with sea level pressure anomalies over the North Atlantic in October–March 1873–1996. International Journal of Climatology: A Journal of the Royal Meteorological Society, 23(2):143–155.

Cited p. 7.

Narita, N., Takahara, Y., and Higashida, K. (2002). Brittle-to-ductile transition and slip band structure in ionic crystals. Philosophical Magazine A, 82(17-18):3229–3239.

Cited p. 61.

Neev, D. and Emery, K. (1967). The Dead Sea, depositional processes and environments of evaporites. Geol. Surv. Israel Bull, 41:147.

Cited p. 126.

Neugebauer, I., Brauer, A., Schwab, M. J., Waldmann, N. D., Enzel, Y., Kitagawa, H., Torfstein, A., Frank, U., Dulski, P., Agnon, A., Ariztegui, D., Ben-Avraham, Z., Goldstein, S. L., and Stein, M. (2014). Lithology of the long sediment record recovered by the ICDP Dead Sea Deep Drilling Project (DSDDP). Quaternary Science Reviews, 102:149–165.

Cited p. 120, 126, 127, 128 et 146.

Neugebauer, I., Schwab, M. J., Waldmann, N. D., Tjallingii, R., Frank, U., Hadzhiivanova, E., Naumann, R., Taha, N., Agnon, A., Enzel, Y., and Brauer, A. (2016). Hydroclimatic variability in the Levant during the early last glacial (11775 ka) derived from micro-facies analyses of deep Dead Sea sediments. Climate of the Past, 12(1):75–90.

Cited p. 128, 144 et 149.

Niemi, B.-A. G., Ben-Avraham, Z., and Gat, J. R., editors (1997). The Dead Sea: The Lake and Its Setting. Oxford University Press, New York. Google-Books-ID: nlWRHnz7zSsC.

Cited p. 45.

Nürnberg, D., Bijma, J., and Hemleben, C. (1996). Assessing the reliability of magnesium in foraminiferal calcite as a proxy for water mass temperatures. Geochimica et Cosmochimica Acta, 60(5):803–814.

Cited p. 16.

Ohno, I., Harada, K., and Yoshitomi, C. (2006). Temperature variation of elastic constants of quartz across the α - β transition. Phys Chem Minerals, 33(1):1–9.

Cited p. 95.

Okumura, Y., Xie, S.-P., Numaguti, A., and Tanimoto, Y. (2001). Tropical Atlantic air-sea interaction and its influence on the NAO. Geophysical Research Letters, 28(8):1507–1510.

Cited p. 3.

O'Neill, L. W., Chelton, D. B., and Esbensen, S. K. (2003). Observations of SST-Induced Perturbations of the Wind Stress Field over the Southern Ocean on Seasonal Timescales. J. Climate, 16(14):2340–2354.

Cited p. 4.

Opdyke, N. D. (1976). Pacific Core V28-239 Late Pliocene to Latest Pleistocene. Investigation of late Quaternary paleoceanography and paleoclimatology, 145:449.

Cited p. 12.

Oppo, D. W., Keigwin, L. D., McManus, J. F., and Cullen, J. L. (2001). Persistent suborbital climate variability in marine isotope stage 5 and termination II. Paleoceanography, 16(3):280–292.

Cited p. 148 et 150.

Oppo, D. W., McManus, J. F., and Cullen, J. L. (2006). Evolution and demise of the Last Interglacial warmth in the subpolar North Atlantic. Quaternary Science Reviews, 25(23):3268–3277.

Cited p. 148 et 150.

Orozco, E. and Agulló-López, F. (1986). Hardening and serrated flow behaviour in the 300–500 K range for Eu-doped alkali halides. Acta Metallurgica, 34(9):1701–1709.

Cited p. 63.

Osborn, T. J. (2004). Simulating the winter North Atlantic Oscillation: the roles of internal variability and greenhouse gas forcing. Climate Dynamics, 22(6-7):605–623.

Cited p. 7.

Osborn, T. J., Briffa, K. R., Tett, S. F. B., Jones, P. D., and Trigo, R. M. (1999). Evaluation of the North Atlantic Oscillation as simulated by a coupled climate model. Climate Dynamics, 15(9):685–702.

Cited p. 7.

Otto-Bliesner, B. L., Rosenbloom, N., Stone, E. J., McKay, N. P., Lunt, D. J., Brady, E. C., and Overpeck, J. T. (2013). How warm was the last interglacial? New modeldata comparisons. Philosophical Transactions of the Royal Society A: Mathematical, Physical and Engineering Sciences, 371(2001):20130097.

Cited p. 18, 153 et 154.

Palchan, D., Neugebauer, I., Amitai, Y., Waldmann, N. D., Schwab, M. J., Dulski, P., Brauer, A., Stein, M., Erel, Y., and Enzel, Y. (2017). North Atlantic controlled depositional cycles in MIS 5e layered sediments from the deep Dead Sea basin. Quaternary Research, 87(1):168–179.

Cited p. 127 et 148.

Palchan, D. and Torfstein, A. (2019). A drop in Sahara dust fluxes records the northern limits of the African Humid Period. Nat Commun, 10.

Cited p. 145.

Pallares, G., Azouzi, M. E. M., González, M. A., Aragones, J. L., Abascal, J. L., Valeriani, C., and Caupin, F. (2014). Anomalies in bulk supercooled water at negative pressure. Proceedings of the National Academy of Sciences, 111(22):7936–7941.

Cited p. 28, 29, 34 et 47.

Pallares, G., Gonzalez, M. A., Abascal, J. L. F., Valeriani, C., and Caupin, F. (2016). Equation of state for water and its line of density maxima down to- 120 MPa. Physical Chemistry Chemical Physics, 18(8):5896–5900.

Cited p. 28, 34, 47 et 91.

Parkhurst, D. L. and Appelo, C. (2013). Description of input and examples for PHREEQC version 3: a computer program for speciation, batch-reaction, one-dimensional transport, and inverse geochemical calculations. USGS Numbered Series 6-A43, U.S. Geological Survey, Reston, VA.

Cited p. 96.

Parton, A., Clark-Balzan, L., Parker, A. G., Preston, G. W., Sung, W. W., Breeze, P. S., Leng, M. J., Groucutt, H. S., White, T. S., Alsharekh, A., and Petraglia, M. D. (2018). Middle-late Quaternary palaeoclimate variability from lake and wetland deposits in the Nefud Desert, Northern Arabia. Quaternary Science Reviews, 202:78–97.

Cited p. 145.

Past Interglacials Working Group of PAGES (2016). Interglacials of the last 800,000years. Reviews of Geophysics, 54(1):162–219.

Cited p. 8, 9, 10 et 18.

Pegram, L. M. and Record, M. T. (2007). Hofmeister Salt Effects on Surface Tension Arise from Partitioning of Anions and Cations between Bulk Water and the AirWater Interface. J. Phys. Chem. B, 111(19):5411–5417.

Cited p. 62 et 82.

Penck, A. and Brückner, E. (1909). Die alpen im Eiszeitalter, volume 3. CH Tauchnitz.

Cited p. 10.

Petit, J. R., Jouzel, J., Raynaud, D., Barkov, N. I., Barnola, J.-M., Basile, I., Bender, M., Chappellaz, J., Davis, M., Delaygue, G., Delmotte, M., Kotlyakov, V. M., Legrand, M., Lipenkov, V. Y., Lorius, C., PÉpin, L., Ritz, C., Saltzman, E., and Stievenard, M. (1999). Climate and atmospheric history of the past 420,000 years from the Vostok ice core, Antarctica. Nature, 399(6735):429–436.

Cited p. 14, 15 et 145.

Peyron, O., Goring, S., Dormoy, I., Kotthoff, U., Pross, J., De Beaulieu, J.-L., Drescher-Schneider, R., Vannière, B., and Magny, M. (2011). Holocene seasonality changes in the central Mediterranean region reconstructed from the pollen sequences of Lake Accesa (Italy) and Tenaghi Philippon (Greece). The Holocene, 21(1):131–146.

Cited p. 17.

Pickarski, N., Kwiecien, O., Djamali, M., and Litt, T. (2015). Vegetation and environmental changes during the last interglacial in eastern Anatolia (Turkey): a new high-resolution pollen record from Lake Van. Palaeogeography, Palaeoclimatology, Palaeoecology, 435:145–158.

Cited p. 153.

Pidwirny, M. (2006). Global Heat Balance: Introduction to Heat Fluxes. In Fundamentals of Physical Geography. 2nd edition.

Cited p. 1.

Piovano, E. L., Ariztegui, D., and Moreira, S. D. (2002). Recent environmental changes in Laguna Mar Chiquita (central Argentina): a sedimentary model for a highly variable saline lake. Sedimentology, 49(6):1371–1384.

Cited p. 45.

Pisias, N. G. and Moore Jr, T. C. (1981). The evolution of Pleistocene climate: a time series approach. Earth and Planetary Science Letters, 52(2):450–458.

Cited p. 12.

Pitzer, K. S. (1973). Thermodynamics of electrolytes. I. Theoretical basis and general equations. J. Phys. Chem., 77(2):268–277.

Cited p. 89.

Pitzer, K. S. (1991). Ion interaction approach: theory and data correlation. Activity coefficients in electrolyte solutions, 2:75–153.

Cited p. 89.

Potter, R. W. and Brown, D. L. (1975). The volumetric properties of aqueous sodium chloride solutions from 0 degrees to 500 degrees C at pressures up to 2000 bars based on a regression of the available literature data. USGS Numbered Series 75-636, U.S. Geological Survey,.

Cited p. 87.

Prahl, F. G. and Wakeham, S. G. (1987). Calibration of unsaturation patterns in long-chain ketone compositions for palaeotemperature assessment. Nature, 330(6146):367.

Cited p. 16.

Prell, W. L. (1981). Faunal and isotopic indices of monsoonal upwelling: Western Arabian Sea. Oceanologica Acta, 4:91–98.

Cited p. 16.

Prell, W. L. (1985). Stability of low-latitude sea-surface temperatures: an evaluation of the CLIMAP reconstruction with emphasis on the positive SST anomalies. Final report. Technical report, Brown Univ., Providence, RI (USA). Dept. of Geological Sciences.

Cited p. 16.

Prell, W. L. and Hutson, W. H. (1979). Zonal temperature-anomaly maps of Indian Ocean surface waters: Modern and ice-age patterns. Science, 206(4417):454–456.

Cited p. 16.

Prell, W. L. and Kutzbach, J. E. (1987). Monsoon variability over the past 150,000 years. Journal of Geophysical Research: Atmospheres, 92(D7):8411–8425.

Cited p. 145.

Raymo, M. E. (1997). The timing of major climate terminations. Paleoceanography, 12(4):577–585.

Cited p. 15.

Raz, U., Girsperger, S., and Thompson, A. B. (2002). Thermal expansion, compressibility and volumetric changes of quartz obtained by single crystal dilatometry to 700řC and 3.5 kilobars (0.35 GPa). Technical report, ETH, Eidgenössische Technische Hochschule Zürich, Department of Earth Sciences.

Cited p. 95.

Regattieri, E., Zanchetta, G., Drysdale, R. N., Isola, I., Woodhead, J. D., Hellstrom, J. C., Giaccio, B., Greig, A., Baneschi, I., and Dotsika, E. (2016). Environmental variability between the penultimate deglaciation and the mid Eemian: Insights from Tana che Urla (central Italy) speleothem trace element record. Quaternary Science Reviews, 152:80–92.

Cited p. 149.

Renssen, H., Seppä, H., Heiri, O., Roche, D. M., Goosse, H., and Fichefet, T. (2009). The spatial and temporal complexity of the Holocene thermal maximum. Nature Geoscience, 2(6):411.

Cited p. 22.

Rigaudier, T., Gardien, V., Martineau, F., Reverdy, G., and Lécuyer, C. (2012). Hydrogen and oxygen isotope reference materials for the analysis of water inclusions in halite. Geostandards and Geoanalytical Research, 36(1):51–59.

Cited p. 45.

Rigaudier, T., Lécuyer, C., Gardien, V., Suc, J.-P., and Martineau, F. (2011). The record of temperature, wind velocity and air humidity in the δD and δ^{18}O of water inclusions in synthetic and Messinian halites. Geochimica et Cosmochimica Acta, 75(16):4637–4652.

Cited p. 45 et 46.

Risacher, F. and Clement, A. (2001). A computer program for the simulation of evaporation of natural waters to high concentration. Computers & Geosciences, 27(2):191–201.

Cited p. 104.

Risacher, F. and Fritz, B. (1991). Geochemistry of Bolivian salars, Lipez, southern Altiplano: Origin of solutes and brine evolution. Geochimica et Cosmochimica Acta, 55(3):687–705.

Cited p. 86 et 87.

Ritchie, J. C., Eyles, C. H., and Haynes, C. V. (1985). Sediment and pollen evidence for an early to mid-Holocene humid period in the eastern Sahara. Nature, 314(6009):352–355.

Cited p. 145.

Roberts, S. M. and Spencer, R. J. (1995). Paleotemperatures preserved in fluid inclusions in halite. Geochimica et Cosmochimica Acta, 59(19):3929–3942.

Cited p. ix, xi, 25, 45, 46, 59, 65, 66 et 83.

Robertson, E. C. (1988). Thermal Properties of Rocks. U.S. Geological Survey. Google-Books-ID: 7N6hSgAACAAJ.

Cited p. 33.

Rodwell, M. J. and Folland, C. K. (2002). Atlantic airsea interaction and seasonal predictability. Quarterly Journal of the Royal Meteorological Society: A journal of the atmospheric sciences, applied meteorology and physical oceanography, 128(583):1413–1443.

Cited p. 7.

Rodwell, M. J., Rowell, D. P., and Folland, C. K. (1999). Oceanic forcing of the wintertime North Atlantic Oscillation and European climate. Nature, 398(6725):320–323.

Cited p. 7 et 151.

Roedder, E. (1962a). Ancient fluids in crystals. Scientific American, 207(4):38–47.

Cited p. 24 et 50.

Roedder, E. (1962b). Studies of fluid inclusions; Part 1, Low temperature application of a dual-purpose freezing and heating stage. Economic Geology, 57(7):1045–1061.

Cited p. 87.

Roedder, E. (1963). Studies of fluid inclusions; [Part] 2, Freezing data and their interpretation. Economic Geology, 58(2):167–211.

Cited p. 87.

Roedder, E. (1984). Changes in Inclusions after Trapping. In Fluid inclusions, volume 12, pages 47 – 78. Mineralogical Society of America.

Cited p. 24, 46 et 53.

Roedder, E. and Belkin, H. E. (1979). Application of Studies of Fluid Inclusions in Permian Salado Salt, New Mexico, to Problems of Siting the Waste Isolation Pilot Plant. In McCarthy, G. J., Schwoebel, R. L., Potter, R. W., Friedman, A. M., Moore, J. G., Burkholder, H. C., and Lutze, W., editors, Scientific Basis for Nuclear Waste Management, pages 313–321. Springer US.

Cited p. 86.

Roedder, E. and Bodnar, R. (1980). Geologic pressure determinations from fluid inclusion studies. Annual review of earth and planetary sciences, 8(1):263–301.

Cited p. 24.

Rohling, E. J., Cane, T. R., Cooke, S., Sprovieri, M., Bouloubassi, I., Emeis, K. C., Schiebel, R., Kroon, D., Jorissen, F. J., Lorre, A., and Kemp, A. E. S. (2002). African monsoon variability during the previous interglacial maximum. Earth and Planetary Science Letters, 202(1):61–75.

Cited p. 148.

Rohling, E. J., Marino, G., and Grant, K. M. (2015). Mediterranean climate and oceanography, and the periodic development of anoxic events (sapropels). Earth-Science Reviews, 143:62–97.

Cited p. 145.

Rohling, E. J., Sprovieri, M., Cane, T., Casford, J. S. L., Cooke, S., Bouloubassi, I., Emeis, K. C., Schiebel, R., Rogerson, M., Hayes, A., Jorissen, F. J., and Kroon, D. (2004). Reconstructing past planktic foraminiferal habitats using stable isotope data: a case history for Mediterranean sapropel S5. Marine Micropaleontology, 50(1):89–123.

Cited p. 148.

Rosenberg, T. M., Preusser, F., Risberg, J., Plikk, A., Kadi, K. A., Matter, A., and Fleitmann, D. (2013). Middle and Late Pleistocene humid periods recorded in palaeolake deposits of the Nafud desert, Saudi Arabia. Quaternary Science Reviews, 70:109–123.

Cited p. 145.

Rossignol-Strick, M. (1985). Mediterranean Quaternary sapropels, an immediate response of the African monsoon to variation of insolation. Palaeogeography, Palaeoclimatology, Palaeoecology, 49(3):237–263.

Cited p. 146.

Rossignol-Strick, M., Nesteroff, W., Olive, P., and Vergnaud-Grazzini, C. (1982). After the deluge: Mediterranean stagnation and sapropel formation. Nature, 295(5845):105–110.

Cited p. 146.

Rossignol-Strick, M. and Paterne, M. (1999). A synthetic pollen record of the eastern Mediterranean sapropels of the last 1 Ma: implications for the time-scale and formation of sapropels. Marine Geology, 153(1):221–237.

Cited p. 146.

Rothwell, W. S. and Greenler, R. G. (1964). Annealing and Yield Stress of NaCl Single Crystals. Journal of the American Ceramic Society, 47(11):585–587.

Cited p. 61.

Rouault, M., Reason, C. J. C., Lutjeharms, J. R. E., and Beljaars, A. C. M. (2003). Underestimation of Latent and Sensible Heat Fluxes above the Agulhas Current in NCEP and ECMWF Analyses. J. Climate, 16(4):776–782.

Cited p. 4.

Rousseau, D. D., Hatté, C., Guiot, J., Duzer, D., Schevin, P., and Kukla, G. (2006). Reconstruction of the Grande Pile Eemian using inverse modeling of biomes and 13c. Quaternary Science Reviews, 25(21):2806–2819.

Cited p. 17 et 153.

Rowland, D., Königsberger, E., Hefter, G., and May, P. M. (2015). Aqueous electrolyte solution modelling: Some limitations of the Pitzer equations. Applied Geochemistry, 55:170–183.

Cited p. 90 et 91.

Rowland, D. and May, P. M. (2013). A Pitzer-based characterization of aqueous magnesium chloride, calcium chloride and potassium iodide solution densities to high temperature and pressure. Fluid Phase Equilibria, 338:54–62.

Cited p. 90.

S. Z. Rogers, P. and S. Pitzer, K. (1982). Volumetric Properties of Aqueous Sodium Chloride Solution. Journal of Physical and Chemical Reference Data - J PHYS CHEM REF DATA, 11:15–81.

Cited p. 90.

Sade, A., Hall, J. K., Sade, H., Amit, G., Tibor, G., Schulze, B., Gur-Arieh, L., Ten Brink, U., Ben-Avraham, Z., and Keller, C. (2014). Multibeam bathymetric map of the Dead Sea. Geological Survey of Israel Report GSI/01.

Cited p. 133 et 157.

Salhov, S., Teleman, E., Shulman, H., Gardosh, M., and Baker, S. (1994). Sedom Deep-1, Geological completion report. The Israel.

Cited p. 141.

Saluja, P. P., Jobe, D. J., LeBlanc, J. C., and Lemire, R. J. (1995). Apparent molar heat capacities and volumes of mixed electrolytes:[NaCl (aq)+ $CaCl_2$ (aq)], [NaCl (aq)+ $MgCl_2$ (aq)], and [$CaCl_2$ (aq)+ $MgCl_2$ (aq)]. Journal of Chemical and Engineering Data, 40(2):398–406.

Cited p. 116 et 117.

Samartin, S., Heiri, O., Joos, F., Renssen, H., Franke, J., Brönnimann, S., and Tinner, W. (2017). Warm Mediterranean mid-Holocene summers inferred from fossil midge assemblages. Nature geoscience, 10(3):207.

Cited p. 22.

Sanchez Goñi, M. F. and Harrison, S. P. (2010). Millennial-scale climate variability and vegetation changes during the Last Glacial: Concepts and terminology. Quaternary Science Reviews, 29(21-22):2823–2827.

Cited p. 10.

Sanjuan, B., Michard, G., and Michard, A. (1990). Origine des substances dissoutes dans les eaux des sources thermales et des forages de la région Asal-Ghoubbet (République de Djibouti). Journal of Volcanology and Geothermal Research, 43(1):333–352.

Cited p. 87.

Satterfield, C. L., Lowenstein, T. K., Vreeland, R. H., and Rosenzweig, W. D. (2005a). Paleobrine temperatures, chemistries, and paleoenvironments of Silurian Salina Formation F-1 Salt, Michigan Basin, USA, from petrography and fluid inclusions in halite. Journal of Sedimentary Research, 75(4):534–546.

Cited p. 46 et 59.

Satterfield, C. L., Lowenstein, T. K., Vreeland, R. H., Rosenzweig, W. D., and Powers, D. W. (2005b). New evidence for 250 Ma age of halotolerant bacterium from a Permian salt crystal. Geology, 33(4):265–268.

Cited p. 46.

Sawamura, S., Egoshi, N., Setoguchi, Y., and Matsuo, H. (2007). Solubility of sodium chloride in water under high pressure. Fluid phase equilibria, 254(1-2):158–162.

Cited p. 31, 37, 60, 73, 92 et 94.

Scaife, A. A., Copsey, D., Gordon, C., Harris, C., Hinton, T., Keeley, S., O'Neill, A., Roberts, M., and Williams, K. (2011). Improved Atlantic winter blocking in a climate model. Geophysical Research Letters, 38(23).

Cited p. 7.

Scaife, A. A., Ineson, S., Knight, J. R., Gray, L., Kodera, K., and Smith, D. M. (2013). A mechanism for lagged North Atlantic climate response to solar variability. Geophysical Research Letters, 40(2):434–439.

Cited p. 7.

Schnitker, D. (1979). The deep waters of the western North Atlantic during the past 24,000 years, and the re-initiation of the Western Boundary Undercurrent. Marine Micropaleontology, 4:265–280.

Cited p. 14.

Schouten, S., Hopmans, E. C., SchefuSS, E., and Damste, J. S. S. (2002). Distributional variations in marine crenarchaeotal membrane lipids: a new tool for reconstructing ancient sea water temperatures? Earth and Planetary Science Letters, 204(1-2):265–274.

Cited p. 16.

Schreiber, B. C. and El Tabakh, M. (2000). Deposition and early alteration of evaporites. Sedimentology, 47:215–238.

Cited p. 45.

Shackleton, N. (1967). Oxygen Isotope Analyses and Pleistocene Temperatures Re-assessed. Nature, 215(5096):15–17.

Cited p. 8 et 12.

Shackleton, N. J. (2000). The 100,000-year ice-age cycle identified and found to lag temperature, carbon dioxide, and orbital eccentricity. Science, 289(5486):1897–1902.

Cited p. 15.

Shackleton, N. J., Chapman, M., Sánchez-Goñi, M. F., Pailler, D., and Lancelot, Y. (2002). The Classic Marine Isotope Substage 5e. Quaternary Research, 58(1):14–16.

Cited p. 153.

Shackleton, N. J. and Opdyke, N. D. (1973). Oxygen isotope and palaeomagnetic stratigraphy of Equatorial Pacific core V28-238: Oxygen isotope temperatures and ice volumes on a 10^5 year and 10^6 year scale. Quaternary research, 3(1):39–55.

Cited p. 12.

Shackleton, N. J., Sánchez-Goñi, M. F., Pailler, D., and Lancelot, Y. (2003). Marine Isotope Substage 5e and the Eemian Interglacial. Global and Planetary Change, 36(3):151–155.

Cited p. 8, 145 et 150.

Shackleton, N. J. and West, R. G. (1969). The last interglacial in the marine and terrestrial records. Proceedings of the Royal Society of London. Series B. Biological Sciences, 174(1034):135–154.

Cited p. 8.

Shakun, J. D. and Carlson, A. E. (2010). A global perspective on Last Glacial Maximum to Holocene climate change. Quaternary Science Reviews, 29(15):1801–1816.

Cited p. 9 et 14.

Shakun, J. D., Clark, P. U., He, F., Marcott, S. A., Mix, A. C., Liu, Z., Otto-Bliesner, B., Schmittner, A., and Bard, E. (2012). Global warming preceded by increasing carbon dioxide concentrations during the last deglaciation. Nature, 484(7392):49.

Cited p. 15.

Sharp, J. D., Albehadili, M. H. M., Millero, F. J., and Woosley, R. J. (2015). Estimating the Density and Compressibility of Natural Hypersaline Brines Using the Pitzer Ionic Interaction Model. Aquatic Geochemistry, 21(1):11–29.

Cited p. 117.

Sierro, F. J., Hodell, D. A., Curtis, J. H., Flores, J. A., Reguera, I., ColmeneroHidalgo, E., Bárcena, M. A., Grimalt, J. O., Cacho, I., Frigola, J., and Canals, M. (2005). Impact of iceberg melting on Mediterranean thermohaline circulation during Heinrich events. Paleoceanography, 20(2).

Cited p. 149.

Sirota, I., Arnon, A., and Lensky, N. G. (2016). Seasonal variations of halite saturation in the Dead Sea. Water Resources Research, 52(9):7151–7162.

Cited p. 87, 122, 123, 142 et 167.

Sirota, I., Enzel, Y., and Lensky, N. G. (2017). Temperature seasonality control on modern halite layers in the Dead Sea: In situ observations. GSA Bulletin, 129(9-10):1181–1194.

Cited p. 123 et 167.

Sirota, I., Enzel, Y., and Lensky, N. G. (2018). Halite focusing and amplification of salt layer thickness: From the Dead Sea to deep hypersaline basins. Geology, 46(10):851–854.

Cited p. 123, 124, 134 et 143.

Skinner, B. J. (1953). Some considerations regarding liquid inclusions as geologic thermometers. Economic Geology, 48(7):541–550.

Cited p. 87.

Skrotzki, W. and Haasen, P. (1981). Hardening mechanisms of ionic crystals on {110} and {100} slip planes. J. Phys. Colloques, 42(C3):C3–119–C3–148.

Cited p. 61 et 63.

Small, R. J., Bacmeister, J., Bailey, D., Baker, A., Bishop, S., Bryan, F., Caron, J., Dennis, J., Gent, P., and Hsu, H.-m. (2014). A new synoptic scale resolving global climate simulation using the Community Earth System Model. Journal of Advances in Modeling Earth Systems, 6(4):1065–1094.

Cited p. 4 et 154.

Small, R. J., deSzoeke, S. P., Xie, S. P., ONeill, L., Seo, H., Song, Q., Cornillon, P., Spall, M., and Minobe, S. (2008). Airsea interaction over ocean fronts and eddies. Dynamics of Atmospheres and Oceans, 45(3):274–319.

Cited p. 154.

Small, R. J., Xie, S.-P., and Hafner, J. (2005). Satellite observations of mesoscale ocean features and copropagating atmospheric surface fields in the tropical belt. Journal of Geophysical Research: Oceans, 110(C2).

Cited p. 3.

Smith, D. M., Scaife, A. A., Eade, R., and Knight, J. R. (2016). Seasonal to decadal prediction of the winter North Atlantic Oscillation: emerging capability and future prospects. Quarterly Journal of the Royal Meteorological Society, 142(695):611–617.

Cited p. 7 et 151.

Sánchez Goñi, M. F., Eynaud, F., Turon, J. L., and Shackleton, N. J. (1999). High resolution palynological record off the Iberian margin: direct land-sea correlation for the Last Interglacial complex. Earth and Planetary Science Letters, 171(1):123–137.

Cited p. 146.

Sánchez Goñi, M. F., Landais, A., Fletcher, W. J., Naughton, F., Desprat, S., and Duprat, J. (2008). Contrasting impacts of DansgaardOeschger events over a western European latitudinal transect modulated by orbital parameters. Quaternary Science Reviews, 27(11):1136–1151.

Cited p. 10.

Sorby, H. C. (1858). On the Microscopical, Structure of Crystals, indicating the Origin of Minerals and Rocks. Quarterly Journal of the Geological Society, 14(1-2):453–500.

Cited p. 24 et 45.

Sourirajan, S. and Kennedy, G. C. (1962). The system H_2O-NaCl at elevated temperatures and pressures. Am J Sci, 260(2):115–141.

Cited p. 87.

Spadin, F., Marti, D., Hidalgo-Staub, R., Ricka, J., Fleitmann, D., and Frenz, M. (2015). Technical note: how accurate can stalagmite formation temperatures be determined using vapour bubble radius measurements in fluid inclusions? Climate of the Past, 11:905–913.

Cited p. 25 et 66.

Speranza, G., Cosentino, D., Tecce, F., and Faccenna, C. (2013). Paleoclimate reconstruction during the Messinian evaporative drawdown of the Mediterranean Basin: insights from microthermometry on halite fluid inclusions. Geochemistry, Geophysics, Geosystems, 14(12):5054–5077.

Cited p. 46, 50 et 59.

Steffensen, J. P., Andersen, K. K., Bigler, M., Clausen, H. B., Dahl-Jensen, D., Fischer, H., Goto-Azuma, K., Hansson, M., Johnsen, S. J., Jouzel, J., Masson-Delmotte, V., Popp, T., Rasmussen, S. O., Röthlisberger, R., Ruth, U., Stauffer, B., Siggaard-Andersen, M.-L., Sveinbjörnsdóttir, r. E., Svensson, A., and White, J. W. C. (2008). High-Resolution Greenland Ice Core Data Show Abrupt Climate Change Happens in Few Years. Science, 321(5889):680–684.

Cited p. 9.

Stein, M. (2001). The sedimentary and geochemical record of Neogene-Quaternary water bodies in the Dead Sea Basin - inferences for the regional paleoclimatic history. Journal of Paleolimnology, 26(3):271–282.

Cited p. 126.

Stein, M., BenAvraham, Z., and Goldstein, S. L. (2011). Dead Sea deep cores: A window into past climate and seismicity. Eos, Transactions American Geophysical Union, 92(49):453–454.

Cited p. 120.

Stein, M., Starinsky, A., Katz, A., Goldstein, S. L., Machlus, M., and Schramm, A. (1997). Strontium isotopic, chemical, and sedimentological evidence for the evolution of Lake Lisan and the Dead Sea. Geochimica et Cosmochimica Acta, 61(18):3975–3992.

Cited p. 96 et 141.

Stein, M., Torfstein, A., Gavrieli, I., and Yechieli, Y. (2010). Abrupt aridities and salt deposition in the post-glacial Dead Sea and their North Atlantic connection. Quaternary Science Reviews, 29(3):567–575.

Cited p. 141.

Steinhorn, I. (1983). In situ salt precipitation at the Dead Sea. Limnology and Oceanography, 28(3):580–583.

Cited p. 123.

Steinhorn, I. (1985). The disappearance of the long term meromictic stratification of the Dead Sea. Limnology and Oceanography, 30(3):451–472.

Cited p. 122.

Stephenson, D. B., Wanner, H., Brönnimann, S., and Luterbacher, J. (2003). The history of scientific research on the North Atlantic Oscillation. Washington DC American Geophysical Union Geophysical Monograph Series, 134:37–50.

Cited p. 6.

Stern, M. E. (1960). The salt-fountain and thermohaline convection. Tellus, 12(2):172–175.

Cited p. 123.

Sterner, S. M. and Bodnar, R. J. (1984). Synthetic fluid inclusions in natural quartz I. Compositional types synthesized and applications to experimental geochemistry. Geochimica et Cosmochimica Acta, 48(12):2659–2668.

Cited p. 87.

Stiller, M. and Chung, Y. C. (1984). Radium in the Dead Sea: A possible tracer for the duration of meromixis1. Limnology and Oceanography, 29(3):574–586.

Cited p. 122.

Stocker, T. F. (1998). The seesaw effect. Science, 282(5386):61–62.

Cited p. 10 et 15.

Stocker, T. F. and Johnsen, S. J. (2003). A minimum thermodynamic model for the bipolar seesaw. Paleoceanography, 18(4).

Cited p. 10 et 15.

Stott, L., Poulsen, C., Lund, S., and Thunell, R. (2002). Super ENSO and Global Climate Oscillations at Millennial Time Scales. Science, 297(5579):222–226.

Cited p. 153.

Stuiver, M., Grootes, P. M., and Braziunas, T. F. (1995). The GISP2 δ^{18}O Climate Record of the Past 16,500 Years and the Role of the Sun, Ocean, and Volcanoes. Quaternary Research, 44(3):341–354.

Cited p. 8.

Sturluson, S. and Brodeur, A. G. (2006). The Prose Edda: Tales from Norse Mythology. Courier Corporation. Google-Books-ID: Wj81AwAAQBAJ.

Cited p. 6.

Sun, X.-h., Zhao, Y.-j., Liu, C.-l., Jiao, P.-c., Zhang, H., and Wu, C.-h. (2017). Paleoclimatic information recorded in fluid inclusions in halites from Lop Nur, Western China. Scientific reports, 7(1):16411.

Cited p. 46 et 59.

Szomor, P. O. (1968). Elastic Constants and Tensile Strength of NaCl-Type Alkali Halides. physica status solidi (b), 28(2):529–537.

Cited p. 48.

Tabor, C. R. and Poulsen, C. J. (2016). Simulating the mid-Pleistocene transition through regolith removal. Earth and Planetary Science Letters, 434:231–240.

Cited p. 15.

Tan, N., Ladant, J.-B., Ramstein, G., Dumas, C., Bachem, P., and Jansen, E. (2018). Dynamic Greenland ice sheet driven by pCO_2 variations across the Pliocene Pleistocene transition. Nature communications, 9(1):4755.

Cited p. 15.

Taylor, G. I. (1934). The mechanism of plastic deformation of crystals. Part I.Theoretical. Proceedings of the Royal Society of London. Series A, Containing Papers of a Mathematical and Physical Character, 145(855):362–387.

Cited p. 83.

Teisserenc de Bort, L. P. (1883). Etude sur lhiver de 187980 et recherches sur linfluence de la position des grands centres daction de latmosphère dans les hivers anormaux. Ann. de la soc. Météor. de France, 31:70–79.

Cited p. 6.

Thompson, D. W., Lee, S., and Baldwin, M. P. (2003). Atmospheric processes governing the northern hemisphere annular mode/North Atlantic oscillation. Geophysical Monograph-American Geophysical Union, 134:81–112.

Cited p. 7.

Thompson, D. W. J. and Wallace, J. M. (1998). The Arctic oscillation signature in the wintertime geopotential height and temperature fields. Geophysical Research Letters, 25(9):1297–1300.

Cited p. 6.

Thompson, D. W. J. and Wallace, J. M. (2001). Regional Climate Impacts of the Northern Hemisphere Annular Mode. Science, 293(5527):85–89.

Cited p. 5 et 6.

Timofeeff, M. N., Lowenstein, T. K., Brennan, S. T., Demicco, R. V., Zimmermann, H., Horita, J., and Von Borstel, L. E. (2001). Evaluating seawater chemistry from fluid inclusions in halite: Examples from modern marine and nonmarine environments. Geochimica et Cosmochimica Acta, 65(14):2293–2300.

Cited p. 45.

Tokinaga, H., Tanimoto, Y., and Xie, S.-P. (2005). SST-Induced Surface Wind Variations over the BrazilMalvinas Confluence: Satellite and In Situ Observations. J. Climate, 18(17):3470–3482.

Cited p. 4.

Torfstein, A. (2019). Climate cycles in the southern Levant and their global climatic connections. Quaternary Science Reviews, 221:105881.

Cited p. 120, 139 et 146.

Torfstein, A., Goldstein, S. L., Kushnir, Y., Enzel, Y., Haug, G., and Stein, M. (2015). Dead Sea drawdown and monsoonal impacts in the Levant during the last interglacial. Earth and Planetary Science Letters, 412:235–244.

Cited p. 120, 127, 128, 144, 146, 147 et 148.

Torfstein, A., Haase-Schramm, A., Waldmann, N., Kolodny, Y., and Stein, M. (2009). U-series and oxygen isotope chronology of the mid-Pleistocene Lake Amora (Dead Sea basin). Geochimica et Cosmochimica Acta, 73(9):2603–2630.

Cited p. 141, 143 et 144.

Touret, J. (2001). Fluids in metamorphic rocks. Lithos, 55(1-4):1–25.

Cited p. 24.

Trouet, V., Esper, J., Graham, N. E., Baker, A., Scourse, J. D., and Frank, D. C. (2009). Persistent Positive North Atlantic Oscillation Mode Dominated the Medieval Climate Anomaly. Science, 324(5923):78–80.

Cited p. 6.

Turley, J. and Sines, G. (1971). The anisotropy of Young\textquotesingles modulus, shear modulus and Poisson\textquotesingles ratio in cubic materials. J. Phys. D: Appl. Phys., 4(2):264–271.

Cited p. 92.

Turney, C. S. M. and Jones, R. T. (2010). Does the Agulhas Current amplify global temperatures during superinterglacials? Journal of Quaternary Science, 25(6):839–843.

Cited p. 145.

Tzedakis, P. C. (2005). Towards an understanding of the response of southern European vegetation to orbital and suborbital climate variability. Quaternary Science Reviews, 24(14):1585–1599.

Cited p. 154.

Tzedakis, P. C. (2007). Seven ambiguities in the Mediterranean palaeoenvironmental narrative. Quaternary Science Reviews, 26(17):2042–2066.

Cited p. 146.

Tzedakis, P. C., Drysdale, R. N., Margari, V., Skinner, L. C., Menviel, L., Rhodes, R. H., Taschetto, A. S., Hodell, D. A., Crowhurst, S. J., Hellstrom, J. C., Fallick, A. E., Grimalt, J. O., McManus, J. F., Martrat, B., Mokeddem, Z., Parrenin, F., Regattieri, E., Roe, K., and Zanchetta, G. (2018). Enhanced climate instability in the North Atlantic and southern Europe during the Last Interglacial. Nat Commun, 9(1):1–14.

Cited p. 148 et 150.

Tzedakis, P. C., Frogley, M. R., and Heaton, T. H. E. (2003). Last Interglacial conditions in southern Europe: evidence from Ioannina, northwest Greece. Global and Planetary Change, 36(3):157–170.

Cited p. 146, 149 et 154.

Tzedakis, P. C., Hooghiemstra, H., and Pälike, H. (2006). The last 1.35 million years at Tenaghi Philippon: revised chronostratigraphy and long-term vegetation trends. Quaternary Science Reviews, 25(23):3416–3430.

Cited p. 146.

Vaks, A., Bar-Matthews, M., Ayalon, A., Matthews, A., Frumkin, A., Dayan, U., Halicz, L., Almogi-Labin, A., and Schilman, B. (2006). Paleoclimate and location of the border between Mediterranean climate region and the SaharoArabian Desert as revealed by speleothems from the northern Negev Desert, Israel. Earth and Planetary Science Letters, 249(3):384–399.

Cited p. 120 et 146.

Vaks, A., Bar-Matthews, M., Ayalon, A., Matthews, A., Halicz, L., and Frumkin, A. (2007). Desert speleothems reveal climatic window for African exodus of early modern humans. GEOLOGY, 35(9).

Cited p. 120.

Vaks, A., Bar-Matthews, M., Matthews, A., Ayalon, A., and Frumkin, A. (2010). Middle-Late Quaternary paleoclimate of northern margins of the Saharan-Arabian Desert: reconstruction from speleothems of Negev Desert, Israel. Quaternary Science Reviews, 29(19):2647–2662.

Cited p. 120, 146 et 148.

Valiashko, M. G. (1956). Geochemistry of bromide in the processes of salt deposition and the use of the bromide content as a genetic and prospecting tool. Geochemistry USSR, 6:570–587.

Cited p. 45.

Van den Kerkhof, A. M. and Hein, U. F. (2001). Fluid inclusion petrography. Lithos, 55(1-4):27–47.

Cited p. 24.

van Loon, H. and Rogers, J. C. (1978). The Seesaw in Winter Temperatures between Greenland and Northern Europe. Part I: General Description. Mon. Wea. Rev., 106(3):296–310.

Cited p. 6.

Vengosh, A., Chivas, A. R., Starinsky, A., Kolodny, Y., Baozhen, Z., and Pengxi, Z. (1995). Chemical and boron isotope compositions of non-marine brines from the Qaidam Basin, Qinghai, China. Chemical Geology, 120(1):135–154.

Cited p. 87.

Viau, A. E., Gajewski, K., Sawada, M. C., and Fines, P. (2006). Millennial-scale temperature variations in North America during the Holocene. Journal of Geophysical Research: Atmospheres, 111(D9).

Cited p. 21.

Vitagliano, V. and Lyons, P. A. (1956). Diffusion coefficients for aqueous solutions of sodium chloride and barium chloride. Journal of the American Chemical Society, 78(8):1549–1552.

Cited p. 37.

Vityk, M. O. and Bodnar, R. J. (1998). Statistical microthermometry of synthetic fluid inclusions in quartz during decompression reequilibration. Contrib Mineral Petrol, 132(2):149–162.

Cited p. 64.

Volmer, M. and Weber, . (1926). Keimbildung in übersättigten Gebilden. Zeitschrift für Physikalische Chemie, 119U(1):277–301.

Cited p. 61.

Waelbroeck, C., Labeyrie, L., Michel, E., Duplessy, J. C., McManus, J. F., Lambeck, K., Balbon, E., and Labracherie, M. (2002). Sea-level and deep water temperature changes derived from benthic foraminifera isotopic records. Quaternary Science Reviews, 21(1):295–305.

Cited p. 8.

Wagner, W. and PruSS, A. (2002). The IAPWS Formulation 1995 for the Thermodynamic Properties of Ordinary Water Substance for General and Scientific Use. Journal of Physical and Chemical Reference Data, 31(2):387–535.

Cited p. 36 et 88.

Waldmann, N. and , . (2002). The geology of the Samra formation in the Dead Sea basin. Hebrew University of Jerusalem.

Cited p. 123 et 143.

Waldmann, N., Starinsky, A., and Stein, M. (2007). Primary carbonates and Ca-chloride brines as monitors of a paleo-hydrological regime in the Dead Sea basin. Quaternary Science Reviews, 26(17):2219–2228.

Cited p. 144.

Waldmann, N., Stein, M., Ariztegui, D., and Starinsky, A. (2009). Stratigraphy, depositional environments and level reconstruction of the last interglacial Lake Samra in the Dead Sea basin. Quaternary Research, 72(1):1–15.

Cited p. 133, 139, 141, 144, 146 et 163.

Waldmann, N., Torfstein, A., and Stein, M. (2010). Northward intrusions of low- and mid-latitude storms across the Saharo-Arabian belt during past interglacials. Geology, 38(6):567–570.

Cited p. 146, 147 et 148.

Walrafen, G. E. (1964). Raman Spectral Studies of Water Structure. J. Chem. Phys., 40(11):3249–3256.

Cited p. 40.

Wang, Y., Cheng, H., Edwards, R. L., Kong, X., Shao, X., Chen, S., Wu, J., Jiang, X., Wang, X., and An, Z. (2008). Millennial-and orbital-scale changes in the East Asian monsoon over the past 224,000 years. Nature, 451(7182):1090.

Cited p. 10.

Wanner, H., Beer, J., Bütikofer, J., Crowley, T. J., Cubasch, U., Flückiger, J., Goosse, H., Grosjean, M., Joos, F., and Kaplan, J. O. (2008). Mid-to Late Holocene climate change: an overview. Quaternary Science Reviews, 27(19-20):1791–1828.

Cited p. 10.

Warren, J. K. (2010). Evaporites through time: Tectonic, climatic and eustatic controls in marine and nonmarine deposits. Earth-Science Reviews, 98(3):217–268.

Cited p. 45.

Warren, J. K. (2016). Evaporites: A geological compendium. Springer International Publishing, Berlin.

Cited p. 45.

Weaver, A. J., Saenko, O. A., Clark, P. U., and Mitrovica, J. X. (2003). Meltwater Pulse 1a from Antarctica as a Trigger of the Bølling-Allerød Warm Interval. Science, 299(5613):1709–1713.

Cited p. 8.

Weber, N., Yechieli, Y., Stein, M., Yokochi, R., Gavrieli, I., Zappala, J., Mueller, P., and Lazar, B. (2018). The circulation of the Dead Sea brine in the regional aquifer. Earth and Planetary Science Letters, 493:242–261.

Cited p. 141 et 163.

Weinberger, R., Begin, Z. B., Waldmann, N., Gardosh, M., Baer, G., Frumkin, A., and Wdowinski, S. (2006). Quaternary rise of the Sedom diapir, Dead Sea basin. SPECIAL PAPERS-GEOLOGICAL SOCIETY OF AMERICA, 401:33.

Cited p. 120.

Weissenborn, P. K. and Pugh, R. J. (1996). Surface Tension of Aqueous Solutions of Electrolytes: Relationship with Ion Hydration, Oxygen Solubility, and Bubble Coalescence. Journal of Colloid and Interface Science, 184(2):550–563.

Cited p. 62, 64 et 82.

Wentz, F. J., Gentemann, C., Smith, D., and Chelton, D. (2000). Satellite Measurements of Sea Surface Temperature Through Clouds. Science, 288(5467):847–850.

Cited p. 3.

White, W. B. and Annis, J. L. (2003). Coupling of Extratropical Mesoscale Eddies in the Ocean to Westerly Winds in the Atmospheric Boundary Layer. J. Phys. Oceanogr., 33(5):1095–1107.

Cited p. 3.

Willeit, M., Ganopolski, A., Calov, R., and Brovkin, V. (2019). Mid-Pleistocene transition in glacial cycles explained by declining CO_2 and regolith removal. Science Advances, 5(4):eaav7337.

Cited p. 15.

Willeit, M., Ganopolski, A., Calov, R., Robinson, A., and Maslin, M. (2015). The role of CO_2 decline for the onset of Northern Hemisphere glaciation. Quaternary Science Reviews, 119:22–34.

Cited p. 15.

Willison, J., Robinson, W. A., and Lackmann, G. M. (2013). The Importance of Resolving Mesoscale Latent Heating in the North Atlantic Storm Track. J. Atmos. Sci., 70(7):2234–2250.

Cited p. 4.

Witherow, R. A. and Lyons, W. B. (2011). The fate of minor alkali elements in the chemical evolution of salt lakes. Saline Systems, 7(1):2.

Cited p. 108.

Wolff, E. W., Chappellaz, J., Blunier, T., Rasmussen, S. O., and Svensson, A. (2010). Millennial-scale variability during the last glacial: The ice core record. Quaternary Science Reviews, 29(21):2828–2838.

Cited p. 8 et 10.

Xu, Y., Liu, C., Cao, Y., and Zhang, H. (2019). Quantitative temperature recovery from middle Eocene halite fluid inclusions in the easternmost Tethys realm. International Journal of Earth Sciences, 108(1):173–182.

Cited p. 46.

Yang, C. (2016). Homogenization Temperatures of All-liquid Fluid Inclusions in Halite from the Middle Devonian Prairie Evaporite, Southern Saskatchewan. In Summary of Investigations 2016, Volume 1, Saskatchewan Geological Survey, Saskatchewan Ministry of the Economy, Miscellaneous Report 2016-4.1, Paper A-1, page 13.

Cited p. 46.

Yechieli, Y., Magaritz, M., Levy, Y., Weber, U., Kafri, U., Woelfli, W., and Bonani, G. (1993). Late Quaternary Geological History of the Dead Sea Area, Israel. Quaternary Research, 39(1):59–67.

Cited p. 141.

Young, T. (1805). An essay on the cohesion of fluids. Philosophical Transactions of the Royal Society of London, 95:65–87.

Cited p. 64.

Young, T. F. and Smith, M. B. (1954). Thermodynamic Properties of Mixtures of Electrolytes in Aqueous Solutions. J. Phys. Chem., 58(9):716–724.

Cited p. 91 et 105.

Zagwijn, W. H. (1996). An analysis of Eemian climate in Western and Central Europe. Quaternary Science Reviews, 15(5):451–469.

Cited p. 153.

Zak, I. (1997). Evolution of the Dead Sea brines. In Oxford monographs on geology and geophysics, volume 36, pages 133–144. Oxford University Press, New York.

Cited p. 96.

Zambito, J. J. and Benison, K. C. (2013). Extremely high temperatures and paleoclimate trends recorded in Permian ephemeral lake halite. Geology, 41(5):587–590.

Cited p. 46.

Zanchetta, G., Regattieri, E., Giaccio, B., Wagner, B., Sulpizio, R., Francke, A., Vogel, L. H., Sadori, L., Masi, A., Sinopoli, G., Lacey, J. H., Leng, M. L., and Leicher, N. (2015). Aligning MIS5 proxy records from Lake Ohrid (FYROM) with independently dated Mediterranean archives: implications for core chronology. Biogeosciences Discussions, 12:16979–17007.

Cited p. 149.

Zezin, D. and Driesner, T. (2017). Thermodynamic properties of aqueous KCl solution at temperatures to 600 K, pressures to 150 MPa, and concentrations to saturation. Fluid Phase Equilibria, 453:24–39.

Cited p. 90.

Zezin, D., Driesner, T., and Sanchez-Valle, C. (2014a). Volumetric Properties of Mixed Electrolyte Aqueous Solutions at Elevated Temperatures and Pressures. The System KClNaClH2o to 523.15 K, 40 MPa, and Ionic Strength from (0.1 to 5.8) molů kg1. Journal of Chemical & Engineering Data, 59(3):736–749.

Cited p. 90.

Zezin, D., Driesner, T., Scott, S., Sanchez-Valle, C., and Wagner, T. (2014b). Volumetric Properties of Mixed Electrolyte Aqueous Solutions at Elevated Temperatures and Pressures. The Systems $CaCl_2NaClH_2O$ and $MgCl_2NaClH_2O$ to 523.15 K, 70 MPa, and Ionic Strength from (0.1 to 18) $mol{\cdot}kg^1$. J. Chem. Eng. Data, 59(8):2570–2588.

Cited p. 82, 116 et 117.

Zhang, H., Lü, F., Mischke, S., Fan, M., Zhang, F., and Liu, C. (2017). Halite fluid inclusions and the late Aptian sea surface temperatures of the Congo Basin, northern South Atlantic Ocean. Cretaceous Research, 71:85–95.

Cited p. 46, 59 et 83.

Zhang, H., Liu, C., Zhao, Y., Mischke, S., Fang, X., and Ding, T. (2015). Quantitative temperature records of mid Cretaceous hothouse: Evidence from halite fluid inclusions. Palaeogeography, Palaeoclimatology, Palaeoecology, 437:33–41.

Cited p. 46, 59 et 83.

Zhang, X.-Y., Meng, F.-W., Li, W.-X., Tang, Q.-L., and Ni, P. (2016). Reconstruction of Late Cretaceous coastal paleotemperature from halite deposits of the Late Cretaceous Nongbok Formation (Khorat Plateau, Laos). Palaeoworld, 25(3):425–430.

Cited p. 46.

Zhang, Y. (1998). Mechanical and phase equilibria in inclusionhost systems. Earth and Planetary Science Letters, 157(3-4):209–222.

Cited p. 54 et 102.

Zhang, Y.-G. and Frantz, J. D. (1987). Determination of the homogenization temperatures and densities of supercritical fluids in the system NaClKClCaCl2H_2O using synthetic fluid inclusions. Chemical Geology, 64(3):335–350.

Cited p. 88.

Zhao, Y.-j., Zhang, H., Liu, C.-l., Liu, B.-k., Ma, L.-c., and Wang, L.-c. (2014). Late Eocene to early Oligocene quantitative paleotemperature record: Evidence from continental halite fluid inclusions. Scientific reports, 4:5776.

Cited p. 46.

Zhuravleva, A., Bauch, H. A., and Van Nieuwenhove, N. (2017). Last Interglacial (MIS5e) hydrographic shifts linked to meltwater discharges from the East Greenland margin. Quaternary Science Reviews, 164:95–109.

Cited p. 150.

Zimmerman, R. W. (1990). Compressibility of Sandstones. Elsevier. Google-Books-ID: tbQ6ye5yYukC.

Cited p. 91, 92, 95 et 102.

Zimmermann, H. (2001). On the origin of fluids included in Phanerozoic marine halitebasic interpretation strategies. Geochimica et Cosmochimica Acta, 65(1):35–45.

Cited p. 45.

Ziv, B., Dayan, U., Kushnir, Y., Roth, C., and Enzel, Y. (2006). Regional and global atmospheric patterns governing rainfall in the southern Levant. International Journal of Climatology, 26(1):55–73.

Cited p. 120.

Zou, Y. and Spolenak, R. (2013). Size-dependent plasticity in micron-and submicron-sized ionic crystals. Philosophical magazine letters, 93(7):431–438.

Cited p. 59 et 61.

Zou, Y. and Spolenak, R. (2015). Size-dependent plasticity in KCl and LiF single crystals: influence of orientation, temperature, pre-straining and doping. Philosophical Magazine, 95(16-18):1795–1813.

Cited p. 63.